Technische Universität München
TUM School of Engineering and Design

# Rotor Inflow Modeling using a Lattice-Boltzmann Method based Flow Solver

Bastian Horvat

Vollständiger Abdruck der von der TUM School of Engineering and Design der Technischen Universität München zur Erlangung eines

Doktors der Ingenieurwissenschaften (Dr.-Ing.)

genehmigten Dissertation.

Vorsitz: Prof. Dr. Ilkay Yavrucuk

Prüfende der Dissertation:

1. Prof. Dr.-Ing. Manfred Hajek
2. Prof. Dr. Juergen Rauleder

Die Dissertation wurde am 27.06.2024 bei der Technischen Universität München eingereicht und durch die TUM School of Engineering and Design am 11.10.2024 angenommen.

To all the PhD students who thought they would change the world.

# Acknowledgments

I would like to thank my doctoral supervisor, Prof. Manfred Hajek, for allowing me to join the institute and for his support over all these years. He provided an environment where I could freely explore the topics I was passionate about and built my PhD on top of that.

I would further like to thank Prof. Juergen Rauleder for bringing me on to the topic of LBM and for the chance he gave me to research abroad at Georgia Tech. Further, I am very happy about his ability to get funding for whatever was needed during my time.

Furthermore, Martina Thieme was key to accomplishing this work by managing all the bureaucratic hurdles of TUM and always having time for a good chat or an open ear when needed.

Of course, during my time, I had the pleasure of working with awesome colleagues who were there for technical discussions, encouragement when motivation was low, and just a great working environment. I especially want to thank my office colleagues Jakob Bludau and Andreas Reiser, whom I could talk to about anything: the good, the bad, and the random. Stefan Platzer, who always had the time for any technical questions or just a conversation to take my mind off things, Sören Süße for introducing me to the world of investment, and Sumeet Kumar, who not only gave technical advice but also made for a good talk, especially when motivation was low.

Last but not least, I would like to thank my friends and my wife for hearing me complain about my thesis all this time and still providing moral support and encouragement.

# Abstract

This thesis presents an analysis of rotor inflow models using a Lattice-Boltzmann method (LBM) based fluid solver, incorporating surrounding flow conditions and rotor interactions with its environment. The focus is on mid-fidelity rotor modeling, which consists of actuator disk and actuator line models. A novel actuator disk model was developed that is based on Bessel- Fourier functions enhancing a linear-harmonic disk model from literature. Additionally, two actuator line model approaches from literature were implemented, with different blade force distribution approaches within the flow simulation. Inflow sampling mechanisms, comprising integrated inflow sampling and inflow correction, were investigated. Environmental flow conditions and solid obstacles were modeled using precomputed external flow fields as boundary conditions for the rotor simulation domain. The well-established Peters–He inflow model was used for comparison, incorporating the superposition of external flow velocity to account for the surrounding flow environment.

The validation of the inflow models was split into two parts. The first consisted of an experimental teetering rotor with measurements available from hover and wind tunnel experiments. In hover conditions, all models captured trends in power, blade flap, and control inputs. The actuator line and Bessel-Fourier models accurately predicted radial load distribution, whereas the linear-harmonic model failed due to its limited base functions. Instabilities were observed in actuator line models with restricted force kernels and inflow correction at low $C_T$. Wind tunnel results showed significant deviations in power predictions across all inflow models, though control inputs and blade flapping were consistent. Optimal results were achieved with a tip loss of 9% and a flow field resolution of 64 cells per radius. The second part was the comparison of UH60A rotor results against measured wind tunnel and flight test data. The UH60A rotor simulations confirmed the validity of these parameters, showing excellent agreement with power measurements, control inputs, and blade flap angles.

The comparative study of inflow models in vortex encounters demonstrated consistent rotor thrust responses across all models. Power impacts were comparable for LBM models but stronger for the Peters–He model. Pitch moment impacts were significant for the Bessel-Fourier and actuator line models, while the linear-harmonic model exhibited strong filtering. In ship wake scenarios, the LBM models showed the influence on the wake due to landing platform blockage, unlike the Peters–He model.

In conclusion, the LBM inflow models provided comparable or superior results to the Peters–He model in hover and forward flight conditions. The Bessel-Fourier actuator disk and actuator line models accurately predicted radial loads, while the linear-harmonic model was insufficient due to its limited base functions. Inflow sampling and force distribution significantly impacted actuator line model stability, with a spherical force kernel and integral inflow sampling proving effective. LBM models outperformed the Peters–He model in environments containing obstacles, while in free flight, all models showed comparable responses.

# Kurzfassung

Diese Arbeit analysiert Rotordurchflussmodelle auf Basis eines Lattice-Boltzmann-Methode (LBM) basierten Strömungslösers, der die umgebenden Strömungsbedingungen und die Wechselwirkungen des Rotors mit seiner Umgebung berücksichtigt. Der Schwerpunkt liegt auf einer Mid-Fidelity-Rotormodellierung, die aus Aktuatorscheiben- und Aktuatorlinienmodellen besteht. Es wurde ein neuartiges Aktuatorscheibenmodell entwickelt, das auf Bessel-Fourier-Funktionen basiert und ein linear-harmonisches Scheibenmodell aus der Literatur verbessert. Zusätzlich wurden zwei Aktuatorlinienmodelle aus der Literatur implementiert, mit unterschiedlichen Ansätzen zur Verteilung der Blattkräfte innerhalb der Strömungssimulation. Unterschiedliche Ansätze zur Durchflussextraktion wurden untersucht, einerseits ein integraler Ansatz und andererseits ein Ansatz mit nachträglicher Korrektur. Umgebungsströmungsbedingungen und feste Hindernisse wurden mit Hilfe von vorab berechneten externen Strömungsfeldern als Randbedingungen für die Rotorsimulationsdomäne modelliert. Zum Vergleich wurde das bewährte Peters–He Durchflussmodell verwendet, bei dem die externe Strömungsgeschwindigkeit überlagert wird, um die umgebende Strömungsumgebung zu berücksichtigen.

Die Validierung der Durchflussmodelle wurde in zwei Teile aufgeteilt. Der erste Teil bestand aus einem experimentellen Teeterrotor mit Messungen aus Hover- und Windkanalexperimenten. Unter Hoverbedingungen erfassten alle Modelle die Trends bei Leistung, Blattklappe und Steuereingängen. Die Aktuatorlinien- und Bessel-Fourier-Modelle sagten die radiale Lastverteilung gut voraus, während das linear-harmonische Modell aufgrund seiner begrenzten Basisfunktionen Schwächen zeigte. Instabilitäten wurden bei Aktuatorlinienmodellen mit beschränkter Kraftverteilung und Durchflusskorrektur bei niedriger $C_T$ beobachtet. Die Ergebnisse im Windkanal zeigten signifikante Abweichungen bei den Leistungsvorhersagen für alle Durchflussmodelle, obwohl die Steuereingänge und das Schlagen der Blätter konsistent waren. Optimale Ergebnisse wurden mit einem Blattspitzenverlus von 9% und einer Strömungsfeldauflösung von 64 Zellen pro Radius erzielt. Der zweite Teil war der Vergleich der Ergebnisse des UH60A-Rotors mit gemessenen Windkanal- und Flugtestdaten. Die Simulationen des UH60A-Rotors bestätigten die Gültigkeit dieser Parameter und zeigten eine gute Übereinstimmung mit Leistungsmessungen, Steuereingängen und Blattklappenwinkeln. Die vergleichende Studie der Druchflussmodelle bei Wirbelbegegnungen zeigte konsistente Rotorschubreaktionen bei allen Modellen. Die Auswirkungen auf die Leistung waren bei den LBM-Modellen vergleichbar, bei dem Peters–He Modell jedoch stärker. Die Auswirkungen auf das Nickmoment waren bei den Bessel-Fourier- und Aktuatorlinienmodellen signifikant, während das linear-harmonische Modell eine starke Filterwirkung aufwies. In Schiffsnachlaufszenarien zeigten die LBM-Modelle den Einfluss auf den Rotorabwind aufgrund der Blockierung durch die Landeplattform, im Gegensatz zum Peters–He Modell.

Zusammenfassend lässt sich sagen, dass die LBM-Durchflussmodelle unter Hover- und Vorwärtsflugbedingungen vergleichbare oder bessere Ergebnisse als das Peters–He Modell liefern. Die Bessel-Fourier-Modelle für die Aktuatorscheibe und die Aktuatorlinie sagten die radialen Lasten genau voraus, während das linear-harmonische Modell aufgrund seiner beschränkten Basisfunktionen unzureichend war. Die Anströmung und die Kraftverteilung wirkten sich erheblich auf die Stabilität des Aktuatorlinienmodells aus, wobei sich eine sphärischer Kraftverteilung und eine integrale Durchflussauswertung als wirksam erwiesen. LBM-Modelle übertrafen das Peters–He Modell in Umgebungen mit Hindernissen, während im freien Flug alle Modelle vergleichbare Reaktionen zeigten.

# Contents

# Abbreviations

| | |
|---|---|
| ACE | actuator curve embedded |
| ACL | actuator line |
| AD | actuator disk |
| ALE | Arbitrary-Lagrangian-Eulerian |
| BB | bounce-back |
| BEMT | blade element momentum theory |
| BET | blade element theory |
| BGK | Bhatnagar–Gross–Krook |
| CFD | computational fluid dynamics |
| LBM | Lattice-Boltzmann method |
| LES | large eddy simulation |
| MBB | modified bounce-back |
| MRT | multiple relaxation time |
| RPM | revolutions per minute |
| VTM | vorticity transport method |
| VVPM | viscous vortex particle method |

# Nomenclature

| | |
|---|---|
| $\Omega_i$ | collision operator for i-th population |
| $\alpha$ | angle of attack |
| $\alpha_i$ | rotor disk angle of attack |
| $\alpha_s$ | shaft angle of attack |
| $J_i$ | i-th Bessel function of the first kind |
| $j_{j,i}$ | i-th root of the j-th Bessel function of the first kind |
| $t_{i,c}$ | cosine coefficient for linear harmonic coupling |
| $C_d$ | drag coefficient |
| $\chi$ | interpolation weight |
| $c$ | chord |
| $\overline{c}$ | average chord |
| $C_l$ | lift coefficient |
| $\cdot_c$ | denote cosine component |
| $c_s$ | lattice speed of sound |
| $C_s$ | Smagorinsky constant |
| $C_T$ | thrust coefficient |
| $C_{\mathrm{tl}}$ | tip loss factor |
| $C_{\mathrm{tl},\%}$ | tip loss factor percentage |
| $\delta$ | partial derivative |
| $\Delta\Psi$ | azimuth increment |
| $\Delta r$ | non-dimensional blade element span |
| $\Delta_s$ | Smagorinsky model filter width |

| | |
|---|---|
| $d_I$ | moving porosity for regularized Lattice-Boltzmann method (LBM) boundary implementation |
| $\Delta x$ | grid spacing |
| $\vec{e}_i$ | particle velocity vector in $i$ direction |
| $\epsilon$ | force distribution kernel width |
| $\epsilon_{\mathrm{min}}$ | minimum force distribution kernel width |
| $\eta$ | distribution kernel function |
| $F$ | external lattice force, e.g. rotor forces |
| $F_i$ | forcing term |
| $f_i$ | particle distribution function with velocity in $i$ |
| $f_i^{eq}$ | equilibrium partice distribution function in $i$ direction |
| $f_{\bar{i}}$ | distribution function in opposite direction of $f_i$ |
| $F$ | physical force term |
| $f_{\mathrm{tl}}$ | local tip loss factor |
| $\underline{I}$ | identity matrix |
| $J_{CV}$ | momentum change per control volume |
| $J_{flx}$ | momentum flux |
| $\cdot_0$ | denotes mean component |
| $\mu$ | advance ratio |
| $\mu_t$ | eddy viscosity |
| $M_x$ | rotor hub moment around x-axis |
| $M_y$ | rotor hub moment around y-axis |
| $N_{\mathrm{r}}$ | number of radial Bessel functions |
| $N_{\mathrm{blade}}$ | number of rotor blades |

| | |
|---|---|
| $N_{\mathrm{BE}}$ | number of blade elements |
| $N_{\mathrm{cell}}$ | number of cells |
| $N_{\mathrm{h}}$ | number of harmonics |
| $N_{\mathrm{h},\Psi}$ | number of harmonics in azimuth direction |
| $N_{\Psi}$ | number of discrete azimuth positions |
| $\nu^*$ | non-dimensional viscosity |
| $\Delta\tilde{p}$ | reconstructed pressure from base functions |
| $p_{ij}$ | pressure coefficient for Bessel-Fourier coupling |
| $p$ | pressure |
| $\Psi$ | azimuth angle |
| $q$ | number of $f_i$ |
| $R$ | rotor radius |
| $r$ | non-dimensional radial coordinate |
| $r_{rc}$ | non-dimensional radial root cut out position |
| $\rho$ | density |
| s | fluid domain scaling factor |
| $t_{i,s}$ | sine coefficient for linear harmonic coupling |
| $\cdot_s$ | denote sine component |
| $\underline{S}$ | stress tensor |
| $t$ | time |
| $\tau$ | relaxation time in BGK collision |
| $\Theta$ | blade pitch |
| $\Theta_0$ | measured blade pitch |

| | |
|---|---|
| $T$ | rotor thrust |
| $T_{\text{blade}}$ | total blade thrust |
| $u$ | velocity |
| $u^*$ | force adjusted lattice velocity |
| $u_b$ | boundary velocity |
| $u_\infty$ | free stream velocity |
| $\vec{v}_i$ | inflow velocity |
| $V_{\text{tip}}$ | blade tip speed |
| $w_i$ | collision weight for $f_i$ |
| $x$ | position |
| $x_b$ | boundary lattice node |
| $\vec{x}_{\text{BE}}$ | blade element position |
| $\vec{x_f}$ | lattice node position next to a solid wall |
| $\vec{x_s}$ | lattice node position in the solid wall |
| $\vec{\cdot}$ | denotes vector |

# List of Figures

# 1. Introduction

In the field of rotorcraft operations, missions in challenging environments pose operational hazards for the pilot and the aircraft and demand extensive pilot training. A better understanding of aerodynamics and flight dynamics can help to increase operational safety. Especially scenarios like ship deck landing or rotorcraft-rotorcraft interaction present challenges that, with the proper modeling, could be made safer and more efficient with the help of simulations.

The dynamics of the rotorcraft in such challenging environments are governed by a multitude of factors, including aerodynamic interactions, structural dynamics, and the influence of environmental conditions. Capturing these phenomena accurately with computational models presents a challenging task due to the nonlinear and unsteady nature of rotor aerodynamics. One of the primary modeling challenges lies in accurately representing the complex flow phenomena, such as the unsteady wake produced by the rotor blades and their interactions with the surrounding environment.

computational fluid dynamics (CFD) emerges as a powerful tool for simulating rotorcraft flight in challenging environments, offering a comprehensive approach to modeling the intricate fluid dynamics surrounding the rotorcraft. By discretizing the governing equations of fluid motion and solving them numerically, CFD enables the exploration of flow phenomena at various spatial and temporal scales. However, achieving high-fidelity simulations with fully resolved models incurs prohibitive computational costs, particularly for complex rotorcraft configurations and turbulent flow regimes.

To address the computational challenges associated with rotorcraft CFD simulations, there is a growing interest in employing fast methods that balance computational efficiency and accuracy. These methods encompass a spectrum of techniques, ranging from simplified empirical models to advanced reduced-order models and hybrid approaches. By leveraging these fast methods, researchers aim to accelerate the simulation process while retaining sufficient accuracy for engineering analysis and design optimization.

The adoption of fast CFD methods holds significant promise for enhancing real-life rotorcraft operations in challenging environments. By providing rapid insights into the aerodynamic performance and dynamic behavior of rotorcraft, these methods empower engineers and pilots with valuable information for mission planning, training, and operational decision-making. Moreover, the ability to quickly assess different design configurations and operational scenarios contributes to the advancement of rotorcraft technology and safety standards.

This thesis aims to explore the accuracy of mid-fidelity modeling of a rotor modeling coupled with CFD. While the focus lies on the possibilities of a so-called LBM in the context of mid-fidelity modeling, the different rotor modeling approaches will be compared in a simulation setting that represents the aforementioned challenging flow environments.

# 2. State of the Art

## 2.1 Related Work

The thesis aims at the inflow computation of a rotor with the means of a mid-fidelity representation and the incorporation of ambient flow conditions in the rotor inflow. The aerodynamic modeling of a rotor in order to gain insight in rotor behavior has been a research topic that is pursued since almost a hundred years. As a consequence a wide spectrum of approaches and solutions for the computation of rotor inflow and the consideration of external flow effects on the inflow have been derived over the years.

First approaches based on momentum theory assumed the rotor as a continuous disk with a constant pressure jump that resulted in an immediate inflow velocity [49]. The theory was applied to hover and forward flight cases but gives not an accurate force and inflow distribution. An extension was blade element momentum theory (BEMT) where momentum theory and blade element theory (BET) were combined and allowed a better approximation of the radial inflow distribution and therefore the radial blade loading [62]. While this improved results it is still far from accurate and the inflow is still instantaneous and does not allow its usage for dynamic rotor inputs. This changed with the publication of the first finite state dynamic inflow model by Pitt and Peters [82]. This model relates transient aerodynamic thrust and moments to a transient inflow response. However, limitations existed with respect to the linear inflow representation. The model was further extended Peters and He [81] to include all harmonics of the radial inflow component and lead to a generalized theory. The model was refined over the years to include the wake curvature [115]. Further extensions included the incorporation of ground effect [113] and the effect of swirl [68] for a better power prediction. A good overview of the timeline was given by Peters [80].

The dynamic inflow models present a good and widely used approach for flight simulation including maneuvering flight. However, they do not inherently account for disturbances in the surrounding flow or complex flow phenomena due to blockage effects (except the aforementioned ground effect). To overcome this drawback a serious of studies was conducted where a dynamic inflow model was used and the vortex induced velocities were simply superpositioned at the local blade element positions [76, 101, 77]. The aim of these studies was to deterimne the severity of a trailing vortex encounter of a rotorcraft. The analysis was taken further and implemented in real-time for piloted studies in [60]. This superposition approach was also applied to piloted studies for ship airwake encounters [42] and [116]. The advantage of this approach is its straight forward implementation and the high computational speed that allows real-time pilot-in-the-loop investigations. The major disadvantage is the missing mutual interaction between the external flow, e.g. the trailing vortex and the rotor wake, which could significantly alter the results.

Besides dynamic inflow models, other rotor specific methods to compute the rotor wake and the resulting inflow have been developed to capture the major phenomena of the wake. Brown developed a lattice based vorticity conserving formulation of the fluid equations, the vorticity transport method (VTM) [16, 17]. As the wake is dominated by the trailing blade vortices this presents a natural description of the wake. A further advantage is the ability to model mutual interaction with vortex structures to overcome the disadvantage of the superposition approach. Whitehouse and Brown [104, 105] investigated the validity of this superposition approach in simulating helicopter dynamics during encounters with vortices from other aircraft. Their study suggests that simplistic models, assuming a frozen vortex, may adequately describe rotor response at high forward speeds but overpredict responses at low speeds relevant to airport operations. Low-speed interactions exhibit significant rotor response fluctuations, impacting helicopter handling qualities, potentially negating benefits of reduced mean loading. The study underscores the complexity of wake interactions and advocates for comprehensive experimental validation to accurately assess hazards during low-speed terminal flight. They further studied interactions between helicopters and fixed-wing aircraft wakes during takeoff and landing, particularly at low forward speeds and significant ground effect [106] [18]. Their findings showed that modeling rotor flow in ground effect poses challenges, with the VTM model showing promise in capturing evolving vortical features. Flow regimes in ground effect transition as rotor speed increases, influenced by changes in wake vorticity behavior near the ground. Preliminary calculations suggested that rotor interactions with aircraft wakes in ground effect are more severe than in free air due to the ground's constraining effect on wake displacement. These findings underscore the complexity of rotor-ground interactions and highlight the importance of accurate modeling for safety and operational efficiency.

Other vorticity based formulations to compute the rotor wake and the resulting inflow gained traction over the last three decades. The first where the wake development was not prescribed was the free-wake formulation. The wake region is represented by a series of discrete vortex filaments that are shed from the trailing edge of the blade, which interact with each other and with the free-stream flow. The strength and position of these vortex filaments depend hereby on the blade loads [48, 63]. Early work by Bagai and Leishman at Maryland used a pseudo-implicit formulation for a relaxed wake computation and was used to show predictive capabilities for single rotors [4] and was later on applied to multi rotor configurations [3]. The Maryland free-wake was later extended with a time-marching approach by Bhagwat and Leishman [8] which showed good agreement with transient control inputs. Later work added additional trailers, not only at the blade tip but over the whole blade span, e.g. [64] which showed improvement in the results. The success of the free-wake methods lead to its application not only for rotors in experimental settings but to the application in complex flow environments such as ship airwakes. Keller et al. presented a progression in that direction over the years with their framework CHARM. A first study showed real-time capability of the free-wake method [55] and in principal modeling of rotor interaction with ship structures and airwake. The ship airwake interaction modeling was further investigated by representing a CFD computed airwake as a vorticity field and feed this in a region of interest for interaction with the rotor wake [54]. Further research [53] and [52] showed that the CHARM/SI software module enhances rotorcraft simulations by accurately modeling rotor/wake interactions, particularly in scenarios like vortex ring state and shipboard operations. Developed with advanced free-vortex rotor wake and fast panel models, it effectively captures physical interactions between rotorcraft and ship airwake flow fields in real-time simulations. Integrated into the MH-60 Multi-Mission Helicopter simulation, it underwent pilot evaluations, but despite improvements, it wasn't deemed necessary to replace existing aerodynamic models for most scenarios. Besides its usage for isolated rotors and interactional phenomena the method showed promising results to predict structural loads due to the wake [89, 65], underlining the capablilty of mid-fidelity models to capture essential effects. These advances showed that a free-wake model is capable of modeling mutual interaction between environmental flow and the rotor wake. A drawback so far is the limitation of the region of interest for the mutual interaction that has to be a fixed reference. In the case of long approaches where strong interaction is expected for the whole approach this increases computational time significantly.

Due to the interconnected vortex filaments of the free-wake method mesh distortion can arise further down the wake or when strong wake interaction happens. Furthermore, if the wake, e.g. a vortex line, is 'cut' by a blade this is a challenging modeling issue. Therefore, a new wake approach has gained traction that is based on Lagrangian vortex particles without interconnecting filaments, the viscous vortex particle method (VVPM). In this method, the flow field is discretized into computational particles, each representing a vortex element. These particles carry properties such as position, strength, and circulation, which determine their influence on the flow. Unlike traditional vortex methods, which neglect viscosity and treat the flow as inviscid, the viscous vortex particle method incorporates the effects of viscosity through additional computations. The particles themselves get shed from the blades according to the viscosity distribution over the blade span. More details on the method can be found in literature, e.g. [107]. He and Zhao [40] conducted a validation study of the VVPM for the resulting rotor wake and the wake diffusion as well as the rotor response to a dynamic ramp input of the collective. The findings showed good results and the capability of using VVPM for rotor simulations. A later study by the authors investigated different speed up methods and modeled the rotor in ship board operations [114]. However, in this study no mutual wake interaction between ship wake and rotor wake was present, but rather an averaged side wind was superpositioned on the vortex particles. This was resolved by Rajmohan et al. [87] when the influence of the ship wake on the rotor wake and vice versa was modeled with flux correction terms in the equations. This approach did not allow for rotorcraft maneuvering as it was only a loose coupling and could therefore only account for stationary conditions. A tight coupling approach was presented in [86] where the flux correction takes place every time step. In this setup a region of interest on whose boundaries the exchange between the ship airwake and the rotor wake takes place needs to be defined. The size of this region of interest has to account for the full flight path where the mutual interaction might be critical. This approach was validated in a further study by Bae and He [2]. Contrary to a fully coupled simulation, Saetti derived a linearized state space vortex model based on VVPM [90] and applied it to a real time simulation of a rotor above a ship deck [91]. The advantage is a high computational speed that captures the major wake geometry. However, this did not include the ship airwake interaction nor allowed movement of the rotor. Besides ship deck operations the VVPM is also used for multi-copter predictions [102] and research tries to model active rotors [57].

The presented vorticity based methods so far have proven to be well suited for the simulation of rotor wake and use the resulting inflow velocities for the blade aerodynamics. They are applied in complex environment conditions with mutual interactions and were even used to conduct pilot-in-the-loop simulator studies. Furthermore, they can be fast since speed up algorithms are available such as tree-methods or the fast multipole method [103]. However, they do require the transformation of wake fields that are normally computed with Eulerian Navier–Stokes based flow solvers to be transformed in an equivalent vorticity formulation. Therefore, simulation of rotor wake and inflow is still often pursued via 'classical' CFD, e.g. grid based Navier-Stokes solvers. While high-fidelity simulations are possible with this approach, a mid-fidelity representaiton of the rotor in the flow field is often preferred to save computational time and limit grid requirements.

Early research was done by Chaffin and Berry [20] where they had the need for viscosity in their wake simulations, thus free-wake or dynamic inflow models were not applicable. Due to limited computational resources at the time the modeling of blades was not feasible. They modeled the rotor with an actuator disk method to investigate fuselage downwash. The actuator disk approach allowed for variation of inflow and thrust over the rotor area in a time averaged fashion. Boyd and Barnwell [15] and Boyd [14] modeled the rotor with an actuator disk as well but chose to use it as a correction via loose-coupling to an internal Peters–He inflow model for the force computation in order to reduce the required time steps in the flow solver and incorporate the effect of a fuselage below the rotor. They show time averaged results, but also limited the blade forces to a wedge shaped area of the rotor for unsteady load and inflow results which were agreeable with measurements. Later studies by Tadghighi et al. [98, 99] used an actuator disk approach where they either used time averaged quantities or restricted the forcing to the blade position in the disk for rotor fuselage interactions as well with good results. O'Brien and Smith [74] compared momentum theory actuator disk against actuator disks with force terms from BET in unsteady and steady conditions and used blade modeled simulations as a high-fidelity reference. Results showed, that time-averaged BET actuator disks show good agreement against averaged loads, while unsteady actuator disks where only the blade section receives source terms is promising for unsteady flow results. This proofed that while the actuator disk model is simple it can still be usable when fast computational times are required. Therefore, it is still used in recent years [1] for single rotor configurations or for multi-rotor vehicles [24, 22, 25]. Barakos et al. [5] proposed different actuator disk models that do not require BET but rather derive blade forces from first principles. The results compared against fully modeled blades were promising and could lead to quick estimates about the rotor wake. While actuator disk approaches provide a straight forward implementation in the flow solver, grids in the presented methods were often adjusted to the circular disk area and included gradual refinement towards the blade tip. In contrast Bludau et al. [10] used an actuator disk approach on a coarse Cartesian grid that uses a set of linear-harmonic base functions based on the Pitt–Peters inflow model to reduce grid requirements and speed up simulation up to real-time inflow computation [13].

However, since time-averaged actuator disks do not provide unsteady data and and unsteady disks where only the current blade position receives source terms are still limited to 2D distributions further research extended this to 3D via actuator line or actuator surface modeling. The actuator line modeling is a commonly used approach for mid-fidelity blade modeling of rotors in a rotorcraft or wind turbine context, e.g. [96]. The goal of the approach is a more realistic blade modeling while having reduced computational effort for the study of complex interactional effects. Research in the modeling of actuator lines or surfaces is still ongoing with respect to the three-dimensional force distribution and the correct inflow sampling to compute the blade loads. Jha et al. [46] published a set of guidelines for an optimal force distribution and grid resolution. However, their results were compared against wing and wind turbine results. They further enhanced their forcing approach by limiting the influence of each blade section in the flow field [47]. Churchfield et al. [27] proposed a non-isotropic force distribution to better reflect the actual blade geometry. A similar approach is pursued by Linton et al. [66] with the actuator surface method. However, in order to get similarity between blade shape and force distribution a the grid needs a finer resolution than for a pure isotropic forcing kernel as used in earlier studies. Nevertheless, results proved promising. The second step of this kind of blade representation is the sampling of the inflow velocity. Due to the forcing a local flow field disturbance is introduced that does not reflect the flow conditions for which airfoil tables were obtained. Various approaches were proposed in literature. A commonly used approach is an integrated average around the forcing position that cancels out the local disturbance [51, 23, 27]. Others propose the sampling at the quarter chord line and correct the inflow with analytical corrections based on lifting line theory [70]. Another approach to correct the inflow when sampling from a single location for each blade element is the incorporation of a vortex particle wake that gets propagated by the flow solution [30, 66]. However, this requires additional computational resources since the vorticity particles have to be stored and propagated in each time step. While research in the best modeling approach is still ongoing actuator line models are frequently used in research and a widely investigated phenomena is again the interaction of helicopters with ship airwakes as was conducted by various authors [35, 67, 78, 28, 29, 100]. The modeling approach included the simultaneous computation of rotor wake and ship air wake and thereby the mutual interaction. However, the rotorcraft was placed in the same grid as the ship and was therefore at a stationary position or the complete approach path required a fine enough grid to capture the rotorcraft adequately.

The mentioned actuator disk and line approaches are normally used in Navier–Stokes based solvers that are normally solved via finite volume or finite differences approaches. In recent years the LBM gained attention with respect to rotorcraft related simulation. While it's formulation is not based on the Navier–Stokes equations they can be recovered in the weakly compressible regime and it can therefore recover all corresponding flow phenomena. Due to its formulation it is highly parallelizable and leverage the computing power of GPUs. First attempts for a real-time LBM solver to compute simple flows up to a coarsely resolved ship wake were conducted by Woodgate et al. [109, 111, 110]. Friedmann et al. [36] and Bludau et al. [13] used the LBM for a real-time inflow computation and showed encouraging results. A more recent publication showed the drag predictions of a drone body [75] against a Navier–Stokes based solver. While results show room for improvement the computational speed gain was significant. Therefore, further research in the application of the LBM with respect to rotor inflow computation seems promising.

In summary research has progressed or simultaneously developed a variety of modeling approaches to capture the rotor inflow and rotor wake. Dynamic finite-state inflow models are well established and used in flight simulators or in general for flight dynamic investigations. With the superposition approach they can account for arbitrary environmental conditions, but still lack the interactional effects between the surrounding flow or obstacles in their vicinity. Vortex based formulations on the other hand can account for these conditions and are tailored to maintain the main wake structures while keeping computational efforts lower than regular CFD. Nevertheless, the incorporation of arbitrary environment conditions is not straight forward and therefore regular CFD is still employed. To reduce computational run times mid-fidelity rotor models are used which still give good overall results and are still actively pursued. With the rise of GPUs being used for computational efforts and the for this hardware well suited LBM research on mid-fidelity inflow modeling with LBM seems a promising endeavor.

## 2.2 Research Obejctives

Based on the current state of art this thesis further investigates the application of LBM in the simulation of rotor inflow, focusing on achieving fast computation times for multi-second flight maneuvers.

The key objectives of this thesis are:

1. The mid-fidelity representation will be enhanced. The previously used actuator disk representation will be expanded to account for radial degrees of freedom in the inflow and thrust modeling. This will be further refined by an implementation of an actuator line model for the rotor. All results will be compared against the Peters–He inflow model incorporating superposition when necessary.
2. A further validation of the inflow modeling than [10] will be conducted. In the previous study comparison against flight test data of a single Bo105 model was made. This work will extend the validation to the UH60A model as well as compare results against an experimental rotor. The simulation setup will be evaluated with respect to its capability

to accurately predict thrust versus power, the lift distribution along the blade, and the influence of the modeling strategies on accuracy of simulation outcomes. This achieved by using data from experimental investigations and flight tests. Key parameters such as the grid resolution will be defined for future usage.

3. The simulation setup is expanded to account for environmental conditions such as ambient wind speeds or complex wakes. This extension is used to examine the efficacy of coupling models in real-world deployment scenarios, namely a isolated vortex encounter and flight in a ship airwake, exploring whether the enhanced rotor models justify their utilization in complex rotor experiments or a simple superposition approach gives similar results.

By addressing these aspects, the thesis contributes to advancing the efficiency and reliability of rotorcraft flight simulations and an understanding of mid-fidelity rotor models with the LBM, thereby facilitating more informed decision-making in aerospace engineering.

In chapter 3 the models and methods used in this thesis are covered. First, section 3.3 explains the basics of the LBM used for the flow simulation. Second, section 3.2 will detail the coupling between the flow and the rotor dynamics solver including the extension of the actuator disk and actuator line models. Next, chapter 4 gives an overview of the simulation setups for the validation cases as well as the application to vortex interaction and ship approach. The simulations results of the coupling validation are presented in chapter 5. In section 5.1 the results for the experimental rotor are covered and in section 5.2 the results for the UH60A. The findings for the applied cases with respect to the differences in the different rotor modeling strategies are shown in chapter 6. First for the vortex encounter in section 6.1 and then for the ship approach in section 6.2. A summary of the work done within the scope of this thesis and the major conclusion can be found in chapter 7. At last chapter 8 gives a brief outlook regarding potential future research that could advance rotor simulation with the LBM.

# 3. Methodology

The present chapter covers the setup of the two-coupled simulation framework and gives a theoretical overview where necessary. The first section gives a brief introduction to the Lattice-Boltzmann method that solves a general three-dimensional flow field and the respective boundary conditions formulations relevant for the rotorcraft simulations. This section also highlights the details that show the suitability of LBM for GPU computations. The second part provides a detailed overview of the different coupling approaches investigated in this thesis, focusing on the mathematical description and details of practical implementation.

## 3.1 Lattice-Boltzmann method

### 3.1.1 Governing equations

The Lattice-Boltzmann method (LBM) is a formulation that allows the computational solving of general flow problems. The underlying idea is that one does not discretize a set of continuum equations such as the Navier–Stokes equations but rather looks at a microscopic scale with mesoscopic kinetic equations and derive the macroscopic quantities of the flow from the current system state [21]. It originated from lattice gas automata [39] that was a method to model particle kinetics on a discrete lattice with discrete time steps. One important aspect is the application of simple kinetics, or otherwise, the solution procedure for a real-world application would not be feasible. The lattice gas automata formulation is based on a discrete grid with a certain number of boolean states that correspond to a given velocity direction of a particle. In each time step, the particles move along their direction to the next grid point, and the boolean state indicates if a particle is present or not. At the lattice location, the scattering of the particles is computed based on simple kinetics [37]. The following equations and explanations are meant to give a brief overview of the math behind the LBM and are adapted from [39] unless stated otherwise. The LBM bases its formulation not on discrete particles but rather on the distribution of the particle velocities in a discrete direction. The distribution averages for all directions represent the primitive variables of the LBM. The equation for the evolution of the particle distribution function $f_i$ in its velocity direction $\vec{e}_i$ is given as

$$f_i(\vec{x} + \vec{e}_i \Delta x, t + \Delta t) = f_i(\vec{x}, t) + \Omega_i(f(\vec{x}, t)) \tag{3.1}$$

with $x$ denoting the position at the current time $t$, $\Delta x$ the grid spacing, $\Delta t$ the time step and $\Omega_i$ is the collision operator. The distribution in the next time step $t + \Delta t$ is the distribution of the current time step $f_i(\vec{x}, t)$ propagated to the next node at $\vec{x} + \vec{e}_i$ along its direction $\vec{e}_i$ plus the collision operator that accounts for the rate of change of $f_i$ due to the particle interaction at the current node. The macroscopic physical quantities better suited to investigate the flow field are computed with the so-called momenta of the $f_i$. The first momenta being the density

$\rho$ and the velocity vector $u$ given as

$$\rho = \sum_{i=0}^{q} f_i \tag{3.2}$$

$$\vec{u} = \frac{1}{\rho} \sum_{i=0}^{q} f_i \vec{e}_i \tag{3.3}$$

where $q$ is the number of directions, e.g. the number of $f_i$. The collision operator is given by the Bhatnagar–Gross–Krook (BGK) collision operator presented by [9] as

$$\Omega_i = -\frac{f_i(\vec{x}, t) - f_i^{eq}(\vec{x}, t)}{\tau} \tag{3.4}$$

where $\tau$ is the relaxation time denoting how fast the particle's state decays to the equilibrium state $f_i^{eq}$. The equilibrium state $f_i^{eq}$ is given as

$$f_i^{eq} = \rho w_i \left[ 1 + 3\vec{e}_i \cdot \vec{u} + \frac{9}{2}(\vec{e}_i \cdot \vec{u})^2 - \frac{3}{2}\vec{u}^2 \right] \tag{3.5}$$

where $w_i$ are the collision weights for the corresponding $f_i$. The application of the Chapman–Enskog expansion shows that the LBM recovers the Naver–Stokes equations in the low compressible regime. The relaxation time $\tau$ is given as

$$\tau = \frac{\nu^*}{c_s^2} + 0.5 \quad \text{with} \quad \tau > 0.5 \tag{3.6}$$

where $\nu^*$ is the non-dimensional viscosity and $c_s$ the lattice speed of sound. Stability analysis provides the lower bound for tau, where in reality, values close to 0.5 already lead to numerical instabilities and require additional treatment [21].

From the above equations, two important properties of the LBM can be derived that sets it aside from other CFD methods, e.g., finite volume method or finite difference method. First, Equation 3.1 shows that the streaming step, e.g., the convection of flow information, is linear [21]. In the Navier–Stokes equations, this is a non-linear term. This property simplifies the streaming to a simple copy of the $f_i$ at the end of the time step along their specified direction to the next lattice point [108]. Second, the BGK collision term is a fully local function with respect to the information needed. The fact that no neighboring $f_i$ are needed allows for a fully parallel collision step in the LBM simulation.

The first step from the theoretical equations to the application of LBM lies in the choice of the directions or $\vec{e}_i$ of the $f_i$. The choice has to fulfill certain symmetry criteria [19]. In the following, the set of $\vec{e}_i$ and the streaming and collision operations are explained for a D2Q9 lattice, meaning a two-dimensional lattice with $q = 9$. A commonly used three-dimensional lattice is the D3Q19 shown in Figure 1. In the two-dimensional case, the directions are along the two axes in positive and negative directions and the diagonals in every quadrant, plus a 0-th distribution function that stays at the lattice location. A reduced set that could

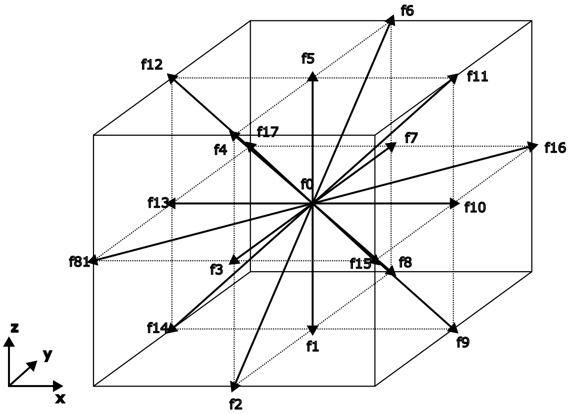

**Figure 1** Example of the D3Q19 lattice with the $f_i$ and their respective $\vec{e_i}$. The D3Q19 only includes diagonal $\vec{e_i}$ in the main axis planes, but not diagonal directions to the corners.

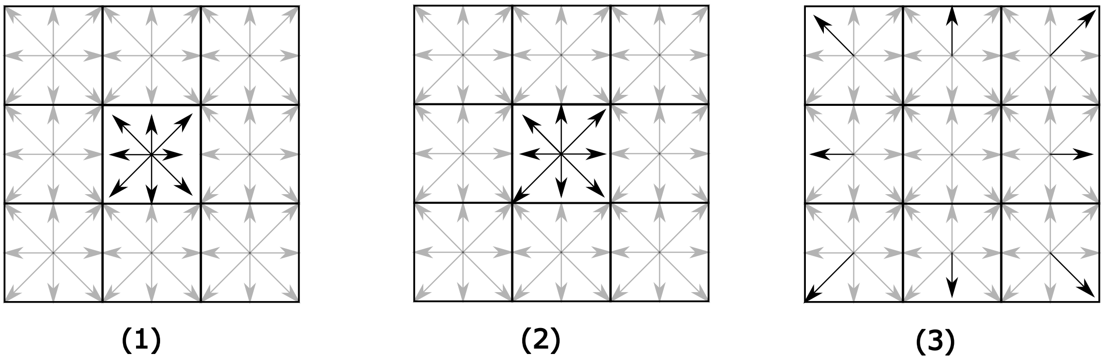

**Figure 2** Visualization of collision and streaming in one LBM time step from left to right. Colliding the $f_i$ at the beginning of the time step (1) results in new distributions at (2), which then get streamed to the neighboring cells (3).

also be used, is the D2Q5, where no diagonal directions are considered. This would lead to reduced memory consumption and less computational effort as the collision is only computed for half the populations, but by reducing the set of $f_i$ in general, the stability and accuracy of the simulation is reduced as well [21]. Considering that for a three-dimensional case, usually $q \in [15, 19, 27]$, it is obvious that the memory consumption is far higher than for a Navier–Stokes-based solver, where only velocity and pressure have to be stored for each cell. Furthermore, due to the simple computational operations but high memory demand, the LBM is usually a memory-bound problem, benefiting from hardware with high memory bandwidth and thus giving the usage of GPUs another advantage. The collision and streaming are visualized in Figure 2, whereby the magnitude of the arrows indicate the value of $f_i$. The collision changes the $f_i$ distributions, as can be seen by the change in magnitude, but mass and momentum are retained [39]. The post-collision distributions get streamed along the grid directions to the neighboring cell. By repeating this step, the evolution of the flow field is computed.

The basic equations of the LBM and their application are easy enough. The complexity comes from the handling of the domain boundaries and internal boundaries from objects and the respective efficient implementation. Besides the basic BGK formulation, there is a variety of adjustments and alternative approaches presented in the literature that will not be discussed in detail here. It should be mentioned that another well-known approach is the multiple relaxation time (MRT) model, where the collision is not based on the $f_i$ but rather on the momenta with an adjusted $\tau$ for each momenta to ensure maximum stability. [59]

### 3.1.2 Boundary treatment

As common in CFD, the boundary treatment is an important step for a flow simulation to get meaningful results. The most important boundaries are inlet and outlet boundary conditions and the treatment of solid walls. Contrary to other other methods, the LBM faces some specific problems that come from the necessity of the uniform cartesian grid constraints and the number of degrees of freedom at each lattice point. While the cartesian grid requires special treatment for solid walls that are not perfectly grid aligned, e.g., straight and along the major axes, certain boundary nodes require special treatment that is independent of the boundary type. Depending on the exact node position, e.g., boundary surface, boundary corner, or in three-dimensional problems, also the boundary edge, a varying number of unknown populations "stream" into the simulation domain from the outside. This leads to a closure problem as, in general, more unknowns than equations are present at the node. In general, a boundary formulation needs certain assumptions in order to close the problem. In the following section, a brief overview of the most important boundary conditions with respect to the application of this thesis is given.

#### Bounce-Back boundary condition

The bounce-back (BB) [41] boundary formulation introduces a no-slip wall boundary with zero velocity. In this scheme, the particle distribution is reflected by the wall, meaning that $f_i$ is streamed in the opposite direction for the wall node. The BB and modified bounce-back (MBB) [58] boundary conditions are commonly used in LBM to handle solid walls and interfaces. These conditions ensure that fluid particles interact correctly with the boundary, thereby maintaining the no-slip condition. The equation for the BB at the boundary position $x_b$ is

$$f_i(\vec{x_b}, t) = f_{\bar{i}}^*(\vec{x_b}, t) \tag{3.7}$$

with $f_{\bar{i}}$ being the distribution function in opposite direction of $f_i$ and $^*$ denoting the post-collision distribution function.In order to account for a movement of the boundary Ladd [58] proposed the MBB to account for the additional momentum introduced by the moving wall. This is achieved by introducing an additional momentum term based on the wall velocity $u_b$ before inverting the particle distribution function

$$f_i(\vec{x_b}, t) = f_{\bar{i}}^*(\vec{x_b}, t) - \frac{2\rho w_i}{c_s^2} \vec{u_b} \cdot \vec{e_i} \tag{3.8}$$

Application of the bounce-back scheme is straightforward and can be applied to any boundary node without additional effort. Nevertheless, the simplicity of the formulation is limited to no-slip boundaries. He and Zou [41] have shown that the BB and MBB both introduce spurious velocities near the boundary that can affect results. The treatment of curved boundaries is possible but not very accurate as it does not account for the varying blockage of the wall cell, and the solid boundary has to be placed at the midpoints of the lattice to achieve second-order accuracy. Nevertheless, BB schemes are commonly used for boundaries where a high accuracy of the flow close to a solid boundary is not of utmost importance.

### Extrapolation boundary conditions

The treatment of curved boundary conditions is not adequately solved by BB schemes, but there are multiple propositions to account for arbitrary curved boundaries. One approach is the extrapolation of the fluid velocity onto the wall node, thereby estimating the distribution function streaming from the node $\vec{x_s}$ (see Figure 3). Filippova and Hänel [34] proposed

$$f_{\bar{i}}^*(\vec{x_s}) = (1-\chi) f_i^*(\vec{x_f}) + \chi f_i^*(x_b) + \frac{2 w_i \rho}{c_s^2} \vec{u_b} \cdot \vec{e_i} \tag{3.9}$$

for the distribution function $f_{\bar{i}}^*(\vec{x_s})$ coming from the wall node by interpolation the $f_i$ at the fluid node $\vec{x_f}$ next to the wall and the fictitious $f_i$ at the boundary position $x_b$ and $\chi$ being the weight of the interpolation. The boundary distribution function is given as

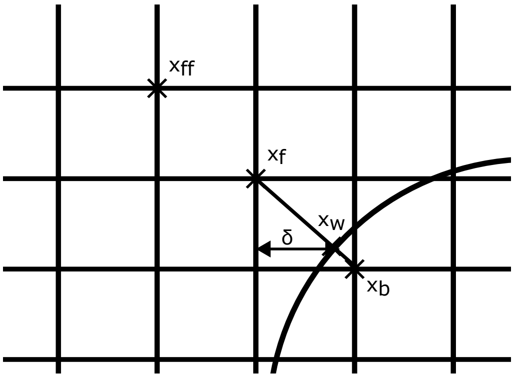

**Figure 3** Depiction of the extrapolation boundary treatment for an arbitrarily shaped solid wall.

$$f_i^*(\vec{u_b}) = w_i \rho_f \left[1 + \frac{\vec{u}_{bf} \cdot \vec{e_i}}{c_s^2} + \frac{(\vec{u_f} \cdot \vec{e_i})^2}{2c_s^4} - \frac{\vec{u}_f^{\,2}}{2c_s^2}\right] \tag{3.10}$$

with $\rho_f = \rho(\vec{x_f})$ and $\vec{u}_f = \vec{u}(\vec{x_f})$. The velocity $\vec{u}_{bf}$ and the weighting $\chi$ are given as

$$\vec{u}_{bf} = \frac{(\delta - 1)\vec{u}_f + \vec{u}_b}{\delta} \tag{3.11}$$

$$\chi = \frac{2\delta - 1}{\tau} \tag{3.12}$$

for $\delta < 1/2$ and

$$\vec{u}_{bf} = \vec{u}_f \tag{3.13}$$

$$\chi = \frac{2\delta - 1}{\tau - 1} \tag{3.14}$$

for $\delta \geq 1/2$. Mei et al. [71] gave a more detailed theoretical derivation for the proposition of Fillipova and Hänel and proposed an improvement with respect to numerical stability. They adjusted $\vec{u}_{bf}$ and $\chi$ for cases where $\delta < 1/2$

$$\vec{u}_{bf} = \vec{u}_{ff} \tag{3.15}$$

$$\chi = \frac{2\delta - 1}{\tau - 2} \tag{3.16}$$

where $\vec{u}_{ff} = \vec{u}(\vec{x}_{ff})$ with $\vec{x}_{ff}$ being one node inboard from $\vec{x}_f$ (see Figure 3). The advantage of this extrapolation boundary approach is that the geometry is not approximated by a stair of steps, but rather, the full geometry is taken into account with the partial blocking of a cell by an obstacle. Mei et al. [71] also showed that in general the results preserve second-order accuracy for the velocity field in space. Nevertheless, the method has restrictions with respect to numerical stability, depending on $\delta$ and the relaxation parameter $\tau$. The disadvantage from a computational point of view is the necessity to access non-local memory from neighboring points, thereby increasing memory usage and creating an unfavorable memory access pattern on GPUs.

### Additional solid wall boundary conditions

There are a variety of other approaches to model solid stationary or moving walls in a LBM simulation that were not used in the works of this thesis. A widely used approach is immersed boundaries originally proposed by Peskin [79] and adopted for various applications. Contrary to modifying the particle distribution functions to enforce a certain velocity at the solid boundary, a forcing term is added in the collision step that ensures that the fluid velocity at the solid boundary corresponds with the wall velocity. The immersed boundary approach is not a specific LBM solution but is also used in classical CFD, e.g., in rotor simulation conducted by Linton et al. [67]. Dorschner et al. [32] proposed a boundary condition based on Grad's approximation. Hereby, the boundary condition is not imposed on the particle distribution functions but on the macroscopic quantities such as density and momentum. In general, the idea is similar to the extrapolation method, which extrapolates the velocity within the solid boundary from the fluid velocity and the desired wall velocity. Additionally, the corresponding stress tensor and density are computed to estimate the missing velocity being streamed out of the wall.

Krause et al. [56] propose a homogenized LBM where the solid wall velocity is given as

$$\vec{u}(\vec{x}, t) = (1 - d_I(\vec{x}, t))\vec{u_f}(\vec{x}, t) + d_I(\vec{x}, t)\vec{u}_b(\vec{x}, t) \tag{3.17}$$

where $d_I$ is a function related to moving porosity. This approach defines a porous area around the solid obstacle and thereby gradually imposes the desired wall velocity. This requires a fine enough resolution to keep the porous area small but does not require any interpolation of neighboring node information as the immersed boundary conditions and pressure fluctuations are reduced [56].

**Free outflow boundary condition**

An important factor of any flow simulation is the outflow boundary condition. In order to avoid disturbances of the solution in the area of interest a reflection free boundary formulation should be used. In accordance with previous publications [36, 13, 10], an impedance boundary formulation developed by Schlaffer [92] was used as an open outflow boundary condition. The method solves the boundary problem in an integral way instead of differential form. Without the need for spatial derivatives, the method retains strict locality, which does not impede parallel performance. It also proved an efficient formulation to handle the impulse of the rotor and the large gradients at the boundary of the rotor wake. A brief overview of the approach is given in the following.

The formulation adapts the state of the particle distribution functions within a boundary cell so that an oncoming momentum flux or pressure sound wave is canceled out. In each time step, the $f_i$ are adapted so that they satisfy

$$\frac{\partial J_{CV}^{(t)}}{\partial A \partial t} + \frac{\partial J_{flx}^{(t)}}{\partial A \partial t} = \mp d\rho^{(t)} c_s^2 \mp \frac{1}{2}\rho^{(t)} \left(du^{(t)}\right)^2 + du^{(t)} \rho^{(t)} c_s = 0 \tag{3.18}$$

where represents $J_{CV}$ the momentum change per area in a given control volume and $J_{flx}$ the momentum flux due to an incoming pressure wave, $\rho$ is the density, $c_s$ the speed of sound, $p$ is the pressure and $u$ the velocity. Applying a finite differences approach with a lattice time step of $\Delta t = 1$ leads to the following non-linear equation.

$$\begin{aligned}
&\mp \left(\rho^{(t)} - \rho^{(t-\Delta t)}\right) c_s^2 \mp \\
&\quad \mp \frac{1}{2}\rho^{(t)} \left[\left(\vec{u}_x^{(t)} - \vec{u}_x^{(t-\Delta t)}\right)^2 + \left(\vec{u}_y^{(t)} - \vec{u}_y^{(t-\Delta t)}\right)^2 + \left(\vec{u}_z^{(t)} - \vec{u}_z^{(t-\Delta t)}\right)^2\right] + \\
&\quad + \text{sign}\left(dv_x\right) \cdot \sqrt{\left(\vec{u}_x^{(t)} - \vec{u}_x^{(t-\Delta t)}\right)^2 + \left(\vec{u}_y^{(t)} - \vec{u}_y^{(t-\Delta t)}\right)^2 + \left(\vec{u}_z^{(t)} - \vec{u}_z^{(t-\Delta t)}\right)^2} \cdot \\
&\quad \cdot \rho^{(t)} c_s = 0
\end{aligned} \tag{3.19}$$

Equation 3.19 cannot be solved directly, and a Newton–Raphson iterative approach is employed. However, the equation shows that only local quantities are needed, providing a memory-efficient formulation. A drawback of the iterative approach is that the solution time is not known a priori per time step. While this approach can handle the high gradients in the wake for an actuator disc approach, stability issues can arise for flows with high temporal gradients, e.g., rotor wake where blade tip vortices or turbulence is present. In this case, the iterative approach might converge very slowly or not at all, leading to numerical instabilities. In this case, the application of a buffer zone close to the boundary might be favorable, where the small-scale disturbances are damped and the boundary stability is improved. Additional information regarding the stability and reflection properties of curved waves can be found in the respective publication [92].

### 3.1.3 Applying external forces

The rotor blade forces acting on the fluid and creating the rotor inflow have to be incorporated in the LBM formulation. This is done with an additional forcing term presented by Guo et al. [38] and an adjusted $u$ for the computation of $f_i^{eq}$ in the collision. The respective equations are

$$\rho\vec{u}^* = \sum_{i=0}^{q} f_i \vec{e}_i + \frac{1}{2}\vec{F} \tag{3.20}$$

$$f_i(\vec{x} + \vec{e}_i \Delta x, t + \Delta t) = f_i(\vec{x}, t) - \frac{f_i(\vec{x}, t) - f_i^{eq}(\vec{x}, t)}{\tau} + F_i \tag{3.21}$$

$$F_i = \left(1 - \frac{1}{2\tau}\right) w_i \left[\frac{\vec{e_i} - \vec{u}^*}{c_s^2} + \frac{\vec{e}_i \cdot \vec{u}^*}{c_s^4}\vec{e_i}\right] \cdot \vec{F} \tag{3.22}$$

with $F$ as the force due to external forces, $u^*$ the adjusted velocity and $F_i$ the forcing term. The formulation of the forcing term shows that the implementation is straightforward and can be applied directly in the collision step.

### 3.1.4 Turbulence modeling/Stability

Considering the mentioned stability concerns for the impedance boundary and the fact that the rotor wake is turbulent the need for a turbulence modeling approach arises. The Smagorinsky turbulence model is an established turbulence model in large eddy simulation (LES) simulations that offers an efficient approach with straightforward implementation to model turbulence in fluid flows. Conceived by Joseph Smagorinsky in the 1960s [95], this model is based on the concept of characterizing turbulent eddies as unresolved, subgrid-scale structures within the flow. These structures are modeled using an eddy viscosity, which is akin to molecular viscosity but dynamically adjusts to local flow conditions.

The fundamental idea of the Smagorinsky model is that the computational grid does not resolve the full turbulent scale but only major eddies are represented. Turbulent eddies that are not resolved are considered subgrid-scale structures. Nevertheless, their effect on the flow has to be taken into account somehow. At the heart of the Smagorinsky model is the premise that the turbulent eddies within a flow field are not fully resolvable on the computational grid. Instead, these eddies are considered subgrid-scale structures, and their effects on the flow are approximated using an eddy viscosity $\mu_t$ that is given by

$$\mu_t = (C_s \Delta_s)^2 |\underline{S}| \tag{3.23}$$

where $C_s$ is the Smagorinsky constant, a parameter that has to be chosen, $\Delta_s$ is the filter width, and $\underline{S}$ is the stress tensor. In practical applications, the filter width is oven chosen as the lattice spacing $\Delta_s = \Delta x$. Expanding the stress tensor magnitude leads to

$$\mu_t = (C_s \Delta x)^2 \sqrt{2 S_{ij} S_{ij}} \tag{3.24}$$

The eddy viscosity gets evaluated independently for each lattice node in the flow simulation. The selection of $C_s$ depends on the application and can, in general, not be accurately predicted. While the choice is influenced by factors such as the flow's Reynolds number, geometry, and the specific numerical method employed in the application of the rotor simulations, the parameter is chosen to maintain numerical stability. Due to the low viscosity of air, the LBM is close to its numerical stability limit of $\tau > 0.5$. Therefore, additional viscosity needs to be added. The value of $C_s$ is chosen appropriately but is around 0.07.

Nevertheless, the Smagorinsky turbulence model is a versatile tool in the field of CFD, offering a pragmatic balance between computational cost and accuracy in many practical applications. However, the model has its limitations. It is less suitable for highly complex, unsteady, or wall-bounded flows, where the turbulence structures are influenced by a wider range of scales. In such cases, more sophisticated turbulence models or LES, which resolves a broader spectrum of eddy sizes, might be more appropriate.

### 3.1.5 Moving grid - Arbitrary–Lagrangian–Eulerian

The modeling of rotorcraft flight scenarios needs to take into account the motion of the rotorcraft. A possible approach is moving the rotorcraft with respect to the computational lattice by an appropriate moving wall boundary condition. This could result in an unfeasible simulation because the lattice has to account for the full flight path, which could extend multiple hundred meters. A more efficient solution is keeping the lattice fixed to the rotorcraft and moving the computational domain itself according to the rotorcraft's motion.

In the Eulerian formulation, the field is normally represented by a fixed grid that does not track individual fluid particles through time but rather describes the current state at a given position. Contrary to that, the Lagrangian formulation follows an individual particle through time. In solid simulations, a Lagrangian formulation is normally employed, while mesh-based fluid simulations such as LBM would make it hard for the mesh points to follow individual particles because of the large resulting mesh distortion. Nevertheless, a deformation or motion, as in this case, of the simulation domain might be desired. To achieve this, an ALE method is included in the LBM framework. The ALE approach was originally proposed by [31]. The idea is that it combines the Eulerian and the Lagrangian approach by allowing independent particle and mesh movement at the same time (see Figure 4). In the general application this not only allows for rigid mesh movement but also for mesh deformation. Due to the necessity of Cartesian grids for the LBM and the goal of the application to match the rigid body modes of the rotorcraft a deformation of the lattice is not necessary and the ALE approach is limited to rigid body modes.

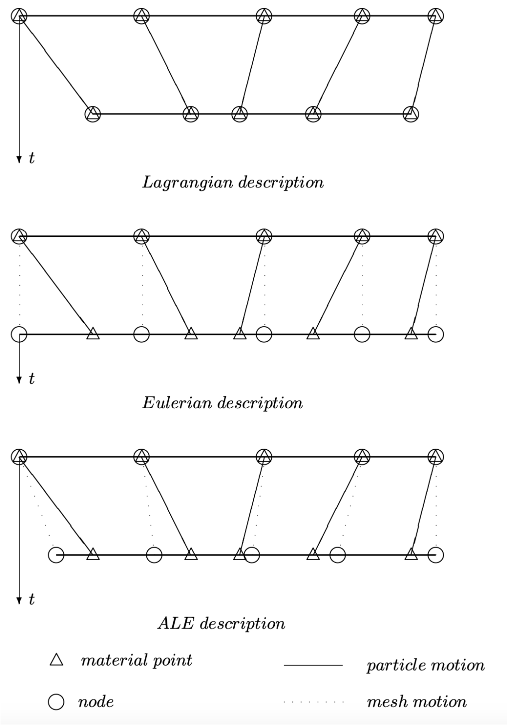

**Figure 4** Comparison of Eulerian, Lagrangian and ALE formulation, adapted from [31]. The Lagrangian approach moves the mesh fixed to the material points, contrary to the Eulerian approach, with the mesh being fixed in space. The ALE approach allows mesh movement independent from material point movement.

Meldi et al. [73] presented the formulation for the ALE approach in the context of the LBM. A detailed derivation of the approach can be found in the respective publication. Nevertheless, a short summary of the approach from an application point of view is given based on the one given in [73]. At each time step, the new lattice positions $\vec{x}(t+1)$ due to the rotorcraft motion are computed. In general, the position of the lattice nodes for time step $t$ will not coincide with the new positions. Therefore, the quantities have to be interpolated from the neighboring nodes to the new lattice position. In order to account for a possible rotation of the grid with respect to the previous time step, the respective quantities have to be rotated as well. Because the $f_i$ cannot be rotated to the new reference frame, one has to rely on macroscopic quantities, such as the velocity $\vec{u}$ and the stress tensor $\underline{S}$. They are rotated from the lattice frame of the previous time step to the new lattice frame. The distribution functions are then recovered by

$$f_i = \rho w_i \left[1 + 3\vec{e}_i \cdot \vec{u} + \frac{9}{2}(\vec{e}_i \cdot \vec{u})^2 - \frac{3}{2}\vec{u}^2\right] - w_i \rho \frac{\tau}{c_s^2} \underline{S}\,(c_i c_i - \underline{I}) \qquad (3.25)$$

with $\underline{I}$ being the identity matrix. Approximately, the macroscopic quantities can also be omitted by directly interpolating the particle distribution functions without the rotational transformation. This approach is only reasonable if the angular rates are small compared to the rate of change in flow conditions.

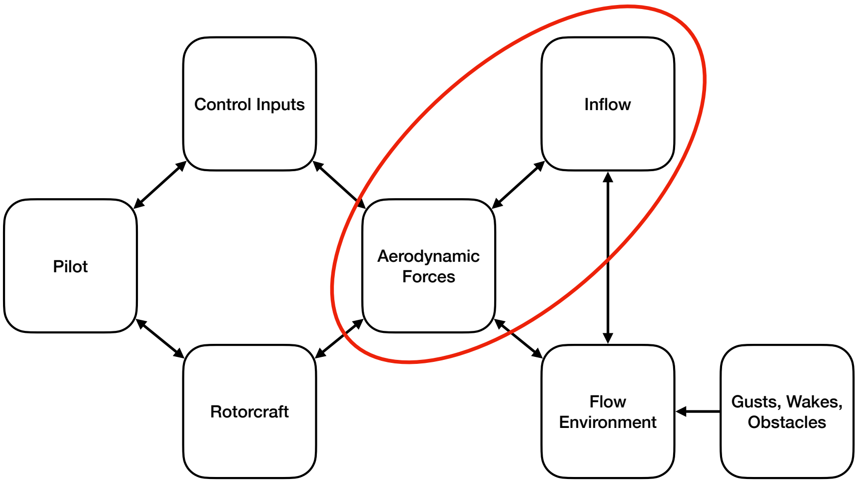

**Figure 5** Influence factors and relevant interfaces on the rotorcraft. Red highlights the main focus of this work.

## 3.2 Rotor Coupling Interface

This section gives a detailed insight into the formulation of the rotor coupling which is a core part of the present work. The rotorcraft is influenced by a multitude of factors during flight, but the motion is dominated by the rotor forces. The rotor forces depend on the pilot inputs, the current rotor state, and the surrounding flow conditions. Additional factors for the rotorcraft's motion are forces due to the lift and drag of the fuselage and the tail rotor. The flow conditions in the vicinity of the rotor are influenced by the rotor downwash due to rotor forces and environmental conditions such as prevailing wind velocity, gusts, vortex structures present in the wake of obstacles such as buildings or ships, and the influence of obstacles on the downwash due to blocking effects. These relations are depicted in Figure 5. The present work focuses largely on the interface between the rotor and surrounding flow conditions. This section gives a short introduction to rotor aerodynamics in subsection 3.2.1 and current inflow modeling techniques in subsection 3.2.2. The inflow coupling modeling is presented in the next section 3.3.

### 3.2.1 Rotor Aerodynamics

In order to model the effect of the flow conditions on the rotor forces and vice versa, a model has to be employed for the rotor aerodynamics. This includes the modeling of the rotor blade forces due to the flow field and the change in the flow due to the blade forces. The rotor forces acting on the fluid are dominated by the air loads of the respective rotor blade, and their computation is crucial for any simulation, including rotor aerodynamics. In the context of this thesis BET in combination with experimental airfoil data is used to predict lift and drag forces for the rotor blades. The approach relies on tabulated airfoil data from either experiments or simulations that provide the lift and drag coefficients $C_l$ and $C_d$ for a given angle of attack $\alpha$ between the blade airfoil and the flow direction [62]. The angle of attack depends on the effective velocity vector $u$ and the airfoil pitch angle $\Theta$ (see Figure 6).

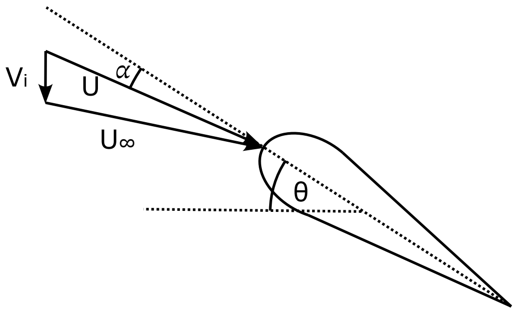

**Figure 6** Depiction of angle of attack $\alpha$ depending on the vector of the free stream velocity $\vec{u}_\infty$, the induced velocity $\vec{v}_i$ and the airfoil pitch angle $\Theta$.

The effective flow velocity vector $u$ can be decomposed and is then given as

$$\vec{u} = \vec{u}_\infty + \vec{v}_i \tag{3.26}$$

where $u_\infty$ is the general surrounding or far-field velocity and $\vec{v}_i$ is the induced velocity component due to the acceleration of the airfoil forces acting on the fluid. While $u_\infty$ might be known in advance, the induced component depends on the rotor forces acting on the fluid, which in reverse depend on $\vec{v}_i$. Thus, a crucial part is the computation of the inflow in the rotor disk that includes $\vec{v}_i$. An overview with regard to the inflow computation is given in the next section. Assuming that an efficient way is available to compute the overall velocity or use a given free stream velocity and compute the induced inflow component the BET with 2D airfoil data provides reasonable results for the blade forces. Nevertheless, this approach assumes only a purely 2D flow over an airfoil with an infinite span. The BET falls short in the region of blade root and blade tip, where three-dimensional flow conditions govern the prevailing air loads, or in the blade midsection where crossflow might occur, which is generally the case for rotating blades. In this case the lift effectiveness is reduced, resulting in lower generated lift. In order to achieve accurate results the modeling of this tip loss is paramount. There are different approaches in the literature that assume a reduced effective rotor area compared to the real one based on geometric rotor properties [50] or just a fixed 3% as a rule of thumb. Prandtl [83][7] proposed a tip loss function based on the radial position of the blade element and the prevailing flow condition with the formula given for a rotor according to [62] as

$$f_{TL}(r) = \frac{2}{\pi} \arccos\left(\exp\left(\frac{-0.5 N_{\text{blade}}(1-r)}{\frac{v_i}{V_{\text{tip}}}}\right)\right) \tag{3.27}$$

where $f_{\text{tl}}$ is the local tip loss factor for the lift component, $N_{\text{blade}}$ is the number of rotor blades, $r$ is the normalized radial position, and $V_{\text{tip}}$ is the blade tip speed. While these approaches provide a good estimate in analytical considerations, they have drawbacks in a numerical application. The approach where an overall reduced effective rotor area is assumed represents an integral approach, where along the blade from a certain radial position, e.g. $r = 0.97$, the effective lift is set to zero. This discontinuity in the lift distribution poses a problem for certain models to compute the inflow component. The approach of Prandtl does not suffer from this, but can for arbitrary flow conditions where $v_i \leq 0$ result in no or a non-physical solution. Therefore, a continuous tip loss approach from the flexible multi-body dynamics code Dymore [6] is used where the tip loss is given as

$$f_{tl}(r) = \tanh\left(\frac{1-r}{1-C_{\mathrm{tl}}}\right)\varphi \tag{3.28}$$

where $C_{\mathrm{tl}}$ is the tip loss factor that represents the parameter similar to the reduction of the effective rotor area. This approach does not take into account the local flow conditions but provides a continuous lift distribution along the blade. The corresponding reduced lift area can be evaluated by integrating $f_{\mathrm{tl}}$ over $R$ and multiplying by 100, which gives the effective tip loss in percent $C_{\mathrm{tl},\%}$.

### 3.2.2 Inflow Computation Models

The computation of the rotor or blade forces with BET and the adjustment for a finite blade is straightforward if the local flow conditions are known. However, the induced velocity component (see Equation 3.26) due to the blade forces is not known a priori because of the interaction between forces and flow. Thus a model for $\vec{v_i}$ has to be employed to close the modeling gap. This is done with so-called inflow models, which try to model the induced velocity component perpendicular to the rotor disk. In the following, induced velocity and inflow are used synonymously. This section gives a very brief overview of different approaches that were developed over time with information about the assumptions and drawbacks.

A very simple approach based on the momentum theory, where a constant inflow over the whole rotor disk is assumed computed from the integrated rotor thrust $T$ given as (see [62, 50])

$$v_i = \frac{T}{2\rho A\sqrt{(V\cos(\alpha_i))^2 + (V\sin(\alpha_i) + v_i)^2}} \tag{3.29}$$

where $\alpha_i$ is the rotor disk angle of attack and $V = |\vec{u_\infty}|$. While this equation, in general, has to be solved iteratively, direct approximations exist depending on the flight state. This approach neglects viscous effects, introduced swirl in the rotor wake, and the uniform inflow is, in general, not a sufficient approximation. A simple non-uniform approximation assumes linear inflow variation over the disk where the gradient depends on the rotor pitch and roll moments. For fully non-uniform load and inflow, the combination of BET and momentum theory leads to blade element momentum theory, where the inflow distribution depends on the local thrust distribution over the rotor disk. A different approach that is based on modeling the bound vorticity and the shedding in the wake is vortex theory where the bound vorticity is used to determine the resulting induced velocities in the rotor wake. An analytical solution exists for a disk with radially constant bound vorticity and only azimuth variation in forward flight and, respectively, in hover. Details on momentum theory and BEMT based modeling can be found in literature, e.g. [62],[49] or [50].

While these approaches can provide useful estimations for a fixed flight state depending on the additional consideration of swirl in the rotor wake or cross flow in the disk, they do not catch the dynamic behavior of the inflow with respect to changes in the rotor forces and moments. The change in inflow is not immediate but rather has the fluid a certain inertia that delays the flow response. Thus other models were needed to account for that in order to be able to model dynamic flight. Most notable are the dynamic inflow models based on potential theory. Pitt and Peters [82] presented a dynamic finite-state inflow model with the linear inflow approximation. This was later enhanced by Peters and He [81] where additional degrees of freedom for the thrust and inflow distribution were included.

Besides the theoretical models, computational models were developed where fewer assumptions had to be made with respect to the model, and arbitrary load distributions and blade forms could be considered. One approach is the discretization of the bound vorticity distribution along the blades, resulting in so-called free-wake methods. In each numerical time step, the trailing and shed vorticity is placed as a marker in the wake, where the markers are connected by filaments. The progression of those markers is computed from the mutual interaction of the filaments according to the Biot-Savart law. The resulting flow velocities at the blade positions can be used to compute the air loads and respectively bound vorticity by BET. A disadvantage of this approach is that with developing wake, the grid spanned by the filaments is distorted, and this can lead to numerical instabilities. An overview of the free-wake approach is given in [62, 50]. A mesh-free approach for this is the application of vortex particle methods where, in a similar fashion, shed and trailing vorticity are placed in the wake in each time step, but the markers represent particles with a given shape and direction [61]. There is no connection between the particles, and therefore, no mesh distortion is present even further down in the wake. These approaches can be enhanced with a panel method to account for the airfoil geometry and compute blade lift directly, thereby getting rid of tabulated airfoil data and BET. Nevertheless, drag estimations are not straightforward with panels [33].

While these numerical methods do account for arbitrary load conditions, they still miss the possibility to account for arbitrary environmental flow conditions. Homogeneous wind conditions can be taken into account by simply translating the markers with the given speed[55] . Vortex structures can be modeled as well, as they can be inherently formulated within the vortex-based methods, and therefore, interaction can be simulated. Nevertheless, the translation of an arbitrary flow field that is not vorticity-dominated and wall-bound flow in the vorticity notation is not straightforward forward, and therefore, flight in an arbitrary flow environment with the respective two-way interaction is challenging.

All of the above modeling approaches, either analytic or numeric, additionally suffer from limitations with respect to wall-bound flow or obstacles in close vicinity to the rotor. Especially recirculation effects due to vertical walls and ground or partial ground effect cannot be inherently modeled with the analytical or dynamic inflow models. There are enhancements available that try to take into account these effects, however, they are not generalizable for an arbitrary environment. While obstacles can be modeled for free-wake and vortex particle methods, they do not take into account the viscous effects of the flow close to the wall. Furthermore, all models cannot take into account arbitrary surrounding flow with the correct computation of the interaction between rotor wake and surrounding flow. Thus, another approach has to be chosen that is computationally efficient and does not suffer from these limitations.

## 3.3 LBM Inflow Model

The previous section presented various approaches to compute the induced velocity. This section presents the inflow computation with the LBM method that was partially developed in this thesis. In general, the LBM does not suffer from the limitations of the previous methods with respect to the interaction effects between environmental flow and rotor wake or the effects of wall-bound flow as this is inherently captured (assuming proper modeling) in the 3D flow simulation. However, the geometric modeling of the rotor blades in the flow simulation is not possible with the basic LBM formulation as it is restricted to low Mach numbers, and therefore, the resulting wall velocities of a rotating blade would be too high. Furthermore, the geometric representation would require fine grid resolution and increase computational effort significantly. Besides that, the accurate modeling of the curved airfoil shape in a cartesian model while capturing the boundary layer effect is challenging in LBM. As a result the rotor model in the flow field is simplified and can be classified in two different approaches in the context of this thesis. The first modeling approach is an actuator disk (AD) model where the rotor is represented as a continuous infinitely thin pressure disk in the flow field and the other is an actuator line (ACL) model where the blades are represented independently by a local forcing term at the current blade position. In the following, these modeling approaches are presented in detail.

### 3.3.1 Actuator disk model rotor model

The AD with an infinitely thin pressure jump over the rotor disk does not account for the effect of the individual blade but is rather an averaged load distribution with contributions from all blades at each rotor disk position over a full rotor rotation. Because of the requirement of a Cartesian grid for LBM the grid cannot be adjusted to a circular shape and therefore the volume around the lattice nodes has only a partial overlap with the rotor disk (see Figure 7). For each of the only partially overlapped cells a weighting factor is computed by which the force applied to the cell is reduced. The computation of the averaged loads can be achieved by simply simulating the rotor for a full or even multiple rotations, averaging the loading, and then sending it to the LBM simulation. Nevertheless, this does not allow for a tight coupling where the exchange happens in every time step (see subsection 3.3.6 for details on the coupling modes). While a local approach is possible even with a tight coupling, required memory, and network traffic resources would increase depending on the resolution of the flow field. The interpolation of the force and inflow values on the fluid grid and blade elements'

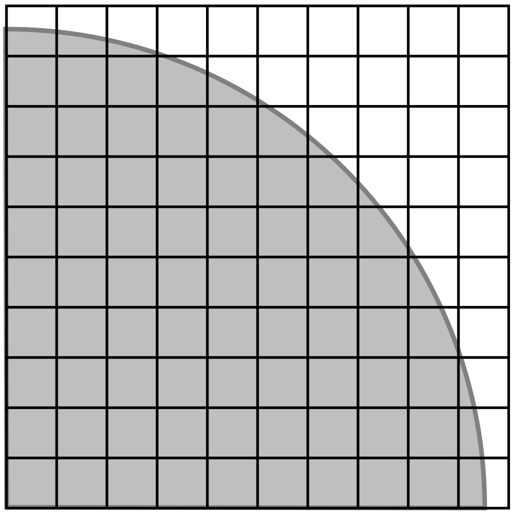

**Figure 7** Partial overlap of the grid (black) by the rotor disk area (grey). Partially overlapped cells get a scaling factor proportionate to the fractional area when forcing is applied.

positions increases computational effort and the coupling time. In order to achieve a fast evaluation of the force and inflow values on both sides of the coupling while maintaining a fixed amount of resources, the thrust distribution is approximated by a set of base functions. The same approach is applied for the inflow, although results showed that this is not generally feasible for all use cases. In the following, the respective coupling modes for the AD models are presented.

### 3.3.2 Linear-Harmonic Coupling

In the linear-harmonic coupling the thrust and inflow distributions are represented with a Fourier series. This approach was published previously by Bludau et al. [13] and is used for comparison in this thesis. The thrust $T$ is hereby represented as a function that assumes a constant pressure jump along the radial coordinate and only varies in a harmonic fashion in the azimuth direction given as

$$T(r,\Psi) = \sum_{i=0}^{N_\mathrm{h}} t_{i,c}\cos(\Psi i) + t_{i,s}\sin(\Psi i) \tag{3.30}$$

where $N_\mathrm{h}$ is the number of harmonics, $\Psi$ is the azimuth angle and $t_{i,c}$ and $t_{i,s}$ are the cosine and sine coefficients for the $i$-th harmonic respectively. Equation 3.30 shows only dependence on the azimuth position. The coefficients are computed with a Fourier series

$$t_{i,c} = \frac{\int_0^{2\pi} T_\mathrm{blade}(\Psi)\cos(\Psi)d\Psi}{\int_0^{2\pi}\cos(i\Psi)d\Psi} \tag{3.31}$$

$$t_{i,s} = \frac{\int_0^{2\pi} T_\mathrm{blade}(\Psi)\sin(\Psi)d\Psi}{\int_0^{2\pi}\sin(i\Psi)d\Psi} \tag{3.32}$$

where $T_{\text{blade}}$ is the total blade thrust. The evaluation of the integral is approximated by a summation of all azimuth positions for each blade as

$$t_{i,c} \approx \frac{2}{N_\Psi} \sum_{j=1}^{N_{\text{blade}}} \sum_{k=1}^{N_\Psi} T_{\text{blade},j}(\Psi_k) \cos(i\Psi_k) \tag{3.33}$$

$$t_{i,s} \approx \frac{2}{N_\Psi} \sum_{j=1}^{N_{\text{blade}}} \sum_{k=1}^{N_\Psi} T_{\text{blade},j}(\Psi_k) \sin(i\Psi_k) \tag{3.34}$$

with $N_{\text{blade}}$ being the number of blades of the rotor and $N_\Psi$ the number of discrete azimuth positions over a full rotor revolution. This harmonic approach does not account for the radial change of blade air loads but captures the harmonic change of the blade lift over a single rotor rotation. The number of harmonics should be an integer multiple of the rotor blades because non multiple harmonics do not significantly contribute to the series.

In the previous works presenting and using this approximation [13, 10, 44, 45] the rotor code used an inner iteration to compute a full rotor rotation within a single time step and use those values to compute the coefficients. As this approach is not available in all rotor codes another approach was derived in the context of this work. The values are dynamically stored in each time step in a circular buffer, and the coefficients are updated with the respective contribution of the current time step. When the first full rotation of the rotor is finished, the stored values are used to subtract the contributions of the previous rotor rotation at the current azimuth position. This allows changes in the rotor rotational speed, e.g., for run-up or propellers with RPM control. There are several things that should be noted:

- The coefficients of the first rotation do not provide a physically meaningful solution.
- When the rotor is not in a steady state the solution is not accurate because of periodicity requirements for the Fourier series. Nevertheless, it is still a valid approximation because the rotor tends to move towards periodicity faster than compared to the fluid inertia.
- If the azimuth stepping is not constant or does not add up to exactly 360 ° an error is introduced. However, considering small azimuth steps of <1 ° this approach did not show any significant errors in the application.
- The full rotor force due to a pitch input is delayed by one rotor rotation before it takes full effect

Depending on the air load distribution and the grid resolution, the forcing in the flow field is not equal to the total thrust computed directly from the blade loads. Therefore, in each time step the rotor force is scaled with the ratio of exact thrust to the sum of all fluid force terms. The exact thrust from the airloads used for the scaling has to be gradually adjusted similar to the coefficients in order to allow for a smooth increase, otherwise this would introduce instabilities.

Contrary to the sampling of the thrust distribution over the full rotor disk, the inflow distribution can be fully sampled at each time step because the rotor forces are applied over the full rotor disk in each time step. The representation of the inflow is a constant mean inflow with a linear variation over the disk. In visual terms, it is a plane with an offset from the ground and a certain lateral and longitudinal pitch. This approach is inspired by the Pitt–Peters three-state dynamic inflow model [82]. The flow through the rotor disk by linear approximation is given as

$$u_i(r, \Psi) = u_{i0} + u_{is} r \sin(\Psi) + u_{ic} r \cos(\Psi) \tag{3.35}$$

where $u_i$ is the velocity in the i-th direction, $u_{i0}$, $u_{ic}$, $u_{is}$ are the mean, cosine and sine coefficients and $r$ is the non-dimensional radial coordinate. The coefficients are calculated by

$$u_{i0} = \frac{1}{N_{\text{cell}}} \sum_{j=1}^{N_{\text{cell}}} u_j \tag{3.36}$$

$$u_{ic} = \frac{4}{N_{\text{cell}}} \sum_{j=1}^{N_{\text{cell}}} u_j r \cos(\Psi) \tag{3.37}$$

$$u_{is} = \frac{4}{N_{\text{cell}}} \sum_{j=1}^{N_{\text{cell}}} u_j r \sin(\Psi) \tag{3.38}$$

with $u_j$ being the velocity in each cell, $N_{\text{cell}}$ the number of cells within the rotor disk. It should be noted that thrust and velocity coefficients are computed for all directions, so not only the induced velocities perpendicular to the rotor disk are captured but also free stream conditions.

This approach has the advantage that only a small amount of data has to be exchanged, namely three coefficients for each velocity component and two times $N_{\text{h}}$ coefficients for the thrust distribution. Furthermore, thrust and velocity can be easily evaluated at any position in the rotor disk without the need for more costly (higher-order) interpolation. The coefficients are updated and exchanged each time step although an arbitrary exchange rate could be used. Nevertheless, this set of functions acts as a strong filter for both radial changes in the thrust distribution and velocity disturbances less than one rotor radius. While this is considered sufficient for simulator flight mechanics, accounting for smaller disturbances in airflow when flying in challenging conditions such as ship landing operations, flight near buildings, or having interaction of multiple rotors might be necessary. Besides the strong filtering properties, this approach represents thrust and inflow in an idealized state that is not generally the case for all rotors. While modern rotors are designed to achieve optimal thrust and inflow distributions, i.e. uniform load and uniform inflow, this is often not the case with experimental rotors. This could lead to overly optimistic values for performance prediction when validating against experimental rotor measurements.

### 3.3.3 Bessel-Fourier Coupling

In order to overcome the drawbacks of the linear-harmonic coupling with its strong filtering properties and the idealized representation of both the inflow and thrust distribution an extension to the linear-harmonic model was derived and presented in [43]. The new Bessel-Fourier model approximates not the thrust but the pressure distribution of the rotor and uses an additional set of basis functions in the radial direction. This extension is inspired by the enhancement of the Pitt-Peters to the Peters-He inflow model presented in Ref. [81]. Contrary to the linear-harmonic model, the Bessel-Fourier model does not assume a constant pressure distribution in the radial direction but rather uses Bessel functions to represent the radial change. The harmonic part in the azimuth direction is unchanged due to the rotor's approximate harmonic behavior. The choice for the Bessel function is due to the fact that they pose the exact solution for the two-dimensional Fourier series in polar coordinates.

The pressure distribution $\Delta\tilde{p}$ reconstructed from the Bessel-Fourier series is given as

$$\begin{aligned}\Delta\tilde{p}(r,\Psi) = \sum_{j=0}^{N_{\mathrm{h},\Psi}} \sum_{i=0}^{N_{\mathrm{r}}} & p_{ij,c} J_1(j_{1,i}r)\cos(\Psi j) \\ & + p_{ij,s} J_1(j_{1,i}r)\sin(\Psi j)\end{aligned} \tag{3.39}$$

where $p_{ij}$ are the coefficients, $J_i$ the Bessel function of the first kind with order $i = 1$ and $j_{j,i}$ the i-th root to the Bessel function with $j = 1$. The number of the harmonics in azimuth and the number of Bessel functions in the radial direction are denoted as $N_{\mathrm{h},\Psi}$ and $N_{\mathrm{r}}$ respectively. The cosine coefficient is given as

$$\begin{aligned}p_{ij,c} = \sum_{k=0}^{N_{\mathrm{blade}}} & \frac{1}{\int_0^{2\pi} \cos(i\Psi)^2 d\Psi \int_0^1 J_2(j_{1,i},r)^2 dr} \\ & \int_0^{2\pi}\int_0^R \Delta p_k(r,\Psi) J_1(j_{1,i}r)\cos(\Psi j) r dr \mathrm{d}\Psi\end{aligned} \tag{3.40}$$

with the sin coefficient being determined in the same manner. The integrals are approximated again in a similar fashion to Equation 3.33 and 3.34. The approximate solution is given as

$$p_{ij,c} \approx \sum_{k=0}^{N_{\mathrm{blade}}} \sum_{l=0}^{N_{\mathrm{BE}}} \sum_{m=0}^{N_\Psi} \frac{1}{C} \frac{T_{klm}}{2\pi r_l R \Delta r_l R} J_1(j_{1,i}r)\cos(\Psi_m j) r_l \Delta r_l \Delta\Psi_m \tag{3.41}$$

where $N_{\mathrm{BE}}$ denotes the number of radial blade elements, $\Delta r$ the span of the l-th blade element, $\Delta\Psi$ the azimuth increment of the respective time step, and $R$ the radius in physical units. The Bessel functions require $J_1(1) = 0$ and $J_1(0) = 0$. This poses a challenge when modeling a realistic rotor as the lift-producing part of the blade does not start in the center due to root cutout $r_{rc}$ and rotor hub but the approximation is for the full disk, e.g. $T(r) = 0 \forall r \in [0, r_{rc}]$. While this satisfies the boundary condition at $r = 0$, the constant distribution cannot be approximated in a satisfying manner by the Bessel functions or first order. As a solution, the value at the inner 5% position of the lift-producing part of the blade is linearly extrapolated to zero resulting in

$$T(r) = T(r_{5\%})\frac{r}{r_{5\%}}, r \in [0, r_{5\%}] \tag{3.42}$$

$$r_{5\%} = 0.05 \cdot (1 - r_{rc}) + r_{rc} \tag{3.43}$$

The approximation for the inflow can be done in a similar manner. Nevertheless, the condition of $J_1(R) = 0$ makes this approach not feasible for an arbitrary flow state, as non-zero velocities can prevail even further away from the disk. For the further use of the Bessel-Fourier model in this work a more general approach was chosen, where the inflow velocities are interpolated onto the current blade element positions for all rotor blades. The interpolation is done in plane, so no out-of-plane motion of the blades is considered. The interpolation order can, in general, be freely chosen, although cubic interpolation led to satisfactory results in preliminary studies and was used as part of this thesis.

### 3.3.4 Actuator Line Coupling

The ACL modeling pursues a local approach where the effect of the individual blade at its current position is modeled rather than an averaged influence over the whole rotor disk as in the AD models. The current blade forces are interpolated onto the fluid grid at the current blade position. A singular force entry, e.g. for each radial position the LBM forcing term is applied to a single cell, would lead to numerical instabilities. Therefore, the force terms are computed from the blade element forces multiplied with a kernel distribution function. The force term $F$ for an arbitrary cell is then given as

$$F(\vec{x}) = -\sum_{i=0}^{N_{\mathrm{blade}}} \sum_{j=0}^{N_{\mathrm{BE}}} T_{ij}\eta_{ij}(\vec{x}) \tag{3.44}$$

where $\eta$ denotes the kernel distribution function. There are different definitions present in literature for $\eta$. A commonly used approach in literature (see [96] or [26]) is

$$\eta_{ij}(\vec{x}) = \frac{1}{\epsilon^3 \pi^{3/2}} \exp\left[-\left(\frac{r_D}{\epsilon}\right)^2\right] \tag{3.45}$$

$$r_D = \|\vec{x} - \vec{x_{BE}}\| \tag{3.46}$$

with $r_D$ being the shortest distance between the blade element position $\vec{x}_{\mathrm{BE}}$ and the fluid cell position $\vec{x}$ and $\epsilon$ being the kernel width. The kernel is of spherical shape, which leads to an overlap of the contributions from neighboring blade elements to a single fluid cell, and forcing is applied beyond the blade tip and the blade root depending on the value of $\epsilon$ and the position of the first and last blade element. This is not generally regarded as a problem concerning simulation accuracy. Nevertheless [47] proposed an actuator curve embedded (ACE) approach where each cell is only influenced by a single blade element. This is achieved by computing the shortest perpendicular distance $p_N$ between the actuator line, e.g. blade direction, and a respective fluid cell. Then, only the force term of the blade element closest to the intersection between the distance vector and blade radial vector is applied to the fluid

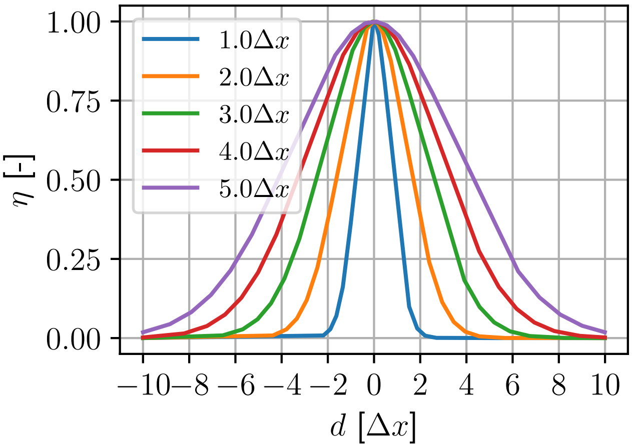

**Figure 8** Influence of the kernel width $\epsilon$ on the force distribution. The distance $d$ can either be $r_D$ or $p_N$.

cell. The restricted kernel is then given by

$$\eta_{ij}(\vec{x}) = \frac{1}{\epsilon^2 \pi \Delta r} \exp\left[-\left(\frac{p_N}{\epsilon}\right)^2\right] \tag{3.47}$$

with $\Delta r$ as the blade element width. Details can be found in the respective publication [47]. This approach ensures that the forcing does not extend beyond the radial direction of the blade. Both approaches for the kernel are applied in this work and compared with respect to overall results and stability.

Contrary to the AD methods, there is the additional parameter $\epsilon$. The choice of $\epsilon$ determines the kernel width and, therefore, how smeared the force entry is in the flow field (see Figure 8). There are various suggestions in literature to choose $\epsilon$ accordingly, e.g. [30, 94]. A common approach is to use a multiple of the grid spacing $\Delta x$ to ensure stability independent of the current resolution of the simulation. As discussed in [70] the distribution kernel introduces a vortex with a vortex core size depending on the kernel size. This also influences the vortex core size of the blade tip vortices. Since the resolutions are in general above the estimated vortex core size of $\tilde{1}5\%$ of the blade chord [69, 50], a correct core size is not achievable anyway and therefore the choice of $\epsilon$ within common limits of $\epsilon \in [2\Delta x...6\Delta x]$ is reasonable [94]. Another approach is the dependency of $\epsilon$ on the blade element chord $c$ as presented in [46], where the ratio between kernel width and chord constant is. They propose the following for $\epsilon$

$$c^* = \frac{4}{\pi}\bar{c}\sqrt{1-r} \tag{3.48}$$

$$\epsilon^* = 0.25\pi AR\left(n_{\max}\frac{\Delta x}{R}\right)c^* \tag{3.49}$$

$$\epsilon = \max(\epsilon_{\min}, \epsilon^*) \tag{3.50}$$

where $\bar{c}$ is the averaged chord of the blade, $\epsilon_{\min}$ the minimum kernel width with $\epsilon_{\min} > 0$

and $n_{\max}$ and $n_{\min}$ are constants imposing upper and lower limits for epsilon, respectively. This represents the actual chord distribution with a quadratic approximation, where $c$ has its maximum value at the blade root and tends to zero at the blade tip. Taking $\epsilon_{\min}$ into account, epsilon is not zero at the blade tip, but at its minimum value, this ensures a minimal extension of the force beyond the blade tip. Considering that the chord variation along a typical rotor blade is not as significant as for wind turbine blades where this approach comes from, it was not pursued further. However, it could be easily adapted for blades with strong taper. For the results in this work $\epsilon$ was set to a constant value of $\epsilon = 5\Delta x$

The inflow sampling is not as straightforward as for the Bessel-Fourier model, where velocities are simply extracted at the current blade position. As mentioned before the forcing introduces a vortex along the quarter chord line of the blade. The forming vortex induces an additional velocity around the blade when sampling the flow velocities for each blade element. This additional component has to be taken into account for the table lookup, as the angle of attacks for the airfoil data are given without this artificial inflow component. There are different approaches in literature to account for this [30, 72, 25, 70, 67].

One of the approaches used in this study is derived from the filtered lifting line theory presented by Martinez-Tossas and Menevau [70]. The authors present an analytical solution for the induced velocities due to a Gaussian kernel that uses a bigger kernel width than would be needed for the correct blade tip vortices. The assumption of their approach is that of a non-rotating blade. The analytical solution is then used to correct the current inflow distribution and move it towards the analytical one. In short, the procedure can be divided into five steps. First, for each blade element the bound circulation is evaluated. In the second step, the derivation of the circulation distribution along the blade is computed. The result is used in the third step to compute the theoretically induced perturbation velocity component. This step is done for the optimal $\epsilon$ to resolve the tip vortices correctly and the actually used $\epsilon$. In the fourth step, the difference between the two resulting perturbation velocities results in the velocity correction increment. Steps one to four are repeated until the correction increment is converged. In the last step, the correction is added to the sampled inflow velocity. This approach introduces additional computational overhead, as in every time step, the sampled velocities have to be corrected with an iterative method, and cost increases $O(N^2)$ with the number of blade elements used. Furthermore, this does not account for the helix-like wake shape of rotating rotor blades and could lead to divergence for rotating blades. A similar proposal by Dağ et al. (Ref. [30]) included a correction for rotating blades where the rotor wake shape is taken into account. However, this includes the storage of the trailing vorticity and the propagation of the vorticity markers according to the flow conditions, i.e. a simplified free wake solver in the LBM framework. As this includes significant computational overhead the basic correction from [70] was used as they applied it successfully for a rotating wind turbine in [97].

As the above approach involves computational overhead and is not guaranteed to converge a second, more straightforward approach was adopted from [51, 25], as well. In this approach, the velocity is not sampled directly at the current blade position but rather as an integral average of the surrounding velocities. The averaging is done in a circular region around each blade element with a freely adjustable radius. This approach is not based on mathematical consideration from lifting line theory, but it uses the fact the vortex-induced velocity profile is radially symmetric. Using this property a circular average negates the effect of the kernel induced vortex. The advantage of this approach is its straightforward implementation, and no assumption about the effect of the blade rotation has been made.

For both approaches concerning the sampling of the inflow velocities for the coupling, the current blade position and blade flap angle are taken into account, contrary to the AD methods where a fixed rotor plane is assumed and a possible out-of-plane motion of the blades is not taken into account.

### 3.3.5 Superposition Coupling

In order to determine if the LBM provides a better inflow prediction than established models used in rotor codes, a superposition approach is used for comparison. In this approach, the inflow is computed by whatever model is available without the influence of surrounding flow. However, when computing the blade forces, the additional velocity component from the surrounding flow is extracted from a previously computed flow field at the current blade position and simply added to the velocity vector used for the computation of the angle of attack. This approach is a one-way coupling where the surroundings influence the rotor forces but no effect of the rotor on the surrounding flow is considered. Furthermore, any information about blocking of the wake due to obstacles is neglected. In the context of this thesis, the Peters-He [81] inflow model is used with velocity data from the pre-computed flow fields.

### 3.3.6 Rotor–Inflow Time Coupling Strategies

The previous sections described the coupling approaches with respect to the inflow computation and velocity and force representation in the flow field. This section gives an overview of the coupling strategy with respect to time coupling. There are different approaches for the two-way coupling with respect to the exchange frequency for inflow and forces. A commonly used approach is a loose coupling, where the exchange of quantities happens after a steady state is reached on both sides of the coupling. To give an example for a rotor simulation in hover with fixed pitch input, one could estimate a mean inflow from momentum theory and simulate the rotor until thrust and power are converged. The result rotor forces are applied in the flow simulation until the flow through the rotor disk is steady. The resulting velocities are sent back to the rotor simulation and the rotor runs until steady state again. This procedure would be repeated until overall convergence is reached. This approach is useful and provides fast convergence but does not account for dynamic changes of rotor inputs or flow environmental conditions, e.g. gusts.

Accounting for dynamic changes on either or both sides of the coupling due to external input does not allow an exchange rate after reaching a steady state for the flow or the rotor. Therefore, a tight coupling approach has to be adopted. In this approach, the exchange happens every time step, although every N steps could be adopted if $N\Delta t$ is still small with respect to the dynamic response of either the flow or the rotor. This approach is straightforward: the current states of the flow simulation and the rotor simulation are exchanged in every (N-th) time step once, and the simulation progresses until the system reaches a desired end condition. This allows the simulation of dynamic inputs on the rotor side or unsteady environmental flow conditions on the LBM side.

The tight coupling can be further enhanced by repeating the exchange with updated values from both sides in the same time step until both solvers converge within that time step. However, the iteration process would require solving the time step multiple times, which would increase the overall simulation time by the number of iterations necessary. Additionally, most codes do not provide an interface for that kind of iteration and would require major changes. The additional computing time, together with the required adaption of code, renders this method unattractive for application.

At last a monolithic approach is possible, where the flow field and the rotor dynamics are solved within a single set of equations. This is similar to the tight coupling approach with the internal iteration for each time step, and the caveats of this approach are the same, plus the additional need to construct a single system of equations that is solved, which does not allow the coupling of arbitrary codes.

**this thesis the tight coupling approach is used, with an exchange of quantities in each time step.**

### 3.3.7 External field coupling

In order to account for interaction effects between the rotor and the surrounding flow environment, the flow field has to be obtained for the LBM simulation. One approach would be the simultaneous simulation of the environment, e.g., a ship's air wake and the rotorcraft. Besides the additional cost of the ship air wake computation, this would require the computational domain to extend far enough to hold the rotorcraft and ship, including any forerun needed to get a realistic incoming flow towards the ship. Depending on the initial distance for the rotorcraft approach, this might require a massive amount of resources. A more efficient approach is needed where the length of the flight trajectory does not impact the computational speed.

The approach developed in the context of this thesis was previously published in [44] and extended in [45]. The approach splits the environmental flow field and the computational grid surrounding the rotorcraft in two independent simulations. The environmental flow field is computed in advance and the result is stored to be used in the actual rotorcraft simulation. The computational method used for the advanced computation is not limited to an LBM simulation but can be done with any available CFD code suited for the specific physical setup. The resulting flow velocities are then applied as a velocity boundary condition on the LBM simulation of the rotorcraft. The application of this approach allows for the minimum computational resources needed for the environmental flow field to capture the desired extent and fidelity. This procedure enables a two-way coupled simulation between the rotorcraft and the surrounding flow in the vicinity of the rotorcraft in the LBM simulation. The interaction between the complete surrounding flow field is just one-way. However, Bludau et al. [12] showed that the extent of the influence region of the rotorcraft is very limited, and thus, the one-way coupling at the LBM domain boundary is justified, assuming the domain size is chosen appropriately. In the case of the rotorcraft starting its trajectory outside the precomputed flow field, consistent ambient flow conditions can be chosen, e.g., ambient free stream velocity, before entering the precomputed domain during the simulation (see Figure 9).

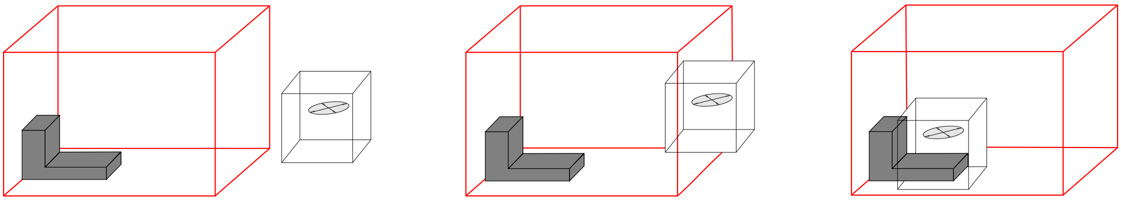

**Figure 9** Different stages of the simulation with an external field (red)) and the rotorcraft simulation domain (black) from left to right. Starting outside the precomputed field, upon entry, and within the external field (left to right). The external field contains an obstacle, which is accounted for in the rotorcraft domain upon arrival.

The precomputed external field can either be seen as steady or unsteady. Previous studies in the context of this thesis [44] and from literature, e.g., [104] show that with increasing flight speed, a steady, thus not time-resolved field does not deteriorate simulation results. Low-speed flight does require a time-resolved solution of the external field. Considering that in low-speed forward flight, the interaction with the same flow structure, e.g., a vortex, evolves over time, contrary to high-speed forward flight, where the interaction with the same vortex would be too short to see significant time-dependent evolution of the vortex. Thus, depending on the flight scenario under consideration, a steady external field could be sufficient, therefore saving memory resources as only the solution of a single time step is required.

The implementation for the steady flow field is straightforward; the respective solution is loaded into memory, and the velocity values are extracted from the respective location within the external field depending on the position of the LBM domain. The extracted velocity values get applied as the value of the velocity boundary at the border of the LBM domain. The procedure is similar for the unsteady external field case, where all time steps are loaded into memory. The respective external field from a time perspective is determined by the simulation time of the LBM simulation. If the time stepping of the external field solution is coarse with respect to the relevant time scales of the field, a linear interpolation between two external field solution files could be implemented to avoid step-wise changes of the boundary conditions in the LBM simulation. Should the memory resources on the GPU not be sufficient to hold all external field solution steps at the same time, an algorithm was implemented where a fixed amount of time step data is loaded onto the GPU and unloaded after their usage. This loading and unloading is done in a way that runs parallel to the flow computation. This procedure could be extended to include a loading routine from the hard drive if CPU memory is not sufficient but was not necessary in the course of this work. It should be noted that in the case of a rotor-vortex encounter where the vortex is represented by an analytical function, the external field does not have to be an actual solution file but can be represented by a function object returning the appropriate values at the requested location. This increases computation speed and reduces memory usage significantly.

The influence of external obstacles like ships or buildings is taken into account in a similar manner. For each external field velocity solution a mask file exists where a boolean value determines if the position is blocked or not. The respective values are read in each time step for all LBM domain nodes (not just at the boundary) and interpolated onto the LBM grid. If the value passes a certain threshold, e.g. 0.5, the lattice cell is assumed a solid boundary in the next time step. With this approach, a ship encounter can be taken into account with respect to arising blockage or ground effects.

Considering that the interaction with the external field is just one-way, the external field solution cannot be prescribed on all boundaries because the rotor wake could not leave the computational domain and would severely alter the results. Thus one has to choose the position of free outflow and velocity boundaries carefully to not obstruct the rotor wake and get meaningful flow results. Depending on the scenario this might change. The appropriate settings are given in chapter 4 for each use case.

This external field approach was successfully used by the author for rotorcraft vortex interaction with an analytical external field [44] and a flight path analysis in a wind farm [45] where steady and unsteady flow solutions of a wind turbine wake were used. Bludau et al. [12] used this approach for a simplified simulation of the rotorcraft approach on a ship vessel. The approach can be enhanced by incorporating the fluid stresses as they are an independent variable in the LBM method as was done by Bludau [11]. In order to reduce the computational or memory overhead, the equilibrium state for the $f_i$ was assumed, and the additional stress information was not needed in the previous publications. However, in this thesis the free flight cases with a precomputed ship wake do incorporate the stresses as well.

# 4. Simulation setup

This chapter covers the different simulation setups used for the validation of the coupling methods and the comparison of the inflow models in different flight scenarios with external flow fields. The Cartesian grid of the flow field has a uniform spacing for the whole domain for all considered setups in this thesis. The grid resolution is defined as cells per rotor radius to account for the different rotors used. As the appropriate grid spacing is a parameter to be determined as part of the validation it will be stated explicitly in the results sections. Due to the simplicity of the meshing, the setup description is condensed as only the rotor positioning, the domain size, and the boundary definitions are necessary. The validation cases are compared against measurements from hover and wind tunnel experiments. The respective hover and wind tunnel setups are described below, as well as the setup for the flight scenarios.

## 4.1 Hover

The hover scenarios consist of a cuboid where all boundary surfaces are treated with the free flow boundary conditions described in section 3.1.2. The rotor is placed in the center of the cuboid (see Figure 10). The default size of the edge length is six rotor radii in the x and y-direction and eight rotor radii in the z-direction. The edge length guarantees that the influence of the boundaries is minimal with respect to the rotor results while keeping computational times low. In order to avoid upflow in the center region of the rotor where the rotor hub would be, a spherical solid blockage is placed.

## 4.2 Wind tunnel

The wind tunnel scenarios consist of a cuboid with a significant extent along the x-direction (see Figure 11). In the experimental setup, the rotor shaft has an inclination angle or shaft angle of attack $\alpha_s$ depending on the wind tunnel speed. Because the AD models are required to be grid aligned, the rotor cannot be tilted in the LBM setup. Thus, the wind tunnel is tilted in the opposite direction to account for the angle of the free stream velocity relative to the rotor disk. The same procedure is applied for the ACL model although it would not require any alignment of the rotor to the grid, however, consistency for all models was desired.

In order to avoid reflections from the inclined walls of the wind tunnel, the walls in z+ and z- directions have a curved slip boundary condition prescribed. The grid-aligned walls in y+ and y- directions use a bounce-back boundary condition. The inlet is a velocity boundary where the wind tunnel speed is prescribed. The outlet boundary is a free stream impedance boundary condition. Special care has to be taken for the edges of the inlet and outlet domain faces, as the conjunction of multiple boundary types can lead to instabilities. Therefore, all edge and corner nodes were classified as bounce-back nodes. The extent of the domain is 24

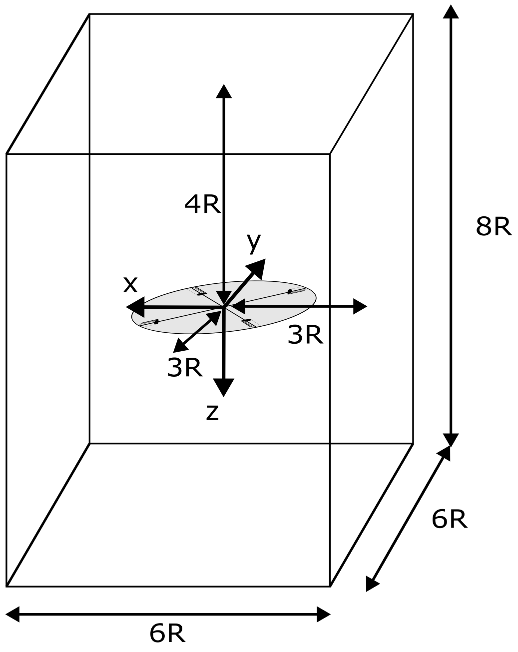

**Figure 10** Hover setup with the rotor placed in the center (not to scale). All boundary faces are free outflow boundaries.

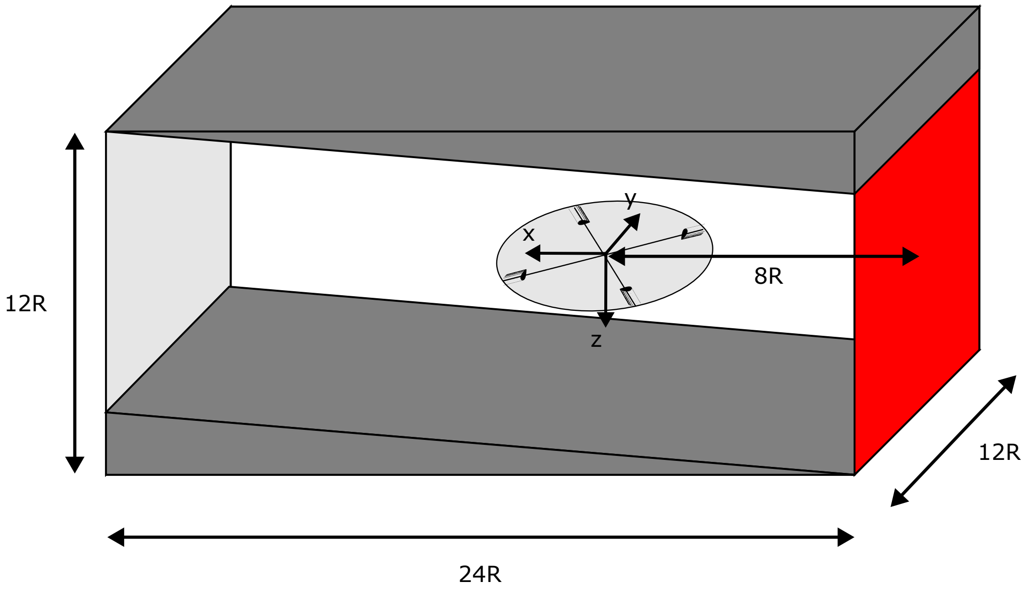

**Figure 11** Rotor position for the wind tunnel setup. The light gray surface denotes the velocity inlet boundary, and the red surface denotes the impedance outflow boundary. Dark grey ramps indicate curved slip boundary treatment, which accounts for a rotor angle of attack. Surface in y-directions as straight slip wall conditions. In z- and y-direction, the rotor is positioned in the center.

rotor radii in x-direction and twelve rotor radii in y and z-direction. It can not be ruled out that this might be too small to avoid wall effects of the wind tunnel. Considering the mid-fidelity approach of the coupling and without any grid refinement capabilities a further extent was not

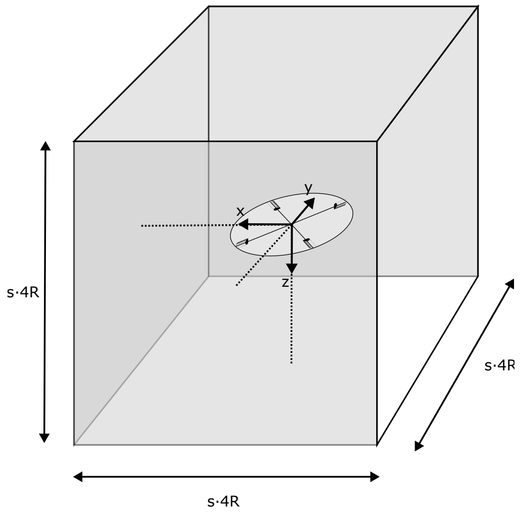

**Figure 12** Free flight setup with the rotor placed at the center of the domain. Gray faced boundaries (x+,y+,y-direction) denote velocity boundaries with values prescribed from an external field, the remaining boundaries are free outflow boundaries. The actual domain size scaling factor s will be determined as part of the application chapter.

computationally reasonable while keeping the domain size constant for all considered grid resolutions and maintain comparability of the results.

## 4.3 Free flight

The setup for the free flight scenarios consists of a cubic where the rotor is placed in the center (see Figure 12). The edge length has to be determined. The boundaries are a mixture of velocity and free outflow boundaries. In order to capture the environmental condition, the boundaries in the x+, y-, and y+ directions are velocity boundaries, and the remaining boundaries are free outflow impedance boundaries. This is under the assumption that the main free-stream direction is towards the rotorcraft heading or sideways but not from the back. The free outflow boundaries in z-, z+, and x- directions allow for an unobstructed wake in forward flight and hover conditions.

# 5. Validation Results

The different coupling modes presented in section 3.2 are validated against experimental measurements and flight test data from two different rotors. One is an experimental two-bladed rotor with a teetering hinge and rectangular blades that are assumed stiff [84]. The simple mechanical setup and the homogeneous airfoil properties, together with the stiffness assumption, reduce the error sources from the mechanical model. After the validation against the experimental rotor data the coupling was compared to UH60A rotor results from wind tunnel measurements [93] and measurements from flight tests [112]. Parts of the following results have previously been presented in [43] as part of this thesis.

## 5.1 Experimental Two-Bladed Rotor

The measurements of the experimental rotor in hover are taken from [84] and the rotor is trimmed to the respective $C_T$ values. The measured data from the wind tunnel experiments are taken from [85]. In this case, the rotor is trimmed to the measured lift and drag values and zero side force, as stated in the report. The measured quantities include power and lift measurements, as well as radial pressure distribution. The focus of the validation against the experimental rotor was to determine the ability of the coupling modes to match measurements as well as the influence of the variation of the flow field resolution and the tip loss factor on the results. The findings are later applied to the UH60A rotor simulations in the second part of the validation study to confirm their portability. The experimental rotor is modeled with two stiff blades with a radius of $R = 2.32\mathrm{m}$ and a central teetering hinge. The blade pitch input is realized directly at the blade and is thus an idealized input without any bearing clearances or pitch link deformations. The investigated coupling approaches include both AD models, as well as the ACL model with the spherical kernel and the integrated inflow sampling, the spherical kernel with the inflow correction and the restricted kernel with the integrated inflow sampling (see subsection 3.3.4). Preliminary studies showed that the restricted kernel with the inflow correction did not converge and results could not be used for the validation.

### 5.1.1 Hover results

**Linear-harmonic coupling model**

In the following, the results for the linear-harmonic coupling model are presented. The power predictions for the LBM inflow computation using the linear-harmonic coupling model are depicted in Figure 13. The model predicts an up to ~28% higher power consumption in comparison to the measurements for the lowest $C_T$. The predicted power decreases with increasing $C_T$ until it is below the actual measured power. A slight upward trend is seen for the highest $C_T$. An explanation for this trend is not possible due to the lack of additional experimental data such as airfoil drag along the blade or velocity measurements in the downwash. The influence of $C_{\mathrm{tl},\%}$ on the power is low, with differences in the low single-digit percentage.

However, the resolution shows a visible influence on the power results with differences of up to 10% between the lowest resolution of 16 cells per radius and 80 cells per resolution. The power results show grid convergence for 64 cells per radius. In general, the power predictions are within a 15% error bandwidth except for the lowest $C_T$ or within 10% if the simulation uses at least 64 cells per radius.

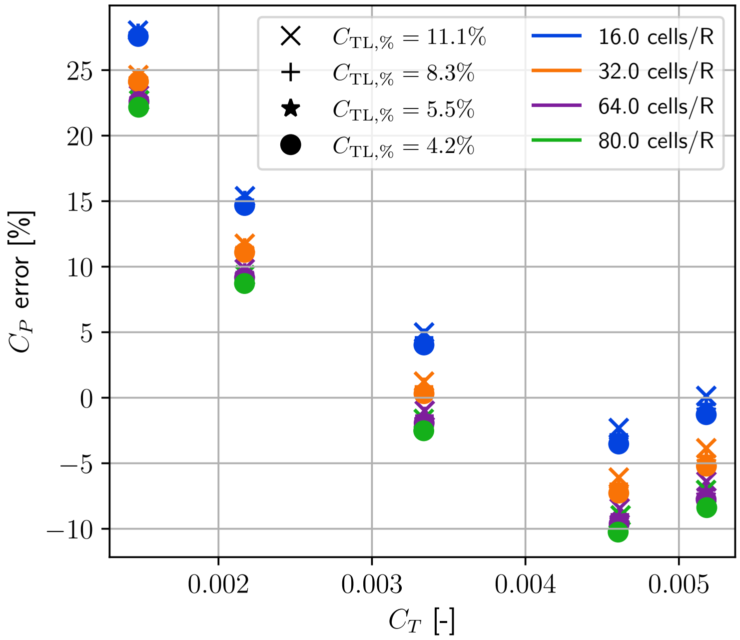

**Figure 13** Power error of the linear-harmonic coupling for the experimental rotor compared to measurements. The results show the variation of the flow field resolution in combination with a variation of the effective tip loss factor $C_{\mathrm{tl},\%}$. Experimental reference data is taken from [84].

The inflow distribution for the linear-harmonic case is exemplary shown for the measured pitch input $\Theta_0$ of 3.0° and 9.2° cases in Figure 14 and Figure 15 which correspond to the lowest and highest $C_T$ measurements, respectively. Due to the restriction of the base functions (see Equation 3.35), the inflow is represented by a constant value for a symmetric inflow distribution that is the result of an AD in the hover condition. An increase in $C_T$, which corresponds to the increase in $\Theta_0$, only increases the magnitude of the inflow as is to be expected. The influence of the flow field resolution is visible with grid convergence being achieved at around 64 cells per radius. The tip loss, in turn, plays a minor role in the inflow distribution. This is in accordance with the power results for the linear-harmonic model as shown before. The influence of $C_{\mathrm{tl},\%}$ is low because the thrust distribution in hover is constant for the linear-harmonic model and the overall thrust is the same for all $C_{\mathrm{tl},\%}$ as per trim condition. A higher $C_T$ or $\Theta_0$ only increases the inflow magnitude but does not impact the results otherwise.

The lift distribution for both trim states (see Figure 16 and Figure 17) do not show a significant change with respect to the resolution. The effect of the tip loss, on the other hand, is visible

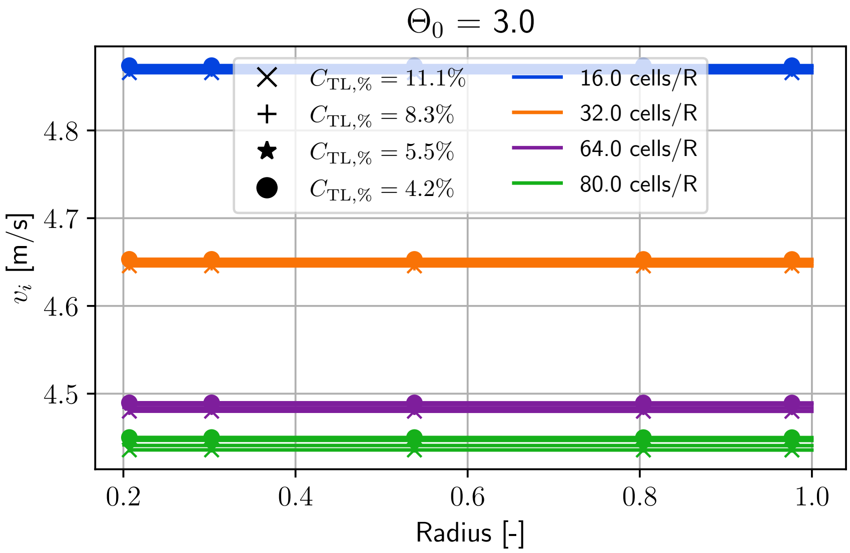

**Figure 14** Radial inflow distribution computed by the linear-harmonic inflow model, with variations in $C_{\mathrm{tl},\%}$ and flow field resolution at $\Theta_0 = 3.0$.

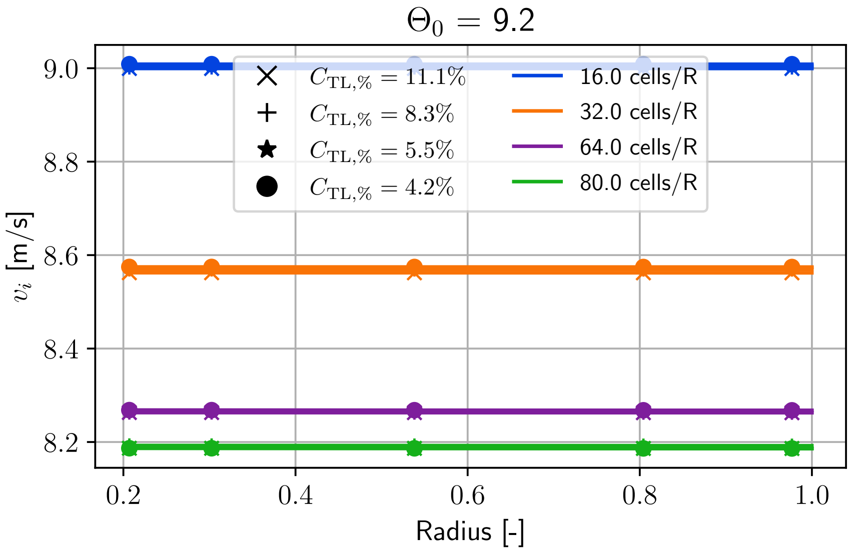

**Figure 15** Radial inflow distribution computed by the linear-harmonic inflow model, with variations in $C_{\mathrm{tl},\%}$ and flow field resolution at $\Theta_0 = 9.2$.

with a higher tip loss reducing the peak magnitude outboard on the blade and a higher $C_{\mathrm{tl},\%}$ moving the peak further inward. This is in accordance with the impact of the tip loss function formulation and the constant inflow distribution. The constant inflow distribution in radial direction leads to the given shape of the thrust distribution which is the same for all simulations with the same tip loss. The fact that all simulations trim the rotor thrust the lift amplitudes of the distribution must be independent from the flow field resolution to ensure the same overall thrust. The angle of attack is negative in the inner blade section as the averaged inflow is higher than it would be in reality, which leads to negative lift values inboard of the blade.

Furthermore, the lift distribution cannot follow the shape of the experimental measurements. Thus the lift is overpredicted outboard of the blade and underpredicted inboard. Overall, the deviation of the lift distribution is significant for all hover trim states. The only influence is the tip loss to adjust the outboard peak towards the experimental measurements. Combining the influence of the tip loss and the fact that the lift distribution is the same for a given tip loss independent of resolution while the inflow amplitude changes with a given resolution but not the tip loss leads to the assumption that the blade pitch input must be dependent on both tip loss and resolution.

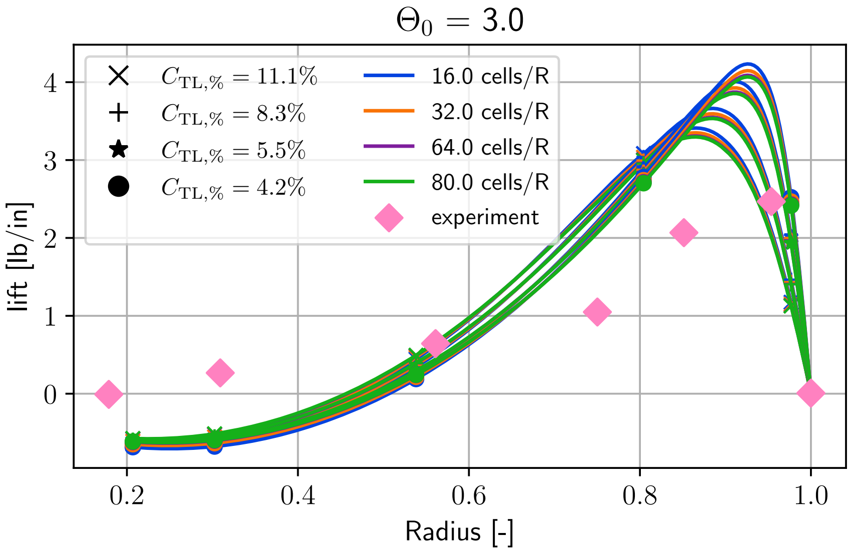

**Figure 16** Radial lift distribution computed by the linear-harmonic inflow model, with variations in $C_{\mathrm{tl},\%}$ and flow field resolution at $\Theta_0 = 3.0$. Experimental reference data is taken from [84].

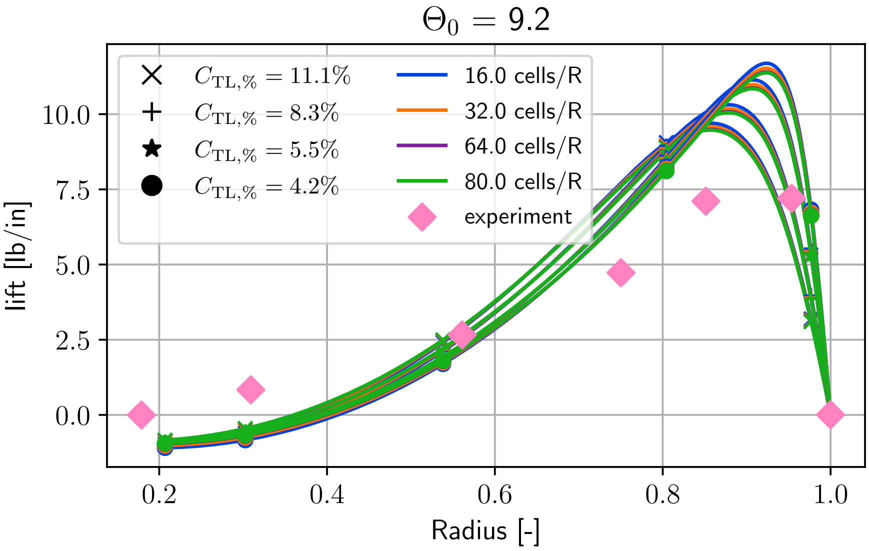

**Figure 17** Radial lift distribution computed by the linear-harmonic inflow model, with variations in $C_{\mathrm{tl},\%}$ and flow field resolution at $\Theta_0 = 9.2$. Experimental reference data is taken from [84].

Comparing the predicted blade pitch angle $\Theta$ with $\Theta_0$ underlines this assumption and the results show the same trend as the power predictions. The input overshoots experimental measurements for the low pitch experiments and underestimates the required pitch for the higher pitch input measurements. The influence of fluid grid resolution and tip loss is visible with lower resolution and higher tip loss leading to higher $\Theta$, which is in accordance with the power predictions. From a physical perspective, the results look plausible.

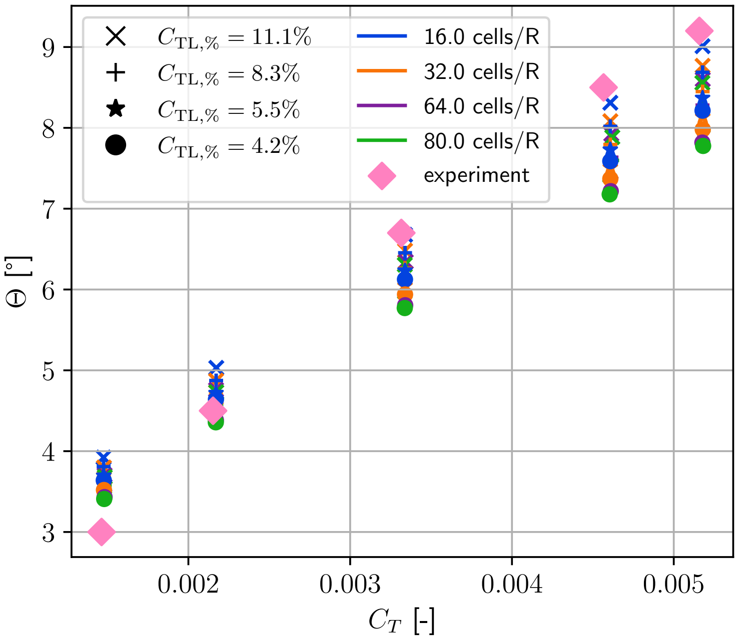

**Figure 18** Predicted pitch input $\Theta$ required for $C_T$ trim compared to measured pitch input $\Theta_0$ for different $C_{\mathrm{tl},\%}$ and flow field resolution. Computed with the linear-harmonic inflow model in hover condition. Experimental reference data is taken from [84].

### Bessel-Fourier coupling model

The Bessel-Fourier coupling model predicts an up to ~27% higher power consumption in comparison to the measurements for the lowest $C_T$ (see Figure 19). The predicted power decreases with increasing $C_T$ until the last measured $C_T$ where a slight upward trend is visible. For the lowest $C_T$ and a resolution of 64 cells per radius, the results show an outlier, which will be addressed later. Higher resolutions and lower $C_{\mathrm{tl},\%}$ did not converge for this trim state, which will be discussed with the inflow and lift results. The variation due to $C_{\mathrm{tl},\%}$ increases with increasing $C_T$ with a higher tip loss leading to a higher power consumption. This is to be expected since a higher tip loss leads to a reduced blade lift in the tip region, and therefore, a higher pitch input at the blade is needed to reach the trim values. The increase in the blade pitch comes with an increase in the blade profile drag. The influence of the resolution is negligible except for the gap between the resolution of 16 cells per radius and the rest of the results. For higher resolutions, the overall variation of the predicted power is within a 5% bandwidth. Grid convergence is reached with 64 cells per radius which is the same as for the linear-harmonic coupling case.

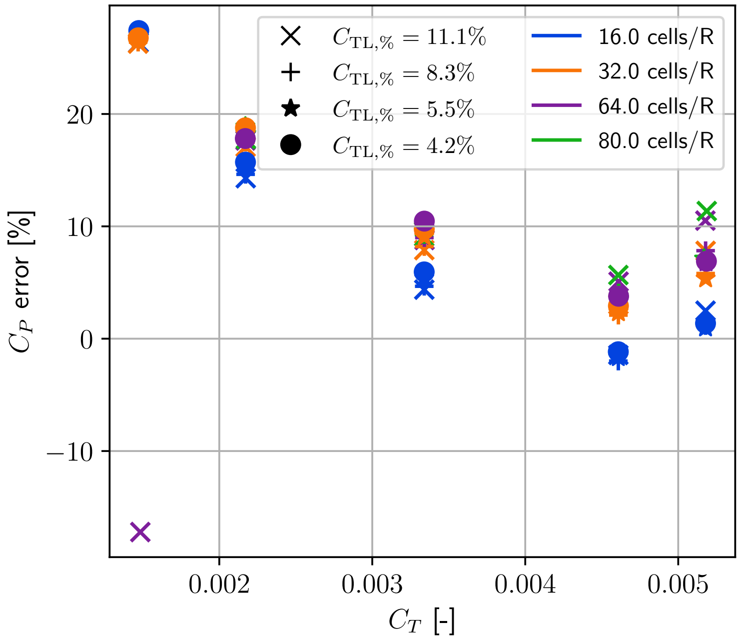

**Figure 19** Power error of the Bessel-Fourier coupling for the experimental rotor compared to measurements. The results show the variation of the flow field resolution in combination with a variation of the effective tip loss factor $C_{\mathrm{tl},\%}$. Experimental reference data is taken from [84].

The inflow results (see Figure 20 to Figure 22) are shown for a subset of $C_{\mathrm{tl},\%}$ for clarity. Contrary to the power results, the inflow distribution for the low $C_T$ case ($\Theta_0 = 3.0°$) shows a clear influence of the resolution with increasing numerical instabilities at the inner blade section starting from the blade root. The instabilities are already visible with a resolution of 32 cells per radius. For lower $C_{\mathrm{tl},\%}$ the simulation did diverge and results are therefore not shown. The cause of this instability is a combination of the flow conditions at the blade root, the influence of the simplified hub representation, and the approximation with Bessel functions.

In general, the load at the blade root for an untwisted rectangular blade is low and results in low induced flow velocities. In the simulation, the blade root vortex is not resolved because of a lack of cells due to the cartesian grid. The spherical hub shape additionally introduces disturbances in the flow that are significant with respect to the induced flow velocity. Thus a low flow velocity with potential upflow regions and disturbances is sent to the mechanical solver computing the air loads of the blade. Considering the low blade speed at the blade root, small changes in the inflow have a significant influence on the angle of attack and on the blade loads in that section. The approximation of the Bessel functions due to the finite amount of shape modes used always introduces errors with regard to the amplitude and phase of the inflow representation. This phase error is then introduced in the flow field. As a result, sinks and heaps of the inflow distribution are not in phase with the resulting load distribution and can build up to instabilities. The flow grid acts as a filter, so with coarser resolution those errors are filtered out when the force is introduced in the flow. Thus the lowest resolution does not show signs of instabilities. With increasing thrust and resulting increasing inflow velocity at the inner section the instabilities move to higher resolution (see Figure 21) or vanish completely (see Figure 22). The lowest tip loss with the highest resolution was still not achievable.

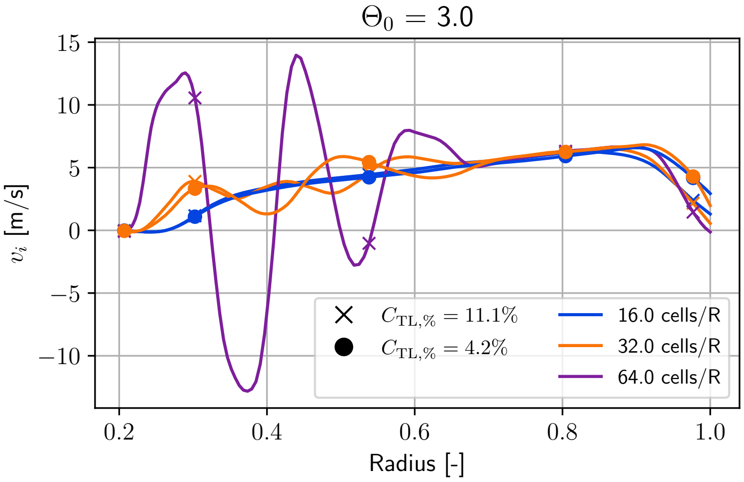

**Figure 20** Radial inflow distribution computed by the Bessel-Fourier inflow model, with variations in $C_{\mathrm{tl},\%}$ and flow field resolution at $\Theta = 3.0$. Only results for the highest and lowest $C_{\mathrm{tl},\%}$ are shown. Cases not shown for these parameters did not converge.

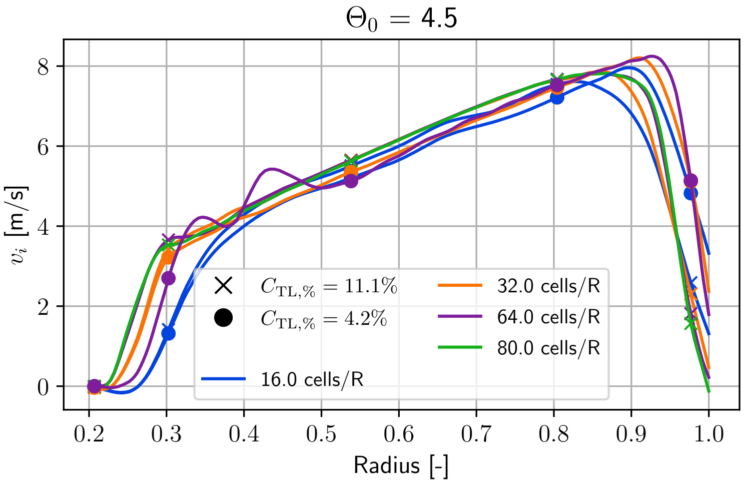

**Figure 21** Radial inflow distribution computed by the Bessel-Fourier inflow model, with variations in $C_{\mathrm{tl},\%}$ and flow field resolution at $\Theta = 4.5$. Only results for the highest and lowest $C_{\mathrm{tl},\%}$ are shown. Cases not shown for these parameters did not converge.

In general, the inflow follows a linear profile with a sharp drop in the blade tip region due to the steady disk vortex at the boundary of the AD. The peak position and the steepness of the drop are influenced by the tip loss factor where a smaller tip loss leads to a higher

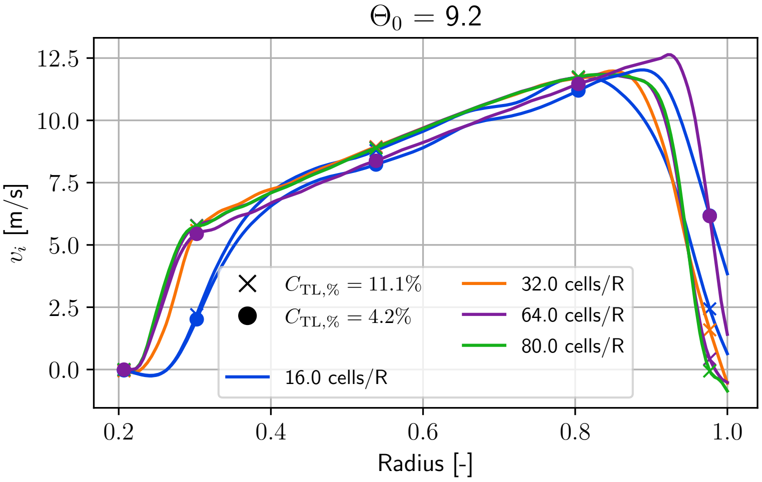

**Figure 22** Radial inflow distribution computed by the Bessel-Fourier inflow model, with variations in $C_{\mathrm{tl},\%}$ and flow field resolution at $\Theta = 9.2$. Only results for the highest and lowest $C_{\mathrm{tl},\%}$ are shown. Cases not shown for these parameters did not converge.

and later peak and a sharper drop. The influence of the resolution is also visible where a higher resolution pushes the drop further outboard. Considering the dependence of the AD boundary vortex size on the resolution this is a reasonable behavior. Furthermore, grid convergence is reached at around 64 cells per radius. As expected the general shape is the same for all trim conditions, except at the root where the low resolution pushes the initial rise outboard. This is due to the approximated blockage of the hub with few cells that partially blocks the lift-producing part of the blade because of the coarse resolution.

The radial lift distribution for the 3.0° trim condition is not plausible with the numerical stability issues starting with the first grid refinement stage (see Figure 23). The results for $\Theta_0 = 4.5°$ show the beginning of the instabilities inboard of the blade. For the midsection between $r = 0.5..0.85$, the results match the experimental values very well, independent of grid resolution and the tip loss factor. These two parameters have a visible impact on the blade tip region. The tip loss has a strong influence on the peak position. Both the tip loss and the fluid grid resolution have a significant impact on the peak magnitude. The slope in the midsection is not exactly represented by the approach with an overshoot of the predicted lift at the measurement point at 0.75R. A lower $C_{\mathrm{tl},\%}$ matches the inner slope better but overshoots the measured lift at the blade tip significantly. The results for $\Theta_0 = 9.2°$ show the same trends excluding instabilities. The results for that trim case also show that the influence of an increased flow resolution from 64 to 80 cells per radius is negligible. The lift results show that an overall match of the lift trend is possible but not completely. Results show that a compromise between matching the midsection of the blade and the tip values is necessary. Higher $C_{\mathrm{tl},\%}$ improves the stability of the simulations and leads to grid convergence with respect to the flow resolution at 64 cells per radius.

Comparing the blade pitch angle with measurements (see Figure 26) the results show the

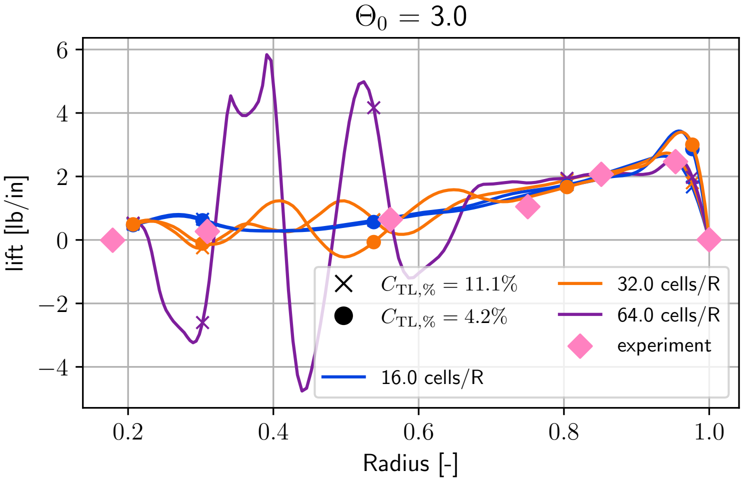

**Figure 23** Radial lift distribution computed by the Bessel-Fourier inflow model, with variations in $C_{\mathrm{tl},\%}$ and flow field resolution at $\Theta = 3.0$. Only results for the highest and lowest $C_{\mathrm{tl},\%}$ are shown. Cases not shown for these parameters did not converge. Experimental reference data is taken from [84].

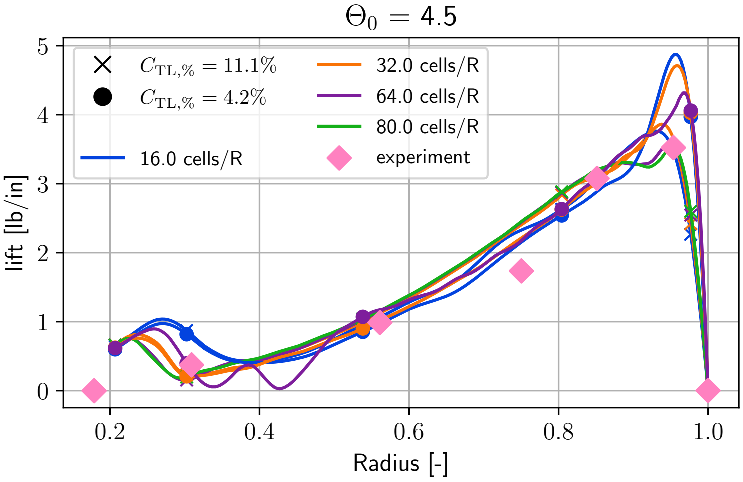

**Figure 24** Radial lift distribution computed by the Bessel-Fourier inflow model, with variations in $C_{\mathrm{tl},\%}$ and flow field resolution at $\Theta = 4.5$. Only results for the highest and lowest $C_{\mathrm{tl},\%}$ are shown. Cases not shown for these parameters did not converge. Experimental reference data is taken from [84].

same trend as the power predictions. The input overshoots experimental measurements for the low pitch experiments with the lowest resolution. The results of the other resolutions seem plausible, but considering the instabilities they cannot be used. For all other trim states the influence of fluid grid resolution and tip loss is visible with lower resolution and higher tip loss leading to higher predicted blade pitch, which is in accordance with the power predictions. The results are in accordance with expectations from physical reasoning. All results are within an error margin of maximum 1 ° with the margin increasing with increasing $C_T$.

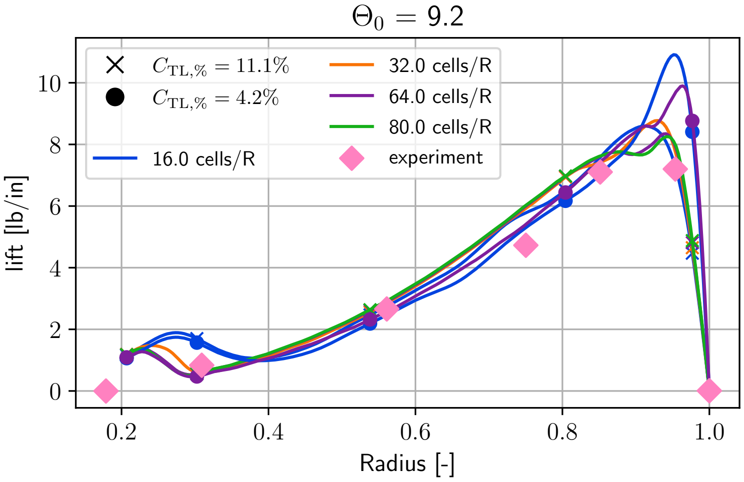

**Figure 25** Radial lift distribution computed by the Bessel-Fourier inflow model, with variations in $C_{\mathrm{t1},\%}$ and flow field resolution at $\Theta = 9.2$. Only results for the highest and lowest $C_{\mathrm{t1},\%}$ are shown. Cases not shown for these parameters did not converge. Experimental reference data is taken from [84].

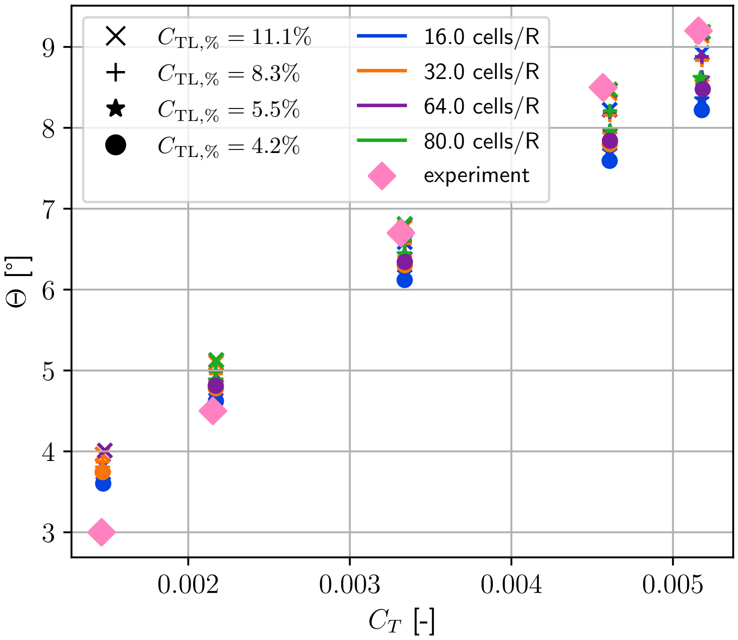

**Figure 26** Predicted pitch input $\Theta$ required for $C_T$ trim compared to measured pitch input $\Theta_0$ for different $C_{\mathrm{t1},\%}$ and flow field resolution. Computed with the Bessel-Fourier inflow model in hover condition. Experimental reference data is taken from [84].

### Actuator line with spherical force kernel

The ACL coupling using a spherical force kernel shows a downward trend for the error in the power prediction (see Figure 27). The model predicts an up to ~25% higher power consumption in comparison to the measurements for the lowest $C_T$. The predicted power decreases with increasing $C_T$ until the last measured $C_T$ where a slight upward trend is visible, similar to the previously discussed AD models. The variation due to $C_{\mathrm{t1},\%}$ increases with increasing $C_T$

with a higher tip loss leading to a higher power consumption. The influence of the resolution is visible for all trim states but the variation increases with increasing $C_T$. There is a distinctive gap between 32 and 64 cells per radius. Lower resolutions were not considered as they defeat the purpose of a concentration of the blade force around the current blade position. An increase in $C_T$ leads to an increasing underestimation in the power consumption. Overall the power is within an error bandwidth of +/-15% except for the lowest $C_T$. As described in [70] and subsection 3.3.4 the correct kernel size is way below a reasonable grid resolution. Using $\epsilon = 5\Delta x$ leads to a dependence of the kernel size on the resolution and true grid convergence is not achieved. However, changes in power are small between the higher resolutions considered and deemed sufficient to speak of grid convergence.

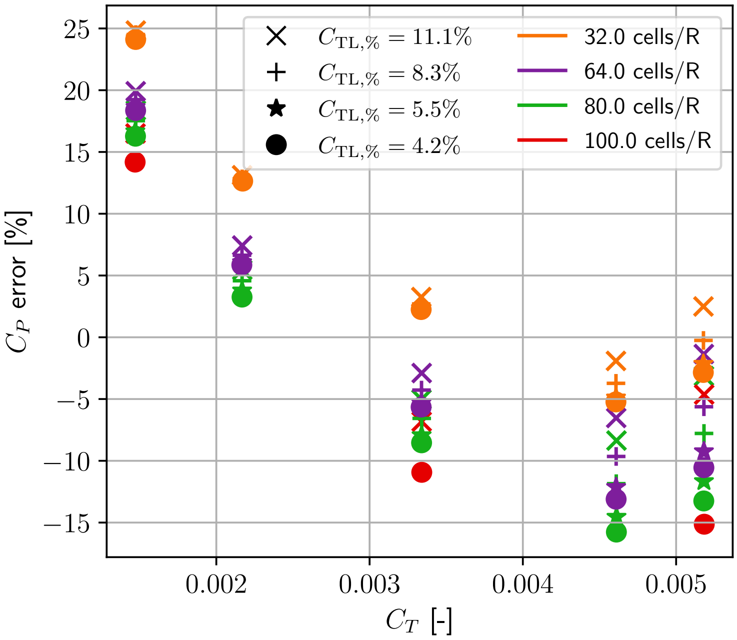

**Figure 27** Power error of the ACL coupling mode with a spherical force kernel for the experimental rotor compared to measurements. The results show the variation of the flow field resolution in combination with a variation of the effective tip loss factor $C_{\mathrm{tl},\%}$. Experimental reference data is taken from [84].

The inflow distribution of the actuator line with the spherical force distribution kernel shows stable results for all trim conditions independent of the flow grid resolution. Figure 28 depicts the inflow for the $\Theta_0 = 3.0°$ case. It shows the linear rise in the inflow velocity for all tip loss values and flow resolutions. The highest resolution of 100 cells per radius deviates slightly at the blade root from the other simulations but this is negligible considering the impact of the root forces on the overall trim. The results show that with increasing resolution the inflow peak moves towards the blade tip with a clear distinction of the lowest considered resolution of 32 cells per radius. A coarser resolution was omitted as the minimum kernel width of the force distribution depends on the resolution and the forcing would be smeared in such a way that the ACL approach would tend towards an AD approach. For resolutions finer than 32 cells per radius, there is a distinct inflow peak at around 0.85R, depending on the parameter set.

Before the rise to the inflow peak, there is a flattening of the inflow gradient, leading even to a small decline for $C_{\mathrm{TL},\%} = 4.2\%$ and 100 cells per radius resolution. This phenomenon comes from a secondary vorticity structure inboard of the blade tip vortex that increases in strength with finer resolutions and reduced tip loss factor (see Figure 29, Figure 30 and Figure 31). The results for the trim conditions with a higher $C_T$ do not show the deviation of the highest resolution of 100 cells per radius at the blade root. The overall shape of the inflow is the same as is to be expected for hover with only a change in inflow magnitude. The findings for the effect of the tip loss and the resolution towards the blade tip stay the same, except that the effect of the secondary vorticity structures is diminishing with increasing $C_T$.

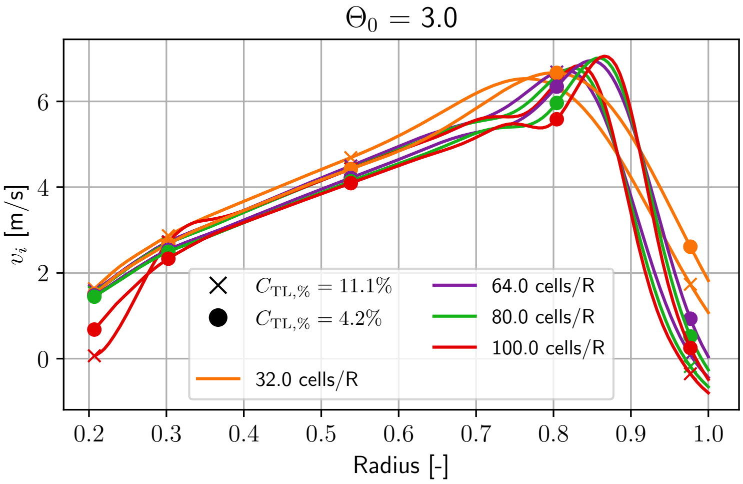

**Figure 28** Radial inflow distribution computed by the ACL inflow model with spherical force kernel, with variations in $C_{\mathrm{tl},\%}$ and flow field resolution at $\Theta = 3.0$. Only results for the highest and lowest $C_{\mathrm{tl},\%}$ are shown.

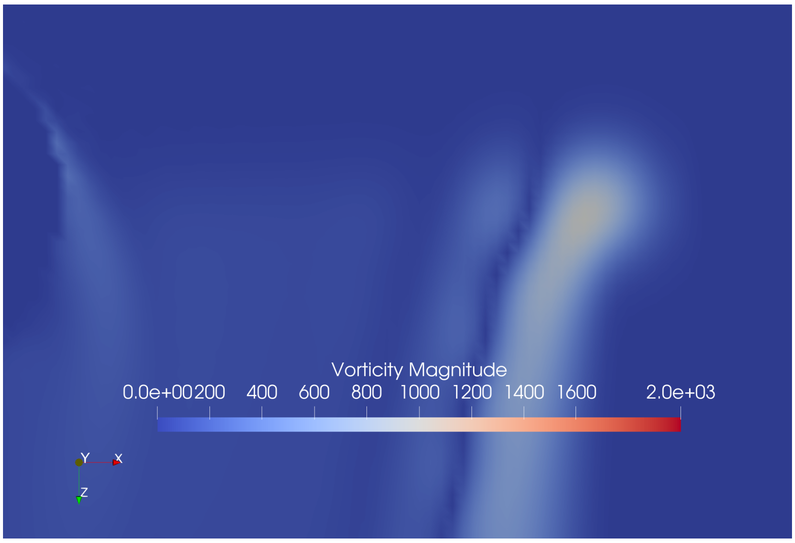

**Figure 29** Vorticity contour for the ACL with spherical force kernel in hover and $\Theta_0 = 3.0°$, $C_{\mathrm{TL},\%} = 4.2\%$ and 64 cells per radius. The plane is perpendicular to the rotor plane at $\Psi = 0°$. Blade direction is along positive x-direction. The left side shows part of the spherical hub approximation.

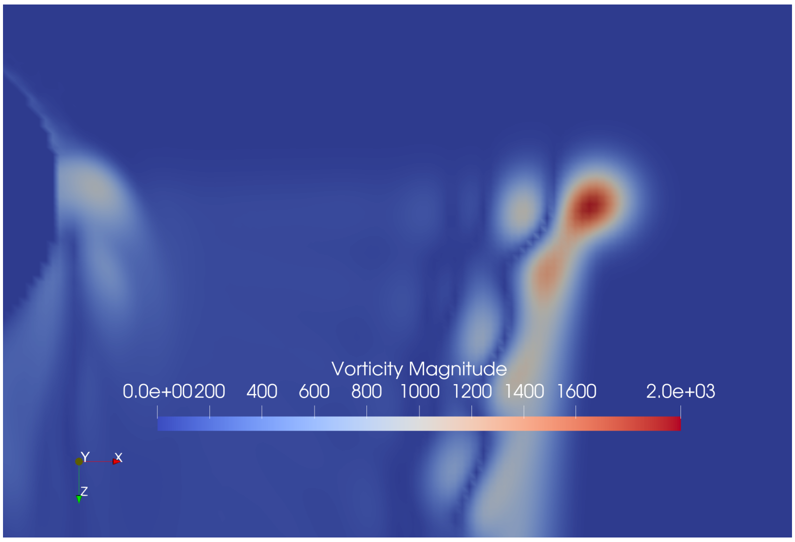

**Figure 30** Vorticity contour for the ACL with spherical force kernel in hover and $\Theta_0 = 3.0°$, $C_{\mathrm{TL},\%} = 4.2\%$ and 100 cells per radius. The plane is perpendicular to the rotor plane at $\Psi = 0°$. Blade direction is along positive x-direction. The left side shows part of the spherical hub approximation.

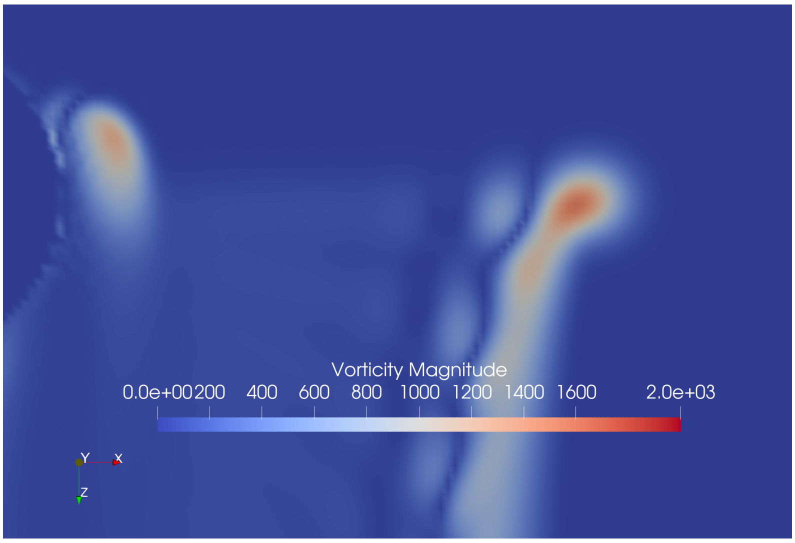

**Figure 31** Vorticity contour for the ACL with spherical force kernel in hover and $\Theta_0 = 3.0°$, $C_{\mathrm{TL},\%} = 11.1\%$ and 100 cells per radius. The plane is perpendicular to the rotor plane at $\Psi = 0°$. Blade direction is along positive x-direction. The left side shows part of the spherical hub approximation.

The lift distribution for the $\Theta_0 = 3.0$ case is depicted in Figure 33. The trend and magnitude are reasonable for all parameter configurations. At the blade root, the highest resolution of 100 cells per radius shows a slight deviation from the other simulations, which is in accordance with the inflow drop visible in Figure 28. The midsection of the blade from 0.30R to 0.75R is well-met for all configurations. In the outer section, the influence of the resolution and the tip loss factor becomes visible. A lower tip loss leads to a more outboard and higher peak. A higher resolution results in an increasing dent between 0.80R and 0.90R. The dent is due to the aforementioned secondary vorticity structure and its influence on the local inflow velocity. Considering the shape of the lift distribution, the strong gradient inboard of the lift peak leads to a strong trailing vorticity that gives a physical explanation of the formation of the

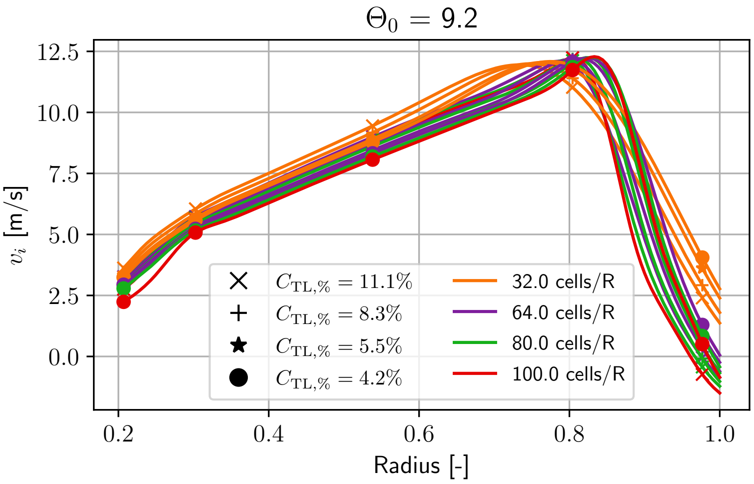

**Figure 32** Radial inflow distribution computed by the ACL inflow model with spherical force kernel, with variations in $C_{\mathrm{t1},\%}$ and flow field resolution at $\Theta = 9.2$. Only results for the highest and lowest $C_{\mathrm{t1},\%}$ are shown.

secondary vorticity structure seen in the flow field. As for the inflow, its effect diminishes with an increasing $C_T$ for the lift distribution. Nevertheless, the coupling approach is able to capture the lift slope between the measurements at 0.75R and 0.85R (see Figure 34) showing that the flow phenomena are reasonable.

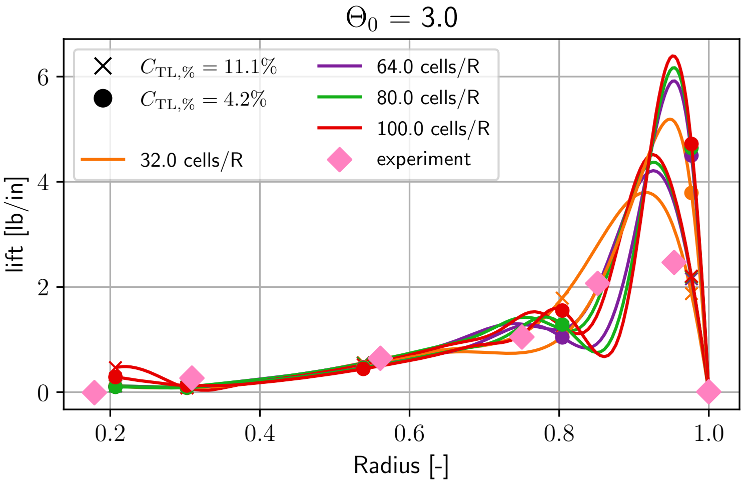

**Figure 33** Radial lift distribution computed by the ACL inflow model with spherical force kernel, with variations in $C_{\mathrm{t1},\%}$ and flow field resolution at $\Theta = 3.0$. Only results for the highest and lowest $C_{\mathrm{t1},\%}$ are shown. Experimental reference data is taken from [84].

Comparing the blade pitch angle with measurements (see Figure 35) the results show the same trend as the power predictions. The input overshoots experimental measurements for the low pitch experiments with the lowest resolution. For all trim states the influence of fluid grid resolution and tip loss is visible with lower resolution and higher tip loss leading to higher predicted blade pitch, which is in accordance with the power predictions. The results are in

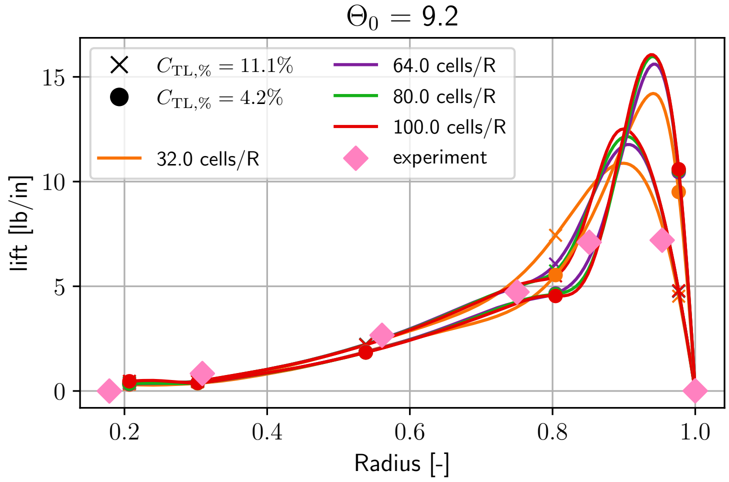

**Figure 34** Radial lift distribution computed by the ACL inflow model with spherical force kernel, with variations in $C_{\mathrm{tl},\%}$ and flow field resolution at $\Theta = 9.2$. Only results for the highest and lowest $C_{\mathrm{tl},\%}$ are shown. Experimental reference data is taken from [84].

accordance with expectations from physical reasoning. All results are within an error margin of a maximum of 1.2° with the margin increasing with increasing $C_T$. The spread between different parameter sets for the same $C_T$ increases, showing the strong effect of $C_{\mathrm{tl},\%}$ and the significance of the lift distribution outboard on the blade.

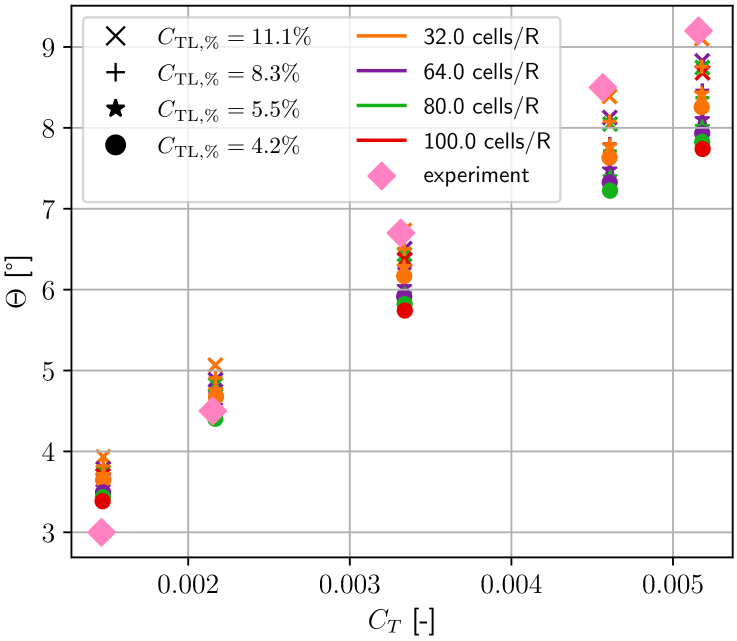

**Figure 35** Predicted pitch input $\Theta$ required for $C_T$ trim compared to measured pitch input $\Theta_0$ for different $C_{\mathrm{tl},\%}$ and flow field resolution. Computed with the ACL inflow model with spherical force kernel in hover condition. Experimental reference data is taken from [84].

### Actuator line with restricted force kernel

The ACL coupling using a restricted force kernel shows a downward trend for the error in the power prediction (see Figure 36). The model predicts an up to ~18% higher power consumption in comparison to the measurements for the lowest $C_T$. The predicted power decreases with increasing $C_T$ until the last measured $C_T$ where a slight upward trend is visible, similar to the previously discussed AD and ACL models. The variation due to $C_{\mathrm{tl},\%}$ increases with increasing $C_T$ with a higher tip loss leading to a higher power consumption. The influence of the resolution is visible for all trim states but the variation increases with increasing $C_T$. There is a distinctive gap between 32 and 64 cells per radius. An increase in $C_T$ leads to an increasing underestimation in the power consumption up to -22%.

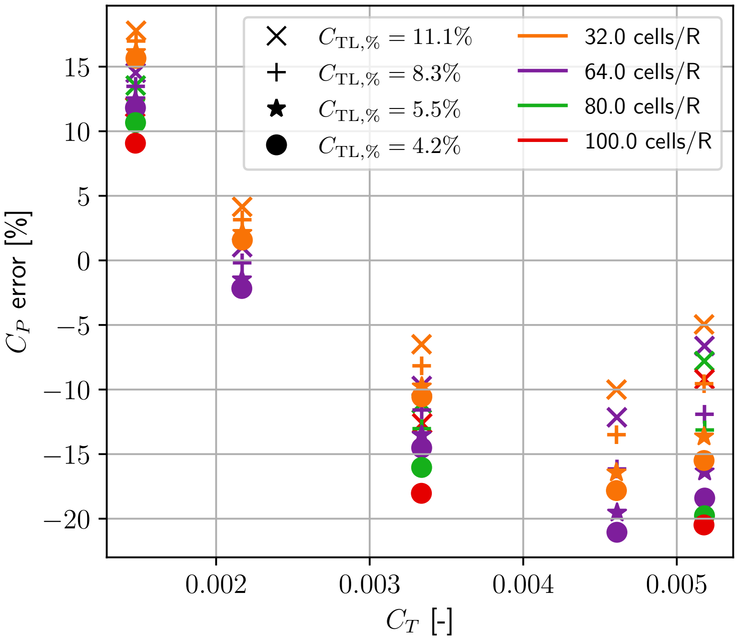

**Figure 36** Power error of the ACL coupling mode with a restricted force kernel for the experimental rotor compared to measurements. The results show the variation of the flow field resolution in combination with a variation of the effective tip loss factor $C_{\mathrm{tl},\%}$. Experimental reference data is taken from [84].

The inflow distributions of the actuator line coupling with the restricted force distribution kernel for the lowest and highest $C_T$ trim conditions are used exemplary (see Figure 37) as higher $C_T$ cases show the same properties. In general the inflow shows a linear increase with a peak inflow at around 0.85R where the exact peak location is influenced by the tip loss and the resolution of the flow simulation, whereas the effect of the tip loss is stronger. A higher tip loss and lower resolution lead both to a more inboard peak. Nevertheless, the effect on the position is within 0.05R and the influence on the peak magnitude is negligible. This coupling approach shows instabilities for the highest considered resolution of 100 cells per radius independently of the trim condition. The cause for this instability could not be determined neither from the flow data nor the results for rotor loads and inflow data.

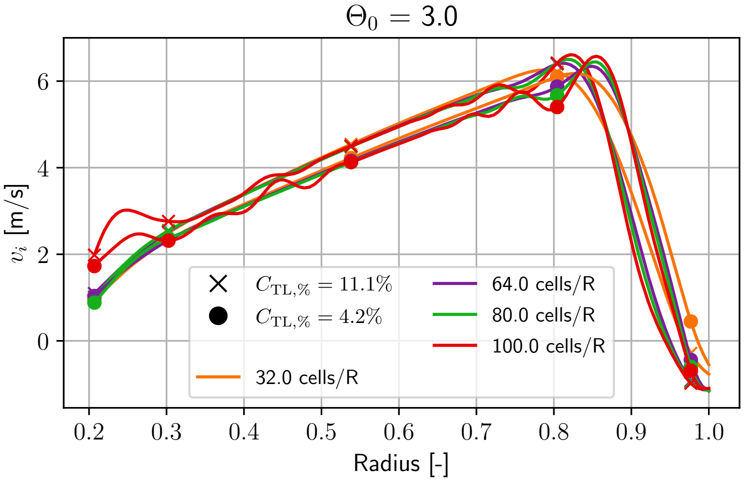

**Figure 37** Radial inflow distribution computed by the ACL inflow model with restricted force kernel, with variations in $C_{\mathrm{t1},\%}$ and flow field resolution at $\Theta = 3.0$. Only results for the highest and lowest $C_{\mathrm{t1},\%}$ are shown.

The lift distribution is depicted in Figure 38 and Figure 39. Besides the occurring numerical instabilities for 100 cells per radius resolution the slope and trend of the experimental measurements are well met. With a lower tip loss factor the measurements are underpredicted in the blade mid section and the measurement at the 0.95R station is overshot as the decrease of the lift curve sets on too late. This is greatly improved with an increased tip loss factor where the match is better for the blade mid section and the most outboard measurement. Furthermore, the results do not change significantly between 64 and 80 cells per radius flow grid resolution. As mentioned before the cause of the instabilities could not be determined, but did not arise from flow instabilities due to high resolutions.

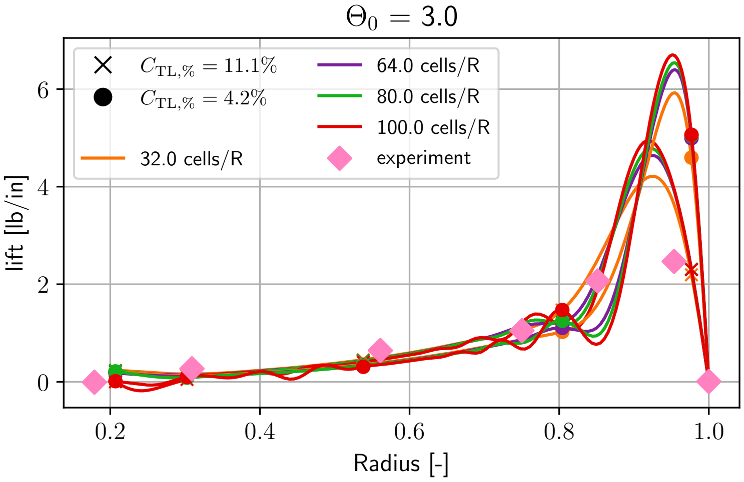

**Figure 38** Radial lift distribution computed by the ACL inflow model with restricted force kernel, with variations in $C_{\mathrm{t1},\%}$ and flow field resolution at $\Theta = 3.0$. Only results for the highest and lowest $C_{\mathrm{t1},\%}$ are shown. Experimental reference data is taken from [84].

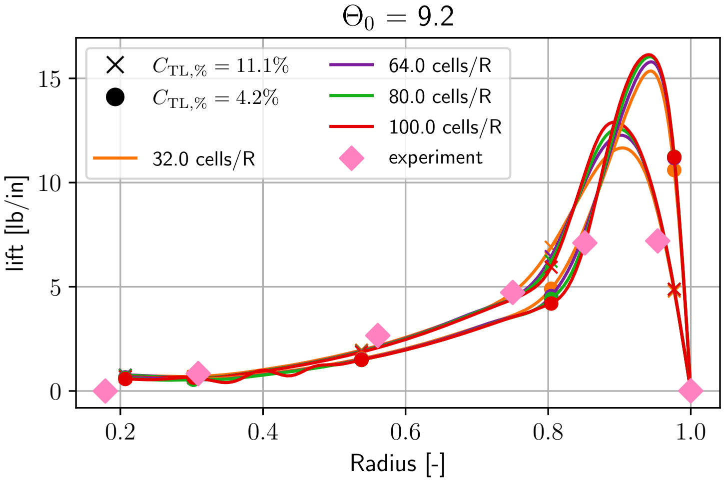

**Figure 39** Radial lift distribution computed by the ACL inflow model with restricted force kernel, with variations in $C_{\mathrm{tl},\%}$ and flow field resolution at $\Theta = 9.2$. Only results for the highest and lowest $C_{\mathrm{tl},\%}$ are shown. Experimental reference data is taken from [84].

The trimmed pitch input values compared to the experimental measurements are shown in Figure 40. The influence of the tip loss is visible, with a higher tip loss requiring a higher pitch input, as is to be expected. While the pitch input is overpredicted for $\Theta_0 = 3.0°$ it is underpredicted for $\Theta_0 > 4.5°$. For the later cases, a higher tip loss is beneficial to reduce the error compared to measurements. The results for the pitch predictions are consistent with the power predictions, where a higher predicted pitch corresponds to higher power consumption.

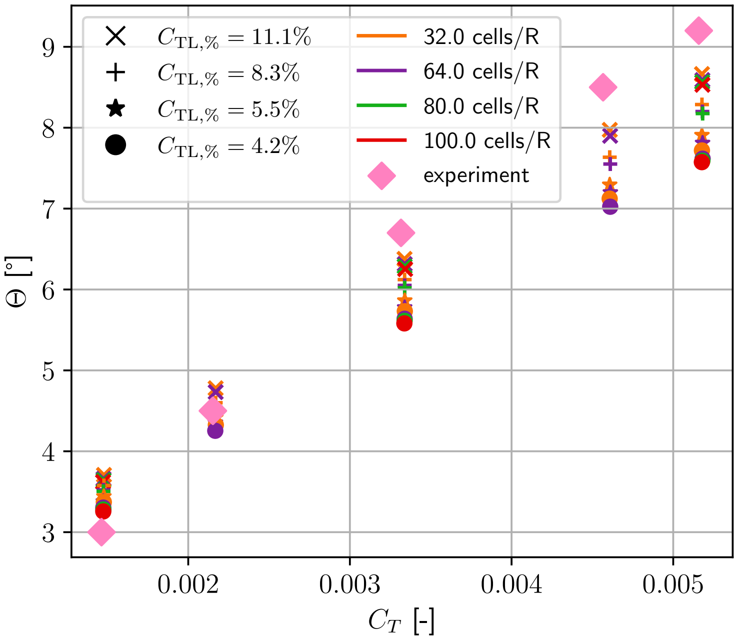

**Figure 40** Predicted pitch input $\Theta$ required for $C_T$ trim compared to measured pitch input $\Theta_0$ for different $C_{\mathrm{tl},\%}$ and flow field resolution. Computed with the ACL inflow model with restricted force kernel in hover condition. Experimental reference data is taken from [84].

### Actuator line with inflow correction

The last actuator line coupling model is a spherical kernel function where the sampled inflow is corrected by adjusting the inflow incrementally towards the expected value when the resolution would permit an optimal kernel size (see subsection 3.3.4). The results show a downward trend for the error in the power prediction (see Figure 41). The model predicts an up to ~28% higher power consumption in comparison to the measurements for the lowest $C_T$. The predicted power decreases with increasing $C_T$ until the last measured $C_T$ where a slight upward trend is visible, similar to the previously discussed AD and ACL models. The variation due to $C_{\mathrm{tl},\%}$ is negligible and independent of $C_T$. The influence of the resolution is visible for all trim states but the variation increases with increasing $C_T$. There is a distinctive gap between 32 and 64 cells per radius. An increase in $C_T$ leads to an increasing underestimation in the power consumption up to -5%.

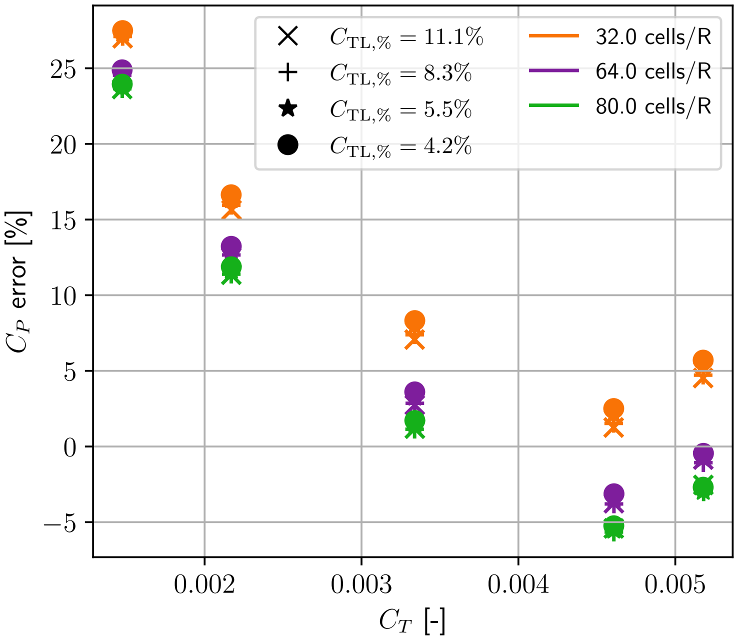

**Figure 41** Power error of the ACL coupling mode with inflow correction for the experimental rotor compared to measurements. The results show the variation of the flow field resolution in combination with a variation of the effective tip loss factor $C_{\mathrm{tl},\%}$. Experimental reference data is taken from [84].

The influence of this correction can be seen in Figure 42. The inflow at the blade root is adjusted so that it tends toward zero. In the blade mid-section, there is a linear increase of the inflow, as is to be expected and flattens out at around 0.8R. The effect of the inflow correction is visible after this first peak where the inflow does not continuously tend towards zero but increases again at around 0.9R until 0.95R and then drops towards zero. The position of this second peak is the same for all resolutions and tip loss factors. The flow grid resolution influences the second peak's amplitude but not its location. The tip loss has a strong effect on the dip between the first and the second peak. The inflow trend due to the correction does not seem plausible. A possible explanation is that this approach was derived from the lifting line solution of a wing and not from a rotating blade. Grid convergence could not be achieved within the considered resolutions. While grid convergence could occur at higher resolutions it would defeat the purpose of a fast mid-fidelity approach and were therefore not further investigated. The results for higher $C_T$ show the same trends.

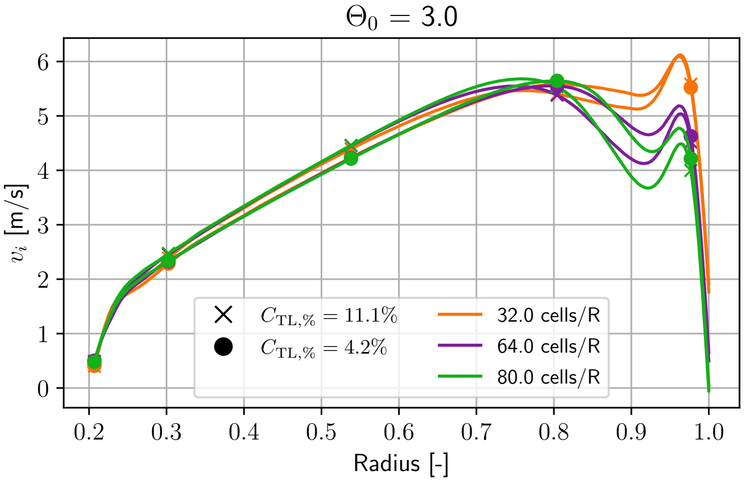

**Figure 42** Radial inflow distribution computed by the ACL inflow model with inflow correction, with variations in $C_{\mathrm{tl},\%}$ and flow field resolution at $\Theta = 3.0$. Only results for the highest and lowest $C_{\mathrm{tl},\%}$ are shown.

The lift distribution for $\Theta_0 = 3.0$° is depicted in Figure 43. The influence of tip loss and resolution is visible. The reduced tip loss leads to higher lift peaks and a stronger curvature in the blade mid-section. The same behavior is visible with respect to the resolution. Considering that the tip loss influenced the dip between the two peaks of the inflow distribution this is only plausible. Overall, the lift measurements are well met, especially in the blade midsection. The measurement at 0.85R could be better matched with a higher resolution and lower tip loss, but this leads to worse results at the measurement at 0.95R and vice versa. However, the measured trend is visible, and the results are within a reasonable error bandwidth. The lift results show little differences between 64 and 80 cells per radius, whereas 32 cells per radius differs from the other results. These findings hold true for the other $C_T$ trim conditions as well.

The trimmed pitch input values compared to the experimental measurements are shown in Figure 44. The influence of the tip loss is visible, with a higher tip loss requiring a higher pitch input, as is to be expected. While the pitch input is overpredicted for $\Theta_0 = 3.0$° it is underpredicted for $\Theta_0 > 4.5$°. For the later cases, a higher tip loss is beneficial to reduce the error compared to measurements. However, the results do not resemble the expectations from the power predictions, where the tip loss has minimal influence and only the flow resolution shows a significant impact.

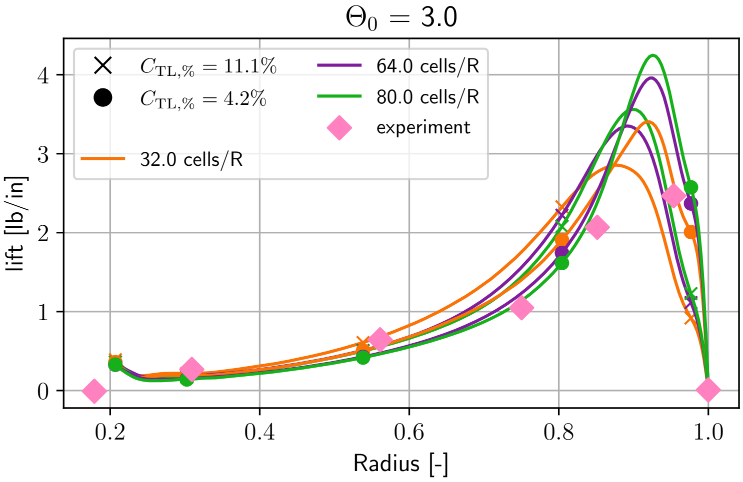

**Figure 43** Radial lift distribution computed by the ACL inflow model with restricted force kernel, with variations in $C_{\mathrm{tl},\%}$ and flow field resolution at $\Theta = 3.0$. Only results for the highest and lowest $C_{\mathrm{tl},\%}$ are shown. Experimental reference data is taken from [84].

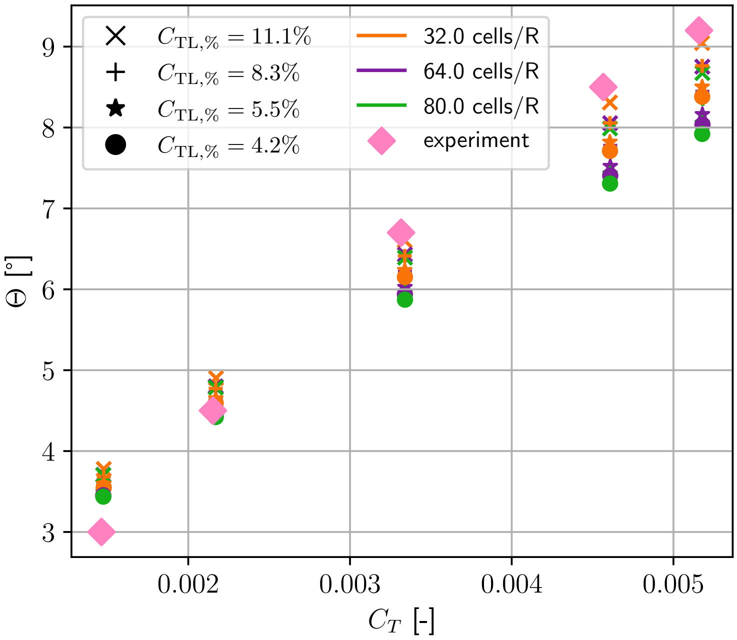

**Figure 44** Predicted pitch input $\Theta$ required for $C_T$ trim compared to measured pitch input $\Theta_0$ for different $C_{\mathrm{tl},\%}$ and flow field resolution. Computed with the ACL inflow model with inflow correction in hover condition. Experimental reference data is taken from [84].

### Peters-He

In the following the dynamic finite-state Peters-He inflow model results are presented. The power predictions for the Peters-He inflow model in Figure 45 show a constant overprediction of the power varying between 10% to 40% with the highest deviation for the low $C_T$ case. For higher $C_T$, the error reduces and only increases for the measurement with the highest $C_T$. The influence of the tip loss factor is negligible with a maximum of a 3% deviation for the highest $C_T$ between the 11% and 4% tip loss.

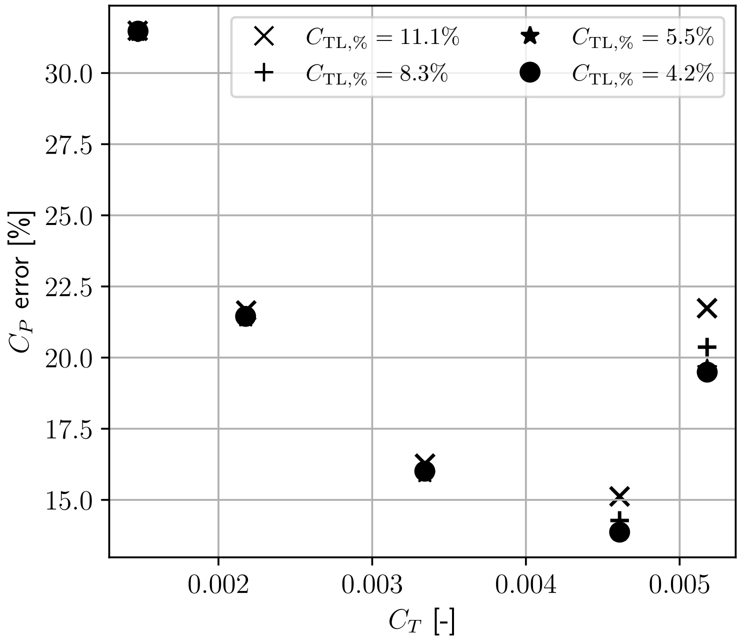

**Figure 45** Power error of the Peters–He for the experimental rotor compared to measurements. The results show the variation of the flow field resolution in combination with a variation of the effective tip loss factor $C_{\mathrm{tl},\%}$. Experimental reference data is taken from [84].

The results for the computed inflow are shown in Figure 46 and Figure 47. For the depicted trim conditions the inflow increases linearly with a peak at 0.85R to 0.95R depending on the tip loss factor, with a low tip loss leading to a higher peak that is further outboard. At the tip the induced velocity tends to zero. The corresponding lift distributions are shown in Figure 48 and Figure 49. The results show a similar trend to the experimental measurements but are not able to match the slope in the mid-blade section, especially for the low $C_T$ value. The magnitude for the outmost measurements station at 0.95R is only met for the lowest tip loss of 4.2%. A further reduction of the tip loss was not possible as this led to instabilities because the sharp drop of lift and inflow could not be approximated by the base functions of the Peters-He model.

The trimmed input values compared to the experimental measurements are shown in Figure 50. The influence of the tip loss is visible, with a higher tip loss requiring a higher pitch input, as is to be expected. While the pitch input is overpredicted for $\Theta_0 = [3.0°, 4.5°]$ it is

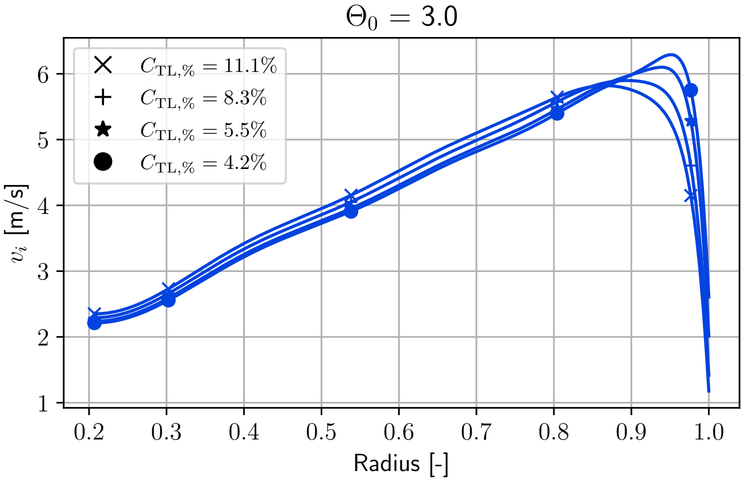

**Figure 46** Radial inflow distribution in hover computed by the Peters-He inflow model, with variations in $C_{\mathrm{tl},\%}$ at $\Theta = 3.0$.

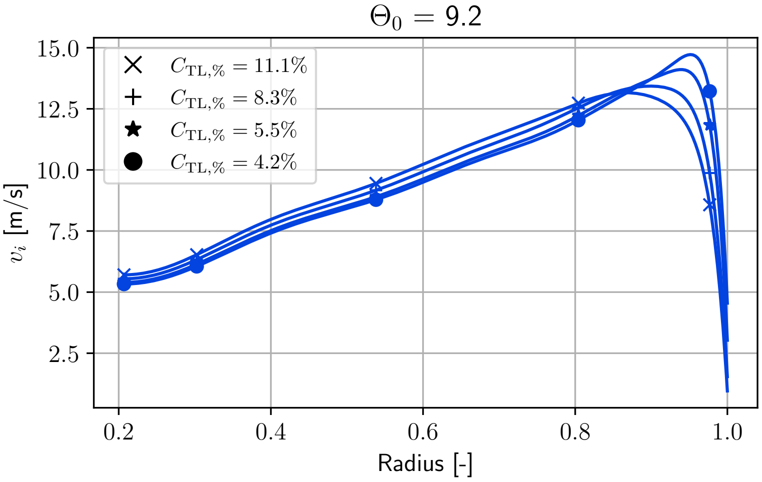

**Figure 47** Radial inflow distribution in hover computed by the Peters-He inflow model, with variations in $C_{\mathrm{tl},\%}$ at $\Theta = 9.2$.

well matched for the other trim conditions depending on the tip loss. Overall the deviation of the Peters-He model from measurements is lower when the tip loss is reduced.

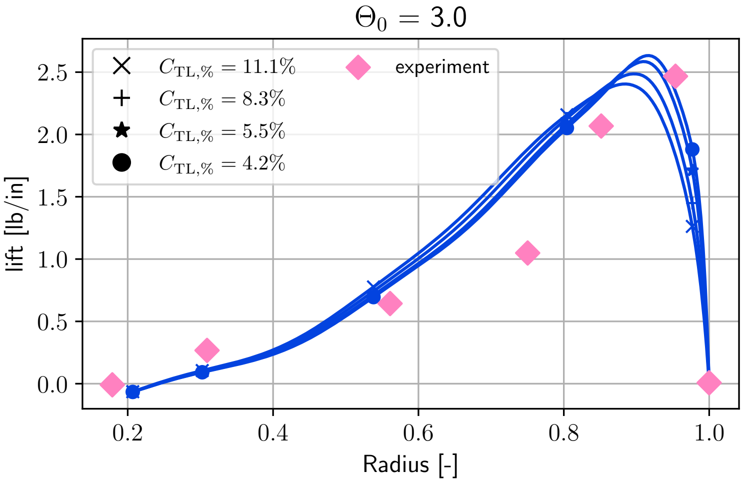

**Figure 48** Radial lift distribution computed by the Peters-He inflow model, with variations in $C_{\mathrm{t1},\%}$ in hover condition at $\Theta = 3.0$. Experimental reference data is taken from [84].

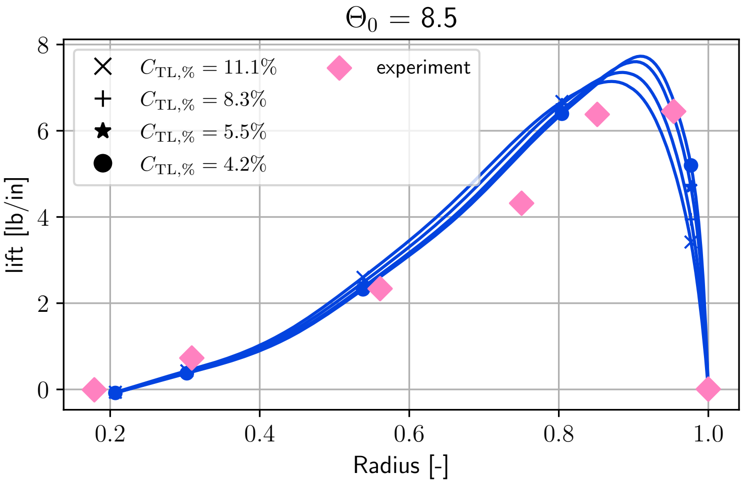

**Figure 49** Radial lift distribution computed by the Peters-He inflow model, with variations in $C_{\mathrm{t1},\%}$ in hover condition at $\Theta = 8.5$. Experimental reference data is taken from [84].

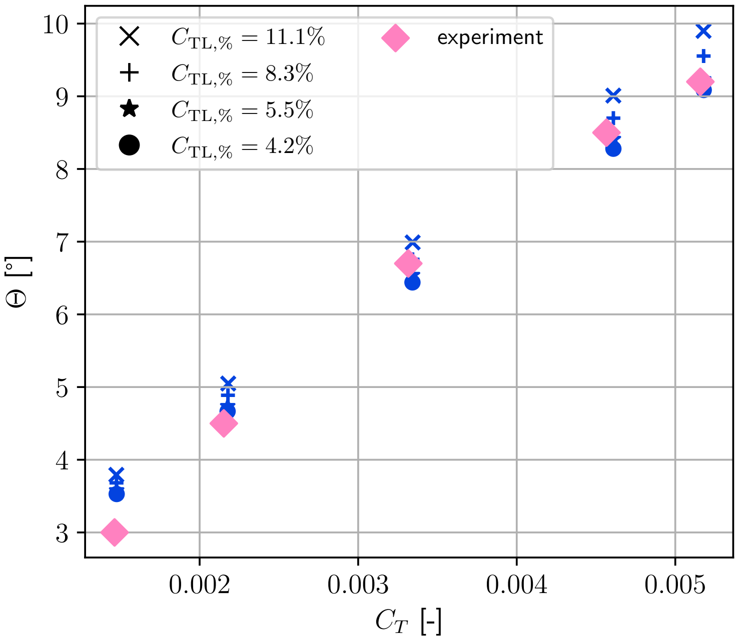

**Figure 50** Predicted pitch input $\Theta$ required for $C_T$ trim compared to measured pitch input $\Theta_0$ for different $C_{\mathrm{tl},\%}$. Computed with the Peters-He inflow model in hover condition. Experimental reference data is taken from [84].

### Inflow Model Comparison in Hover Condition

The performance of a specific coupling is not only determined by its ability to capture the experimental measurements, but in the case of deviations, it is important to evaluate its defectiveness compared to the other modeling approaches. By this an informed decision about the most appropriate model for a given flight condition can be made.

### Required Power

The power estimates for all LBM inflow models and the Peters-He model with the respective parameter variations are shown in Figure 51. For the low $C_T$ or $\Theta_0 = 3.0°$ case, all models overpredict the power. With increasing $C_T$, the models are split into three groups. The Peters-He and the Bessel-Fourier models overpredict the power for all conditions, although the relative error of the models decreases. The actuator line models without inflow correction and the linear harmonic model switch from a power overprediction to an underprediction and the spread for the tip loss and resolution influence increases for the actuator line coupling. The actuator line model with inflow correction, on the other hand, does not show an increased spread with respect to the relative error and stays for the higher $C_T$ cases within the same error bandwidth. From a perspective focusing solely on the power prediction, a higher tip loss is required for the actuator line and the linear harmonic modeling approach, while the Bessel-Fourier and the Peters-He inflow models give better results for a lower tip loss. For the actuator disk models, a distinct gap for the 16 to 32 cells per radius flow resolution can be seen.

### Inflow and Lift Distribution

The results for the inflow and lift distribution for all LBM at a resolution of 64 cells per radius and the Peters-He model are shown in Figure 53 and Figure 52 for the highest and the lowest considered tip loss. The resolution was chosen based on the results shown above, which showed sufficient grid convergence for the models. It should be noted that grid convergence could not be achieved for all inflow models.

The actuator line models with the restricted and the spherical kernel show a very similar performance. Both inflows have an earlier drop compared to the other models with the same magnitude at their peak. The lift distribution is similar as well, where both models show a distinct peak with a higher magnitude than the other models in the blade tip region. Both models overestimate the measured lift for a low tip loss at the most outboard station but show good agreement for the lowest tip loss of 11%. They are able to capture the curvature of the loads between 0.75R and 0.85R. An estimation of the actual peak position based on a spline fit to match the integrated total lift from measurements shows that the estimated peak magnitude is reasonable but slightly exaggerated. The spherical kernel ACL captures the measurements slightly better and did not experience any issues with stability no matter the

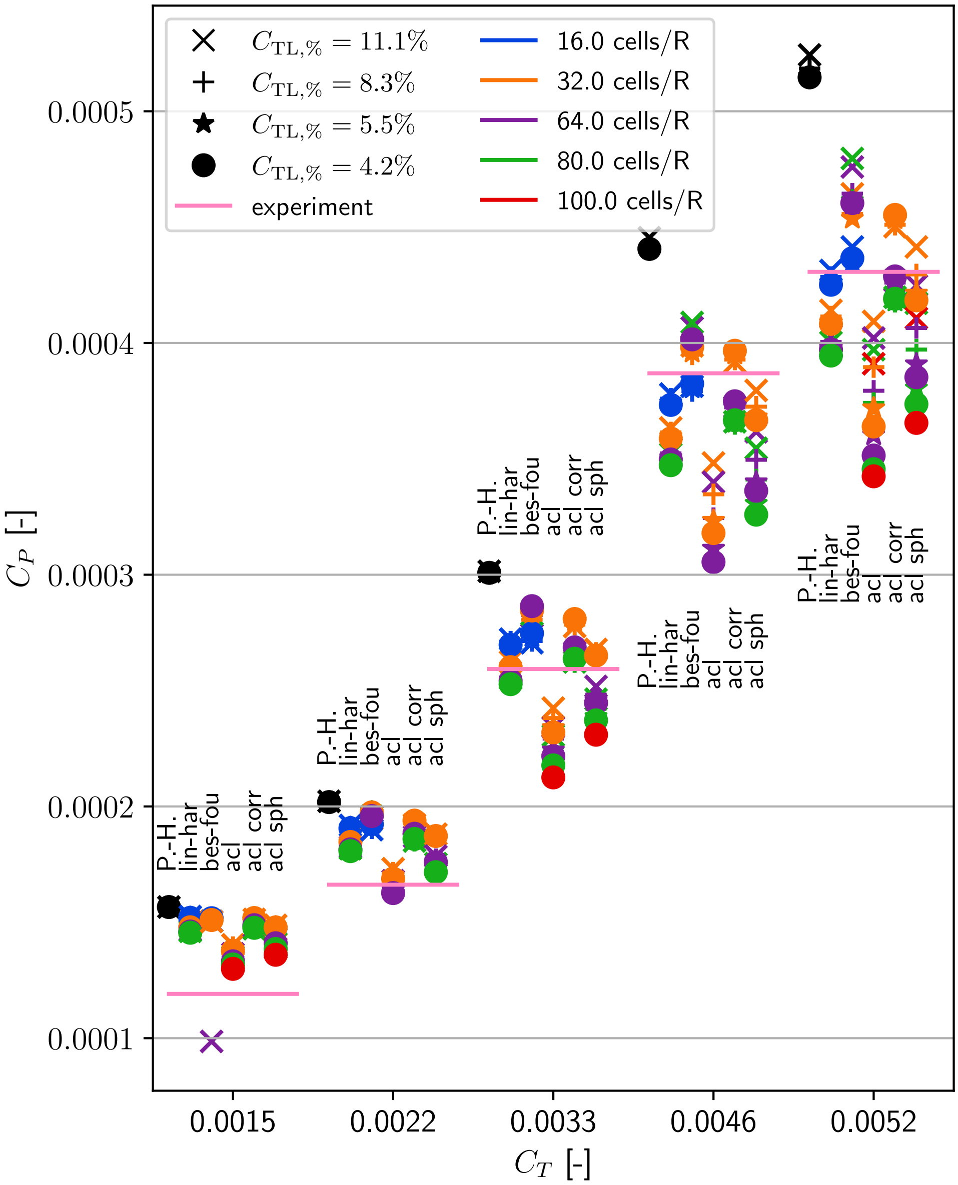

**Figure 51** Comparison of predicted power for all inflow models in hover condition. Experimental reference data is taken from [84].

$C_T$ or resolution. The results for the ACL with the inflow correction show the influence of the correction in the inflow distribution. While all other models, except for the linear-harmonic, show a similar inflow trend with the major difference being the peak location, the corrected model shows two peaks, with the second peak being close to the blade tip and a following sharp drop to zero. The lift distribution compared to the measurements shows that with a lower tip loss, the model is able to capture the trend and measurements very well, including the outmost station at 0.95R. The curvature between 0.75R and 0.85R shows only a slight deviation. The overall lift peak is much lower than for the other ACL models.

The Bessel-Fourier model, in comparison, is closer to the Peters-He model in the inflow and

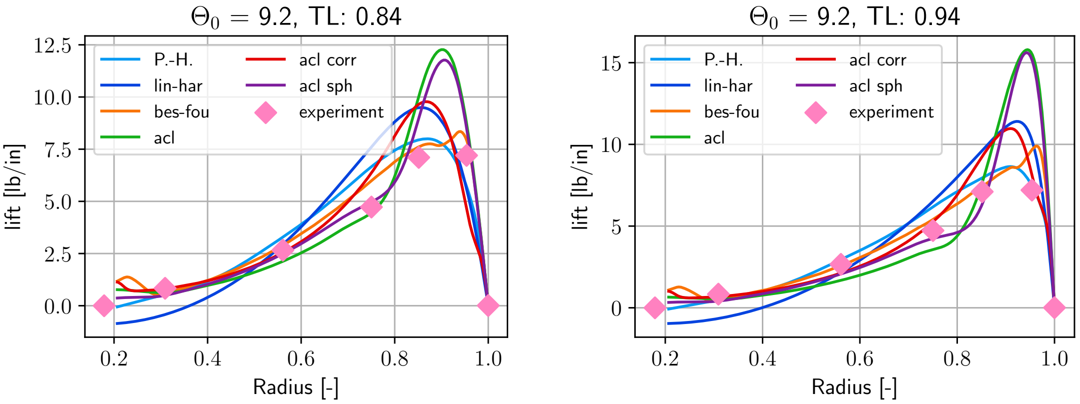

(a) Results for $\Theta = 9.2$ and $C_{\mathrm{TL},\%} = 11.1\%$.

(b) Results for $\Theta = 9.2$ and $C_{\mathrm{TL},\%} = 4.2\%$.

**Figure 52** Comparison of predicted radial lift for all inflow models in hover condition. Experimental reference data is taken from [84].

lift distribution. The inflow peak is further outboard than for the ACL methods but not as far as for the Peters-He model. However, due to that the lift peak is greatly reduced and is able to match the experimental measurements. However, the curvature region of the measurements is not fully met, and thereby, the simulations slightly overshoot the measurement at 0.75R. The position of the induced velocity drop being between the ACL and the Peters-He predictions leads to a higher lift peak compared to Peters-He while moving it further outboard than for the ACL modeling. In comparison, the Peters-He modeling approach barely matches the outmost lift peak, even with the lowest tip loss factor. This would suggest less tip loss is necessary, but this resulted in instabilities for the lift as the base functions were not able to capture the resulting steep drop of the lift at the blade tip anymore. The results for the linear-harmonic inflow coupling do not really represent the shape of the lift or the inflow, which is to be expected, as it merely represents averaged trends instead of more local changes in radial direction.

### Blade Pitch Angle

A comparison of the relative error for the predicted blade pitch compared to the experimental measurements shows the same general trend for all models. The pitch is severely overestimated up to +35% for the lowest measured pitch. The relative error reduces with increasing $C_T$. For the trim points of $\Theta_0 \geq 6.7°$ the error bandwidth is stable for each model. In general, the Peters-He shows the lowest error, although depending on the LBM coupling parameters, the coupled results can be closer to the measurement. For a fixed flow resolution, the spread between the lowest and highest tip loss is 10% relative error for the LBM inflow and the Peters-He inflow model. When the previous findings with regard to the required resolution and the best tip loss with regard to power and lift distribution are taken into account, meaning a high tip loss for the LBM models and a low tip loss for Peters-He, all inflow models match

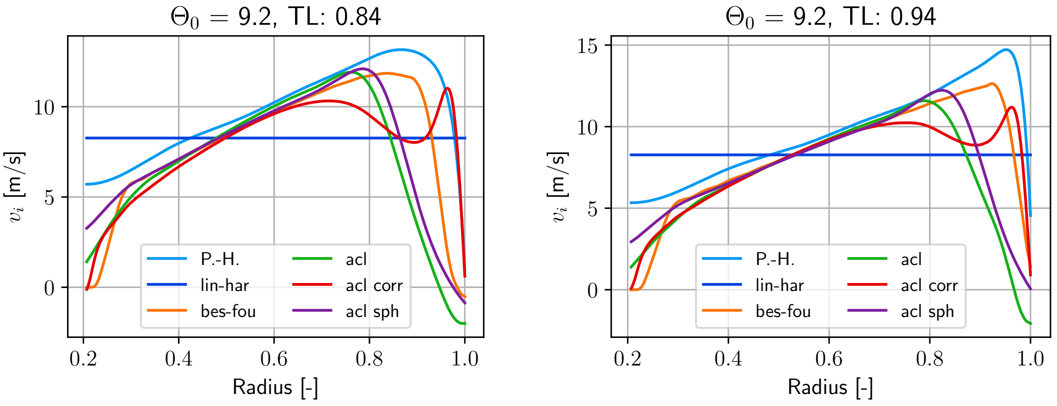

(a) Results for $\Theta = 9.2$ and $C_{\mathrm{TL},\%} = 11.1\%$.

(b) Results for $\Theta = 9.2$ and $C_{\mathrm{TL},\%} = 4.2\%$.

**Figure 53** Comparison of predicted radial inflow distribution for all inflow models in hover condition.

the measurements within a bandwidth of +/-7% for $\Theta_0 \geq 6.7°$.

### 5.1.2 Wind tunnel results

The following section presents the results of the wind tunnel simulations compared to the experimental measurements. The last part will give a comparison of the inflow models against each other. As for the hover cases a special focus will lie on the flow resolution and the influence of the blade tip loss as this proved a strong influence on the overall results. The simulations were run for three different advance ratios $\mu = [0.08, 0.20, 0.29]$. The simulations are trimmed to lift and drag and a zero side force as described in the experimental report [85]. The expected lateral blade flap angle would be zero for this condition but measurements showed a consistent blade flap of around 2°. In the absence of further information, the simulations were trimmed to the stated conditions, and results showed plausible results, so no further action was taken to account for the mismatch of claimed trim conditions and measured results. However, this should be kept in mind as it could be a source of deviation between simulation and experiment.

#### Linear-harmonic coupling

The integrated results for the linear-harmonic inflow model consist of the power predictions and the total blade loading over a full rotation as well as the blade flap angles. The total blade loading (see Figure 54a) shows the limitations of the linear-harmonic coupling in representing the inflow near the hover condition and the resulting radial thrust distribution. As a result, the total blade load for $\mu = 0.08$ does not represent the load variation and is too high in general. The results are greatly improved for higher advance ratios where the results capture the first harmonic well and the magnitudes are close to the measurements. The results are in accordance with the formulation of the model. The linear-harmonic base functions can only capture the mean inflow plus an additional linear part over the whole disk. Thus, for an inflow close to hover condition, only a slight tilt of the inflow distribution is approximated, resulting in only light harmonic variation. With higher advance ratios the overall rotor harmonic is captured better. The influence of $C_{\mathrm{tl},\%}$ is negligible for higher $\mu$. The influence of the flow field resolution is low even for $\mu = 0.08$.

The relative error of the predicted power is depicted in Figure 54b. The results show a clear trend where, with an increasing advance ratio, the error increases linearly. For $\mu = 0.08$ a clear influence of $C_{\mathrm{tl},\%}$ is visible, but the effect of the resolution is low. With increasing $\mu$ the influence of $C_{\mathrm{tl},\%}$ diminishes, whereas the effect of the resolution is more visible but still low. The results for the inplane force distribution, e.g. the force acting against the blade section is shown in Figure 55a. They show an increase in the drag on the retreating blade. This is due to the higher angle of attack necessary to produce enough lift on the retreating side of the rotor. Nevertheless, this does not explain the discrepancies compared to the experimental data for the power. Considering that the longitudinal blade flapping is close to the measurements (see Figure 54c) but the measured lateral flap is not zero (see Figure 86) as should be according to the stated trim conditions this could have an influence on the power results. However, no additional data is available such as measured control input or sectional drag.

The azimuth variation of the lift at the five radial measurement stations is shown in Figure 56a and 56b. Regardless of the advance ratio and the radial measurement station the results for the linear harmonic model do not show a dependency with respect to the resolution. The only influence is the tip loss factor. For the $\mu = 0.08$ case, the overall trend of the results is not met, which is in accordance with the total blade lift results. For the innermost blade sections at $r = [0.31, 0.56]$, the load level is met, and the tip loss has no significant influence. For the sections $r = [0.75, 0.85]$ the loads are higher than the measured peaks and do not match the average level. The outmost station at $r = 0.95$ shows a clear influence of the tip loss and the predicted loads match the averaged loads over one rotation for the highest tip loss. The results for the intermediate advance ratio of $\mu = 0.20$ the trends over one rotation are better met and the load levels for the inner three sections are comparable to measurements. The lift for the two outboard stations is overpredicted but the trends are visible. However, a high tip loss is required for the outmost station. The results for $\mu = 0.29$ are similar to the $\mu = 0.20$ with a better match of the trend as the first harmonic dominates the changes over one rotor/revolution. A comparison of the radial predicted lift against experimental data at the measured azimuth positions is not meaningful for the linear-harmonic model, as the inflow representation in the radial direction is severely limited, and a similar uniformity of the loads can be expected as is the case for the hover condition. For completeness, the results are shown in Appendix A in Figure 96 and Figure 97.

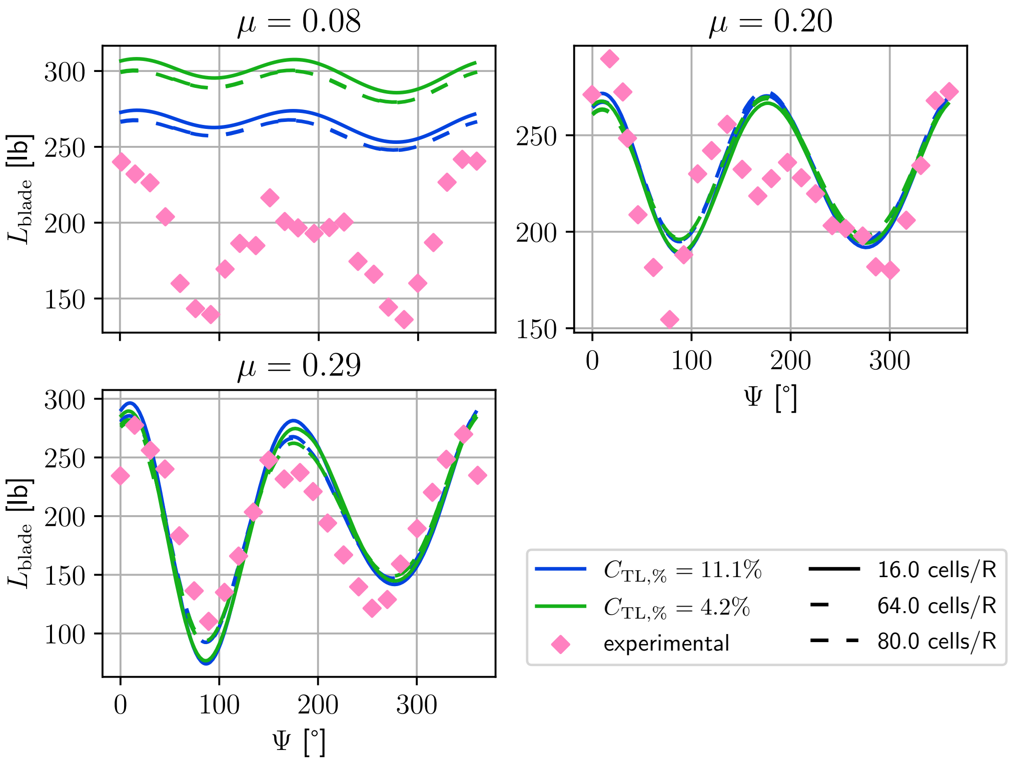

(a) Total blade lift predicted by the linear-harmonic inflow model at different $\mu$ compared to experimental measurements from [85]. Results are shown for a reduced set of considered tip loss and resolutions.

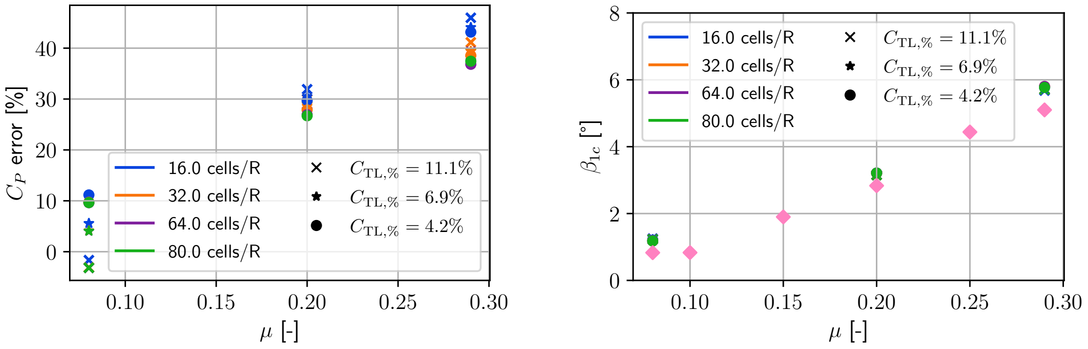

(b) Power error of the linear-harmonic inflow model for the experimental rotor compared to wind tunnel measurements at different $\mu$. Experimental reference data is taken from [85]

(c) Longitudinal blade flap angles predicted by the linear-harmonic inflow model for the experimental rotor compared to wind tunnel measurements at different $\mu$. Experimental reference data is taken from [85]

**Figure 54** Comparison of total blade lift variation (a), power (b), and longitudinal blade flap (c) predicted by the linear-harmonic inflow model against experimental wind tunnel measurements from [85].

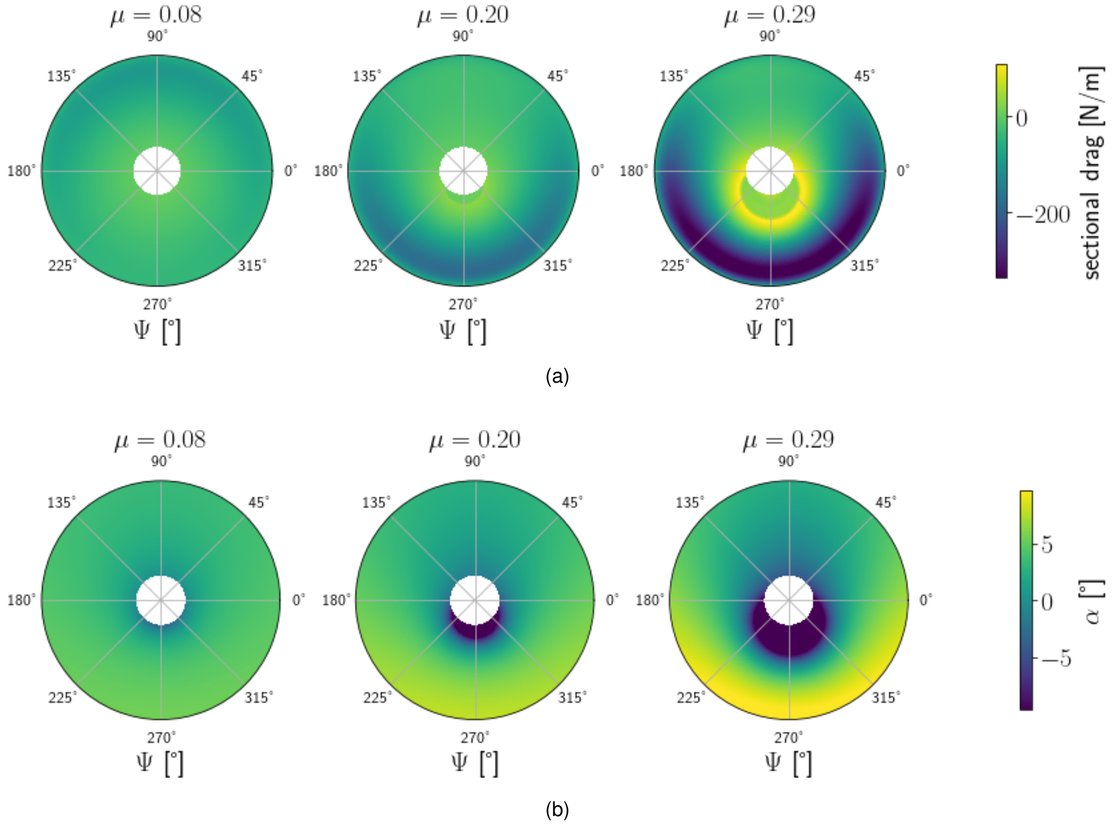

(a)

(b)

**Figure 55** Drag (a) and angle of attack (b) predictions at different $\mu$ by the linear-harmonic inflow model.

### Bessel-Fourier coupling

The integrated quantities for the blade lift, the power error, and the blade flap angle are shown in Figure 57. The trend of the blade lift variation over one revolution is depicted in Figure 57a. For $\mu = 0.08$, the trend is visible, but the simulation results show a positive offset for all azimuth positions compared to the measurements. This improves significantly with increasing advance ratio where the trends and the magnitudes are well met. However, blade lift perturbations with a higher harmonic component are not captured. With increasing advance ratio the influence of the flow field resolution and the tip loss factor diminishes. For the $\mu = 0.08$ trim condition, the influence of the resolution, as well as the tip loss, is visible. The highest tip loss with the highest resolution results in a closer match to the measured data as was already the case for the hover cases. The power predictions are similar to the linear-harmonic coupling, and power consumption is highly overpredicted, with the relative error increasing with increasing advance ratio up to +48%. The effect of the tip loss and the resolution is hereby negligible except for the lowest advance ratio which is in accordance with the results for the total blade lift. The resolution has a limited influence compared to $C_{\mathrm{tl},\%}$. The longitudinal flap angle shows an increasing trend as the measurements, but the predictions are up to one degree higher than in the experimental data.

The distribution for the angle of attack and the resulting in plane drag acting on the blade are comparable to the linear-harmonic inflow model (see Figure 55a) and not explicitly depicted.

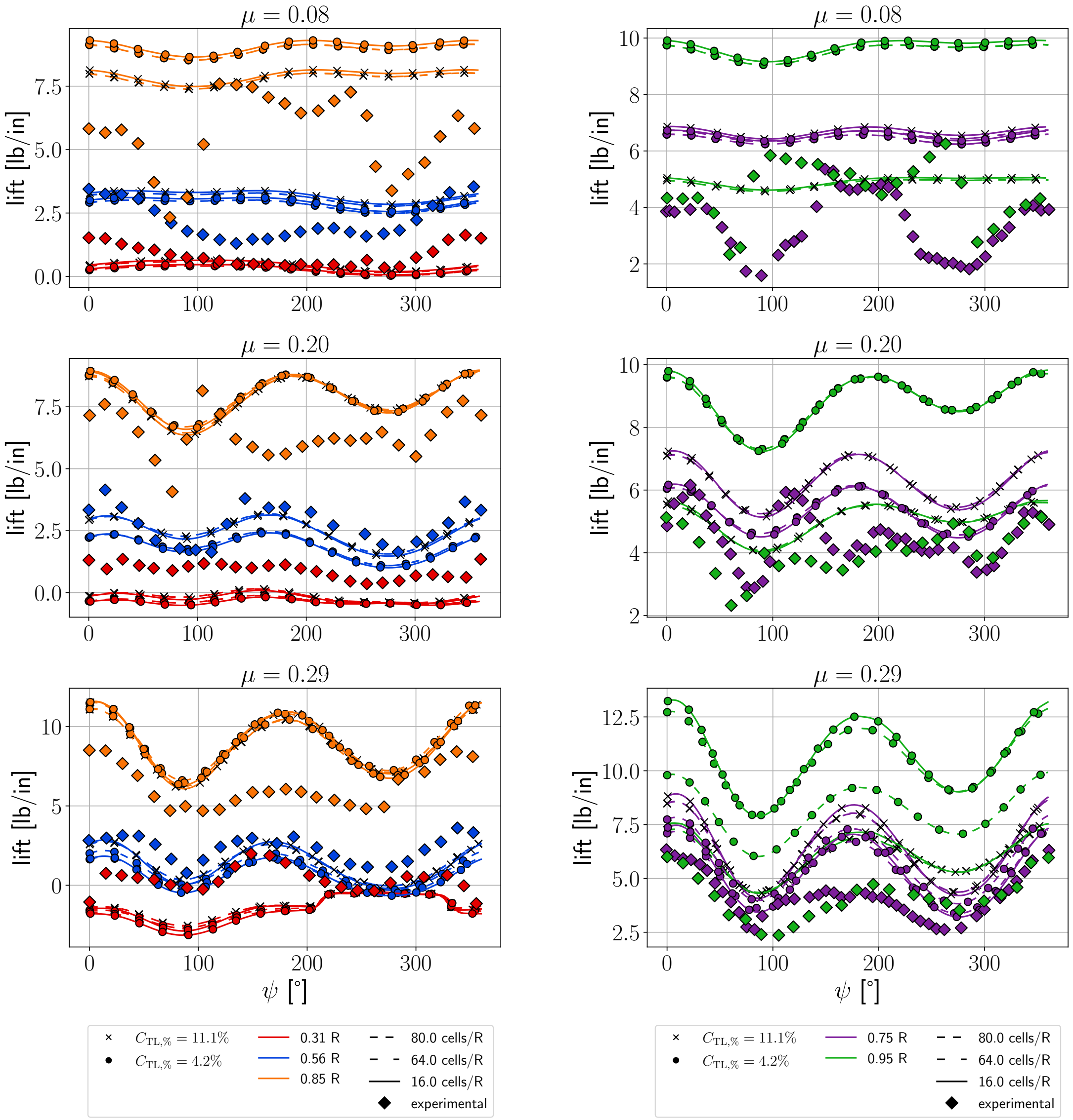

(a)

(b)

**Figure 56** Sectional lift at five radial stations for different $\mu$ predicted by the linear-harmonic inflow model. Results show a variation of $C_{\mathrm{tl},\%}$ and resolution. Experimental measurements from [85].

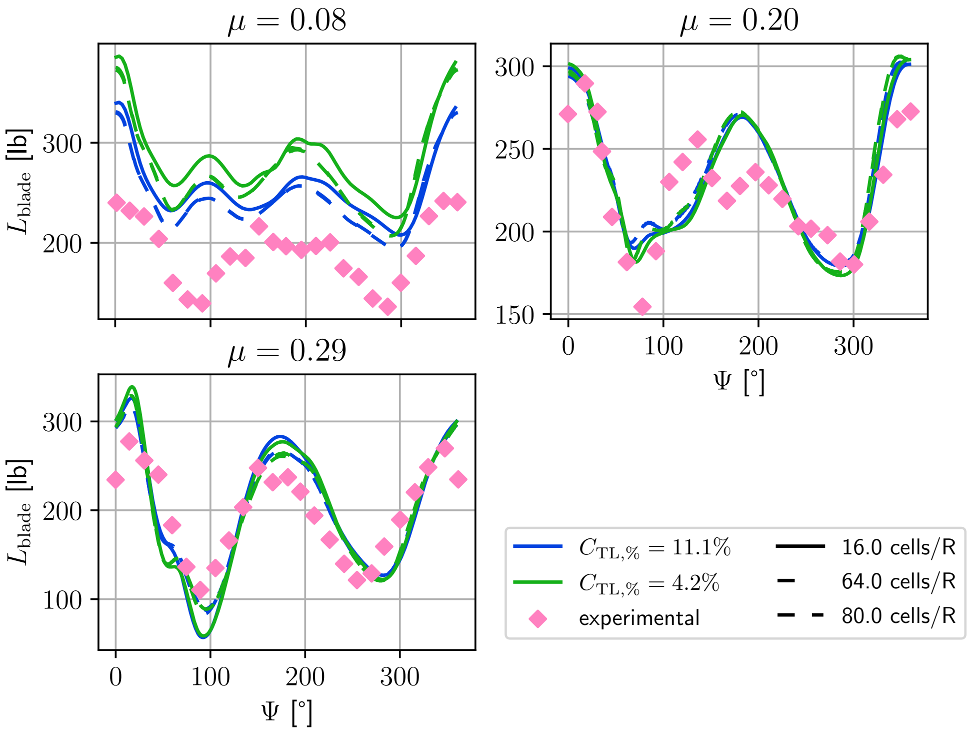

(a) Total blade lift predicted by the Bessel-Fourier inflow model at different $\mu$ compared to experimental measurements from [85]. Results are shown for a reduced set of considered tip loss and resolutions.

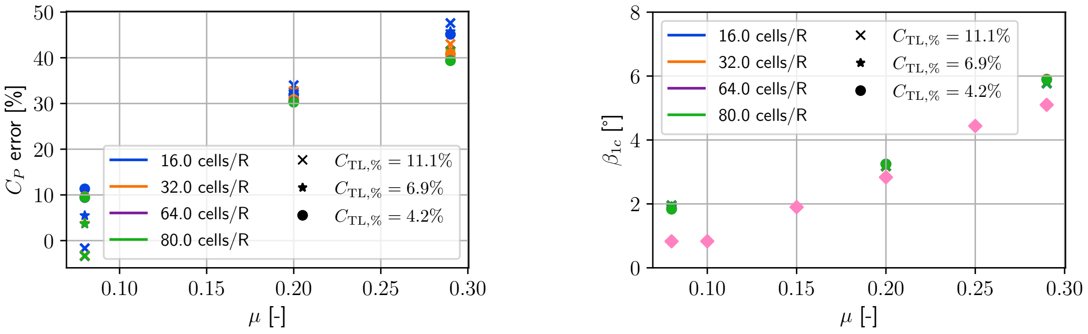

(b) Power error of the Bessel-Fourier inflow model for the experimental rotor compared to wind tunnel measurements at different $\mu$. Experimental reference data is taken from [85]

(c) Longitudinal blade flap angles predicted by the Bessel-Fourier inflow model for the experimental rotor compared to wind tunnel measurements at different $\mu$. Experimental reference data is taken from [85]

**Figure 57** Comparison of total blade lift variation (a), power error (b), and longitudinal blade flap (c) predicted by the Bessel-Fourier inflow model against experimental wind tunnel measurements from [85].

The retreating blade side shows again an increasing drag force from the midsection of the blade until the blade tip with an increasing advance ratio, leading to a higher required power. The lift distribution at the five radial measurement stations over a full rotor revolution is shown in Figures 58a and 58b. The results for $\mu = 0.08$ at the innermost measurement station at $r = 0.31$ match the experimental data in trend and magnitude over the full rotation. The trend for $r = 0.56$ is matched as well but the values are exaggerated around $\psi = 0.0°$. At $r = 0.75$, the data does not predict the measurements very well, and the trend is barely visible. This improves for $r = 0.85$ where the trend is better captured but the overall amplitudes are too high. The predictions for the outmost station are highly dependent on the tip loss, but the trend and magnitudes are captured well with the highest tip loss. Overall, the trends are visible and the results are close to the measurements. The influence of the tip loss is only visible at the blade tip while the influence of the resolution is not noticeable for any radial position.

The results for $\mu = 0.20$ show that the innermost values are not met. Although the simulation results show a similar flat trend the values are close to zero in contrast to the measurements. The trend for the measurements at the next radial station is well met, but the magnitude of the lift is predicted too low on the front of the rotor. The predictions for $r = [0.75, 0.85]$ show the general trend and do match the sinks of the measurements well. However, the predictions are too high around $\Psi = 0°$ and $\Psi = 180°$ where strong cross-flow conditions over the blade arise. For the outmost station close to the blade tip, the trend is recognizable, but the predicted values overshoot the measurements by up to 100% when $C_{\mathrm{tl},\%}$ is low. For the highest considered tip loss the predictions in the back half of the rotor are better, but the foreside suffers the same overshoots as for the other radial stations, leading to the assumption that the two-dimensional BET is not well-suited for the rotor section between $\psi = [110°, 250°]$ at higher advance ratios. The flow field resolution has no influence on the lift results and the tip loss factor only at the most outward measurement station, which is similar to $\mu = 0.08$. The results at $\mu = 0.29$ show the same characteristics as $\mu = 0.20$.

The radial lift predictions over a full rotation at twelve azimuth positions (see Figure 59 and Figure 60 ), when compared to experimental data, exhibit distinct characteristics dependent on the radial position and azimuthal angle. For instances at low $\mu$, radial agreement is observed within the azimuthal range of $\psi = [120°, 240°]$, particularly showcasing optimal tip loss between these angles. However, challenges arise on the backside of the rotor, spanning $\psi = [270°, 90°]$, where the match is less consistent. While inner sections align well, discrepancies arise at the tip around $r = 0.75$, aligning with the findings for the azimuth distribution in Figure 58b. Remarkably, the simulation suggests that resolution exerts negligible influence on results, with tip loss affecting only the outer blade sections concerning lift peak position and magnitude. On the contrary, results for $\mu = 0.29$ paint a different picture. Regardless of the azimuthal position, the overall trends deviate significantly, exhibiting exaggerations, especially on the foreside of the rotor. Analyzing the radial lift distribution reveals underpredictions at the innermost section and overly high predictions outboard, creating a pronounced diver-

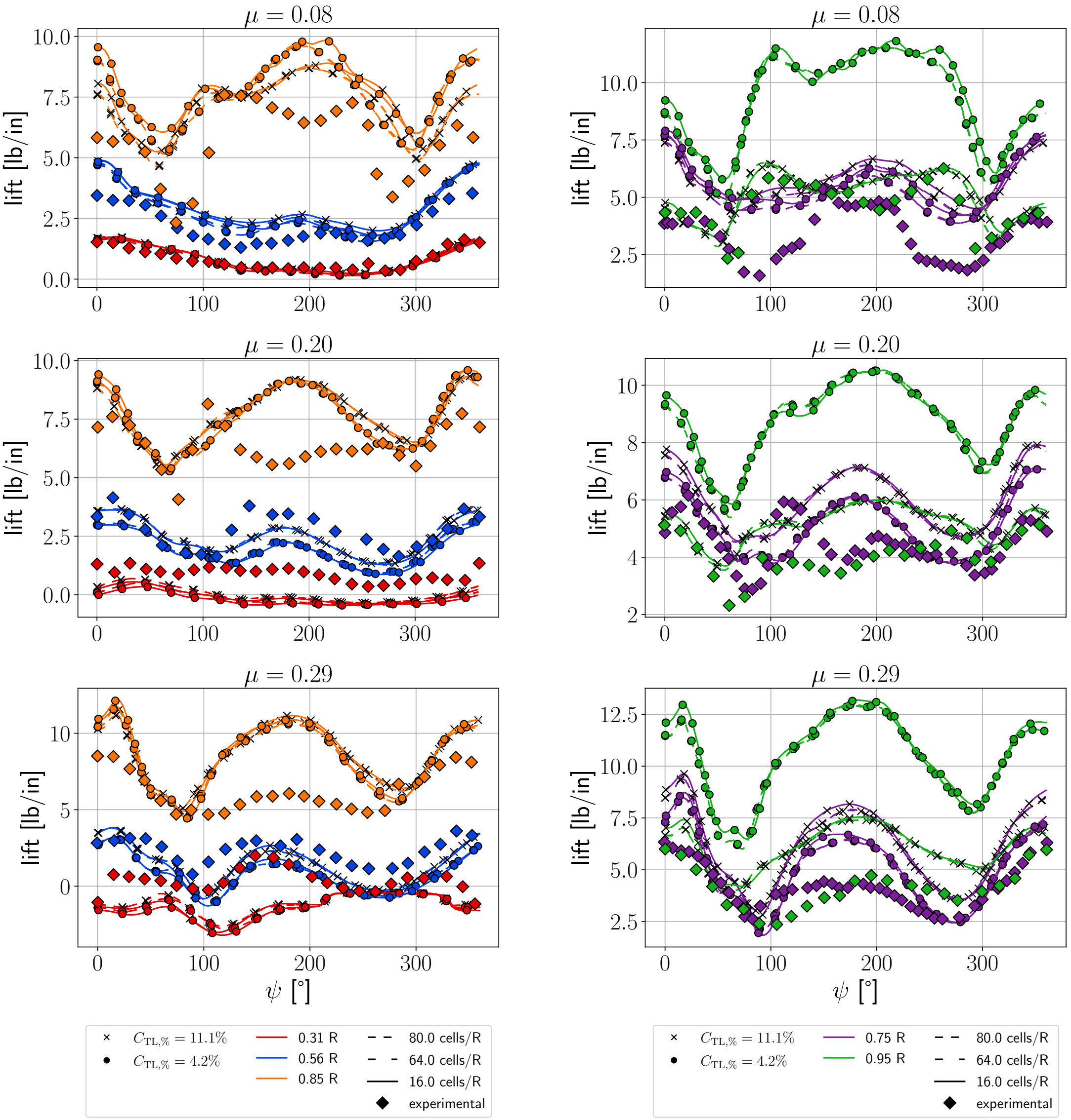

(a)

(b)

**Figure 58** Sectional lift at five radial stations for different $\mu$ predicted by the Bessel-Fourier inflow model. Results show variation of $C_{\mathrm{t1},\%}$ and resolution. Experimental measurements from [85].

gence from experimental trends in the front half of the rotor. While the match at $r = 0.56$ appears somewhat accidental, improvements are noted in the outboard region of the blade in the back half of the rotor; however, alignment with trends at the inner blade sections remains suboptimal.

In summary, the evaluation of integrated quantities for blade lift, power error, and blade flap angle reveals varying results in the comparison between simulation and experimental data. For scenarios with low mu values, commendable radial agreement is achieved within specific azimuth ranges, assuming a higher $C_{\mathrm{tl},\%}$. Challenges emerge on the backside of the rotor, where discrepancies, particularly around $r = 0.75$, are observed. Notably, the influence of flow field resolution is minimal, with tip loss predominantly affecting the outer blade sections. Conversely, for $\mu = 0.29$, overall trends deviate significantly, with exaggerations noted, especially on the fore side of the rotor. Radial distribution analysis exposes underpredictions and overpredictions at the inner and outer blade sections, respectively. This leads to a pronounced divergence from experimental trends in the front half of the rotor. These findings highlight the sensitivity of simulation results to the tip loss parameter and show the limitations of the actuator disc coupling approach, even with the additional degrees of freedom in the radial direction.

### Actuator line coupling

The results for the three actuator line coupling approaches are analyzed together in the following section. The results shown in this section are from the simulations with the restricted force kernel. The respective figures for the spherical kernel and the inflow correction model are shown in Appendix A. The total blade lift for $\mu = 0.08$ shows the general "w" trend of the lift as can be seen in the measurements (see Figure 61a). The trend is well met from $\psi \geq 250°$. The position of the minimum at $\psi \approx 270°$ matches the measurements, but the simulations predict, in general, a higher blade lift. Around zero azimuth the simulations predict the highest blade lift over a full rotation as do the measurements, however, the absolute value is highly overpredicted for the simulations. The dip at $\psi \approx 90°$ is not matched, the position is predicted at $\psi = 50°$ and the drop is not as steep as in the measurements. The same findings apply to the spherical kernel and the inflow-corrected approach (see Figure 92 and Figure 93), but the overall predictions are lower in magnitude, however still with a positive offset to the measurements. The influence of $C_{\mathrm{tl},\%}$ is clearly visible with a higher tip loss bringing the total blade load closer to the measurements. The flow field resolution does play a role as well, however, the differences between 64 and 80 cells per radius are negligible.

The results for $\mu = 0.20$ show a higher predicted peak at around $\psi = 0°$, but the relative error is reduced compared to $\mu = 0.08$. The dip of the measured blade lift at the advancing side is not predicted correctly; the position is too early for the lower advance ratio, and the value is higher than the measurement. The position of the second minimum at $\psi \approx 300°$ is well met, but the prediction is lower than the measurements. The trend of the measurements

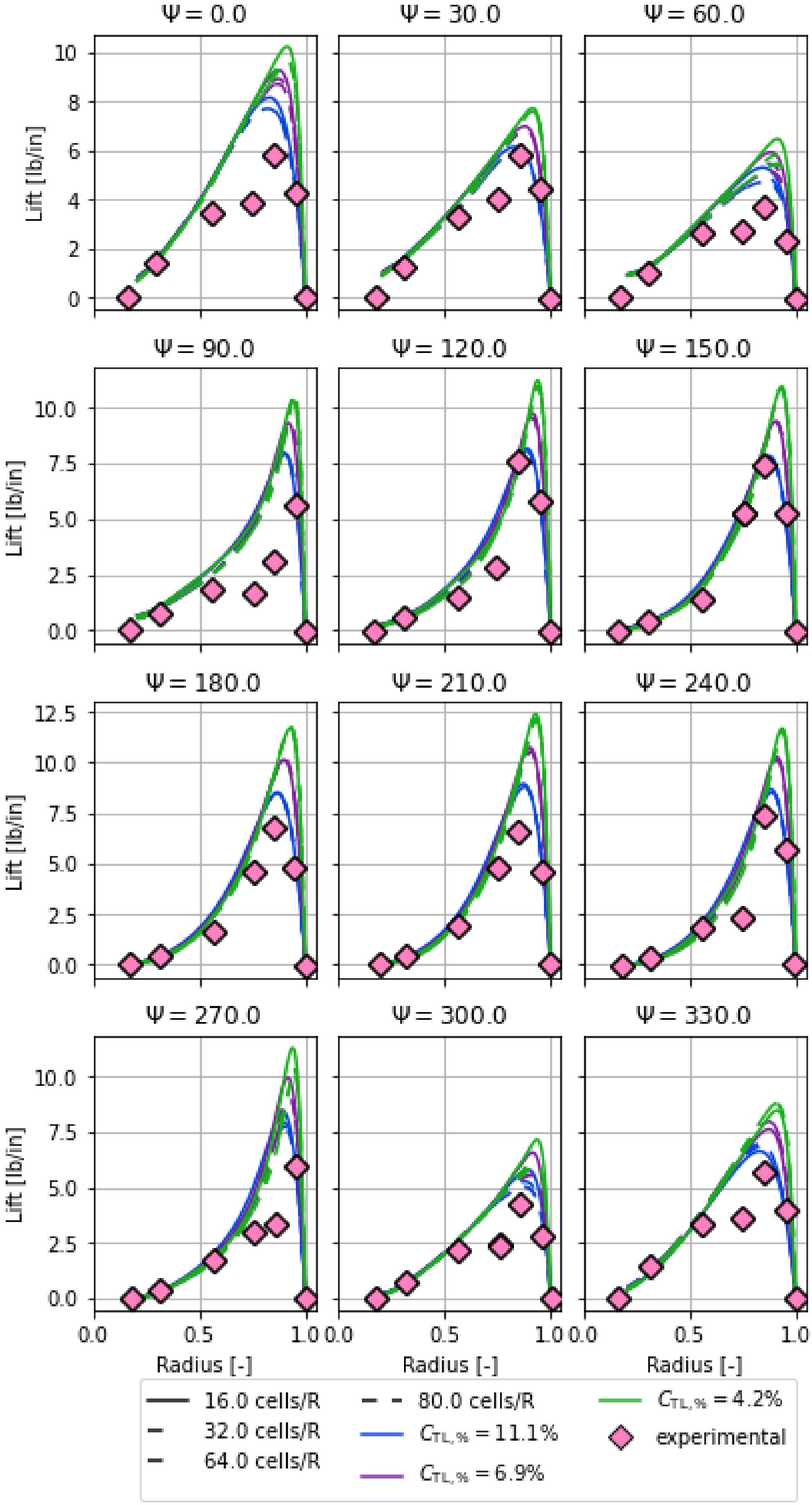

**Figure 59** Radial lift prediction by the Bessel-Fourier inflow model at twelve azimuth locations for $\mu = 0.08$ compared against measurements from [85].

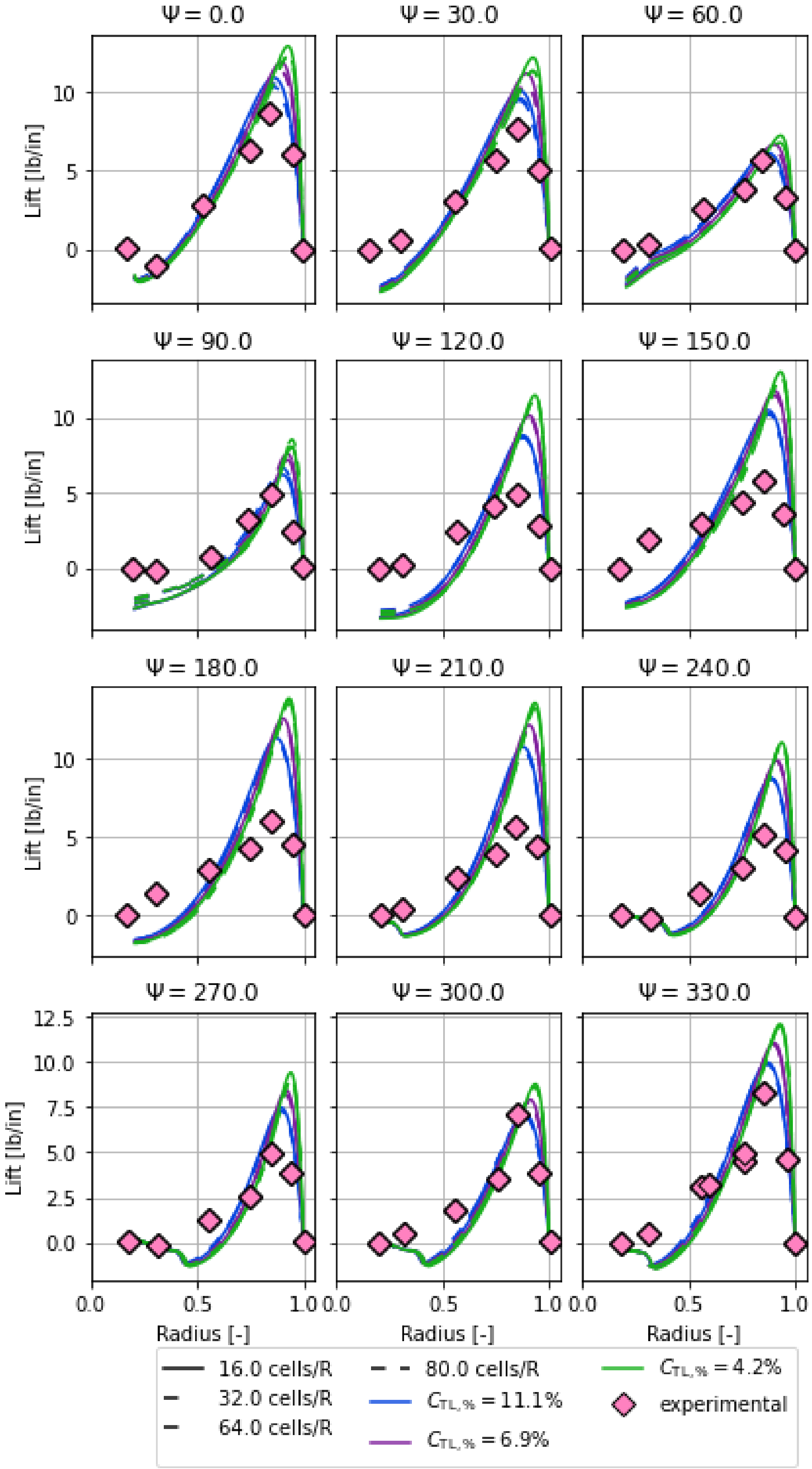

**Figure 60** Radial lift prediction by the Bessel-Fourier inflow model at twelve azimuth locations for $\mu = 0.29$ compared against measurements from [85].

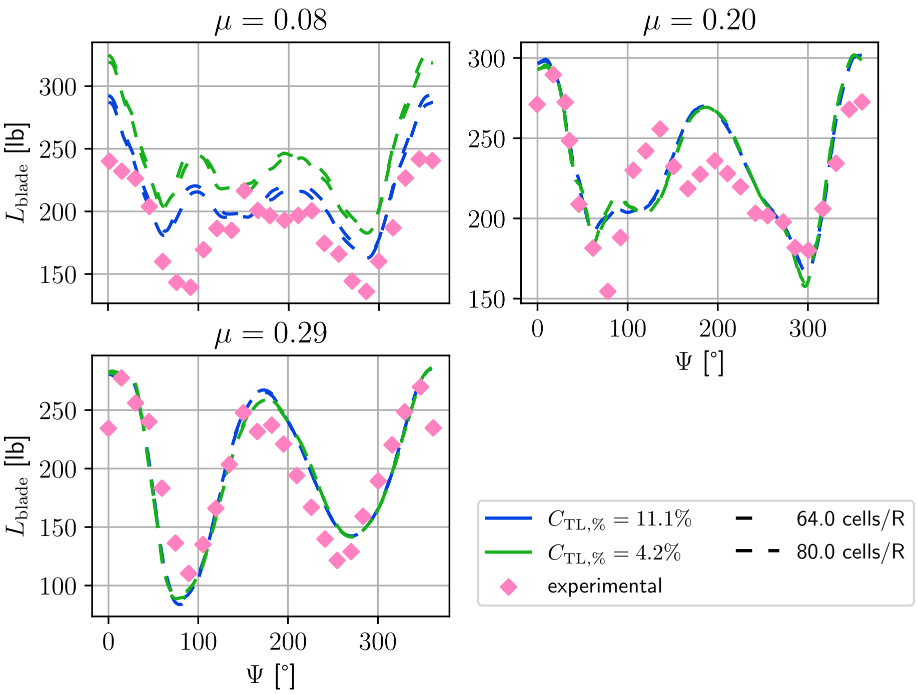

(a) Total blade lift predicted by the ACL model using a restricted force kernel at different $\mu$ compared to experimental measurements from [85]. Results are shown for a reduced set of considered tip loss and resolutions.

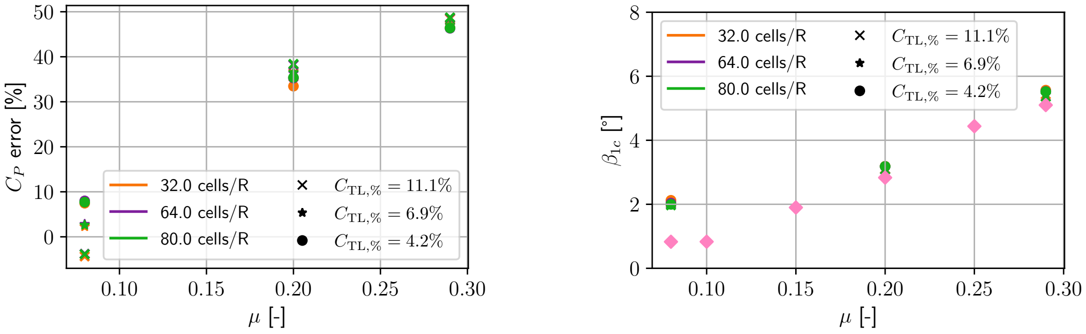

(b) Power error of the ACL model using a restricted force kernel for the experimental rotor compared to wind tunnel measurements at different $\mu$. Experimental reference data is taken from [85]

(c) Longitudinal blade flap angles predicted by the ACL model using a restricted force kernel for the experimental rotor compared to wind tunnel measurements at different $\mu$. Experimental reference data is taken from [85]

**Figure 61** Comparison of total blade lift variation (a), power error (b) and longitudinal blade flap (c) predicted by the ACL model using a restricted force kernel against experimental wind tunnel measurements from [85].

at the front side of the rotor is only roughly approximated. The influence of resolution or tip loss has vanished and does not influence the results. The results for $\mu = 0.29$ show the best agreement with measurements. The minimum and maximum are in good agreement and the position of the first minimum is well met in contrast to the results of the lower advance ratios. From $\psi = 180°$ onward, there is a slight phase shift of around 10°, but otherwise, the trend and magnitudes do agree very well with the measurements. The same statements apply to the spherical kernel and the inflow-corrected couplings.

The power predictions are too high in general for all considered advance ratios, except for $\mu = 0.08$ where an 11% tip loss is within 0 to -5% bandwidth for all models. For higher advance ratios the results are within a relative error range of +35% to +60%. The differences between the actuator line with restricted and spherical force kernel are negligible and are significantly lower than the corrected inflow version for $\mu = [0.20, 0.29]$. For the lowest advance ratio, the tip loss is the major influence on the power predictions, whereas for the other $\mu$ conditions, there is only minimal influence of the resolution. Otherwise, the results do not depend on flow field resolution or tip loss. The blade flapping is predicted too high for the low $\mu$ case where the longitudinal flapping is 1° above the measurements. For the higher advance ratios, the flapping angle is well met with a maximum deviation below 0.5°. The lateral flapping is zero per the trim condition and is therefore not in accordance with the measurements (see Appendix A).

The lift variations over a full rotor rotation are depicted in Figure 62. The results for $\mu = 0.08$ for the inner radial stations are in very good agreement with the measurements. The trends for the blade mid-section are well met as well, with slight deviations from the measurements where the loads are predicted too high around $\Psi$ at 0° and 180°. The outmost station is highly dependent on the tip loss where a small tip loss factor overpredicts the measurements by a factor of up to two. For the highest tip loss of 11%, the trend is clearly visible, and the data is matched on the forefront of the rotor. At the rotor back side lift results are too high compared to the measurements. With an increasing advance ratio, the simulation results at the innermost radial station deviate from the measurements but retain the trend. The predictions at $r = 0.56$ are still consistent with the measurements. The radial stations at 0.75R and 0.85R still match the trend and the minimum and maximum positions well, but predict the lift higher at $\Psi$ around 0° and 180°. The lift at the outmost station at 0.95R is predicted too high even with the highest tip loss, but at least maintains the general trend. The spherical force kernel yields the same results as the restricted force kernel (see Figure 94).

The coupling with the inflow correction gives similar results (see Figure 95), but in general, the offset at the inner blade section is lower when compared to the measurements. Furthermore, the predictions around 0° and 180° azimuth are reduced for the outboard station. With an increasing tip loss, the results at the outmost measurement stations are even predicted too low, showing the effect of the inflow correction on the outboard loads. The results show a low dependence on the resolution and the tip loss exerts a very limited influence except for the outmost station. This is comparable to the findings obtained from the hover investigations.

The radial lift results are depicted in Figure 63 and Figure 64 for the restricted force kernel, the results for the spherical and inflow corrected versions are in Appendix A. The simulation outcome at $\mu = 0.08$ matches the measurements between 120° and 240°. While the trends are met for the blade positions of 90° and 270°, the peak is too high and does not match measurements at $r = 0.85$. The lift magnitudes for the section between 300° and 60° are in general met, but the kink visible in the measurements at 0.75R is not met by the simulations. The resolution does not show any influence on the radial distribution. As is visible in the azimuth load variation data the tip loss exerts a strong influence at the blade tip. Looking at the data for $\mu = 0.29$ the ACL model does not match the radial trend in the inner section of the blade, e.g. $r \leq 0.6$. In the outboard region, the measurements are matched for the section between 300° and 60°, so the opposite of what was the case for the low advance ratio. In the remaining sections of the rotor, the lift is predicted too high for the outboard blade section and does not really represent the trend. The difference between the spherical kernel and the restricted kernel is negligible. The inflow correct ACL shows in principle the same behavior but does not exceed the measurement in the blade outboard section between $\psi = 120°$ and $\psi = 270°$ due to the inflow correction.

The deviations in the radial lift distribution for the low advance ratios on the advancing blade side lead to higher total blade lift predictions. For higher advance ratios, the match with the total blade lift improves, but this seems to be caused by the underprediction of lift in the inner blade section on the advancing side, thereby matching the integrated value. In summary, the trends at the radial stations over a full rotation are met, but the simulation results tend to predict higher lift than the measurements, meaning that the angle of attack is higher considering that the rotational speed and the wind speed are the same as in the experiment. The higher angle of attack could be the reason for the high drag and the resulting significant overshoot of the predicted power. The longitudinal blade flapping is in good agreement with the measurements for higher advance ratios. The sensitivity of macroscopic quantities on tip loss and flow field resolution is limited, but tip loss plays into the prediction of loads at the outer blade section as per its definition. Radial lift predictions are in good agreement with the measurements but deviations on the inner and outer blade section increase with increasing advance ratio. If this is tied to a general limitation of the ACL coupling or the unresolved issue of measured lateral blade flapping contrary to no lateral flapping in the simulation could not be determined.

### Peters–He

The results for the Peters–He inflow model are presented in the following. First, the total blade lift is depicted in Figure 65a. The simulation results for $\mu = 0.08$ show that measured the trend is not met. While the peak position and amplitude are a good match at $\psi = 0°$, the dips at $\psi = 90°$ and $\psi = 270°$ are not met with respect to amplitude. Therefore, the overall

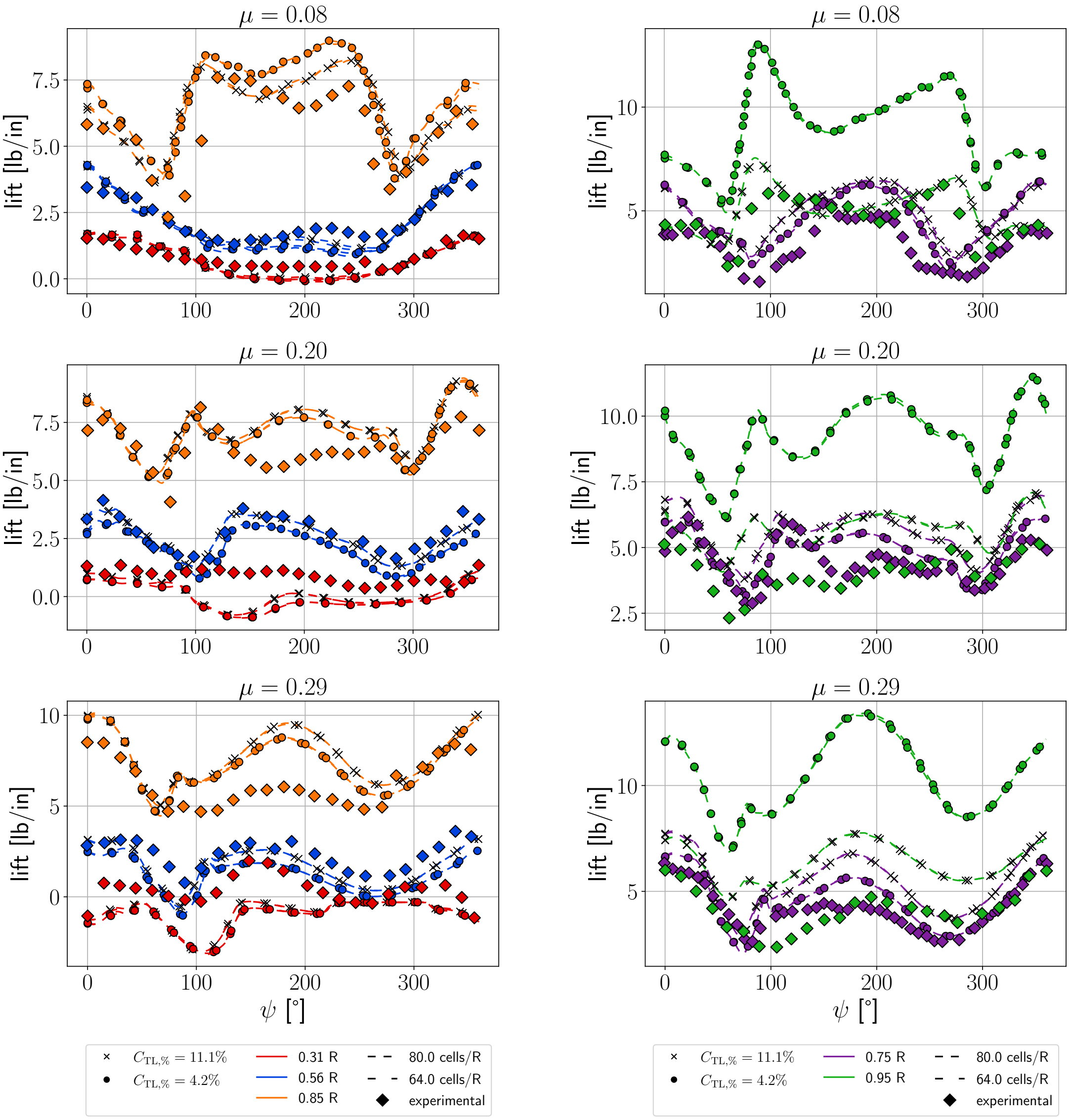

(a)

(b)

**Figure 62** Sectional lift at five radial stations for different $\mu$ predicted by the ACL model using a restricted force kernel. Results show a variation of $C_{\mathrm{tl},\%}$ and resolution. Experimental measurements from [85].

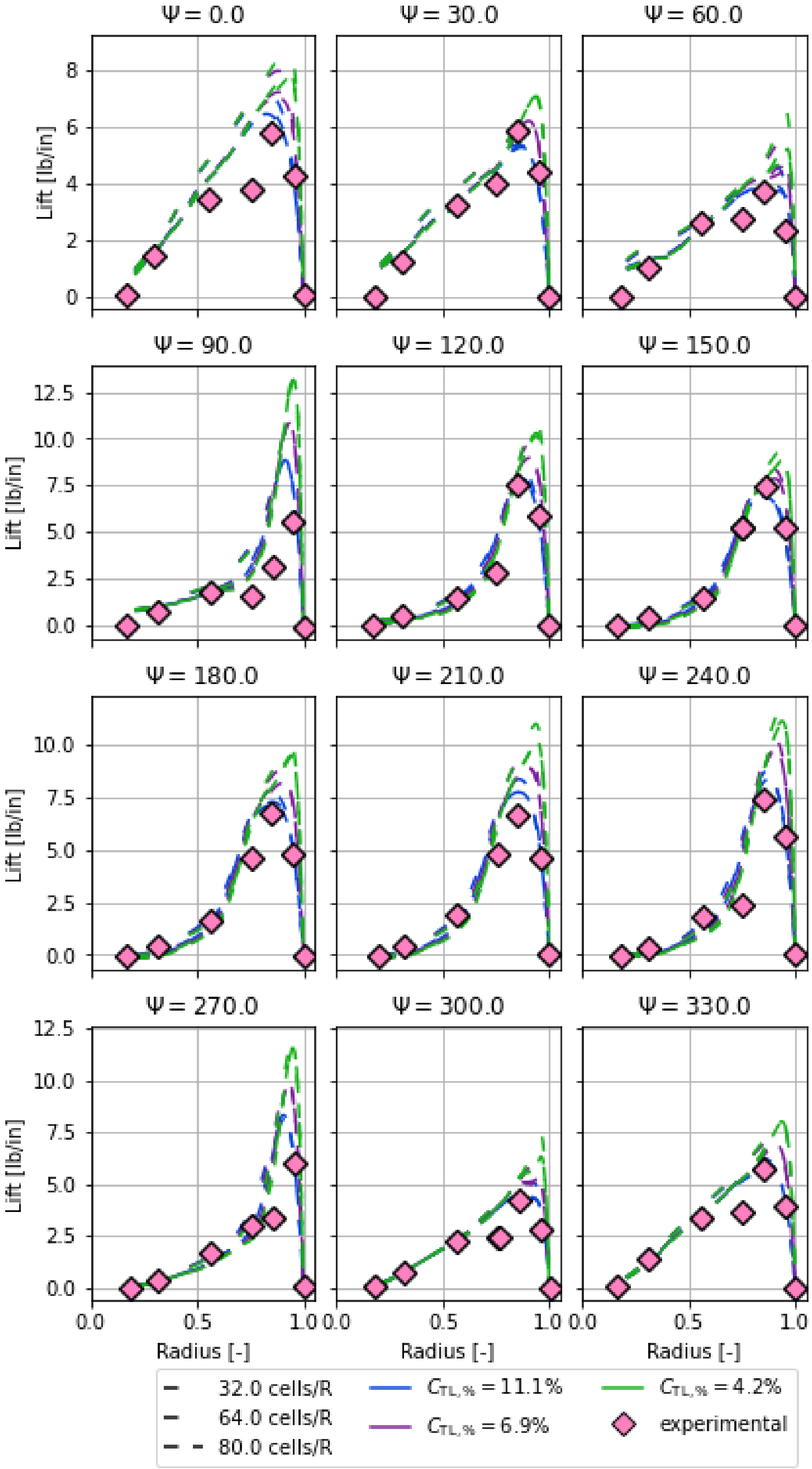

**Figure 63** Radial lift prediction by the ACL model using a restricted force kernel at twelve azimuth locations for $\mu = 0.08$ compared against measurements from [85].

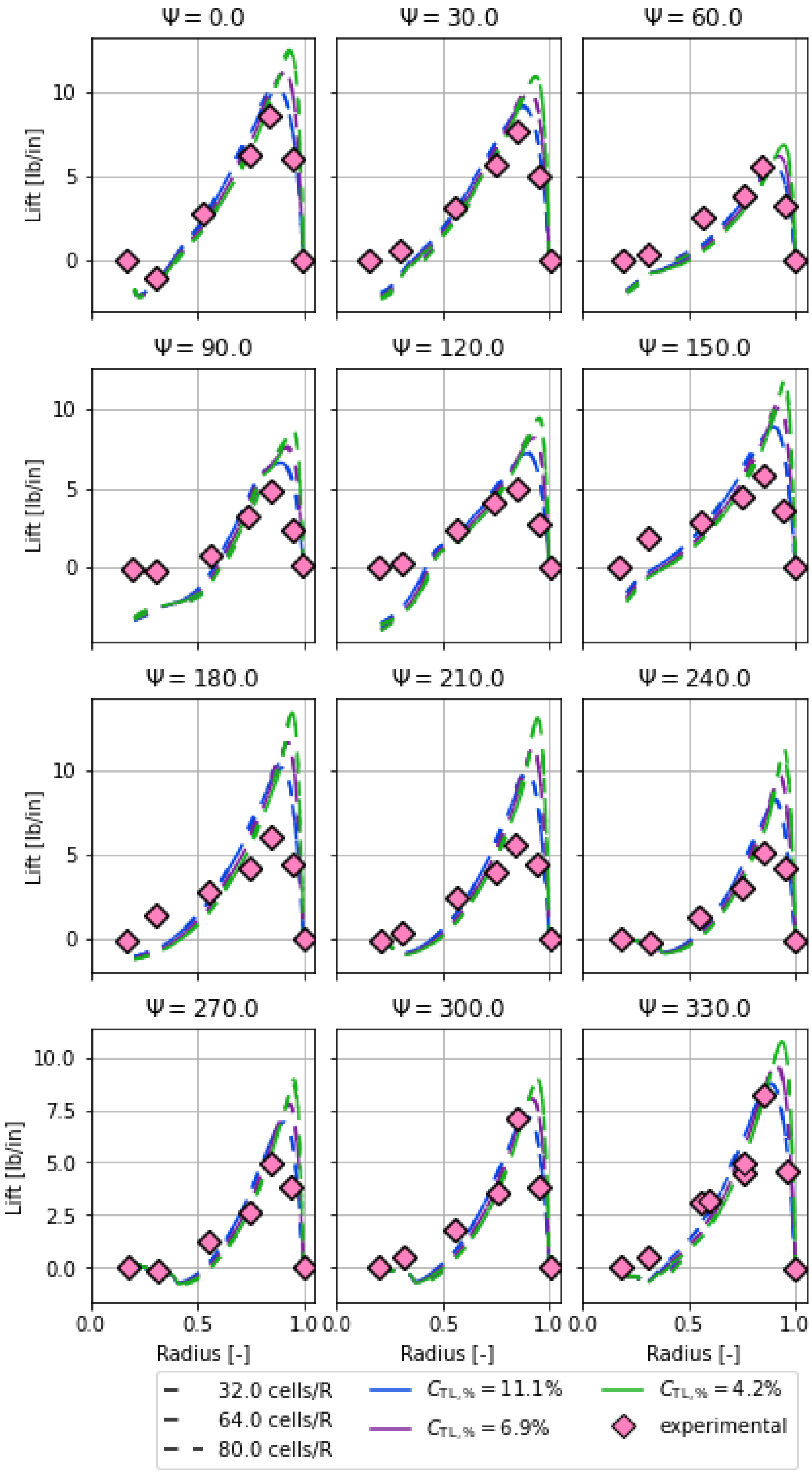

**Figure 64** Radial lift prediction by the ACL model using a restricted force kernel at twelve azimuth locations for $\mu = 0.29$ compared against measurements from [85].

trend does not really represent the measurements. The influence of the tip loss is visible for that condition where the Peters–He model shows better peak agreement with a lower tip loss. The total blade lift trend improves significantly with increasing advance ratio. While the minimum at $\psi = 270°$ is well met for $\mu = 0.20$, the value at the first minimum is predicted too high. Nevertheless, the overall trend is visible. For the $\mu = 0.29$ trim condition, the first minimum is well met in position and value, while the second dip is not completely met, and the trend shows a phase shift compared to the measurements. The influence of the tip loss decreases with increasing advance ratio. The power predictions are up to 18% above the measurements for an advance ratio of 0.08 and steadily increase to an error of 70% for the highest advance ratio. The blade flapping on the other is well met, although at $\mu = 0.08$, the lateral flap is predicted too high.

The lift variations over a full rotor rotation at the five radial measurement stations are depicted in Figure 66. The results for $\mu = 0.08$ for the inner radial measurement stations show a flat trend and do not capture the slight increase at zero azimuth. The trend for $r = 0.56$ is generally met but shows deviations at the advancing blade side. At $r = 0.75$, the lift prediction meets the measurements at around $\psi = 180°$ but does not represent the peak-to-peak behavior. The same goes for 0.85R and 0.95R where the minimums are highly overpredicted. While the peak-to-peak behavior is not satisfying, the peak positions are well predicted. The tip loss influence is visible with increasing radial position as is to be expected. For $\mu = 0.20$, the innermost radial station still shows the flat trend. The trend for 0.56R and 0.85R, on the other hand, is well met in peak position and amplitude. The 0.75R station shows a better agreement with the measurements, but the values are predicted too high in the front half of the rotor and around the peak at $\psi = 0°$. The findings for $\mu = 0.29$ are similar, with the additional phase shift after $\psi = 270°$ that was already visible in the total blade lift predictions. The influence of the tip loss is the same as for $\mu = 0.08$.

The radial lift distribution is depicted in Figure 67 and Figure 68. The simulation outcome at $\mu = 0.08$ matches the measurements between 120° and 240°. The peaks match the data for the lowest tip loss without any overshoots close to the blade tip. Between $\psi = 270°$ and $\psi = 90°$ the peak position and magnitude as well as the inner blade sections are met. However, the trend where the lift has a kink at 0.75R is not matched by the simulation results. The effect of tip loss is visible at all measured positions, and the Peters–He model seems to require a low $C_{\mathrm{tl},\%}$. For the trim condition of $\mu = 0.29$, the simulation results match the measurement data between $\psi = 270°$ to $\psi = 60°$, which is in opposition to the findings for the low advance ratio. For the remaining rotor sections, the simulated results either predict a lower lift for the inner blade section on the advancing side or a higher peak at the retreating side. Overall, the trend is not matched but only roughly represented.

In summary the total blade lift predictions improve with increasing advance ratio. The poor performance of the simulation for $\mu = 0.08$ results from the failure to predict a kink in the lift trend at around 0.75R when the blade is perpendicular to the free stream flow. The power

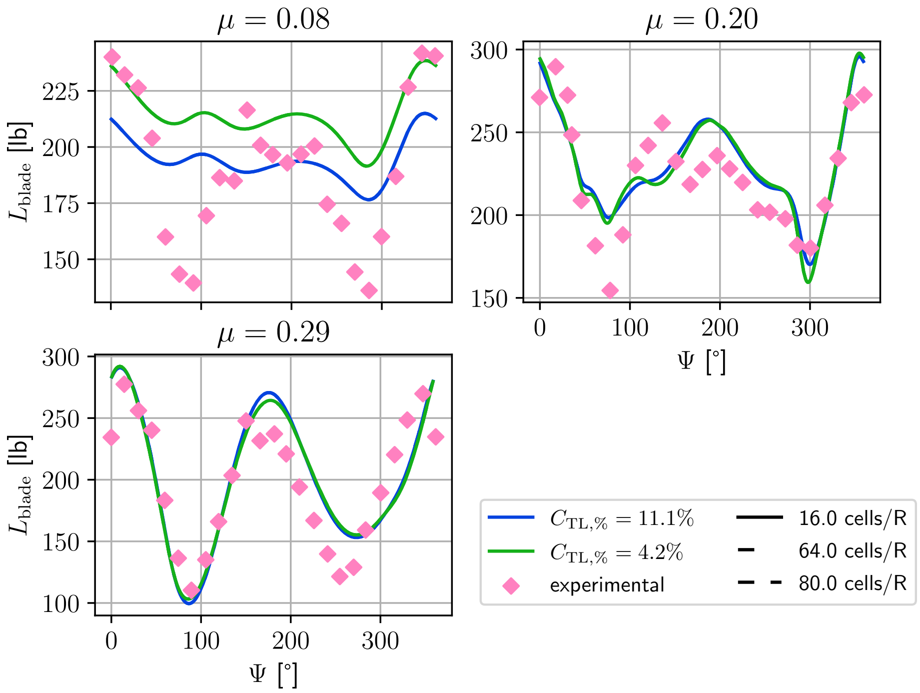

(a) Total blade lift predicted by the Peters–He inflow model at different $\mu$ compared to experimental measurements from [85]. Results are shown for a reduced set of considered tip loss and resolutions.

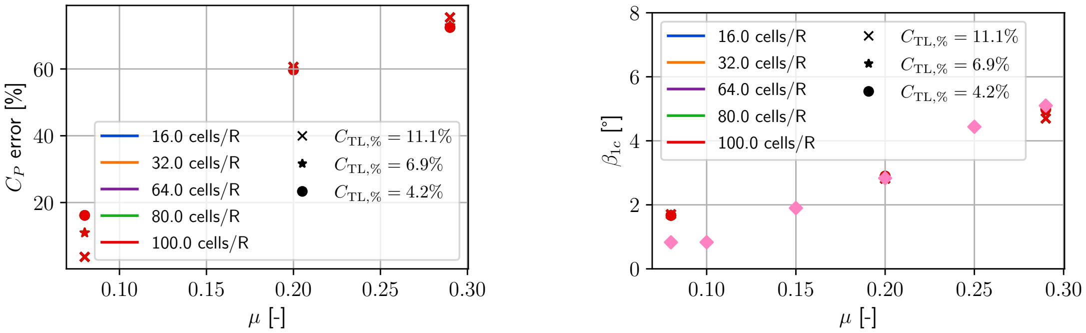

(b) Power error of the Peters–He inflow model for the experimental rotor compared to wind tunnel measurements at different $\mu$. Experimental reference data is taken from [85]

(c) Longitudinal blade flap angles predicted by the Peters–He inflow model for the experimental rotor compared to wind tunnel measurements at different $\mu$. Experimental reference data is taken from [85]

**Figure 65** Comparison of total blade lift variation (a), power error (b), and longitudinal blade flap (c) predicted by the Peters–He inflow model against experimental wind tunnel measurements from [85].

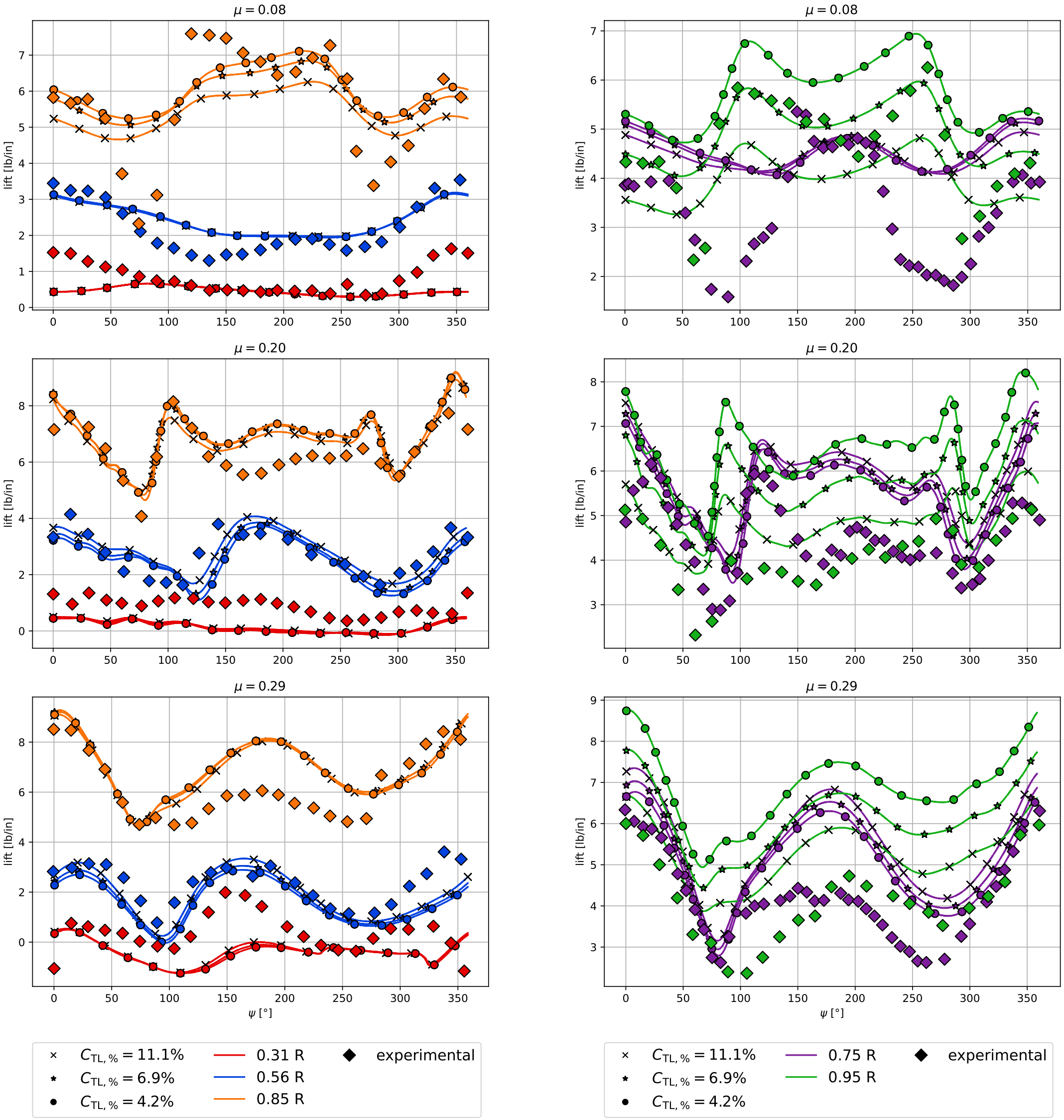

(a) (b)

**Figure 66** Sectional lift at five radial stations for different $\mu$ predicted by the Peters–He inflow model. Results show a variation of $C_{\mathrm{tl},\%}$ and resolution. Experimental measurements from [85].

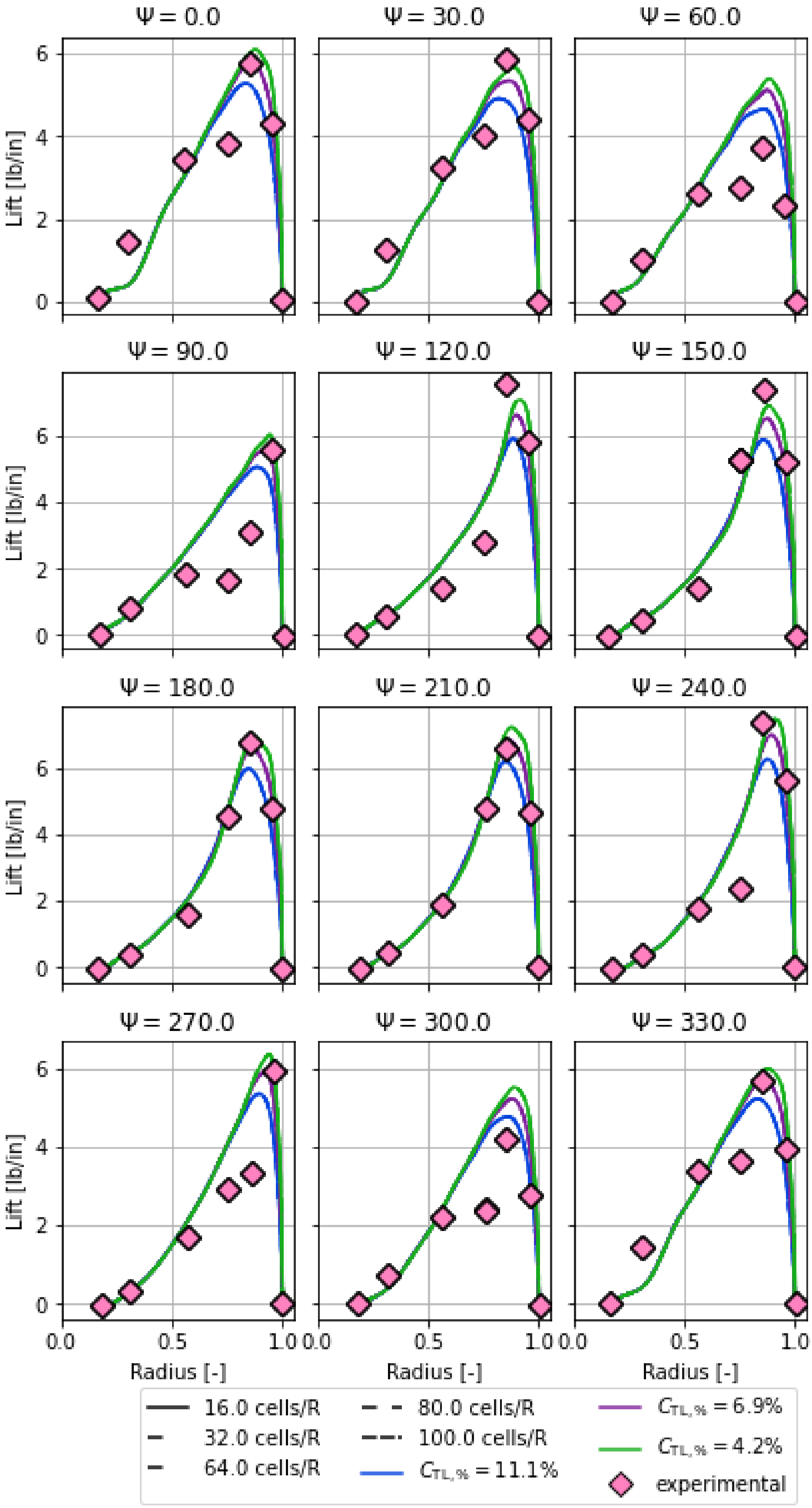

**Figure 67** Radial lift prediction by the Peters–He inflow model at twelve azimuth locations for $\mu = 0.08$ compared against measurements from [85].

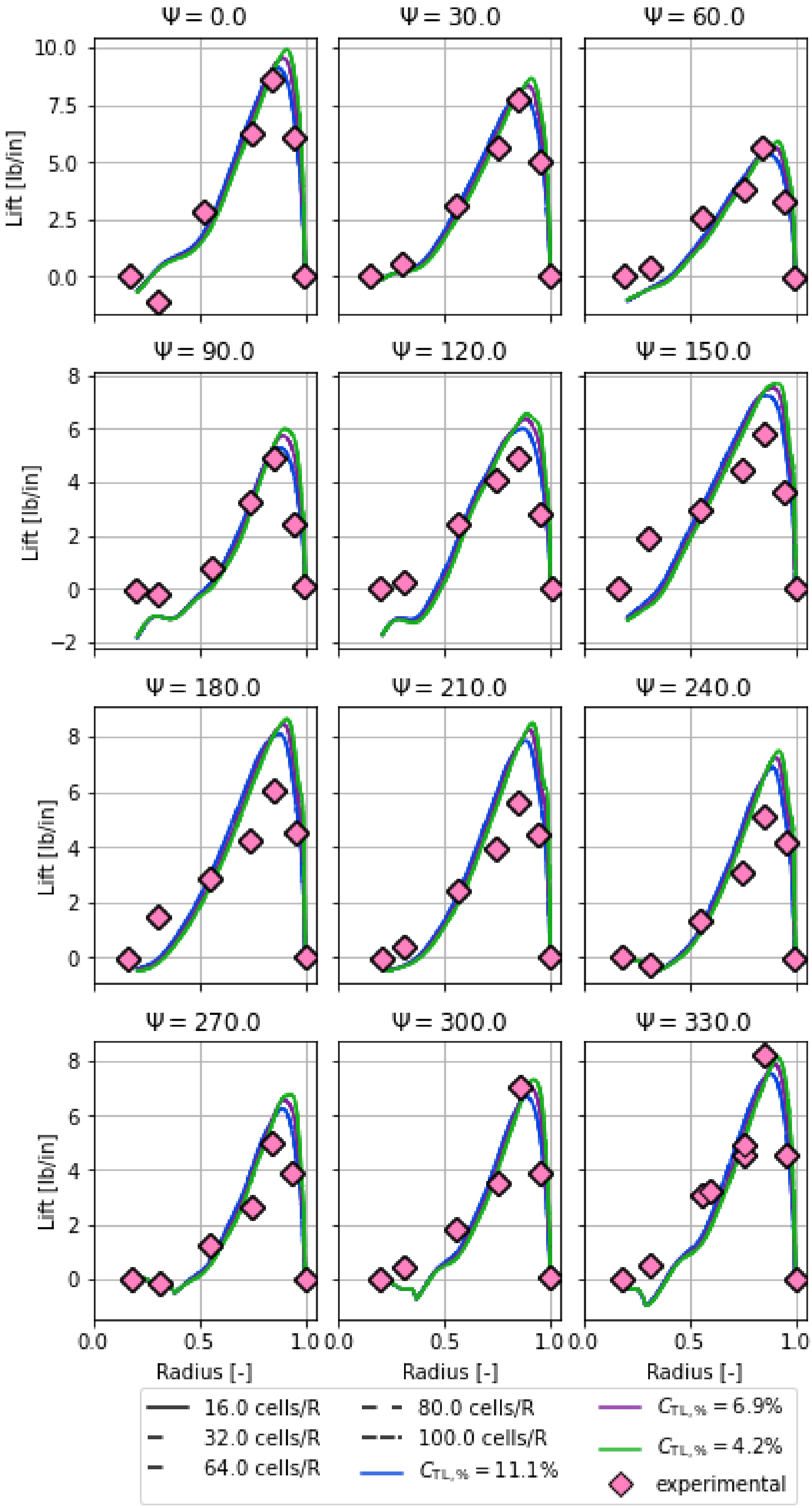

**Figure 68** Radial lift prediction by the Peters–He inflow model at twelve azimuth locations for $\mu = 0.29$ compared against measurements from [85].

prediction is getting worse with increasing advance ratios with an unacceptable error level. With the measurement data at hand, the reason for this is pinned down to the higher predicted lift when the blades are parallel to the free stream velocity, leading to the conclusion that the cross-flow has a huge impact on blade loads that cannot be modeled adequately by 2D airfoil table look up and blade element theory. The resulting higher angle of attack in the simulations leads to higher drag than in reality. This could explain the stark increase in power consumption. The radial lift predictions in general show agreement to measurements, however the regions where predictions are good shift with increasing advance ratio. The longitudinal blade flap angle is in good agreement to measurements with small deviations for the lowest advance ratio. In general, the effect of tip loss is visible, but its effect on the overall results is very limited.

### Inflow Model Comparison for Wind Tunnel Results

The results section for each model gave an insight into the capabilities of each model to predict integrated measured rotor quantities such as total blade lift, power, and blade flaps, as well as for the more detailed blade load distribution. Because no model has a perfect match with experimental data, a comparison of strengths and weaknesses between the models is necessary. The results for the required power can be evaluated in a quantitative matter. A comparison of inflow, angle of attack and lift distribution will be in a qualitative way to highlight major differences between the models and model limitations.

The error for the power predictions is shown in Figure 69 for all models. The trend for an increased error with an increasing advance ratio is visible to all models. The increase in error is the same for all LBM inflow models, the Peters–He model shows a higher increase, leading to the highest error of all the models. All models show a relevant influence of the tip loss factor for $\mu = 0.08$ where the relative errors range from -5% to +18%, depending on $C_{TL,\%}$, and is independent from the resolution. This effect diminishes with increasing advance ratio for the ACL models without inflow correction, where the effect of the tip loss is in the same order of magnitude as the resolution and within a bandwidth of a few percent. For the ACL coupling with the inflow correction, the influence of the resolution is more distinct for higher advance ratios. As the inflow correction depends on the initial inflow distribution from the fluid simulation, where the inflow at the blade tip is heavily influenced by the grid resolution this is to be expected. The AD models show similar behavior, where the lowest resolution of 16 cells per radius is distinct from the other resolution results. The increase in error for the AD is lower than for the other modeling approaches, with the linear harmonic being the most model. Considering that the underlying formulation assumes an idealized inflow and lift state for the rotor aerodynamics it seems reasonable that the power prediction is lower than the other models. The actuator line with the inflow correction gives an up to 10% higher prediction than the other ACL models. All models showed in a more detailed analysis higher lift predictions than the measurements when the blades are parallel to the free stream velocity and an increase of this higher prediction with increasing free stream velocity, meaning that the angle of attack is too high in the BET. This also comes with a higher predicted drag and due to the outboard location of this over-prediction with a higher shaft moment and a resulting significant overestimation of power. This shows the limitation of BET in this specific use case. In summary, none of the models gives a satisfactory power prediction with higher advance ratios.

The predicted lateral blade flap (see Figure 70) at $\mu = 0.08$ is similar for the LBM models with higher degrees of freedom in the radial direction. The Peters–He model predicts a lower flap angle, and the linear-harmonic model is significantly lower by 0.8° than the other models. As a result, it is 0.2° above the measured angle, whereas the remaining models are 1° off. At $\mu = 0.20$ all models are within a bandwidth of 0.2° of the experiments where the Peters–He matches the results. The blade flapping for all LBMmodels is comparable for $\mu = 0.29$ where the differences between the models are within 0.2°. The Peters–He model predicts

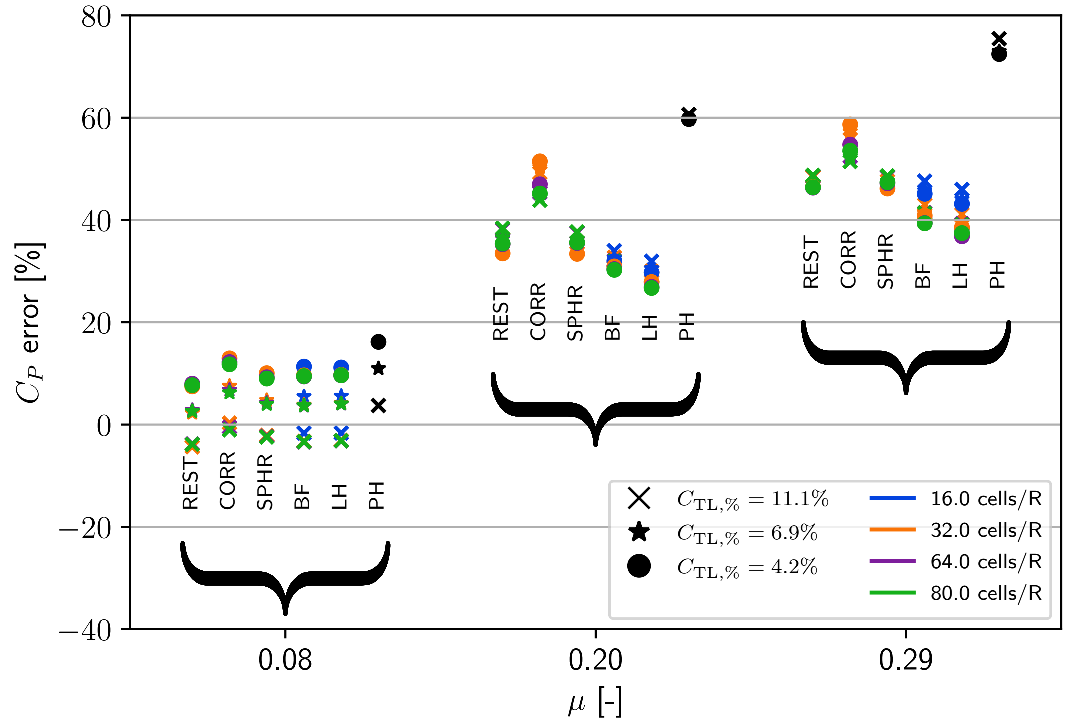

**Figure 69** Comparison of the error in the power prediction for all inflow models at different $\mu$. ACL with restricted force kernel (REST), ACL with spherical force kernel (SPHR), ACL with inflow correction (CORR), linear-harmonic (LH), Bessel-Fourier (BF), Peters–He (PH).

a significantly lower value and is under the measurements but matches the data within an error of 0.2°. Overall, for a higher advance ratio, the match with measurements is in good agreement for all models, no matter the resolution or the tip loss.

For the required control inputs, no measurement data is available, and thus, the inflow modeling approaches are only compared against each other. The differences at $\mu = 0.08$ between the different models are negligible for collective and cyclic inputs and resolution or tip loss do not show a significant influence. With increasing $\mu$, the variation in the predicted collective with varying flow field resolution and tip loss becomes apparent, but it is comparable between all models. The predicted bandwidth is similar for all LBM models. With increasing advance ratio the longitudinal input decreases from around zero to up to -12° and is in the same bandwidth for all models. The lateral input increases but is, in general, very low. The inputs are plausible considering the trim condition for all models. Furthermore, there is no significant difference in the predictions no matter which inflow model is used.

The analysis of aerodynamic characteristics across the different inflow models (see Figure 71 to Figure 73) reveals several key findings. At $mu = 0.08$ lift is observed to be stronger on both the advancing and retreating sectors around $\psi = 100°$ and $\psi = 225°$ compared to the back side of the rotor for all models except the linear-harmonic model. The linear harmonic model shows a rotational symmetry without the local concentration for the lift. The Bessel-Fourier

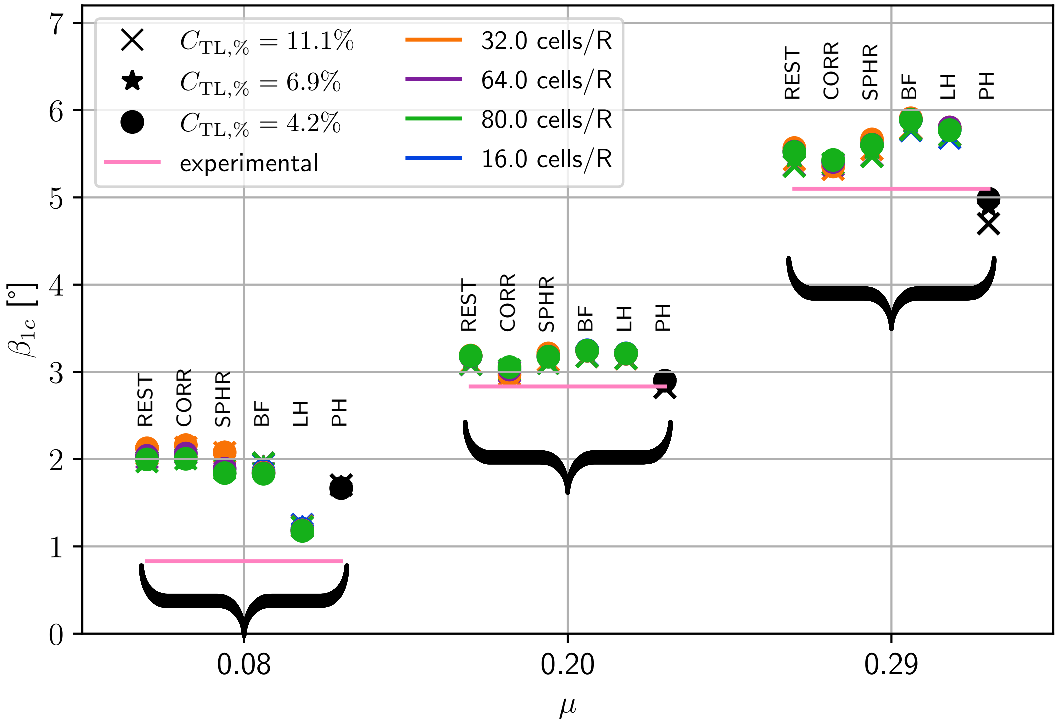

**Figure 70** Comparison of the longitudinal flap angle for all inflow models at different $\mu$. ACL with restricted force kernel (REST), ACL with spherical force kernel (SPHR), ACL with inflow correction (CORR), linear-harmonic (LH), Bessel-Fourier (BF), Peters–He (PH).

model shows an additional lift peak around $\psi = 0°$ that is more pronounced than for the other models. The Peters-He model is similar to the ACL results but the overall magnitudes are lower. Taking into account that the previous analysis showed that the Peters–He model requires a lower tip loss to match the lift peak of the measurements, this seems plausible. Looking at the angle of attack reveals that the ACL models have a region of high angles of attack directly behind the hub and a region of low angles of attack in front of the hub. The same pattern is seen for the Bessel-Fourier model. The areas of high and low angles of attack are less pronounced for the Peters-He results but the distribution is comparable. The linear-harmonic results show a different pattern with a low angle of attack circular around the hub, low at the advancing blade half, and high on the retreating blade half of the rotor. The inflow data for ACL and Bessel-Fourier show low or negative induced velocities at the rotor boundary in the front half and high positive inflow at the back half boundary of the disk. The magnitudes are reduced for the ACL with inflow correction in the front half compared to the non-corrected models. There is a reduced inflow velocity at around zero azimuth, where this section is more pronounced for the Bessel-Fourier model and less for the ACL with inflow correction compared to the other ACL. The Peters-He model is comparable to the ACL models but the magnitudes are lower, which is in agreement with the lift distribution results.

With an increase to $\mu = 0.29$ the lift around $\psi = 0°$ increases significantly and the peak in the front half moves between $\psi = [135°, 225°]$ for all models. For the Bessel-Fourier and the

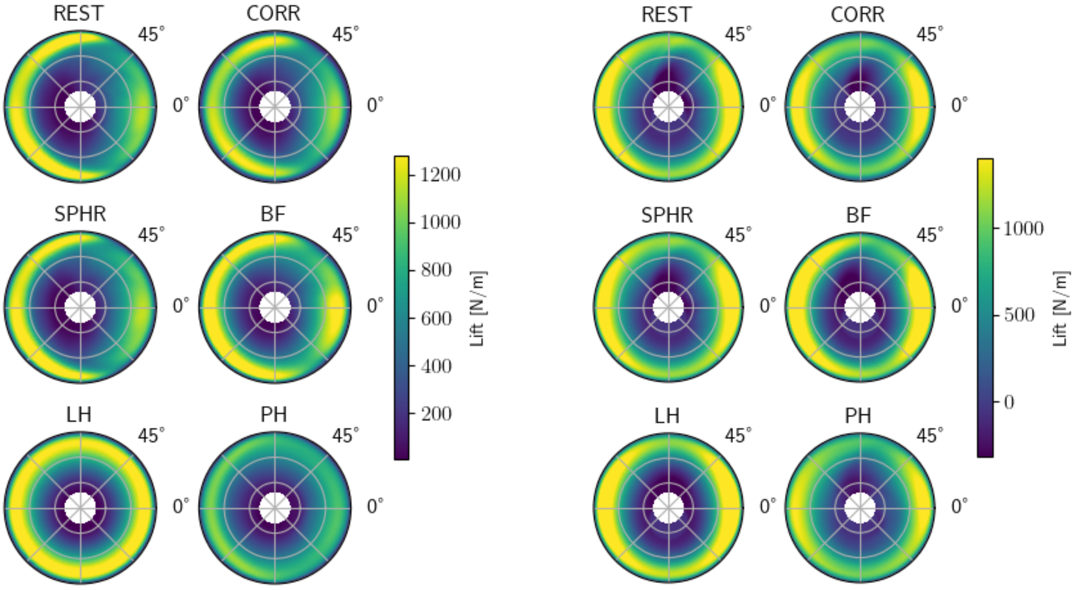

(a) $\mu = 0.08$

(b) $\mu = 0.29$

**Figure 71** Comparison of rotor lift distribution for all inflow models for the experimental rotor in wind tunnel condition with $C_{\mathrm{TL},\%} = 11.1\%$ and a resolution of 64 cells per radius. ACL with restricted force kernel (REST), ACL with spherical force kernel (SPHR), ACL with inflow correction (CORR), linear-harmonic (LH), Bessel-Fourier (BF), Peters–He (PH).

linear-harmonic model, the magnitudes in the front half of the rotor are higher than for the ACL models. The Peters–He inflow model shows the same behavior, but magnitudes are reduced for the chosen tip loss. When comparing the angle of attack the differences between all models are negligible. The inflow distribution is comparable between the ACL and the Bessel-Fourier models, where the ACL with the inflow correction experiences higher magnitudes at the disk boundary, and the peak values for the Bessel-Fourier model are reduced compared to the non-corrected ACL models. The Peters–He model on the other hand shows a large section around the root cutout with a negative inflow value, and the overall magnitudes are greatly reduced. However, when ignoring the magnitude and comparing the trends in the distribution it is similar to the ACL and the Bessel-Fourier results.

In summary, all models showed similar behavior with respect to the blade control angles although measurements were not available. All models predicted comparable blade flap angles that were in good agreement with measurements. The power predictions were not in agreement with the measurements with deviations of up to 75% percent. While all LBM models were close together, the Peters-He model stuck out with even higher predictions. The reason for the bad power predictions could not be determined with certainty, although results point to the limitations of the BET in the region where blades encounter strong cross flow and resulting high forces. This overprediction showed in the comparison of azimuth and radial load variation with experimental data. However, the models with higher degrees of freedom in inflow and thrust representation were able to capture the general trends. Only the linear-harmonic model showed higher deviations, which is to be expected considering the limited

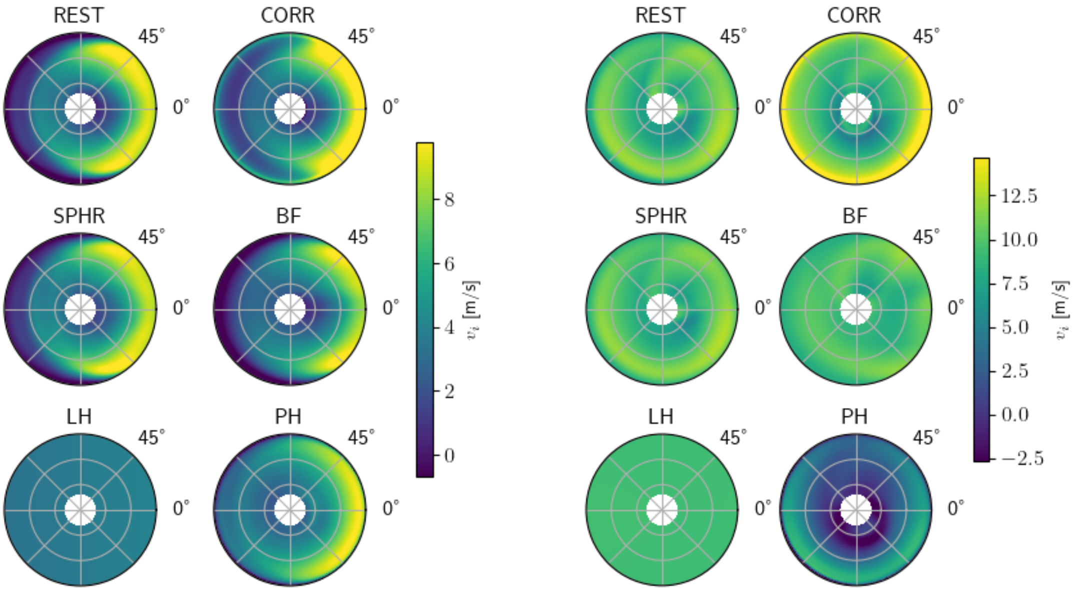

(a) $\mu = 0.08$

(b) $\mu = 0.29$

**Figure 72** Comparison of induced velocity distribution for all inflow models for the experimental rotor in wind tunnel condition with $C_{\mathrm{TL},\%} = 11.1\%$ and a resolution of 64 cells per radius. ACL with restricted force kernel (REST), ACL with spherical force kernel (SPHR), ACL with inflow correction (CORR), linear-harmonic (LH), Bessel-Fourier (BF), Peters–He (PH).

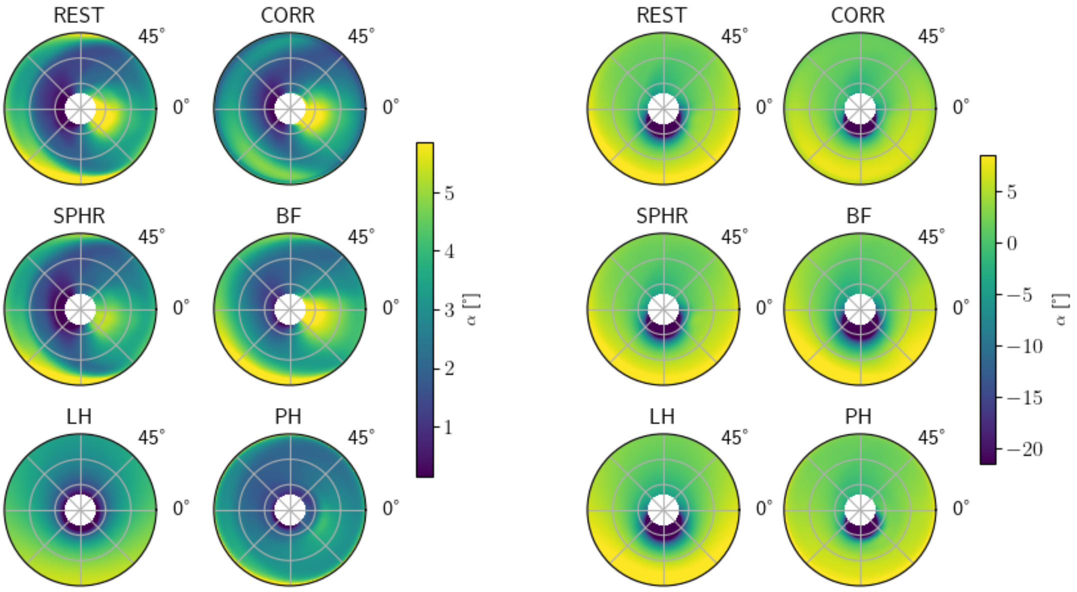

(a) $\mu = 0.08$

(b) $\mu = 0.29$

**Figure 73** Comparison of the angle of attack distribution for all inflow models for the experimental rotor in wind tunnel condition with $C_{\mathrm{TL},\%} = 11.1\%$ and a resolution of 64 cells per radius. ACL with restricted force kernel (REST), ACL with spherical force kernel (SPHR), ACL with inflow correction (CORR), linear-harmonic (LH), Bessel-Fourier (BF), Peters–He (PH).

base functions used in the coupling. However, despite these limitations integrated results were as accurate as the other models. The tip loss showed a stronger influence for the trends along the blade for the LBM inflow models than the Peters-He model. Considering the tip vortex forming in the flow field that yields higher lift with pure 2D airfoil tables in the upflow region this is reasonable. The trends of the angle of attack and the lift force over the whole disk were comparable between the ACL, Bessel-Fourier, and the well-established Peters–He inflow models showing that the LBM inflow is giving reasonable results. Overall, the LBM inflow requires a higher tip loss than the Peters-He model to get the best match with data. In conclusion, the results are satisfying for forward flight condition, with the exception of the power prediction.

### 5.1.3 Preliminary Findings

After simulating the experimental settings for hover and wind tunnel conditions and comparing against experimental measurements, the findings can be used to choose a set of parameters for the simulation of a rotor on a helicopter in service.

The power predictions for the hover results were within a bandwidth of -20% to +20% depending on the model and the chosen parameters. For a higher flow field resolution and a tip loss of 11% the LBM inflow models were within a ten percent bandwidth. In general, the Peters-He inflow model predicted a higher required power and was in a range of 10% to 20%. However, the exception for all models was for the lowest $C_T$ where the models had trouble to match results. For this trim condition, the ACL with the restricted kernel and the inflow correction also experienced stability issues that vanished with increasing $C_T$. The other models were stable for all conditions and flow field resolutions. The models with more degrees of freedom in the radial direction gave good agreement with radial measurements, the linear-harmonic showed clear deficits due to its constant radial thrust representation and the linearized inflow. Overall, considering the rectangular blade shape without twist that results in a heavily blade tip focused lift distribution the power and lift results were in good agreement.

The integral values for the wind tunnel conditions showed good agreement with respect to the blade flapping. The power predictions were far too high for all models with errors between +60% to +80% for the highest advance ratio. For the lowest advance ratio the Peters-He as well as the linear-harmonic model were not able to capture the total lift trend contrary to the other inflow models. With an increasing advance ratio, all models captured the trend of the blade lift but had offsets. The same is true for the radial and azimuth lift distribution, where the models with higher degrees of freedom were able to capture the trends, with shortcomings in the area where the blades experienced strong cross-flow conditions.

In summary, all models have comparable results for the integrated values such as power, flapping, and control input. Differences are visible for the lift distribution over the blade, where the linear-harmonic is not very accurate, and the Peters-He model tends to underpredict the lift peak, whereas the ACL and Bessel-Fourier models tend to overestimate the peaks. Agreement with measurements is visible, although shortcomings exist, and the LBM models tend to be closer to measurements than the Peters-He model. In the case of blade load predictions, the linear-harmonic model is not a good choice due to its limited flexibility. The power predictions for higher advance ratios were not good and will be examined for the next validation case. From the results so far, the following model parameters were estimated and put to test in the next section. The LBM results show convergence for a flow field resolution of 64 cells per radius and require a tip loss of around eight to ten percent, where the tip loss for the Peters-He should be around four percent. The ACL inflow model with the restricted force kernel will not be pursued further due to its stability problem.

## 5.2 UH60A Rotor results

For the UH60A rotor simulations, the parameter settings for grid resolution and $C_{\mathrm{tl},\%}$ were applied, which led to optimal results for the experimental rotor. The UH60A rotor was used because extensive experimental and flight test data is available. The resolution for the flow simulation was set to 64 cells per radius and the tip loss was chosen to nine percent for all LBM simulations. The Peters–He tip loss was set to four percent, the smallest value that did not result in numerical instability. The experimental data is from wind tunnel measurements taken from [93] and the air loads flight test program taken from [112]. The wind tunnel setting of the flow simulation was the same as for the experimental rotor from the section 5.1 scaled to the rotor radius of the UH60A rotor. The trim condition in this setting was trim to zero blade flapping and a given thrust. The flight test setting used the wind tunnel setup of the LBM simulation as well and the rotor was trimmed to measured hub moments and rotor thrust. For all conditions the corresponding forward flight speed was used as a free stream velocity input to the wind tunnel setting. The mechanical rotor model was adopted from [88]. The only ACL model considered is the one with the spherical kernel. The ACL with the restricted kernel gave similar results in the previous studies with the disadvantage of stability issues. The simulations of the ACL with inflow correction excitated the rotor and led to a divergence within the rotor dynamics solver. This issue was not present for the experimental rotor. A possible cause could be the flexible blades and the lead-lag motion of the UH60A that increase the possibility of numerical instability within the rotor solver.

In general, all models match the trends of the $\frac{C_P}{\sigma}$ measurements for both wind tunnel experiments and flight test (see Figure 74 and Figure 75). The Peters–He model's results agree well with flight test data, with an error of no more than -15% for the lowest advance ratio, and the rest of the results falling within a range of +/-6%. The error for the wind tunnel simulation results shows a linear increase in error as the advance ratio increases when comparing against the wind tunnel measurements, but it remains within a bandwidth of -10% to +20% where the largest error occurs at $\mu = 0.19$ and $\frac{C_T}{\sigma} = 0.09$. The flight test data agrees well at this speed, indicating that there may be wind tunnel effects in the measurements that were not modeled in the simulation.

The linear-harmonic model does not show a trend dependent on the advance ratio for either the wind tunnel measurements or the flight test results. The results for the wind tunnel simulations are in a steady bandwidth from zero to negative ten percent for all $\frac{C_T}{\sigma}$ values. The flight test predictions are lower and in a bandwidth of -15% to -8%. The comparison of the absolute values shows that the wind tunnel data has a fixed negative offset to the measurements. The trend for the power required in the flight tests is visible, but with increasing advance ratio the gradient of the simulation results is not as steep as for the actual data.

The results for the ACL with spherical force kernel show a variation of the relative power error for the flight test results. The error is within a bandwidth of +/- 10%. The measured data trend is met and the predictions are good for high advance ratios as well as low forward flight speeds. The wind tunnel results show a decreasing relative error with increasing advance ratio and the relative error increases in general with increasing $\frac{C_T}{\sigma}$. A possible source for this behavior is the influence of the wind tunnel walls in the simulation of the results. For low advance ratios where the wake is not washed out fast enough the top and bottom walls could have an impact on the results. The results for the Bessel-Fourier model show the same behavior as the ACL model. The major difference is the slightly narrower bandwidth of the error for the flight test results where the upper bound is below five percent rather than ten percent. Otherwise, the trends for the relative error and the absolute values are almost identical.

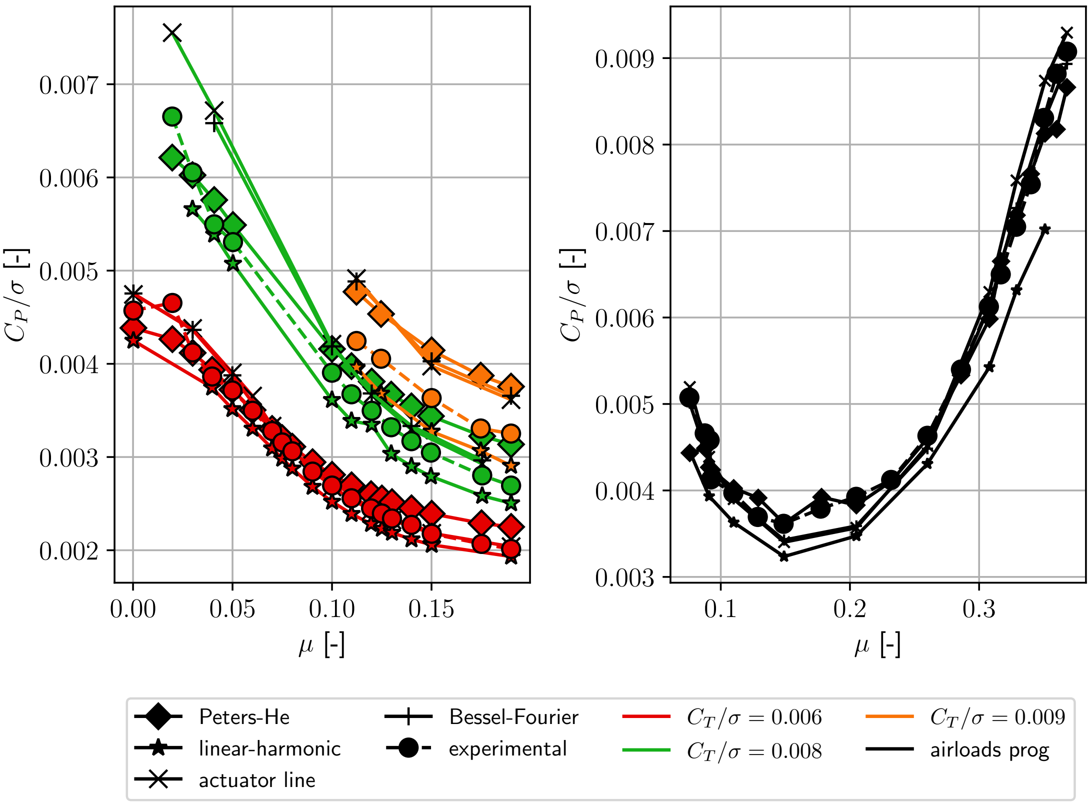

**Figure 74** UH60A rotor power results for all inflow models, experimental results from the air loads program (right) are taken from [93], wind tunnel measurements (left) from [112].

The longitudinal and lateral blade flapping results for the flight tests are depicted in Figure 76 for all simulation models. The experimental data experiences a decrease in lateral and longitudinal flap until $\mu = 0.10$. The lateral flap then steadily increases in a linear fashion with increasing advance ratio. The longitudinal flap increases linearly until $\mu = 0.21$ and then decreases again for higher $\mu$. The Peters–He model captures the decrease for the lateral flap but with a clear offset to the measurements. However, the following linear increase is not captured, but the flap angle is constant until $\mu = 0.21$ and then starts to linearly increase until it matches the measurements for $\mu > 0.35$. The longitudinal flap trend matches the measured data until its peak. After that the linear decrease is visible but with a higher gradient than the actual flight tests show. The ACL and the Bessel-Fourier model results are similar to the Peters–He results. The negative offset for the lateral flap up to $\mu = 0.15$ is smaller than for Peters–He. The longitudinal flap offset to measurements is lower overall, but the

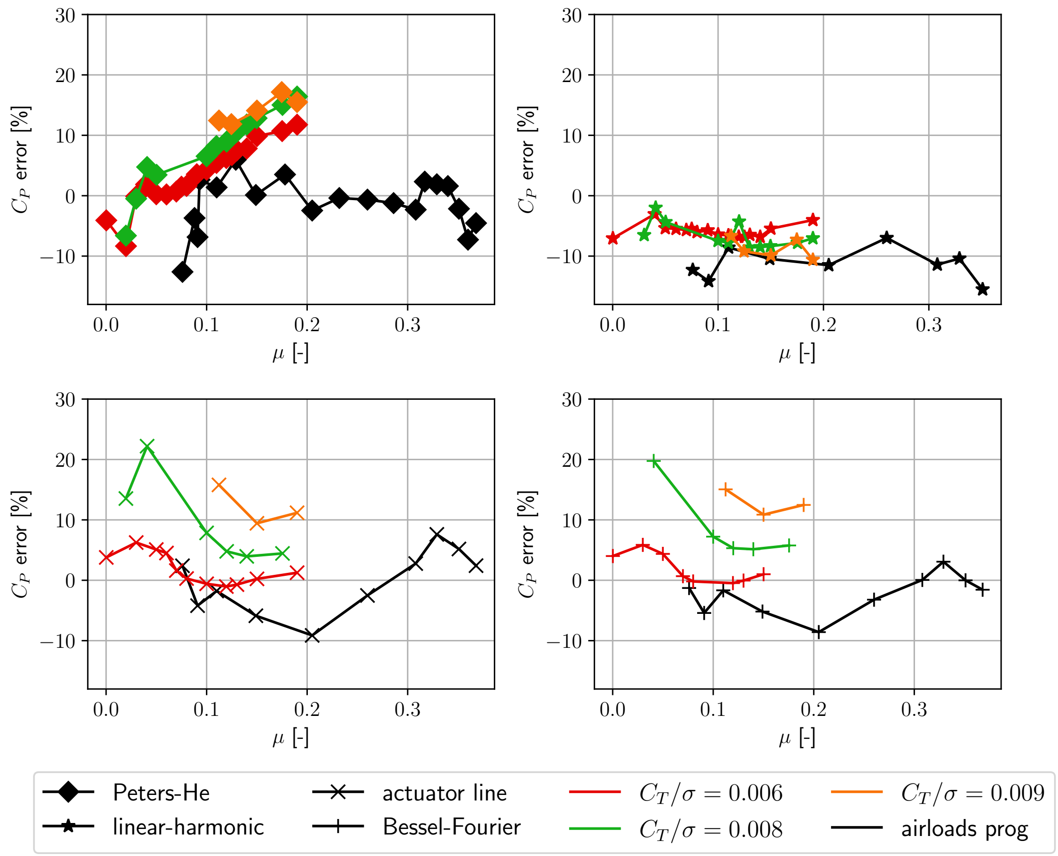

**Figure 75** Error in the power predictions for Peters–He, linear-harmonic, ACL and Bessel-Fourier inflow models (top left to bottom right). Experimental results from the air loads program are taken from Ref. [93], wind tunnel measurements from Ref. [112].

steeper gradient for higher advance ratios than the flight test data is still present. The linear-harmonic model represents the trend better for the lateral flap. The constant trend between $\mu = [0.10, 0.20]$ is not present for this inflow model. However, the increase is steeper than for the flight test data from $\mu = 0.20$ onward and therefore overpredicting the lateral flap at high $\mu$. The longitudinal flap is well represented until the peak, but with higher $\mu$ the descent is even steeper than for the other inflow models, resulting in higher offset for the highest considered advance ratios.

The feathering input at the blade root from flight tests and the simulation results are depicted in Figure 77. The results for the collective input exhibit good agreement with the measurements for all models. All models are within a bandwidth $< 0.5°$ except the linear harmonic that predicts an increasingly lower input for $\mu > 0.25$. This is in accordance with the power predictions where the gradient for power increase was not as steep as the measured data. The longitudinal input is well met for all models, including the peak at around $\mu = 0.10$. The linear-harmonic model inadequately represents the trend for the lateral input for $\mu < 0.10$ and $\mu > 0.25$. However, in between the flat trend for the lateral input is captured, although with a constant offset of 3°. This capture of the trend could explain the better performance of the lateral flap compared to the other models. The collective trend does not fully capture the slope

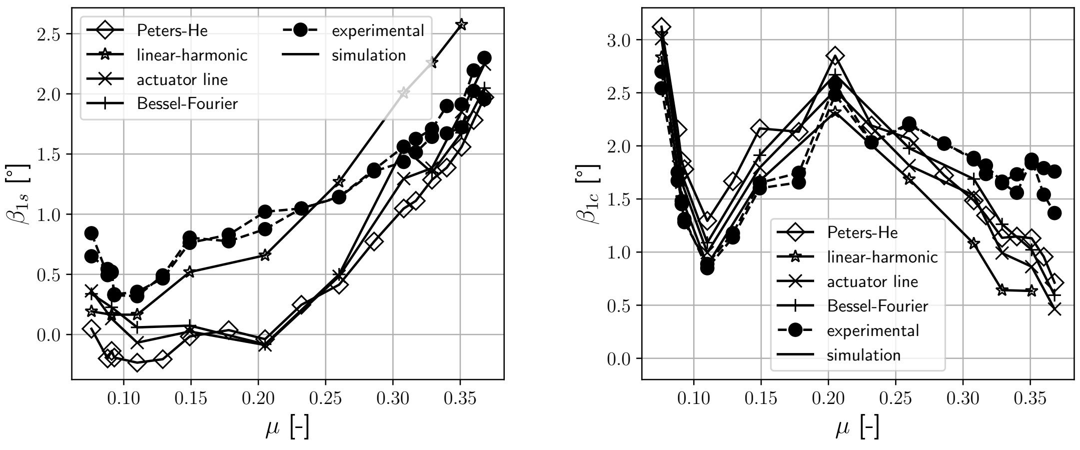

(a) Lateral flap (b) Longitudinal flap

**Figure 76** UH60A rotor blade flapping predictions compared against flight test data from the airloads program taken from Ref. [112].

at higher $\mu$ but is otherwise in agreement. The Peters-He model inadequately represents the trend for low values of $\mu$ but is otherwise on par with the Bessel-Fourier and actuator line models. However, for the intermediate advance ratios, the lateral input is predicted lower for these models as well.

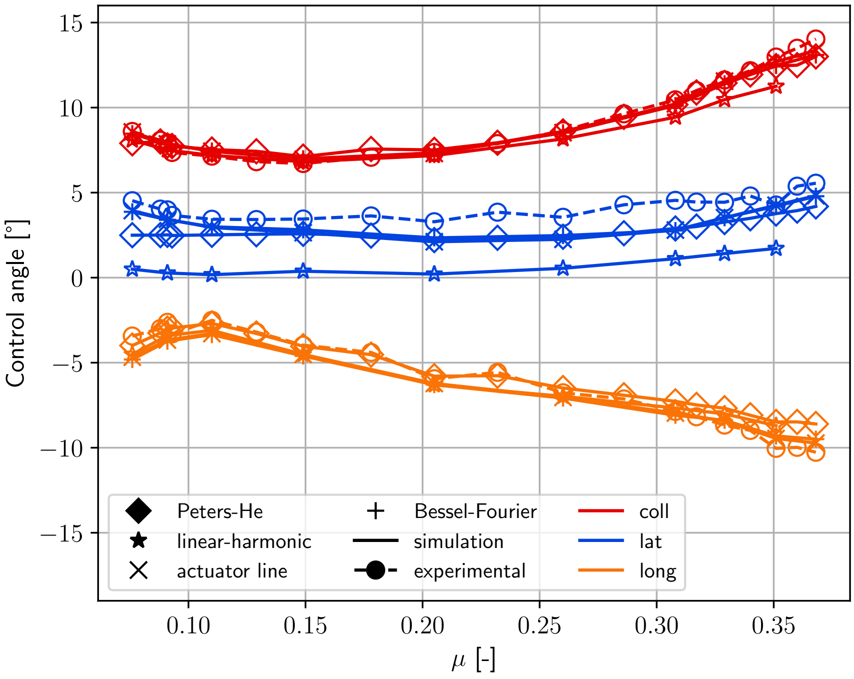

**Figure 77** UH60A rotor feathering input at the blade root for all inflow model simulations. Experimental results from the air loads program are taken from Ref. [112].

In general, the findings are satisfactory. The power predictions are in very good agreement over all models, although some uncertainty remains on the impact of wind tunnel effects on the experimental results. The flight test measurements, however, are for all advance ratios and all inflow models well met. All inflow models are within a comparable range for the integrated power. The better power predictions compared to the experimental rotor results show that the inflow models are not generally inadequate. The longitudinal flap predictions match the measurements from flight tests as well with a maximum deviation of approximately 1 ° for the advance ratios. The lateral flap has some shortcomings for the inflow models with higher degrees of freedom, whereas the linear-harmonic model shows good agreement with the data. The controls are well predicted for all models, with the exception of the linear-harmonic model, which shows a significant offset for the lateral input.

# 6. Application to Interaction Problems

The previous chapter presented validation results that show the capability of the LBM coupled inflow computation with respect to experimental hover and wind tunnel results and against real flight data. This chapter presents the application of the framework to interaction problems with the aim of comparing the rotor response depending on the coupling mode that was chosen. The first interaction problem considered is a simple vortex interaction where the rotor is flying through a straight vortex line. This case is also used to determine a minimal feasible domain size that minimizes the influence of the boundaries on the outside flow disturbances entering the simulation domain. The second interaction scenario models the approach of a rotor onto a moving ship.

The vortex interaction setup was already considered in a previous publication [44] in the context of this thesis. In this paper, a rotorcraft was flying in vortices of different strength and magnitude, and a comparison between the linear-harmonic and superposition coupling was done together with an investigation of the effect of the advance ratio on the results. The study found that the rotorcraft response is much stronger for the superposition than for the LBM coupled inflow computation for low advance ratios, but the differences reduce with increasing $\mu$. This is due to the reduced interaction between the rotor and the vortex, as with increasing flight speed, the time frame where potential interaction would happen is reduced. In simpler terms, the rotor passes the vortex before the inertia of the vortex is overcome.

A more complex scenario involving flight in a wind farm setting was considered as well [45]. In this publication, a rotorcraft was flying behind a wind turbine in a previously computed wind turbine wake using the linear-harmonic inflow model. The results showed a reasonable response of the helicopter although a validation against measurements is not possible. However, this encouraged the further pursuit of the LBM coupled inflow computation. This previous work laid the foundation for the ship deck landing approach to compare the inflow models. The ship approach was chosen because the flight speeds are lower than for a realistic scenario with flight in a wind farm environment, and the ship structure also includes a close-up interaction with the rotor wake.

## 6.1 Vortex Interaction

In this thesis the scenario vortex interaction scenario is analyzed with respect to the differences between all coupling modes. An exact repeat of the investigation in [44] is not possible because the used rotorcraft flight model is limited to eight blade elements and is therefore not capable of including the ACL or Bessel-Fourier coupling approach. The usage of the UH60 rotor model, where the rotor was moving forward with constant velocity, led to instabilities in the dynamic simulation even when the internal Peters-He inflow model was used without any additional flow. A reason for this behavior could not be determined. In order to reduce the influence of the mechanics side of the simulation, the experimental rotor from section 5.1 was used. The vortex line is horizontally oriented and perpendicular to the straightforward flight direction of the rotor. To account for the smaller rotor size the intensity of the vortex was adjusted with $\Gamma_0 = 44.5$ and the vortex core size $r_c = 0.5831$. The vortex is placed 40 meters ahead of the rotor hub and the rotor moves with a constant velocity of 7.5 m/s forward. This ensures that the rotor is far enough away to start without any vortex interference and the flight speed is slow enough to allow rotor vortex interaction. The rotor is trimmed to a given thrust and zero side forces. Besides the forward motion, all other degrees of freedom of the rotor shaft are restricted as no control law is available to keep the rotor on track. However, the controller tries to maintain the prescribed rotor forces. The boundary definitions are equal to the ones used in the previous publication and are described in section 4.3.

### 6.1.1 Domain Convergence

In the previous investigations, the size of the domain was chosen so that it is certain that the boundaries do not interfere. However, for a real flight scenario, the domain size should be as small as possible to keep computational runtimes low. Therefore, a domain size study was conducted where a base cube of four rotor radii edge length is considered and a scaling parameter s is used to scale the domain equally in all directions. The considered model was the linear-harmonic inflow coupling. The results for the domain size study are shown in Figure 78 and Figure 79 for the rotor forces and moments and the blade flap angles respectively. With the given forward speed and starting distance between the rotor hub and vortex center, the vortex center passes the hub after 5.33 seconds. Besides the interaction of rotor and vortex, this is still clearly visible in the variation of rotor forces and moments around this point in time. After reaching the trim condition at around $t = 3s$ the influence of the vortex becomes visible at around $t = 4s$. The rotor thrust shows a decrease in thrust and a following increase after the vortex core passes the rotor hub. Considering the rotation around the positive y-axis the rotor induces an additional downwash when encountering the rotor. Then, the vortex induces downwash and upwash, followed by a phase where only upward velocity is induced when the vortex leaves the rotor area. An increasing domain size reduces the minimum peak of the rotor forces, while the upshot is not significantly influenced by the domain size. The impact on the power reduction is comparable between all domain sizes with slight differences (<5%) in the for and aft power levels. The changes in $M_x$ are negliglible, $M_y$ peaks show a decrease with increasing domain size. The results for $s = 1.2$ show differences after the vortex encounter, which is due to an interaction of the outlet boundary and the vortex that affects the rotor area.

The effect of the vortex encounter on the blade flapping is similar for all domain sizes. The longitudinal blade flap shows a deviation after the vortex encounter but the differences are around 0.2°. Considering the modeling uncertainties this is negligible. The differences in the lateral flap are even smaller and not significant. As a result of this domain size study, a sizing factor of $s = 1.8$ was chosen, resulting in a cube of 7.2 rotor radii edge length.

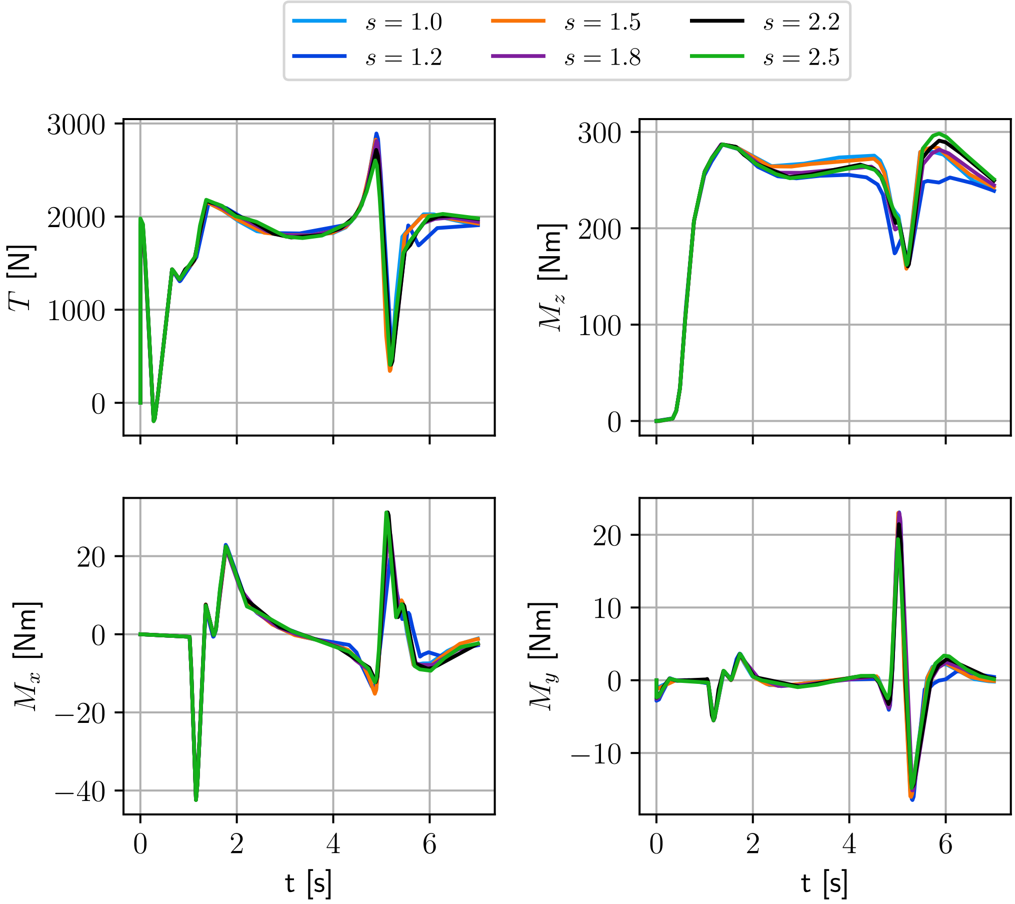

**Figure 78** Rotor forces and moments for different domain sizes computed by the linear-harmonic inflow model. Scaling factor s is based on the reference configuration of four rotor radii edge length of the cubic domain.

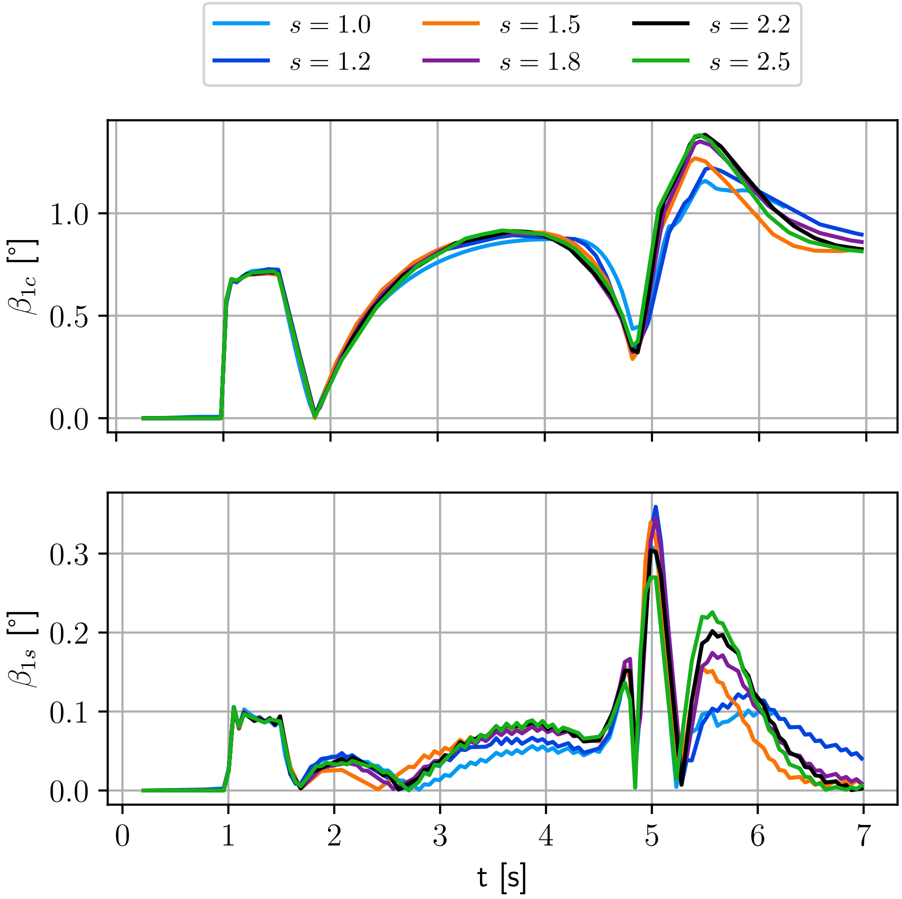

**Figure 79** Rotor lateral and longitudinal flap angles for different domain sizes computed by the linear-harmonic inflow model. Scaling factor s is based on the reference configuration of four rotor radii edge length of the cubic domain.

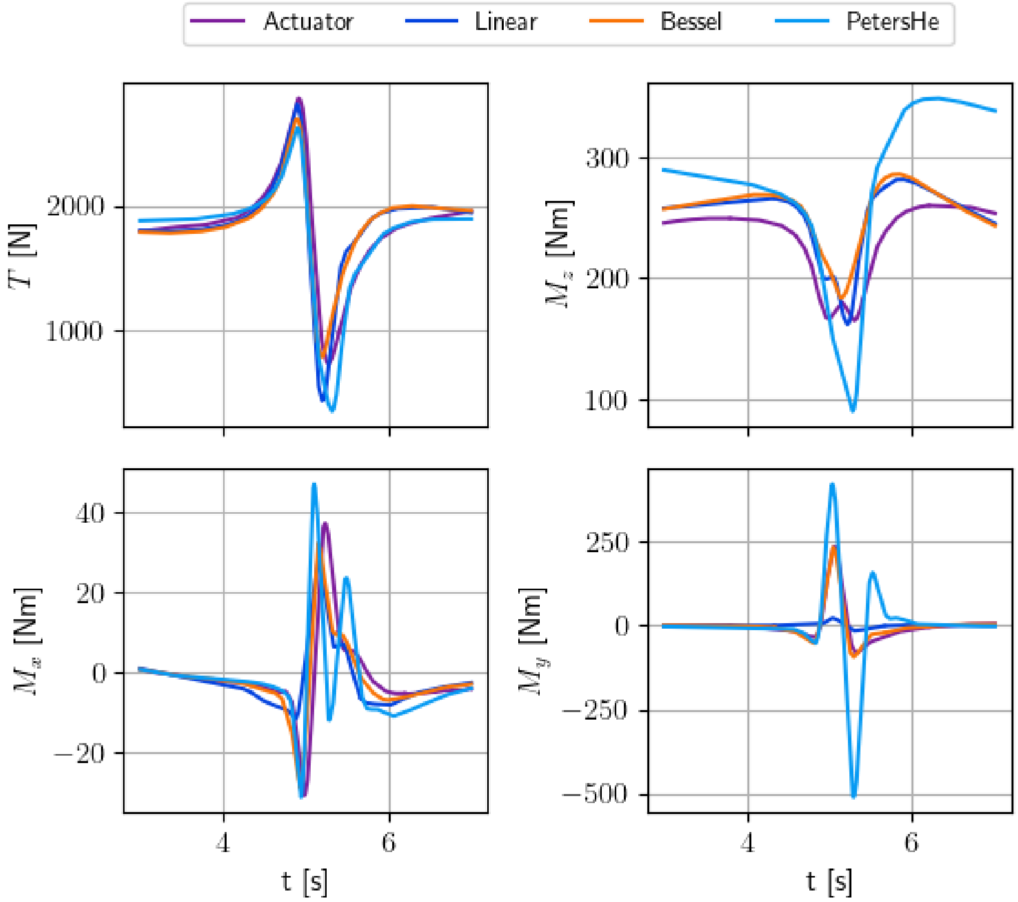

**Figure 80** Rotor forces and moments for all inflow models during a straight vortex line encounter. The vortex center passes the rotor hub at $t = 5.33\mathrm{s}$, notwithstanding interaction effects.

### 6.1.2 Model Comparison

After establishing the domain size used for all coupling modes, the vortex interaction is computed for each model, including the superposition with the Peters–He inflow. The results for the rotor thrust and moments are depicted in Figure 80. The trend for the rotor thrust is the same for all coupling modes. The lower peak is similar for the Bessel-Fourier and the Peters–He inflow as well as for the linear-harmonic and the ACL model, respectively. The peak for the latter coupling modes is thereby about 7% lower. The maximum peak is highest for the Peters–He and the linear-harmonic models, whereas the Bessel-Fourier and the ACL models have a lower value. The impact on the shaft moment is comparable for all LBM models but much higher for the Peters–He inflow model. The differences in $M_x$ are within the same order of magnitude, but the overall magnitude is low, and the small differences between the models therefore not relevant. In contrast, the impact on $M_y$ is present in the data with the strongest impact for the Peters–He model. The Bessel-Fourier and the ACL model show the same response, with the lower peak being an order of magnitude lower than the Peters–He one. The linear-harmonic model's response is an order of magnitude lower than the other models. The approximation used in this coupling acts as too strong a filter to show a distinct impact on the moments.

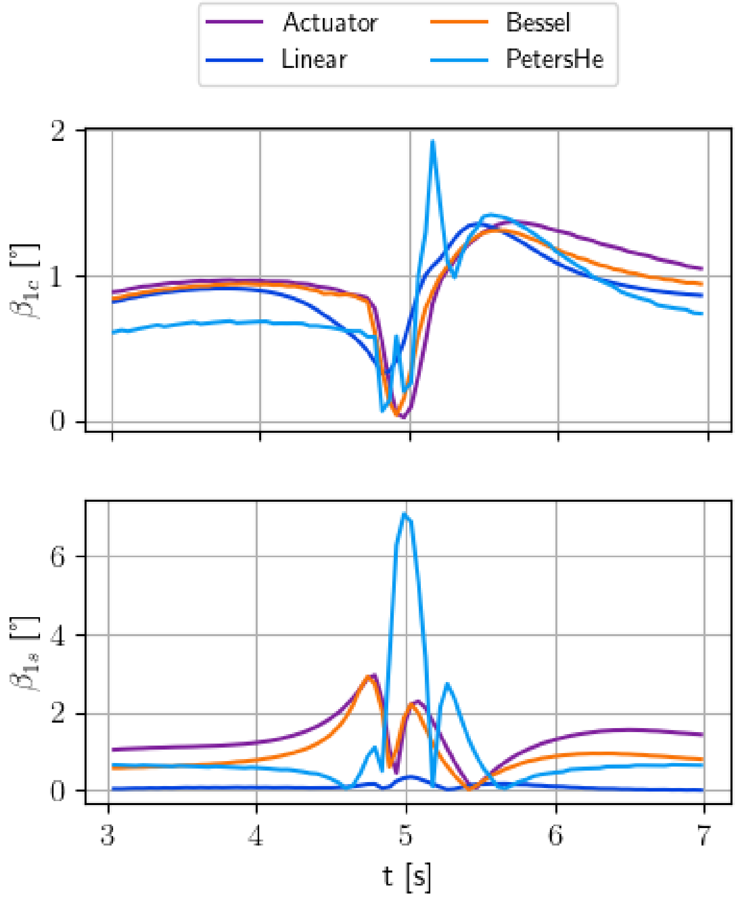

**Figure 81** Lateral and longitudinal blade flap angles for all inflow models during a straight vortex line encounter. The vortex center passes the rotor hub at $t = 5.33\text{s}$, notwithstanding interaction effects.

The longitudinal and lateral flap angles are depicted in Figure 81 for all models. The initial angles resulting from the trim are different depending on the inflow but the changes can still be compared. The effect of the vortex encounter on the longitudinal flap angle is comparable to all LBM inflow models, with the linear harmonic model experiencing an earlier but a more gentle response. The Peters–response is stronger and more sudden than for the LBM models due to the lack of increasing interaction when the vortex approaches the rotor disk. The lateral flap response for the linear-harmonic model is negligible which is in accordance with the rotor moments results. The Bessel-Fourier and the ACL inflow models show the same behavior and magnitude in the flap response. The Peters–He model shows a similar trend but the first peak has a much higher amplitude and the response shows a time delay compared to the other models.

The interaction of the LBM models with the vortex line is shown in Appendix B in Figure 102 to Figure 104. The visual output shows the approach of the vortex line and the rotor wake and the resulting strong interaction. The vortex peels off the wake in the disk and the mutual interaction leads to a distortion of the vortex line, where the position of the vortex moves below the rotor disk. This phenomenon is not present for the Peters–He superposition coupling and explains the stronger response compared to the LBM coupled inflow. While the interaction is comparable for all LBM models, the response for the linear-harmonic in terms of blade flap and rotor moments was a lot weaker. This is due to the strong filtering of the linear-harmonic base functions.

The application to a controlled interaction problem with a vortex line shows differences between the models for a singular large-scale disturbance. The results, although no validation data is available, show a plausible response with clear visibility of the filtering effect of the linear-harmonic approach and the missing interaction of the superposition approach.

## 6.2 Ship Approach

The second scenario where the LBM inflow models compute the additional effect of external flow conditions is the approach of a two-bladed teetering rotor onto a ship deck. As mentioned in the previous section no flight model of a helicopter is available that can capture the higher-order coupling models. Furthermore, no control law is available to stir the rotor along a given landing trajectory. Therefore, a simplified approach scenario was chosen, where the rotor is trimmed in steady wind conditions and then placed behind the ship in the ship wake while controls are held steady. The computation of the ship wakefield was not part of this thesis and was kindly provided by Bludau [11].

The approach trajectory is a straight and level flight path going over the landing deck of the ship until it reaches the ship hangar (see Figure 82). The ship itself experiences heave and roll motion, which are considered in the simulation as well but is otherwise at a stationary position. The ship wake is for a ship experiencing 22 m\s head wind and the rotor is flying with a steady velocity of 3.0 m\s towards the ship. The rotor is placed 35m behind the ship deck landing spot and 6m above. The simulation time is 15.5 seconds, meaning the rotor is flying beyond the landing point until the ship hangar on the landing deck is reached. Due to the strong disturbances, the original experimental rotor proved to be too small to fly stable without any control law or adjusted rotor parameters such as lock number or flap stiffness. As a result, the rotor was kept as a two-bladed teetering rotor with the same properties as the experimental rotor, but with an increased radius of 4.32 meters. Thereby, the disturbances did not lead to such a strong rotor response that would require a robust controller for the inputs.

Although the setup gives limited information with respect to a real helicopter approach, the integrated rotor data can be analyzed. The results for the thrust and the rotor power are depicted in Figure 83. The timeline starts at 2 seconds because placing the rotor in the actual wake after trim results in a phase where the wake washes through the simulation domain and leads to an exaggerated rotor response at first. One can see the disturbances of the ship wake affecting the rotor thrust and power consumption. The rotor starts to fly over the deck at around $t = 8s$. The LBM models responses are the same for the rotor thrust. The increase

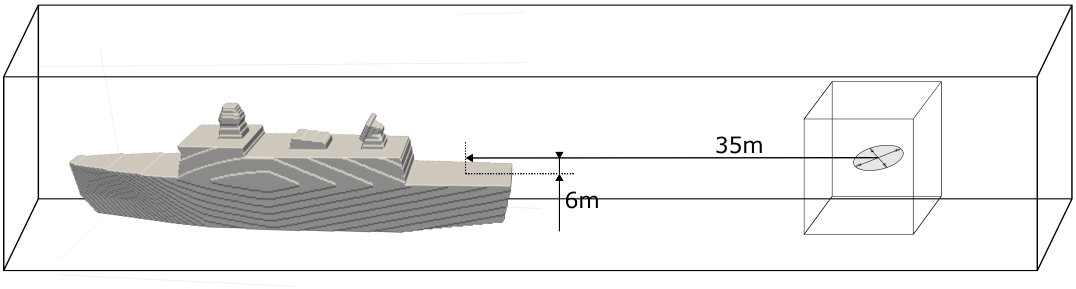

**Figure 82** Schematics of the ship and approach trajectory of the rotor with distance to and height above the deck landing point. The wake and rotor domain and their positioning are not to scale.

is visible as soon as the rotor starts to move above the landing deck. The increase is slightly lower for the linear-harmonic model, the ACL and Bessel-Fourier model experience the same amount of change. The Peters–He model does not show a significant change due to the inherently missing effect of the (partial-) ground effect. The power output does not show a strong response, but rather a slight increase above the deck is visible for the LBM models.

The interpretation of the hub moment signal in the time domain is not meaningful. There is no trend visible for the mean over time, and the high-frequency oscillation does not allow a signal-to-signal comparison in the time domain between the models. In the frequency domain, a comparison in the region of pilot-relevant frequencies is possible. High-frequency disturbances in the rotor forces lead to vibrations, which are felt by the pilot but do not trigger a pilot response as they are too fast to react to them. Therefore, the thrust and moments are depicted only up to 10Hz in Figure 84. The analysis shows that in the low-frequency domain up to 2Hz, all models show a similar amplitude. For higher frequencies the Peters–He inflow shows a multiple magnitudes lower response, whereas the LBM models all show a similar response.

The blade flap response for the first harmonic is depicted in Figure 85. The longitudinal flap is in a similar range for all models, with the linear harmonic showing fewer fluctuations over time. The lateral flap response shows a distinct change when the rotor is fully over the landing deck for the ACL and Bessel-Fourier model, while the linear-harmonic and the Peters–He do not show any response to the changed environment. While the Peters–He did not show any response in the rotor thrust either, this is not surprising. The linear-harmonic, on the other hand, did show a response in the thrust and is aware of a changing environment. However, the thrust is an integrated value that can match the other models' amplitude without a necessarily correct load and inflow distribution. The blade flap response, on the other hand, is dependent on catching the "correct" load distribution acting on the blade. Thus, the shortcomings of the linear-harmonic model with respect to the load distribution, as seen in the validation sections, lead to the reduced flap response when flying over the landing deck.

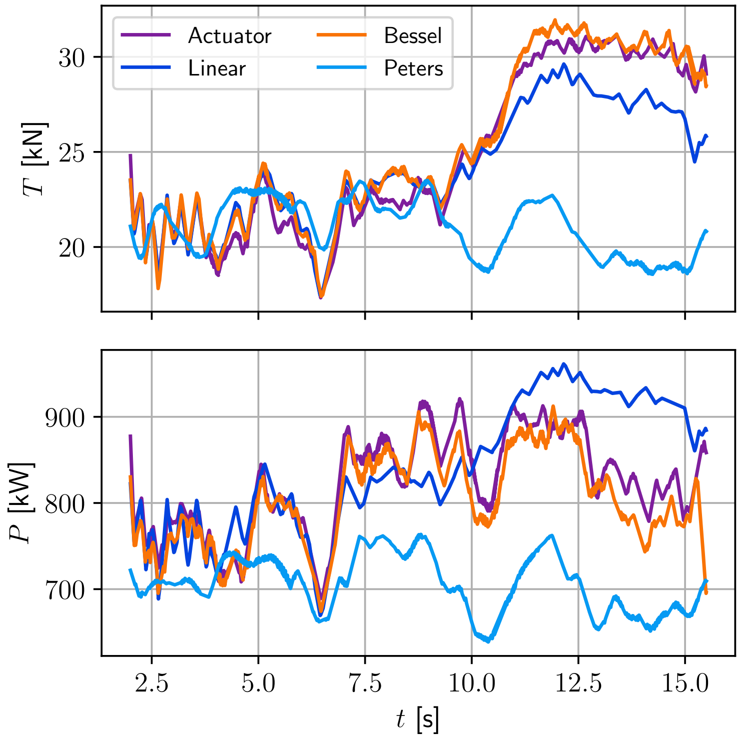

**Figure 83** Rotor thrust and power over the full ship approach for all inflow models. Time starts at $t = 2s$ when the ship wake has washed through the rotor simulation domain after trimming outside the wake.

In summary, the results show the impact of the surrounding flow disturbances as variations in power, rotor forces, and moments, as well as the blade flap. However, the response is not the same for all models. The Peters–He model with the superimposed velocity components does not have information about obstacles in its surroundings and does not show any change of behavior when flying above the landing deck. The LBM models show the influence of the landing deck with an increase in the rotor thrust in the absence of control input. The ACL and Bessel-Fourier model also show the effect of the landing deck in the later flap response. The linear-harmonic inflow model does not show an effect on the blade flap showing that an integral value like the rotor thrust is affected, but rotor responses depending on the load distribution suffer from the filtering effect on inflow and load distribution. The analysis of the frequency spectra of the hub moments shows a similar order of magnitude for the low-frequency domain, which is the most important when it comes to pilot response. Overall, the LBM models show that they not only capture the surrounding flow condition but also the impact of obstacles in the flow. The Peters–He model with the superposition captures the effect of the flow variations in a similar manner, but lacks the impact of the obstacles on the rotor wake.

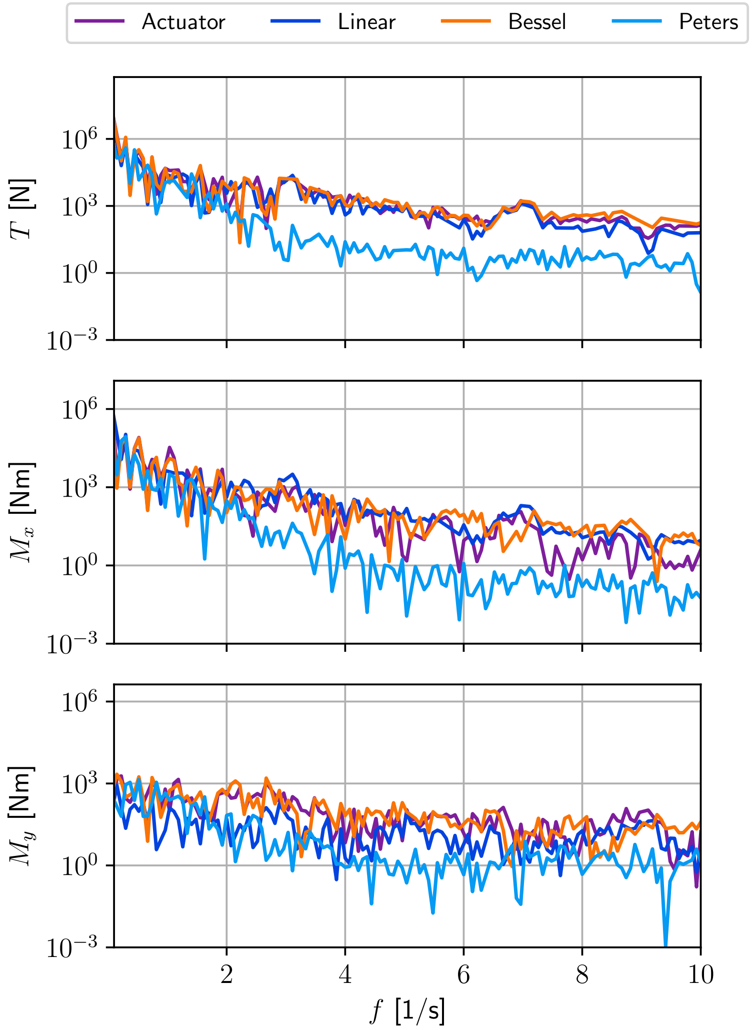

**Figure 84** Rotor thrust and moments in the frequency domain. The plot is cut off at 10Hz because only low-frequency modes are relevant for pilot control input.

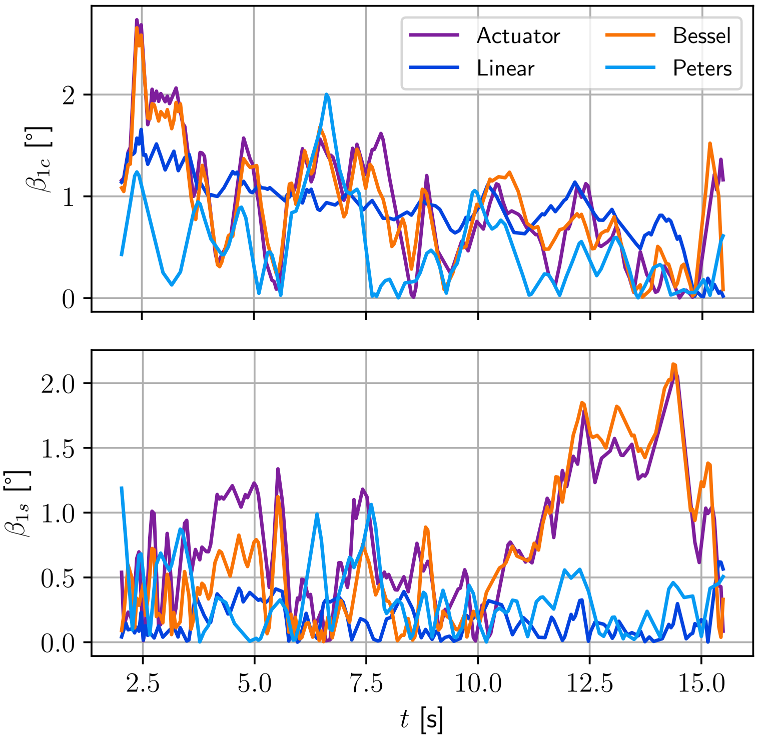

**Figure 85** Rotor lateral and longitudinal flap for all inflow models during the ship approach. Time starts at $t = 2s$ when the ship wake has washed through the rotor simulation domain after trimming outside the wake.

# 7. Summary and Conclusion

## 7.1 Summary

The aim of this thesis was to analyze rotor inflow models based on a Lattice-Boltzmann method based fluid solver that take into account the surrounding flow conditions and the rotor's interaction with its surroundings. Another aim was to use mid-fidelity modeling approaches in order to save computational time. This was achieved by modeling the rotor with an actuator disk and actuator line model instead of geometrically modeling the rotor blades. In summary, the following contributions to the modeling in the LBM solver were made:

- A new actuator disk model was introduced that is based on a previously published linear-harmonic actuator disk model but extended the formulation to the Bessel-Fourier actuator disk model that has additional degrees of freedom in the radial coordinate for inflow and rotor thrust.
- An actuator line model was implemented with a spherical and a restricted distribution of the blade forces. These were implemented according to literature.
- Two different inflow velocity sampling mechanisms were investigated which consisted of an integrated inflow sampling approach and an inflow correction approach.
- The incorporation of the environmental flow conditions and additional boundaries due to solid obstacles in the immediate rotor(craft) surroundings was realized by using a precomputed external flow field as boundary conditions for the rotor simulation domain.
- The well established Peters–He inflow model was used as comparison and a superposition of external flow velocity was employed to account for external flow conditions within the model.

The analysis of the inflow models was split into two parts. The first part validated the inflow models against experimental data. The second part was two different application scenarios where the inflow models were used in the context of a vortex encounter and a ship deck landing. The validation compared the different inflow models against experimental test data for a teetering rotor in hover and wind tunnel conditions. The simulation results were compared against power, control, and blade flap measurements, as well as radial lift distribution from pressure sensor data. The results for the experimental rotor in hover condition showed that all inflow models are able to capture the trends for power, blade flap, and the required control inputs. While the Peters–He overpredicted power consistently over all $C_T$ the actuator line models without inflow correction underpredicted power with increasing $C_T$. The actuator line and the Bessel-Fourier models were able to predict the radial load distribution. The linear-harmonic model is too restricted by its base functions and was not able to capture the load trends. The restricted force kernel and the inflow correction for the actuator line models did show instabilities at low $C_T$ and did not prove a robust modeling. The wind tunnel results showed a strong deviation of more than 60% in the power prediction for all inflow models and were not satisfying. Control inputs and blade flapping were consistent over all inflow models. The load distribution was satisfactorily predicted for the actuator line and the Bessel-Fourier models, followed by a degraded performance of the Peters–He model and, lastly, the linear-harmonic model. These results were used to determine a tip loss of 9% and a flow field resolution of 64 cells per radius necessary for the Lattice-Boltzmann method inflow models in order to gain optimal results. Furthermore, the actuator line models with the restricted force kernel and the inflow correction were not deemed useful due to their stability problems in hover and were not employed further. In a second validation step, the inflow models and the previously established simulation parameters were used to simulate a UH60A rotor. The results were compared against power measurements from wind tunnel investigations and control inputs, power measurements, and blade flap angles from conducted flight tests. The UH60A results showed a very good agreement with power measurements for all models for all advance ratios. The control angles were matched as well. For the flap response, the linear-harmonic model had improved results over the other inflow models, although the reason for this behavior could not be determined. However, overall lateral and longitudinal flap was comparable to measurements.

The comparative study of the inflow models for the vortex encounter scenario showed that all models exhibit a similar response with respect to rotor thrust. The impact on power was comparable for the Lattice-Boltzmann method models and much stronger for the Peters–He model with superposition. The impact on the pitch moment was clearly visible for the Bessel-Fourier and the actuator line model and much stronger for the Peters–He inflow. The linear-harmonic showed strong filtering behavior with barely visible impact on the roll moment. The rotor response in the ship wake showed similar behavior for all models until the rotor reached the landing platform. While the Peters–He showed no change in thrust and blade flap, the Lattice-Boltzmann method models showed an increase in thrust due to the blockage by the landing platform. Furthermore, the Bessel-Fourier and the actuator line model showed a change in the lateral blade flap response, the linear-harmonic however did filter that out as was the case for the vortex encounter.

## 7.2 Conclusion

Based on the results of this work from the validation and the application to flight in complex flow environments the following conclusions can be drawn:

- **Inflow prediction capability**
  The LBM inflow models perform equally or better than the Peters–He inflow model for two different rotor systems in both hover and forward flight conditions. In conclusion, they can be used to compute the inflow. The required model parameters of a tip loss of around 9% and a flow field resolution of 64 cells per radius are transferable between rotor systems

and are therefore recommended for future simulations.

- **Prediction of blade load distribution**
  The ACL models and the Bessel-Fourier actuator disk model both are able to predict radial loads over the blade allowing to use LBM for a more detailed rotor analysis when mid-fidelity methods are sufficient. The linear-harmonic does not provide correct information on that level of detail due to its limitation in the base functions.

- **Stability of ACL models**
  The inflow sampling and force distribution for the ACL methods play a major role with respect to numerical stability. A generally applicable approach independent of rotor loading and flight state proved to be a spherical force kernel with an integral inflow sampling. Aside from stability simulation results are not heavily dependent on the specific ACL approach.

- **Incorporation of external flow fields**
  In free flight with incorporation of an external flow field the Peters–He and the ACL and Bessel-Fourier inflow models show a comparable response, where the Peters–He response is stronger but in the same order of magnitude. The linear-harmonic model shows a heavily reduced flap and moment response. The Peters–He model with superposition proves sufficient in free-flight simulations.

- **Flight close to obstacles**
  In flight in the vicinity of obstacles such as landing platforms, the Peters–He response lacks the influence of the structures whereas all LBM take the effect into account and provide therefore a superior inflow model in such settings.

# 8. Outlook

The present work introduced the LBM based inflow modeling approach for flight in complex flow environments. This is not a final study and recommendations are made for future research in this area.

1. A validation against dynamic flight test data could prove advantageously to build confidence in the dynamic response of the rotorcraft when LBM is used as inflow.
2. A broader investigation of different rotors and comparison against measurements would support the claim of universal application.
3. The validation for more complex interaction configurations such as rotor-rotor and rotor-wing interaction would improve the modeling range of the LBM inflow.
4. Due to the lack of experimental data for complex mission scenarios with respect to the flow environment, a code-to-code comparison with other CFD methods would be beneficial to determine the advantages or shortcomings of the presented modeling approaches.

# Bibliography

[1] J. U. Ahmad. *Application of Rotor Disk Model in the OVERFLOW CFD Code*. Tech. rep. NASA/TM—20220005496. NASA, 2022.

[2] E. S. Bae and C. He. “On High Fidelity Modeling of Aerodynamic Interaction between Ship and Rotor”. In: *35th AIAA Applied Aerodynamics Conference*. Denver, Colorado, June 2017. DOI: `10.2514/6.2017-3051`. URL: `http://dx.doi.org/10.2514/6.2017-3051`.

[3] A. Bagai and J. G. Leishman. “Free-Wake Analysis of Tandem, Tilt-Rotor and Coaxial Rotor Configurations”. In: *Journal of the American Helicopter Society* 41.3 (July 1996), pp. 196–207. ISSN: 2161-6027. DOI: `10.4050/jahs.41.196`. URL: `http://dx.doi.org/10.4050/JAHS.41.196`.

[4] A. Bagai and J. G. Leishman. “Rotor Free-Wake Modeling Using a Pseudo-Implicit Technique — Including Comparisons with Experimental Data”. In: *Journal of the American Helicopter Society* 40.3 (July 1995), pp. 29–41. ISSN: 2161-6027. DOI: `10.4050/jahs.40.29`. URL: `http://dx.doi.org/10.4050/JAHS.40.29`.

[5] G. Barakos, T. Fitzgibbon, A. Kusyumov, S. KUSYUMOV, and S. Mikhailov. “CFD simulation of helicopter rotor flow based on unsteady actuator disk model”. In: *Chinese Journal of Aeronautics* 33.9 (2020), pp. 2313–2328. ISSN: 1000-9361. DOI: `https://doi.org/10.1016/j.cja.2020.03.021`. URL: `https://www.sciencedirect.com/science/article/pii/S1000936120301989`.

[6] O. Bauchau, C. Bottasso, and Y. Nikishkov. “Modeling rotorcraft dynamics with finite element multibody procedures”. In: *Mathematical and Computer Modelling* 33.10–11 (May 2001), pp. 1113–1137. ISSN: 0895-7177. DOI: `10.1016/s0895-7177(00)00303-4`. URL: `http://dx.doi.org/10.1016/S0895-7177(00)00303-4`.

[7] A. Betz. “Schraubenpropeller mit geringstem Energieverlust. Mit einem Zusatz von L. Prandtl”. In: *Nachrichten von der Gesellschaft der Wissenschaften zu Göttingen, Mathematisch-Physikalische Klasse* 1919 (1919), pp. 193–217.

[8] M. Bhagwat and J. Leishman. “Transient rotor inflow using a time-accurate free-vortex wake model”. In: *39th Aerospace Sciences Meeting and Exhibit*. Reno, NV, Jan. 2001. DOI: `10.2514/6.2001-993`. URL: `http://dx.doi.org/10.2514/6.2001-993`.

[9] P. L. Bhatnagar, E. P. Gross, and M. Krook. “A Model for Collision Processes in Gases. I. Small Amplitude Processes in Charged and Neutral One-Component Systems”. In: *Phys. Rev.* 94 (3 1954), pp. 511–525. DOI: `10.1103/PhysRev.94.511`. URL: `https://link.aps.org/doi/10.1103/PhysRev.94.511`.

[10] J Bludau, J Rauleder, and M Hajek. “Validation of a Dynamic Inflow Model Based on a Flight Dynamics Model and a Lattice-Boltzmann Fluid Solver Using Flight Test Data”. In: *43rd European Rotorcraft Forum*. Milan, Italy, 2017.

[11] J. Bludau. “Real-time simulation of the ship-rotorcraft dynamic interface using local recalculation with the Lattice-Boltzmann method”. PhD Thesis under review. Technical University of Munich, 2024.

[12] J. Bludau, M. Hajek, and J. Rauleder. “Solving the Ship-Rotorcraft Dynamic Interface Problem Using Lattice-Boltzmann Aerodynamics Two-Way Coupled with Blade Element Based Flight Dynamics”. In: *Proceedings of the Vertical Flight Society 77th Annual Forum*. Virtual: The Vertical Flight Society, May 2021. DOI: `10.4050/f-0077-2021-16725`. URL: `http://dx.doi.org/10.4050/F-0077-2021-16725`.

[13] J. Bludau, J. Rauleder, L. Friedmann, and M. Hajek. “Real-Time Simulation of Dynamic Inflow Using Rotorcraft Flight Dynamics Coupled With a Lattice-Boltzmann Based Fluid Simulation”. In: *55th AIAA Aerospace Sciences Meeting, AIAA SciTech*. Grapewine, TX, 2017.

[14] D. D. Boyd Jr. “Rotor/fuselage unsteady interactional aerodynamics: a new computational model”. PhD thesis. Virginia Polytechnic Institute and State University, 1999.

[15] D. D. j. Boyd and R. Barnwell. “Rotor-Fuselage Interactional Aerodynamics: An Unsteady Rotor Model”. In: *American Helicopter Society 54th Annual Forum*. Washington D.C., May 1998.

[16] R. E. Brown. “Rotor Wake Modeling for Flight Dynamic Simulation of Helicopters”. In: *AIAA Journal* 38.1 (Jan. 2000), pp. 57–63. ISSN: 1533-385X. DOI: `10.2514/2.922`. URL: `http://dx.doi.org/10.2514/2.922`.

[17] R. E. Brown and A. J. Line. “Efficient High-Resolution Wake Modeling Using the Vorticity Transport Equation”. In: *AIAA Journal* 43.7 (July 2005), pp. 1434–1443. ISSN: 1533-385X. DOI: `10.2514/1.13679`. URL: `http://dx.doi.org/10.2514/1.13679`.

[18] R. E. Brown and G. R. Whitehouse. “Modelling Rotor Wakes in Ground Effect”. In: *Journal of the American Helicopter Society* 49.3 (July 2004), pp. 238–249. ISSN: 2161-6027. DOI: `10.4050/jahs.49.238`. URL: `http://dx.doi.org/10.4050/JAHS.49.238`.

[19] N. Cao, S. Chen, S. Jin, and D. Martínez. “Physical symmetry and lattice symmetry in the lattice Boltzmann method”. In: *Phys. Rev. E* 55 (1 1997), R21–R24. DOI: `10.1103/PhysRevE.55.R21`. URL: `https://link.aps.org/doi/10.1103/PhysRevE.55.R21`.

[20] M. S. Chaffin and J. D. Berry. “Helicopter Fuselage Aerodynamics Under a Rotor by Navier-Stokes Simulation”. In: *Journal of the American Helicopter Society* 42.3 (1997), pp. 235–243.

[21] S. Chen and G. D. Doolen. “LATTICE BOLTZMANN METHOD FOR FLUID FLOWS”. In: *Annual Review of Fluid Mechanics* 30.1 (Jan. 1998), pp. 329–364. ISSN: 1545-4479. DOI: `10.1146/annurev.fluid.30.1.329`. URL: `http://dx.doi.org/10.1146/annurev.fluid.30.1.329`.

[22] J. J. Chiew and M. J. Aftosmis. “Efficient Simulation of Multi-rotor Vehicles with Low Reynolds Number Propellers”. In: *2018 Applied Aerodynamics Conference*. Atlanta, GA, June 2018. DOI: `10.2514/6.2018-4119`. URL: `http://dx.doi.org/10.2514/6.2018-4119`.

[23] J. J. Chiew and M. J. Aftosmis. “Integral Velocity Sampling for Unsteady Rotor Models on Cartesian Meshes”. In: *AIAA AVIATION 2021 FORUM*. Virtual, Jan. 2021. DOI: `10.2514/6.2021-2624`. URL: `https://arc.aiaa.org/doi/abs/10.2514/6.2021-2624`.

[24] J. Chiew and M. J. Aftosmis. “A conservative, scalable, space-time blade element rotor model for multi-rotor vehicles”. In: *AHS Technical Conference on Aeromechanics Design for Transformative Vertical Flight*. ARC-E-DAA-TN45938. San Francisco, CA, May 14-17, 2018.

[25] J. Chiew, M. Aftosmis, and K. L. Manies. “Medium-Fidelity CFD Modeling of Multicopter Wakes for Airborne Sensor Measurements”. In: *78th Annual Vertical Flight Society Forum and Technology Display*. Ft. Worth, Texas, May 10–12, 2022.

[26] M. J. Churchfield, S. Lee, J. Michalakes, and P. J. Moriarty. “A numerical study of the effects of atmospheric and wake turbulence on wind turbine dynamics”. In: *Journal of Turbulence* 13 (2012), N14. DOI: `10.1080/14685248.2012.668191`. eprint: `https://doi.org/10.1080/14685248.2012.668191`. URL: `https://doi.org/10.1080/14685248.2012.668191`.

[27] M. J. Churchfield, S. J. Schreck, L. A. Martinez, C. Meneveau, and P. R. Spalart. “An Advanced Actuator Line Method for Wind Energy Applications and Beyond”. In: *35th Wind Energy Symposium*. Grapevine, TX, Jan. 2017. DOI: `10.2514/6.2017-1998`. URL: `http://dx.doi.org/10.2514/6.2017-1998`.

[28] A. Coyle and B. Thornber. “Actuator Surface Model and Blade Resolved Simulations of an Attack Reconnaissance Class Rotor in Hover and Forward Flight”. In: *49th European Rotorcraft Forum*. Bueckeburg, Germany, Sept. 2023.

[29] C. Crozon, R. Steijl, and G. N. Barakos. “Numerical Study of Helicopter Rotors in a Ship Airwake”. In: *Journal of Aircraft* 51.6 (Nov. 2014), pp. 1813–1832. ISSN: 1533-3868. DOI: `10.2514/1.c032535`. URL: `http://dx.doi.org/10.2514/1.C032535`.

[30] K. O. Dağ and J. N. Sørensen. “A new tip correction for actuator line computations”. In: *Wind Energy* 23.2 (Nov. 2019), pp. 148–160. ISSN: 1099-1824. DOI: `10.1002/we.2419`. URL: `http://dx.doi.org/10.1002/we.2419`.

[31] J. Donea, A. Huerta, J. Ponthot, and A. Rodríguez-Ferran. “Arbitrary-Lagrangian–Eulerian Methods”. In: *Encyclopedia of Computational Mechanics* (2004). DOI: `10.1002/0470091355.ecm009`. URL: `http://dx.doi.org/10.1002/0470091355.ecm009`.

[32] B. Dorschner, S. Chikatamarla, F. Bösch, and I. Karlin. "Grad's approximation for moving and stationary walls in entropic lattice Boltzmann simulations". In: *Journal of Computational Physics* 295 (Aug. 2015), pp. 340–354. ISSN: 0021-9991. DOI: `10.1016/j.jcp.2015.04.017`. URL: `http://dx.doi.org/10.1016/j.jcp.2015.04.017`.

[33] L. L. Erickson. *Panel methods: An introduction*. NASA Technical Paper 2995. National Aeronautics and Space Administration, 1990.

[34] O. Filippova and D. Hänel. "Grid Refinement for Lattice-BGK Models". In: *Journal of Computational Physics* 147.1 (Nov. 1998), pp. 219–228. ISSN: 0021-9991. DOI: `10.1006/jcph.1998.6089`. URL: `http://dx.doi.org/10.1006/jcph.1998.6089`.

[35] J. R. Forsythe, E. Lynch, S. Polsky, and P. Spalart. "Coupled Flight Simulator and CFD Calculations of Ship Airwake using Kestrel". In: *53rd AIAA Aerospace Sciences Meeting*. Kissimmee, FL, Jan. 2015. DOI: `10.2514/6.2015-0556`. URL: `http://dx.doi.org/10.2514/6.2015-0556`.

[36] L Friedmann, P Ohmer, and M Hajek. "Real-time simulation of rotorcraft downwash in proximity of complex obstacles using grid-based approaches". In: *AHS 70th Annual Forum*. Montréal, Québec, CAN, May 2014.

[37] U. Frisch, B. Hasslacher, and Y. Pomeau. "Lattice-Gas Automata for the Navier-Stokes Equation". In: *Phys. Rev. Lett.* 56 (14 1986), pp. 1505–1508. DOI: `10.1103/PhysRevLett.56.1505`. URL: `https://link.aps.org/doi/10.1103/PhysRevLett.56.1505`.

[38] Z. Guo, C. Zheng, and B. Shi. "Discrete lattice effects on the forcing term in the lattice Boltzmann method". In: *Phys. Rev. E* 65 (4 2002), p. 046308. DOI: `10.1103/PhysRevE.65.046308`. URL: `https://link.aps.org/doi/10.1103/PhysRevE.65.046308`.

[39] D. Hänel. *Molekulare Gasdynamik: Einführung in die kinetische Theorie der Gase und Lattice-Boltzmann-Methoden*. Springer-Verlag, 2006.

[40] C. He and J. Zhao. "Modeling Rotor Wake Dynamics with Viscous Vortex Particle Method". In: *AIAA Journal* 47.4 (Apr. 2009), pp. 902–915. ISSN: 1533-385X. DOI: `10.2514/1.36466`. URL: `http://dx.doi.org/10.2514/1.36466`.

[41] X. He, Q. Zou, L.-S. Luo, and M. Dembo. "Analytic solutions of simple flows and analysis of nonslip boundary conditions for the lattice Boltzmann BGK model". In: *Journal of Statistical Physics* 87.1–2 (Apr. 1997), pp. 115–136. ISSN: 1572-9613. DOI: `10.1007/bf02181482`. URL: `http://dx.doi.org/10.1007/BF02181482`.

[42] S. J. Hodge, S. J. Zan, D. M. Roper, G. D. Padfield, and I. Owen. "Time-Accurate Ship Airwake and Unsteady Aerodynamic Loads Modeling for Maritime Helicopter Simulation". In: *Journal of the American Helicopter Society* 54.2 (Apr. 2009), pp. 22005–2200516. ISSN: 2161-6027. DOI: `10.4050/jahs.54.022005`. URL: `http://dx.doi.org/10.4050/JAHS.54.022005`.

[43] B. Horvat and I. Yavrucuk. "Validation of a Mid-Fidelity CFD/CSD Coupling using the Lattice-Boltzmann Method". In: *49th European Rotorcraft Forum*. Bueckeburg, Germany, Sept. 2023.

[44] B. Horvat, M. Hajek, and J. Rauleder. “Analysing Rotorcraft Vortex Encounter Methods with a Lattice-Boltzmann Method Based GPU Framework”. In: *AIAA Scitech 2020 Forum*. Orlando, FL, Jan. 2020. DOI: `10.2514/6.2020-0539`. URL: `http://dx.doi.org/10.2514/6.2020-0539`.

[45] B. Horvat, M. Hajek, and J. Rauleder. “Computational Flight Path Analysis of a Helicopter in an Offshore Wind Farm using a Lattice-Boltzmann Method”. In: *AIAA Scitech 2021 Forum*. Virtual, Jan. 2021. DOI: `10.2514/6.2021-1827`. eprint: `https://arc.aiaa.org/doi/pdf/10.2514/6.2021-1827`. URL: `https://arc.aiaa.org/doi/abs/10.2514/6.2021-1827`.

[46] P. K. Jha, M. J. Churchfield, P. J. Moriarty, and S. Schmitz. “Guidelines for Volume Force Distributions Within Actuator Line Modeling of Wind Turbines on Large-Eddy Simulation-Type Grids”. In: *Journal of Solar Energy Engineering* 136.3 (Jan. 2014), p. 031003. ISSN: 0199-6231. DOI: `10.1115/1.4026252`. eprint: `https://asmedigitalcollection asme.org/solarenergyengineering/article-pdf/136/3/031003/6869367/sol\_136\_03\_031003.pdf`. URL: `https://doi.org/10.1115/1.4026252`.

[47] P. K. Jha and S. Schmitz. “Actuator curve embedding – an advanced actuator line model”. In: *Journal of Fluid Mechanics* 834 (2018), R2. DOI: `10.1017/jfm.2017.793`.

[48] W. Johnson. “A general free wake geometry calculation for wings and rotors”. In: *AHS 51st Annual Forum*. Fort Worth, TX, May 1995.

[49] W. Johnson. *Helicopter theory*. Courier Corporation, 2012.

[50] W. Johnson. *Rotorcraft Aeromechanics*. Cambridge University Press, Apr. 2013. ISBN: 9781139235655. DOI: `10.1017/cbo9781139235655`. URL: `http://dx.doi.org/10.1017/CBO9781139235655`.

[51] E. Jost, L. Klein, H. Leipprand, T. Lutz, and E. Krämer. “Extracting the angle of attack on rotor blades from CFD simulations”. In: *Wind Energy* 21.10 (June 2018), pp. 807–822. ISSN: 1099-1824. DOI: `10.1002/we.2196`. URL: `http://dx.doi.org/10.1002/we.2196`.

[52] J. Keller, D. Wachspress, and J. Hoffler. “Pilot Evaluation of a Real-Time Free Wake Model in a Navy Rotorcraft Fleet Trainer”. In: *73rd Annual Forum of the American Helicopter Society*. Fort Worth, Texas, May 2017.

[53] J. Keller, D. Wachspress, and J. Hoffler. “Real Time Free Wake and Ship Airwake Model for Rotorcraft Flight Training Applications”. In: *71st Annual Forum of the American Helicopter Society*. Virginia Beach, VA, 2015.

[54] J. Keller, D. Wachspress, J. Hoffler, N. Kachman, and J Nichols. “Application of a real time free wake induced velocity model in a Naval rotorcraft flight trainer”. In: *67th Annual Forum of the American Helicopter Society*. Virginia Beach, VA, May 2011, pp. 3–5.

[55] J. D. Keller et al. “Computational fluid dynamics for flight simulator ship airwake modeling”. In: *Interservice/Industry Training, Simulation, and Education Conference (I/ITSEC) 2007*. Orlando, FL, 2007.

[56] M. J. Krause, F. Klemens, T. Henn, R. Trunk, and H. Nirschl. “Particle flow simulations with homogenised lattice Boltzmann methods”. In: *Particuology* 34 (Oct. 2017), pp. 1–13. ISSN: 1674-2001. DOI: `10.1016/j.partic.2016.11.001`. URL: `http://dx.doi.org/10.1016/j.partic.2016.11.001`.

[57] S. Kumar, J. Rauleder, and I. Yavrucuk. “Towards Active Rotor Analysis using Viscous Vortex Particle Method”. en. In: *49th European Rotorcraft Forum*. Bueckeburg, Germany, Sept. 2023.

[58] A. J. C. Ladd. “Numerical simulations of particulate suspensions via a discretized Boltzmann equation. Part 1. Theoretical foundation”. In: *Journal of Fluid Mechanics* 271 (July 1994), pp. 285–309. ISSN: 1469-7645. DOI: `10.1017/s0022112094001771`. URL: `http://dx.doi.org/10.1017/S0022112094001771`.

[59] P. Lallemand and L.-S. Luo. “Theory of the lattice Boltzmann method: Dispersion, dissipation, isotropy, Galilean invariance, and stability”. In: *Phys. Rev. E* 61 (6 2000), pp. 6546–6562. DOI: `10.1103/PhysRevE.61.6546`. URL: `https://link.aps.org/doi/10.1103/PhysRevE.61.6546`.

[60] B. Lawrence and G. D. Padfield. “Wake vortex encounter severity for rotorcraft in final approach”. In: *Aerospace Science and Technology* 12.5 (July 2008), pp. 385–397. ISSN: 1270-9638. DOI: `10.1016/j.ast.2007.09.006`. URL: `http://dx.doi.org/10.1016/j.ast.2007.09.006`.

[61] H. Lee, B. Sengupta, M. S. Araghizadeh, and R. S. Myong. “Review of vortex methods for rotor aerodynamics and wake dynamics”. In: *Advances in Aerodynamics* 4.1 (May 2022). ISSN: 2524-6992. DOI: `10.1186/s42774-022-00111-3`. URL: `http://dx.doi.org/10.1186/s42774-022-00111-3`.

[62] G. J. Leishman. *Principles of helicopter aerodynamics*. Cambridge university press, 2006.

[63] J. G. Leishman, M. J. Bhagwat, and A. Bagai. “Free-Vortex Filament Methods for the Analysis of Helicopter Rotor Wakes”. In: *Journal of Aircraft* 39.5 (Sept. 2002), pp. 759–775. ISSN: 1533-3868. DOI: `10.2514/2.3022`. URL: `http://dx.doi.org/10.2514/2.3022`.

[64] J. W. Lim, Y. H. Yu, and W. Johnson. “Calculation of Rotor Blade-Vortex Interaction Airloads Using a Multiple-Trailer Free-Wake Model”. In: *Journal of Aircraft* 40.6 (Nov. 2003), pp. 1123–1130. ISSN: 1533-3868. DOI: `10.2514/2.7200`. URL: `http://dx.doi.org/10.2514/2.7200`.

[65] M. Linder, M. K. Yurt, J. John, and I. Yavrucuk. “Development of a Mid-Fidelity Aeroelastic Coupling Framework for Analyzing Rotor-Airframe Interactions”. en. In: *49th European Rotorcraft Forum*. Bueckeburg, Germany, Sept. 2023.

[66] D. Linton, G. Barakos, R. Widjaja, and B. Thornber. “Coupling of an Unsteady Aerodynamics Model with a Computational Fluid Dynamics Solver”. In: *AIAA Journal* 56.8 (Aug. 2018), pp. 3153–3166. ISSN: 1533-385X. DOI: `10.2514/1.j056784`. URL: `http://dx.doi.org/10.2514/1.J056784`.

[67] D. Linton and B. Thornber. “An Actuator Surface Method for Ship-Helicopter Dynamic Interface Simulations”. In: *AIAA Scitech 2021 Forum*. Virtual, Jan. 2021. DOI: `10.2514/6.2021-1828`. eprint: `https://arc.aiaa.org/doi/pdf/10.2514/6.2021-1828`. URL: `https://arc.aiaa.org/doi/abs/10.2514/6.2021-1828`.

[68] S. M. Makinen. “Applying dynamic wake models to large swirl velocities for optimal propellers”. PhD thesis. Washington University in Saint Louis, Missouri, Jan. 2005.

[69] P. B. Martin and G. J. Leishman. “Trailing Vortex Measurements in the Wake of a Hovering Rotor Blade with Various Tip Shapes”. In: *58th AHS International Annual Forum, Montréal Canada*. June 11-13, 2002.

[70] L. A. Martínez-Tossas and C. Meneveau. “Filtered lifting line theory and application to the actuator line model”. In: *Journal of Fluid Mechanics* 863 (2019), pp. 269–292.

[71] R. Mei, L.-S. Luo, and W. Shyy. “An Accurate Curved Boundary Treatment in the Lattice Boltzmann Method”. In: *Journal of Computational Physics* 155.2 (1999), pp. 307–330. ISSN: 0021-9991. DOI: `https://doi.org/10.1006/jcph.1999.6334`. URL: `https://www.sciencedirect.com/science/article/pii/S0021999199963349`.

[72] P. Melani, F Balduzzi, and A Bianchini. “Simulating tip effects in vertical-axis wind turbines with the actuator line method”. In: *Journal of Physics: Conference Series* 2265.3 (May 2022), p. 032028. ISSN: 1742-6596. DOI: `10.1088/1742-6596/2265/3/032028`. URL: `http://dx.doi.org/10.1088/1742-6596/2265/3/032028`.

[73] M Meldi, E Vergnault, and P. Sagaut. “An arbitrary Lagrangian–Eulerian approach for the simulation of immersed moving solids with Lattice Boltzmann Method”. In: *Journal of Computational Physics* 235 (2013), pp. 182–198.

[74] D. J. O’Brien and M. Smith. “Understanding the Physical Implications of Approximate Rotor Methods Using an Unstructured CFD Method”. In: *Proceedings of the 31st European Rotorcraft Forum*. Florence, Italy, Sept. 2005.

[75] B. Oates, P. Su, J. Hrynuk, M. Smith, and J. Rauleder. “Evaluation of a Range of Modeling Approaches for UAV Unsteady Aerodynamics”. In: *49th European Rotorcraft Forum*. Bueckeburg, Germany, Sept. 2023.

[76] G. D. Padfield and G. P. Turner. “Helicopter encounters with aircraft vortex wakes”. In: *The Aeronautical Journal* 105.1043 (Jan. 2001), pp. 1–8. ISSN: 2059-6464. DOI: `10.1017/s0001924000095920`. URL: `http://dx.doi.org/10.1017/S0001924000095920`.

[77] G. D. Padfield, B. Manimala, and G. P. Turner. “A Severity Analysis for Rotorcraft Encounters with Vortex Wakes”. In: *Journal of the American Helicopter Society* 49.4 (Oct. 2004), pp. 445–456. ISSN: 2161-6027. DOI: `10.4050/jahs.49.445`. URL: `http://dx.doi.org/10.4050/JAHS.49.445`.

[78] J. Park, D. Linton, and B. Thornber. “Detached-Eddy Simulation of UH-60A Airloads using an Immersed Boundary Method”. In: *49th European Rotorcraft Forum*. Bueckeburg, Germany, Sept. 2023.

[79] C. S. Peskin. “Flow patterns around heart valves: A numerical method”. In: *Journal of Computational Physics* 10.2 (Oct. 1972), pp. 252–271. ISSN: 0021-9991. DOI: `10.1016/0021-9991(72)90065-4`. URL: `http://dx.doi.org/10.1016/0021-9991(72)90065-4`.

[80] D. A. Peters. “How Dynamic Inflow Survives in the Competitive World of Rotorcraft Aerodynamics”. In: *Journal of the American Helicopter Society* 54.1 (Jan. 2009), pp. 11001–1100115. ISSN: 2161-6027. DOI: `10.4050/jahs.54.011001`. URL: `http://dx.doi.org/10.4050/JAHS.54.011001`.

[81] D. A. Peters and C. J. He. “Finite state induced flow models. II-Three-dimensional rotor disk”. In: *Journal of Aircraft* 32.2 (1995), pp. 323–333.

[82] D. M. Pitt and D. A. Peters. “Theoretical prediction of dynamic-inflow derivatives”. In: *6th European Rotorcraft Forum*. Bristol, England, 1980.

[83] L. Prandtl. “Schraubenpropeller mit geringstem Energieverlust. Mit einem Zusatz von L. Prandtl”. In: *Nachrichten von der Gesellschaft der Wissenschaften zu Göttingen, Mathematisch-Physikalische Klasse* 1919 (1919), pp. 193–217.

[84] J. P. Rabbott Jr. *Static-thrust measurements of the aerodynamic loading on a helicopter rotor blade*. Tech. rep. National Aeronautics and Space Administration Washington DC, 1956.

[85] R. P. Rabbott Jr and G. B. Churchill. *Experimental investigation of the aerodynamic loading on a helicopter rotor blade in forward flight*. Tech. rep. National Aeronautics and Space Administration Washington DC, 1956.

[86] N. Rajmohan and C. He. “A VPM/CFD Coupling Methodology to Study Rotor/Ship Aerodynamic Interaction”. In: *AIAA Modeling and Simulation Technologies Conference*. San Diego, CA, Jan. 2016. DOI: `10.2514/6.2016-1915`. URL: `http://dx.doi.org/10.2514/6.2016-1915`.

[87] N. Rajmohan et al. “An efficient pod based technique to model rotor/ship airwake interaction”. In: *Proceedings of the AHS International 68th Annual Forum*. 3. Fort Worth, Texas, May 2012.

[88] W. Rex, T. Pflumm, and M. Hajek. “UH-60A Rotor and Coupled Rotor-Fuselage Simulation Framework Validation and Analysis”. In: *45th European Rotorcraft Forum*. Warsaw, Poland, Sept. 2019.

[89] M. Rinker et al. “Simulation of Rotor-Empennage Interactional Aerodynamics in Comparison to Experimental Data”. In: *Proceedings of the Vertical Flight Society 75th Annual Forum*. Philadelphia, PA, May 2019. DOI: `10.4050/f-0075-2019-14504`. URL: `http://dx.doi.org/10.4050/F-0075-2019-14504`.

[90] U. Saetti. “Linearization of a Rotor Simulation with a State-Space Free-Vortex Wake Model in a Shipboard Environment”. In: *AIAA AVIATION 2022 Forum*. Chicago, IL, June 2022. DOI: `10.2514/6.2022-3646`. URL: `http://dx.doi.org/10.2514/6.2022-3646`.

[91] U. Saetti. “Real-Time Simulation of a Shipborne Rotor via Linearized State-Space Free-Vortex Wake Models”. In: *Journal of Aircraft* (Feb. 2024), pp. 1–9. ISSN: 1533-3868. DOI: `10.2514/1.c037389`. URL: `http://dx.doi.org/10.2514/1.C037389`.

[92] M. B. Schlaffer. “Non-reflecting boundary conditions for the lattice Boltzmann method”. PhD thesis. Technische Universität München, 2013.

[93] P. M. Shinoda, H. Yeo, and T. R. Norman. “Rotor performance of a UH-60 rotor system in the NASA Ames 80-by 120-Foot Wind Tunnel”. In: *Journal of the American Helicopter Society* 49.4 (2004), pp. 401–413.

[94] M. Shives and C. Crawford. “Mesh and load distribution requirements for actuator line CFD simulations”. In: *Wind Energy* 16.8 (Aug. 2012), pp. 1183–1196. ISSN: 1099-1824. DOI: `10.1002/we.1546`. URL: `http://dx.doi.org/10.1002/we.1546`.

[95] J. Smagorinsky. “General Circulation Experiments with the Primitive Equations: I. The Basic Experiment”. In: *Monthly Weather Review* 91.3 (Mar. 1963), pp. 99–164. ISSN: 1520-0493. DOI: `10.1175/1520-0493(1963)091<0099:gcewtp>2.3.co;2`. URL: `http://dx.doi.org/10.1175/1520-0493(1963)091<0099:GCEWTP>2.3.CO;2`.

[96] J. N. Sørensen and W. Z. Shen. “Numerical Modeling of Wind Turbine Wakes ”. In: *Journal of Fluids Engineering* 124.2 (May 2002), pp. 393–399. ISSN: 0098-2202. DOI: `10.1115/1.1471361`. eprint: `https://asmedigitalcollection.asme.org/fluidsengineering/article-pdf/124/2/393/5678518/393\_1.pdf`. URL: `https://doi.org/10.1115/1.1471361`.

[97] R. Stanly, L. A. Martínez-Tossas, S. H. Frankel, and Y. Delorme. “Large-Eddy Simulation of a wind turbine using a Filtered Actuator Line Model”. In: *Journal of Wind Engineering and Industrial Aerodynamics* 222 (2022), p. 104868. ISSN: 0167-6105. DOI: `https://doi.org/10.1016/j.jweia.2021.104868`. URL: `https://www.sciencedirect.com/science/article/pii/S016761052100341X`.

[98] H Tadghighi. “Simulation of rotor-body interactional aerodynamics- An unsteady rotor source distributed disk model”. In: *57th AHS Annual Forum, Washington, DC*. May 2001.

[99] H Tadghighi and V Anand. “Simulation of rotor-body interactional aerodynamics: a time accurate rotor model”. In: *61st Annual Forum of the American Helicopter Society*. 1. Grapevine, TX, June 2005.

[100] J. F. Tan, T. Y. Zhou, Y. M. Sun, and G. N. Barakos. “Numerical investigation of the aerodynamic interaction between a tiltrotor and a tandem rotor during shipboard operations”. In: *Aerospace Science and Technology* 87 (Apr. 2019), pp. 62–72. ISSN: 1270-9638. DOI: `10.1016/j.ast.2019.02.005`. URL: `http://dx.doi.org/10.1016/j.ast.2019.02.005`.

[101] G. P. Turner, G. D. Padfield, and M. Harris. “Encounters with Aircraft Vortex Wakes: The Impact on Helicopter Handling Qualities”. In: *Journal of Aircraft* 39.5 (Sept. 2002), pp. 839–849. ISSN: 1533-3868. DOI: `10.2514/2.3004`. URL: `http://dx.doi.org/10.2514/2.3004`.

[102] J. Valentin and L. Bernardos. “Validation of a New Solver based on the Vortex Particle Method for Wings, Propellers and Rotors”. en. In: *49th European Rotorcraft Forum*. Bueckeburg, Germany, Sept. 2023.

[103] W. R. M. Van Hoydonck, H. Haverdings, and M. D. Pavel. “A Review Of Rotorcraft Wake Modeling Methods for Flight Dynamics Applications”. In: *35th European Rotorcraft Forum*. Hamburg, Germany, Sept. 2009.

[104] G. R. Whitehouse and R. E. Brown. “Modeling the Mutual Distortions of Interacting Helicopter and Aircraft Wakes”. In: *Journal of Aircraft* 40.3 (May 2003), pp. 440–449. ISSN: 1533-3868. DOI: `10.2514/2.3139`. URL: `http://dx.doi.org/10.2514/2.3139`.

[105] G. R. Whitehouse and R. E. Brown. “Modelling a helicopter rotor’s response to wake encounters”. In: *The Aeronautical Journal* 108.1079 (2004), pp. 15–26. DOI: `10.1017/S0001924000004954`.

[106] G. R. Whitehouse, R. E. Brown, and U London. “Helicopter Rotor Response to Wake Encounters in Ground Effect”. In: *59th Annual Forum Proceedings of the American Helicopter Society*. 2. American Helicopter Society. Phoenix, AZ, May 2003, pp. 1802–1817.

[107] G. Winckelmans, R. Cocle, L. Dufresne, and R. Capart. “Vortex methods and their application to trailing wake vortex simulations”. In: *Comptes Rendus. Physique* 6.4–5 (May 2005), pp. 467–486. ISSN: 1878-1535. DOI: `10.1016/j.crhy.2005.05.001`. URL: `http://dx.doi.org/10.1016/j.crhy.2005.05.001`.

[108] M. Wittmann, T. Zeiser, G. Hager, and G. Wellein. “Comparison of different propagation steps for lattice Boltzmann methods”. In: *Computers & Mathematics with Applications* 65.6 (Mar. 2013), pp. 924–935. ISSN: 0898-1221. DOI: `10.1016/j.camwa.2012.05.002`. URL: `http://dx.doi.org/10.1016/j.camwa.2012.05.002`.

[109] M. A. Woodgate, G Barakos, R. Steijl, and G. J. Pringle. “Towards real time wake computations using Lattice Boltzmann Method for flight dynamics simulations”. In: *42nd European Rotorcraft Forum*. Lille, France, Sept. 2016.

[110] M. A. Woodgate, G. N. Barakos, R. Steijl, and G. J. Pringle. “Parallel performance for a real time Lattice Boltzmann code”. In: *Computers & Fluids* 173 (Sept. 2018), pp. 237–258. ISSN: 0045-7930. DOI: `10.1016/j.compfluid.2018.03.004`. URL: `http://dx.doi.org/10.1016/j.compfluid.2018.03.004`.

[111] M. A. Woodgate, R. Steijl, and G. N. Barakos. “Real time wake computations using Lattice Boltzmann method on many integrated core processors”. In: *43rd European Rotorcraft Forum*. Milan, Italy, Sept. 2017.

[112] H. Yeo, W. G. Bousman, and W. Johnson. “Performance analysis of a utility helicopter with standard and advanced rotors”. In: *Journal of the American Helicopter Society* 49.3 (2004), pp. 250–270.

[113] K. Yu and D. A. Peters. “Nonlinear State-Space Modeling of Dynamic Ground Effect”. In: *Journal of the American Helicopter Society* 50.3 (2005), p. 259. ISSN: 0002-8711. DOI: `10.4050/1.3092862`. URL: `http://dx.doi.org/10.4050/1.3092862`.

[114] J. Zhao and C. He. “A Viscous Vortex Particle Model for Rotor Wake and Interference Analysis”. In: *Journal of the American Helicopter Society* 55.1 (Jan. 2010), pp. 12007–1200714. ISSN: 2161-6027. DOI: `10.4050/jahs.55.012007`. URL: `http://dx.doi.org/10.4050/JAHS.55.012007`.

[115] J. Zhao, J. V. R. Prasad, and D. A. Peters. “Rotor Dynamic Wake Distortion Model for Helicopter Maneuvering Flight”. In: *Journal of the American Helicopter Society* 49.4 (Oct. 2004), pp. 414–424. ISSN: 2161-6027. DOI: `10.4050/jahs.49.414`. URL: `http://dx.doi.org/10.4050/JAHS.49.414`.

[116] A. Štrbac, M.-J. Maibach, D. H. Greiwe, A. Kalra, and A. Gardner. “Evaluation of Pilot Assistance Systems for Helicopter Ship Deck Landing”. In: *78th Annual Vertical Flight Society Forum and Technology Display, FORUM 2022*. Forth Worth, TX, May 2022. URL: `https://elib.dlr.de/187052/`.

# A. Experimental Rotor Results

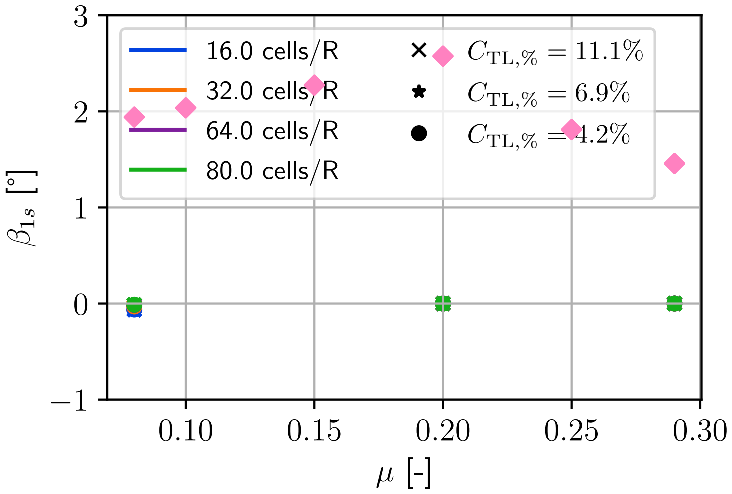

**Figure 86** Lateral blade flap angles predicted by the linear-harmonic inflow model for the experimental rotor compared to wind tunnel measurements at different $\mu$. Experimental reference data is taken from [85]

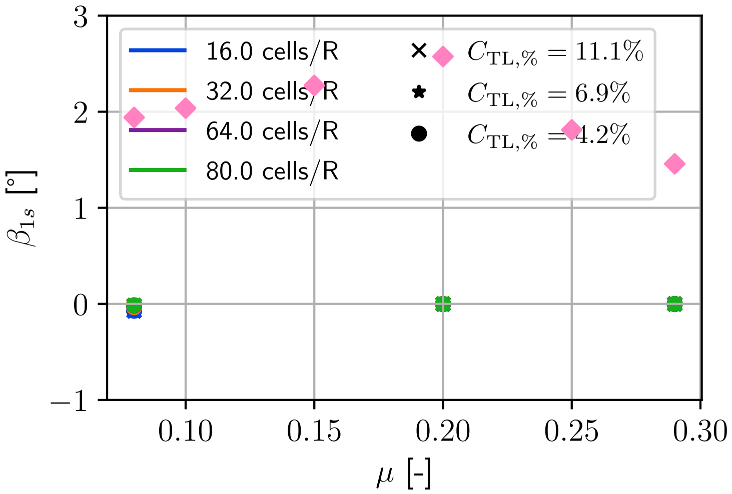

**Figure 87** Lateral blade flap angles predicted by the Bessel-Fourier inflow model for the experimental rotor compared to wind tunnel measurements at different $\mu$. Experimental reference data is taken from [85]

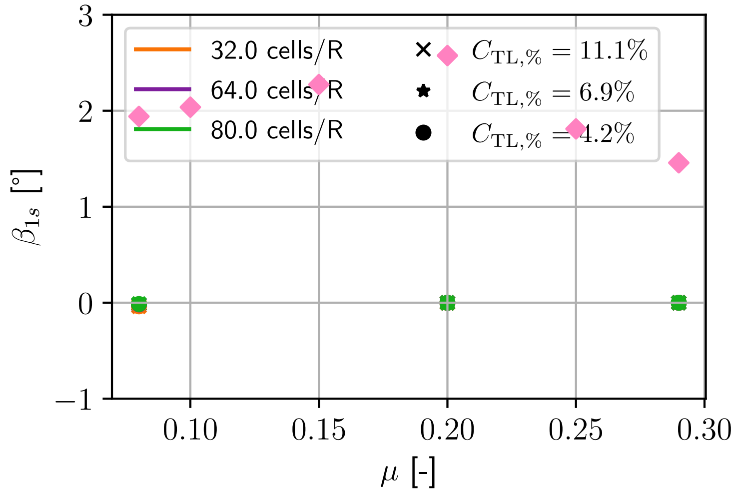

**Figure 88** Lateral blade flap angles predicted by the ACL model using a restricted force kernel for the experimental rotor compared to wind tunnel measurements at different $\mu$. Experimental reference data is taken from [85]

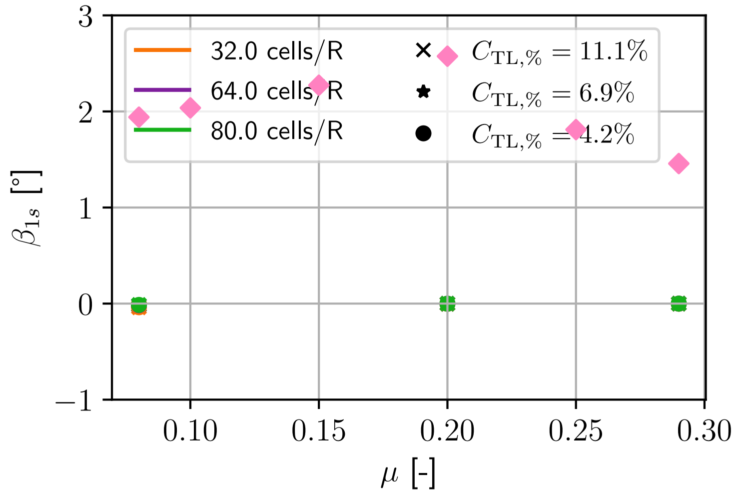

**Figure 89** Lateral blade flap angles predicted by the ACL model using a spherical force kernel for the experimental rotor compared to wind tunnel measurements at different $\mu$. Experimental reference data is taken from [85]

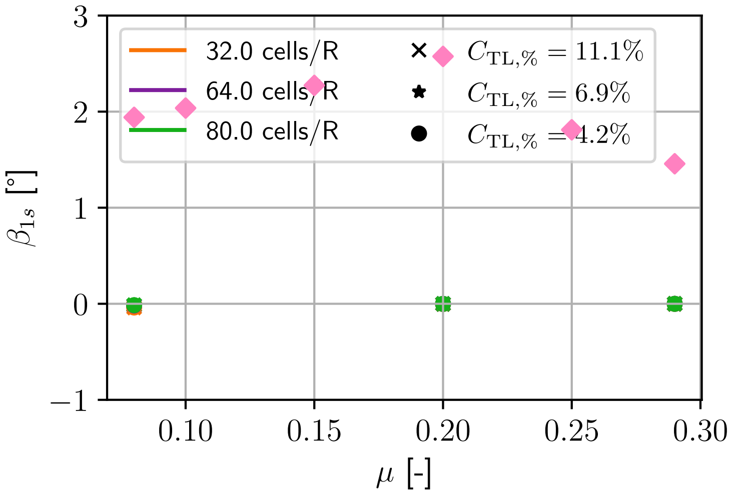

**Figure 90** Lateral blade flap angles predicted by the ACL model with the inflow correction for the experimental rotor compared to wind tunnel measurements at different $\mu$. Experimental reference data is taken from [85]

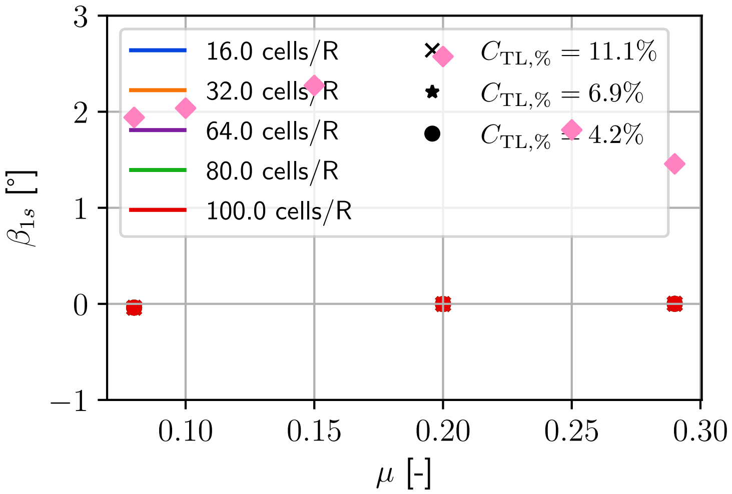

**Figure 91** Lateral blade flap angles predicted by the Peters–He inflow model for the experimental rotor compared to wind tunnel measurements at different $\mu$. Experimental reference data is taken from [85]

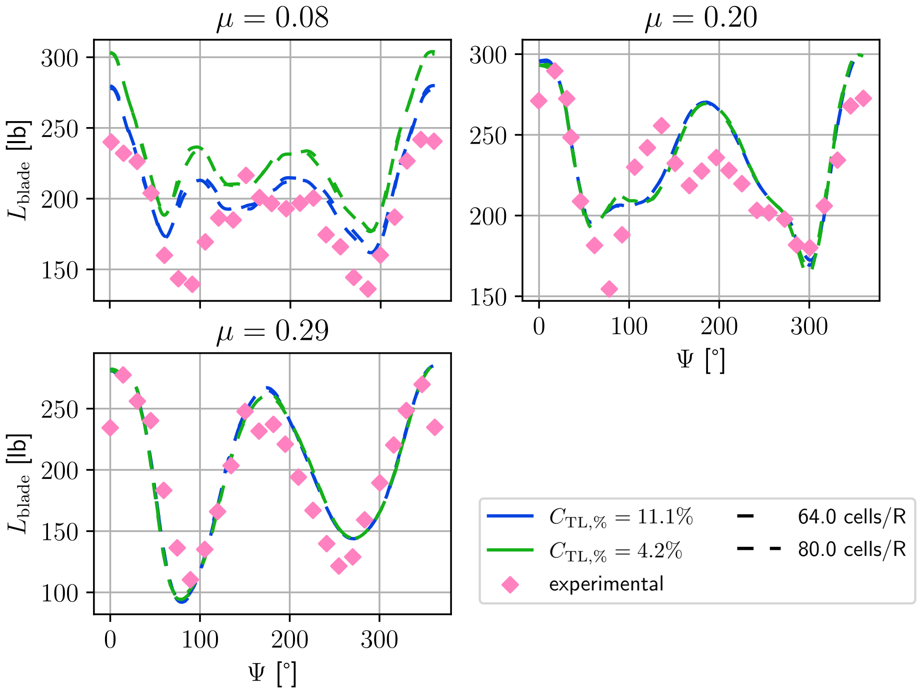

**Figure 92** Total blade lift predicted by the ACL inflow model with inflow correction at different $\mu$ compared to experimental measurements from [85]. Results are shown for a reduced set of considered tip loss and resolutions

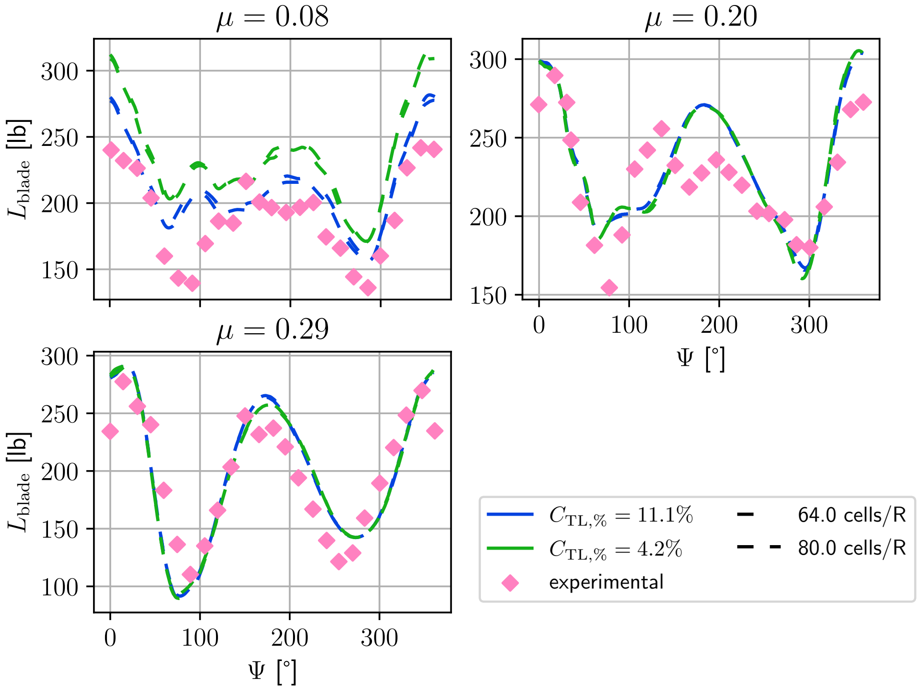

**Figure 93** Total blade lift predicted by the ACL inflow model with a spherical force kernel at different $\mu$ compared to experimental measurements from [85]. Results are shown for a reduced set of considered tip loss and resolutions

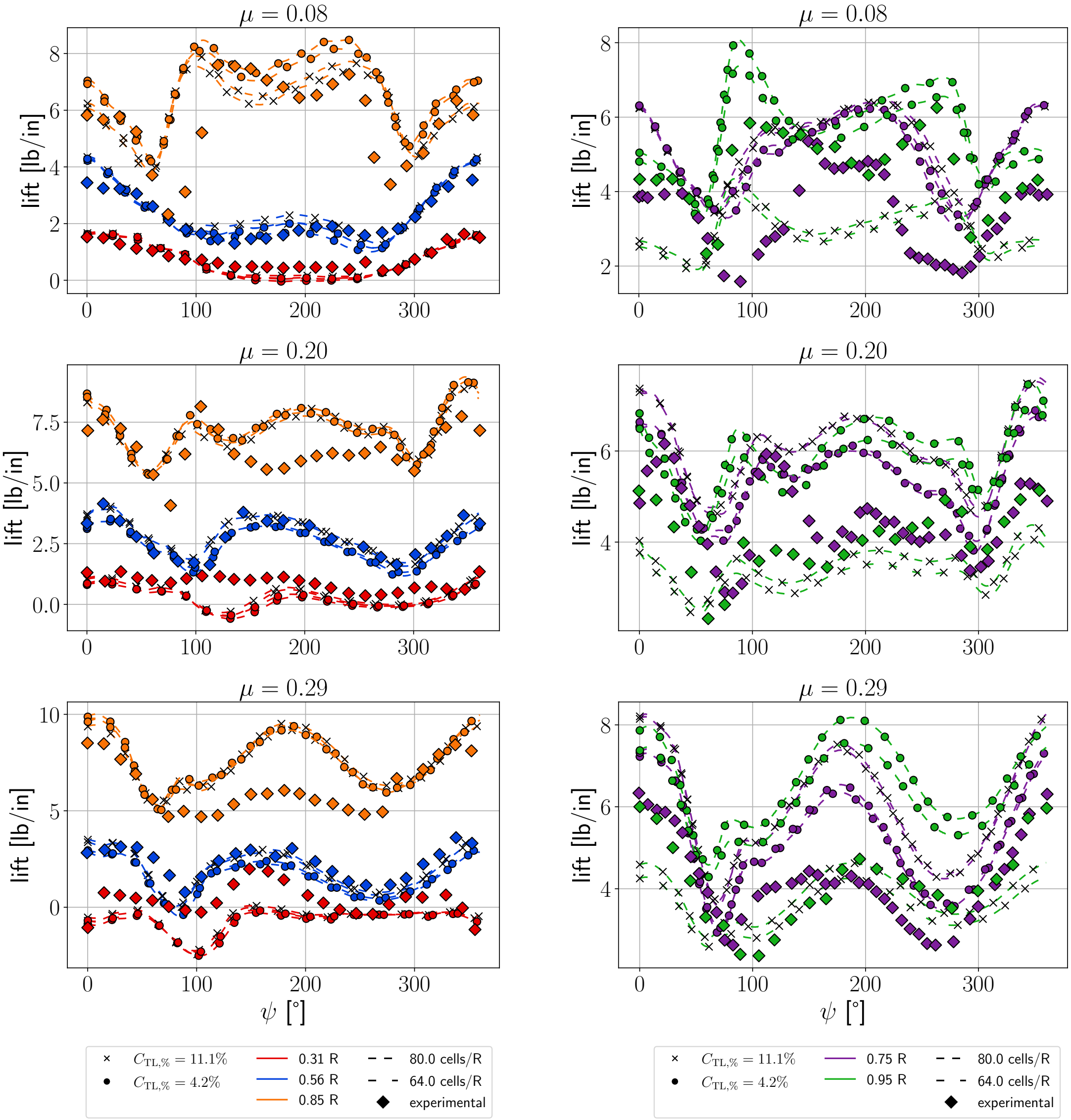

(a) ..

(b) ...

**Figure 94** Sectional lift at five radial stations for different $\mu$ predicted by the ACL inflow model with inflow correction. Results show variation of $C_{\mathrm{t1},\%}$ and resolution. Experimental measurements from [85].

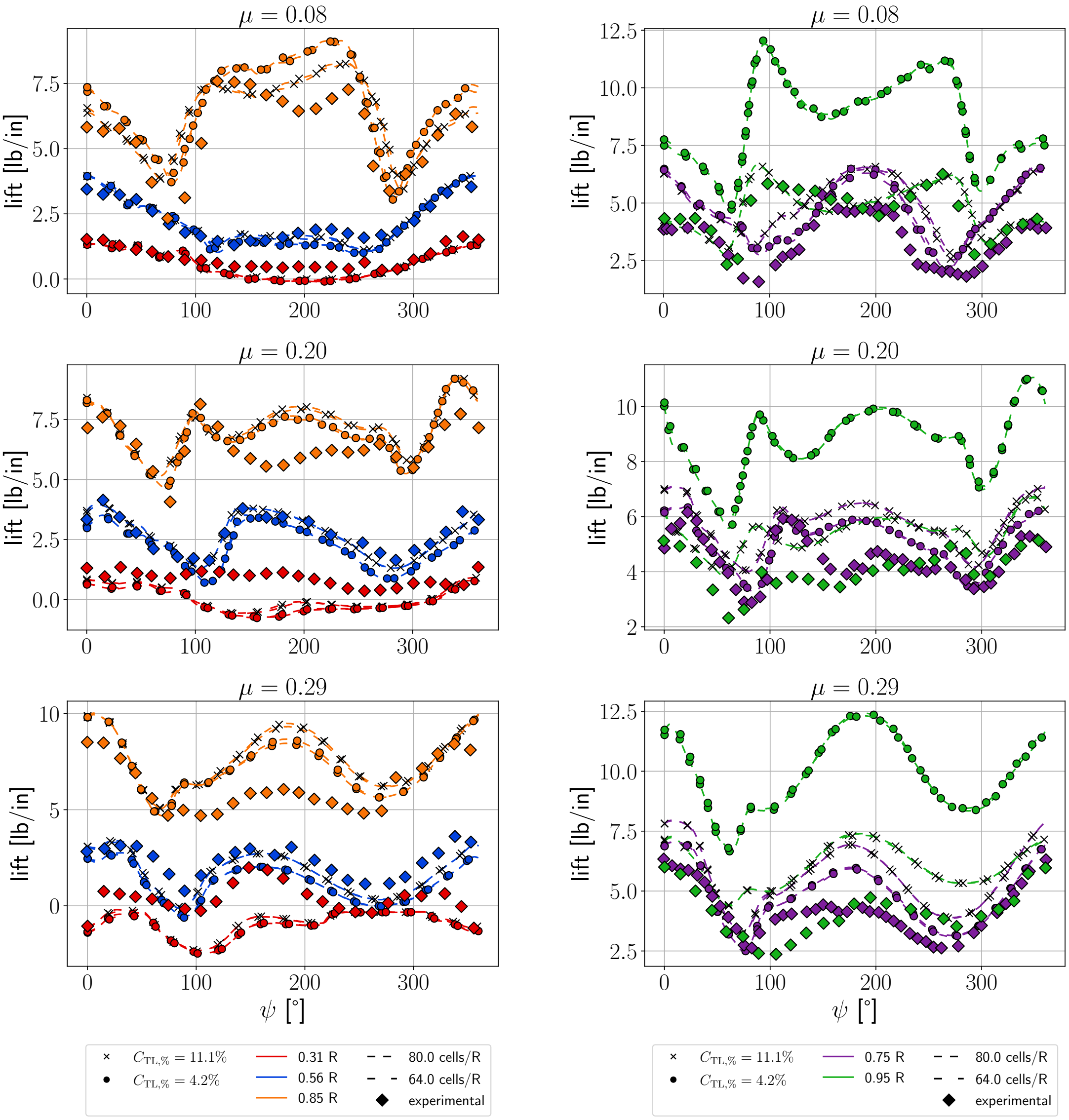

(a) ..

(b) ...

**Figure 95** Sectional lift at five radial stations for different $\mu$ predicted by the ACL inflow model using a spherical force kernel. Results show variation of $C_{\mathrm{t1},\%}$ and resolution. Experimental measurements from [85].

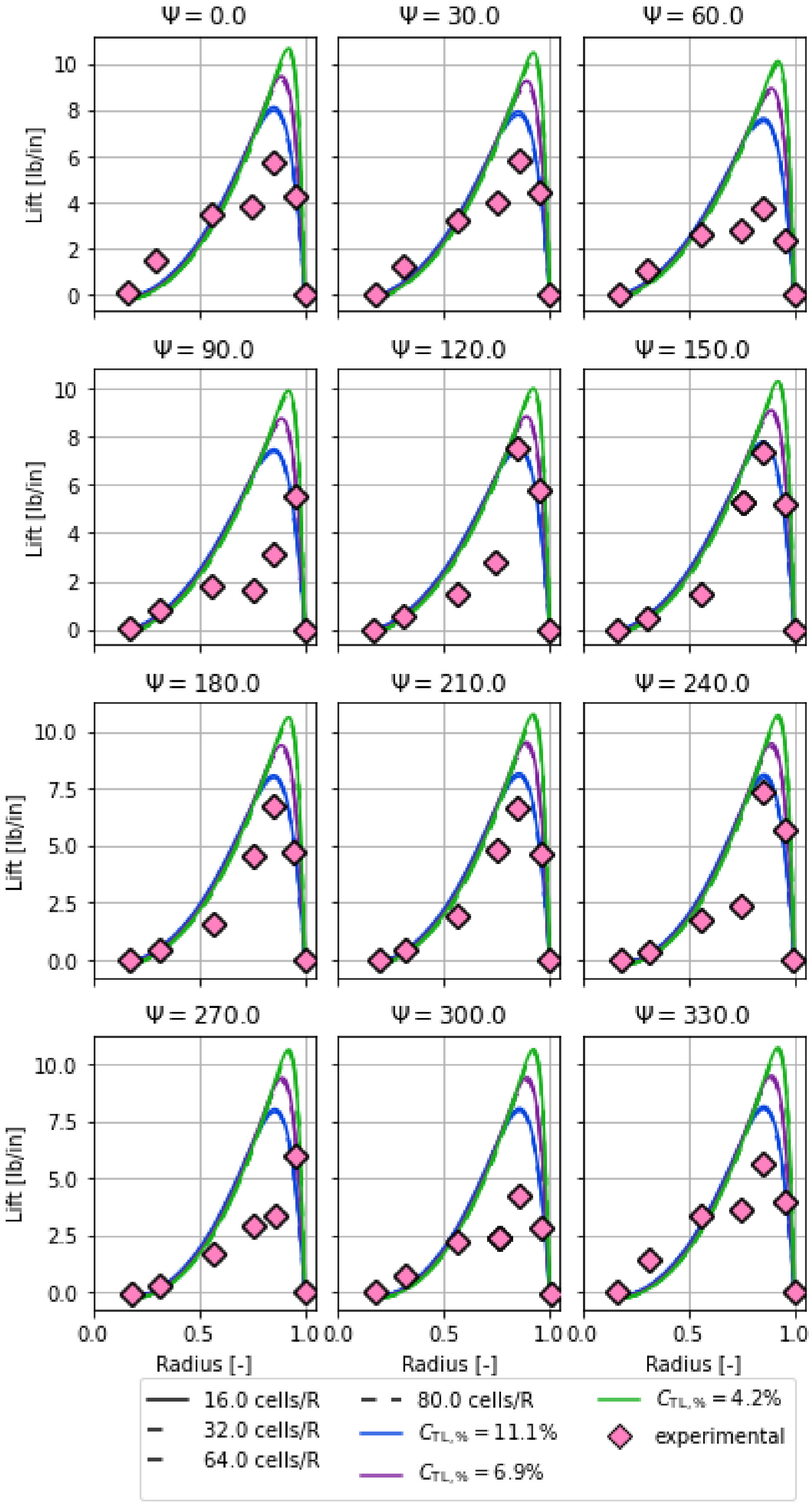

**Figure 96** Radial lift prediction by the linear-harmonic inflow model at twelve azimuth locations for $\mu = 0.08$ compared against measurements from [85].

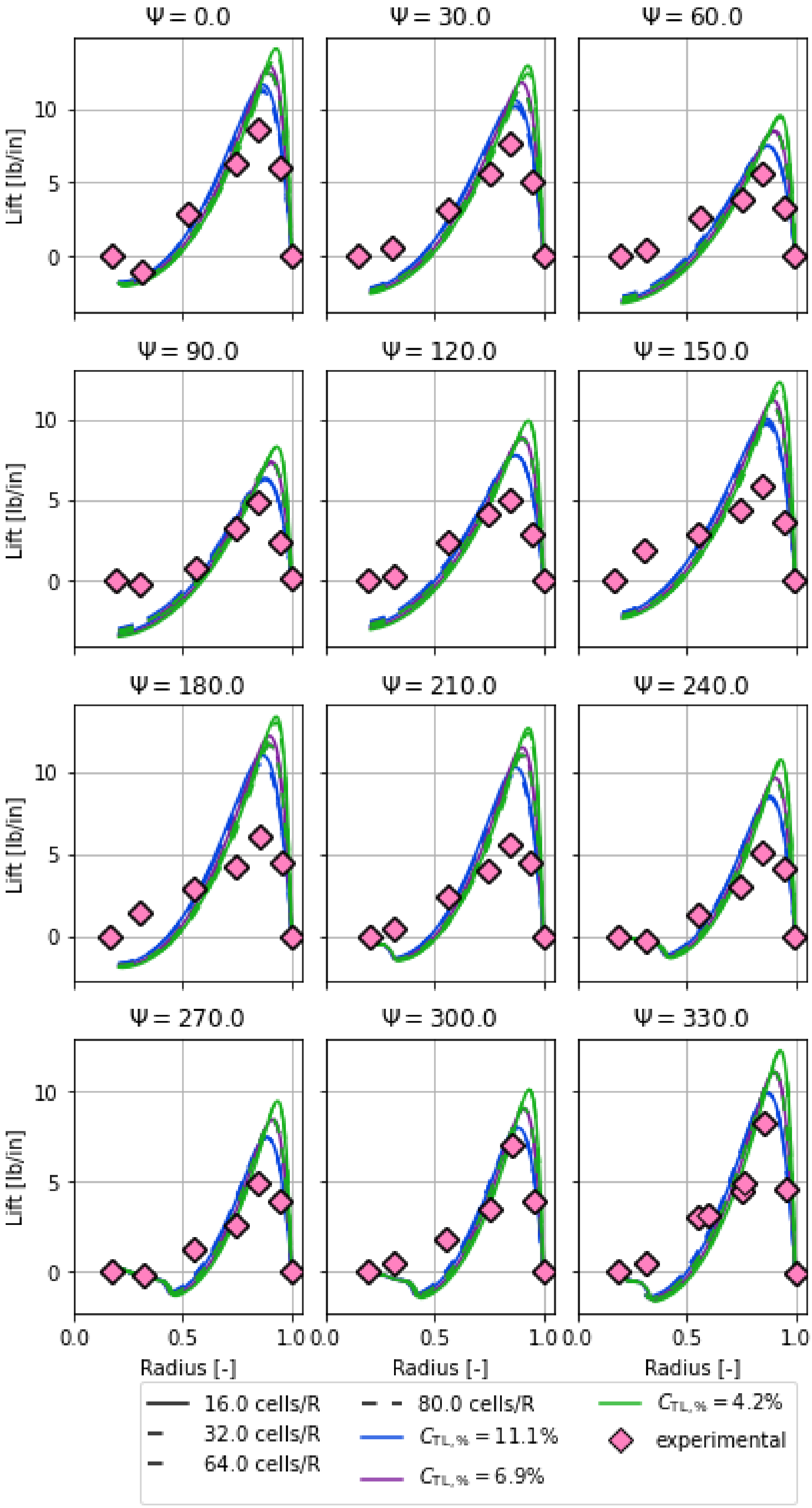

**Figure 97** Radial lift prediction by the linear-harmonic inflow model at twelve azimuth locations for $\mu = 0.29$ compared against measurements from [85].

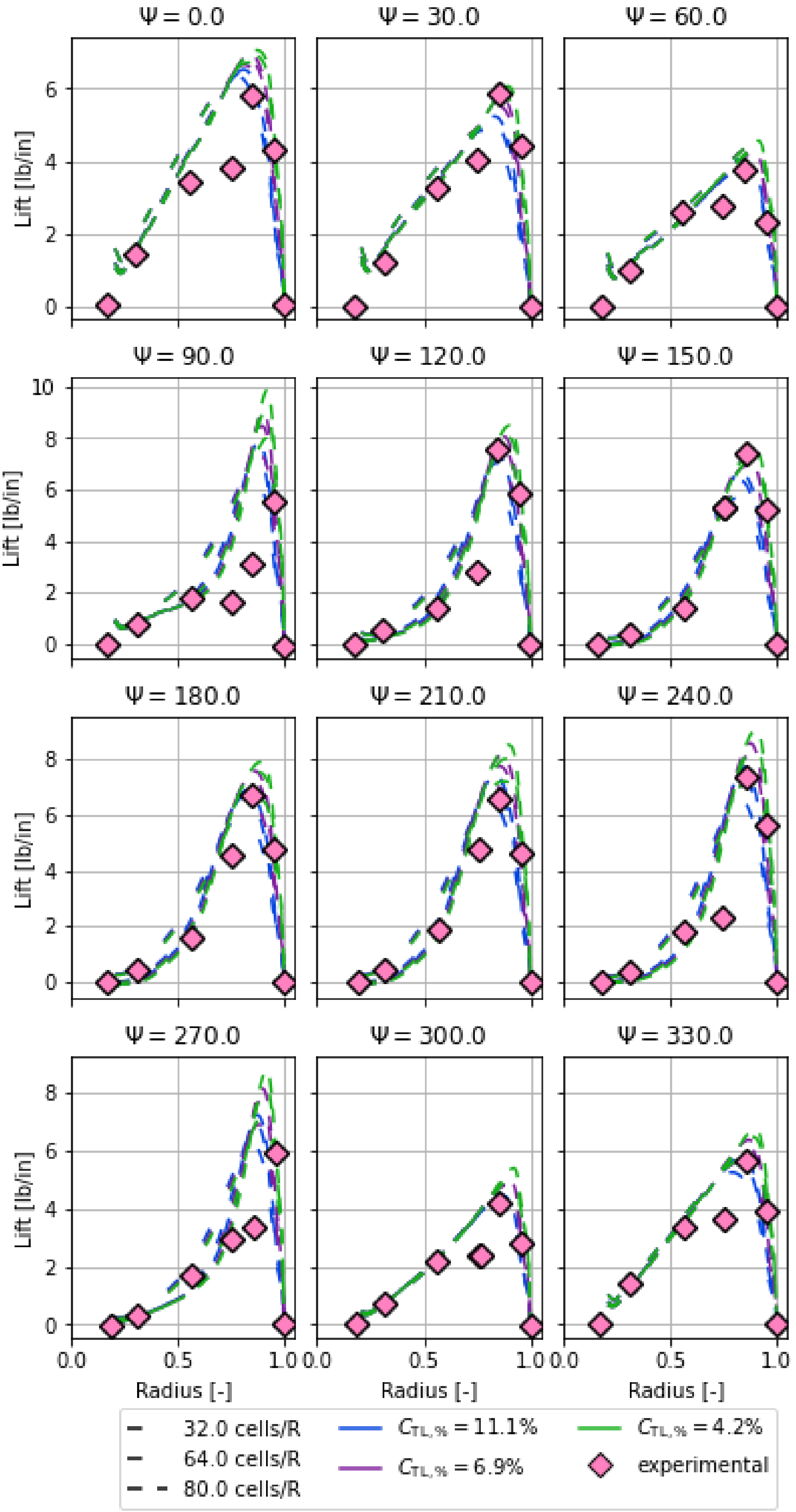

**Figure 98** Radial lift prediction by the ACL inflow model with inflow correction at twelve azimuth locations for $\mu = 0.08$ compared against measurements from [85].

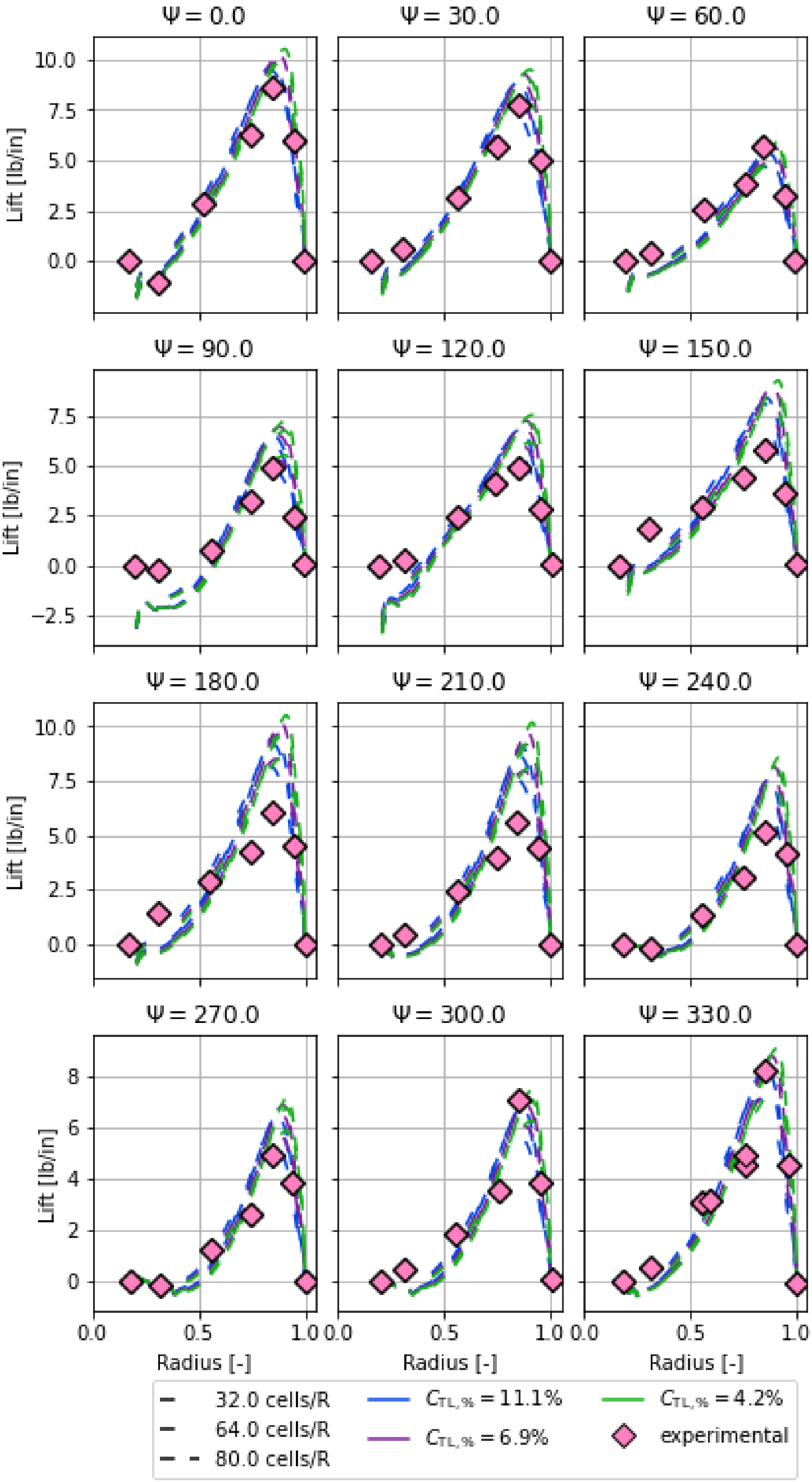

**Figure 99** Radial lift prediction by the ACL inflow model with inflow correction at twelve azimuth locations for $\mu = 0.29$ compared against measurements from [85].

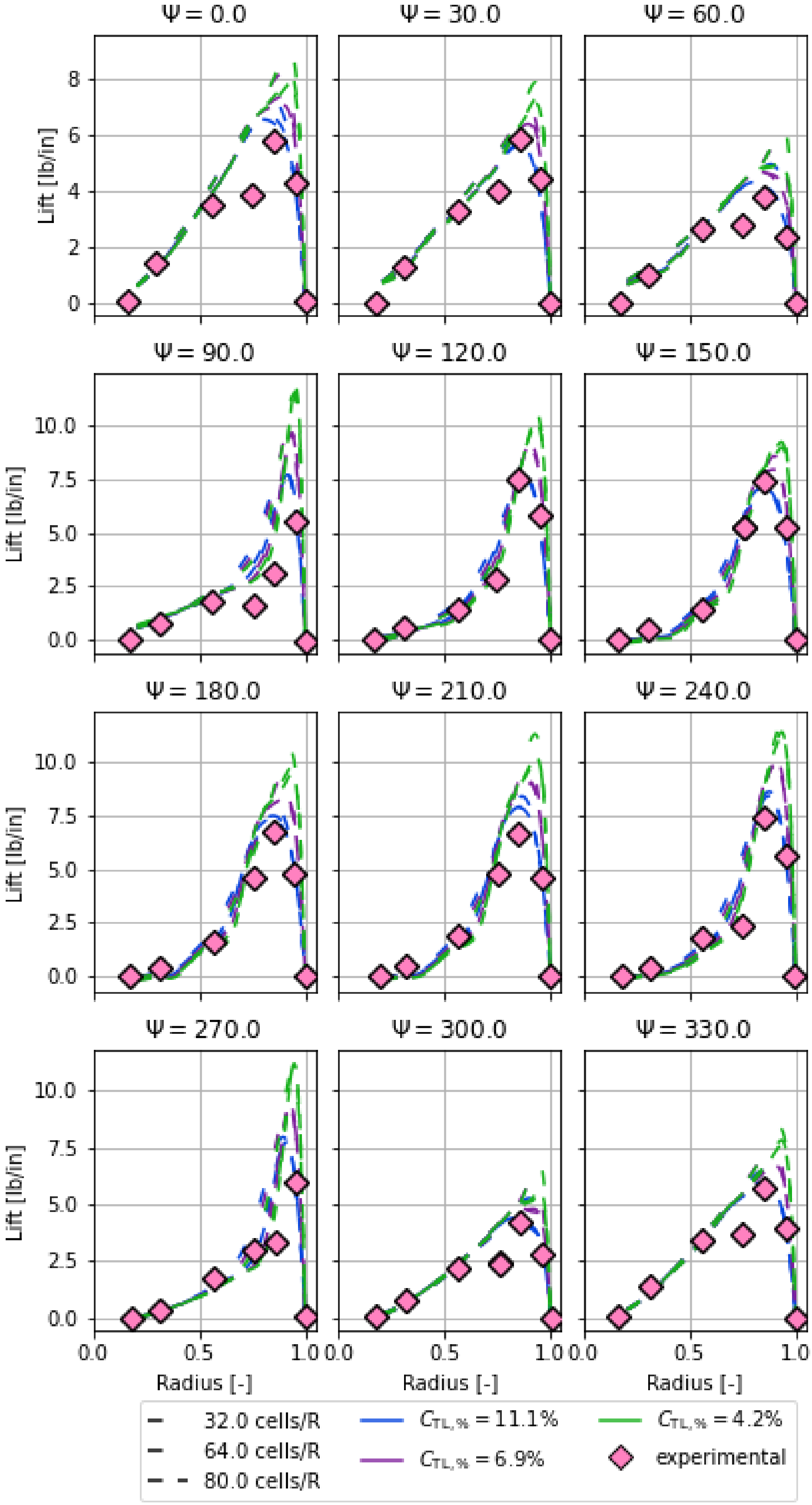

**Figure 100** Radial lift prediction by the ACL inflow model with spherical force kernel at twelve azimuth locations for $\mu = 0.08$ compared against measurements from [85].

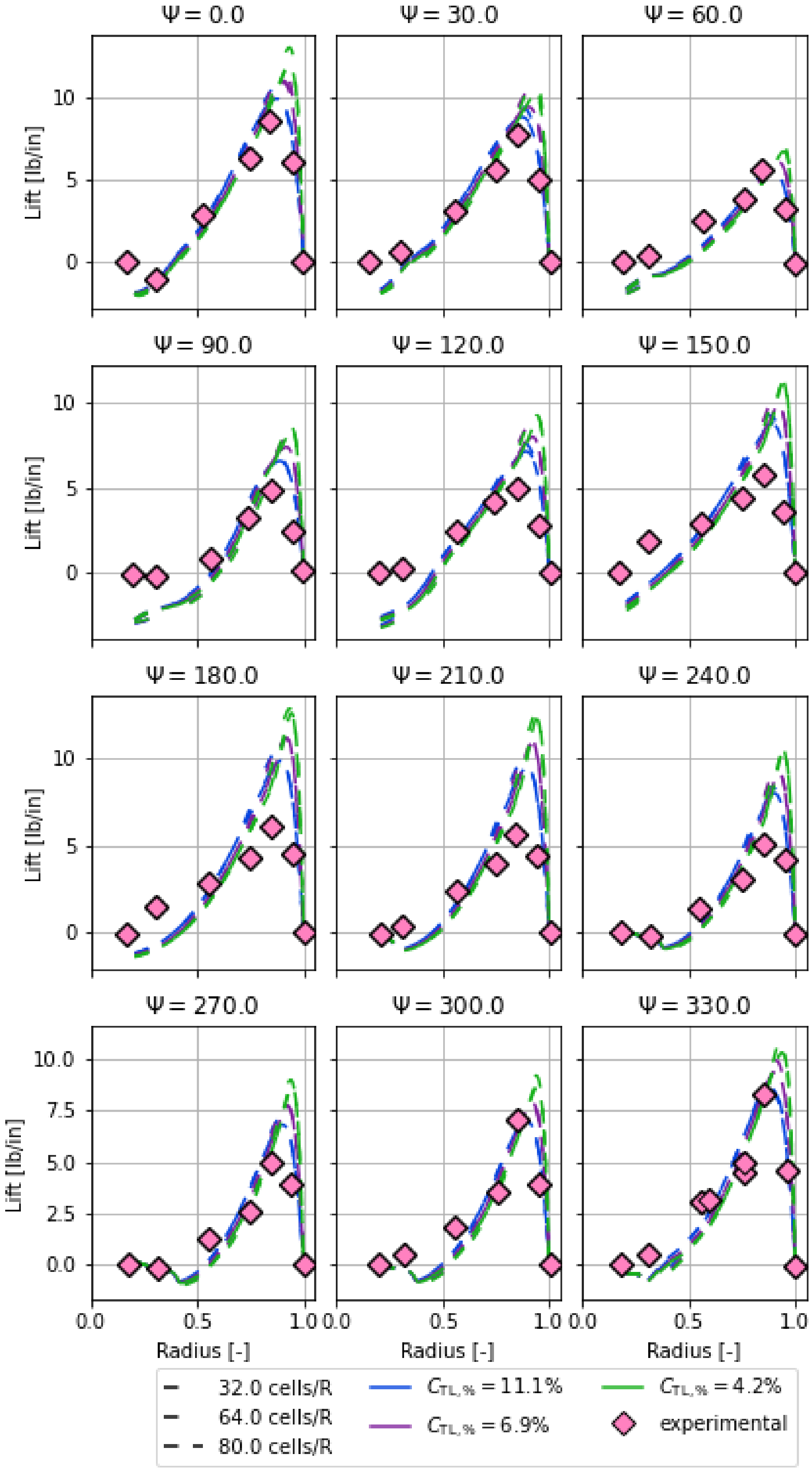

**Figure 101** Radial lift prediction by the ACL inflow model with spherical force kernel at twelve azimuth locations for $\mu = 0.29$ compared against measurements from [85].

# B. Vortex Interaction Results

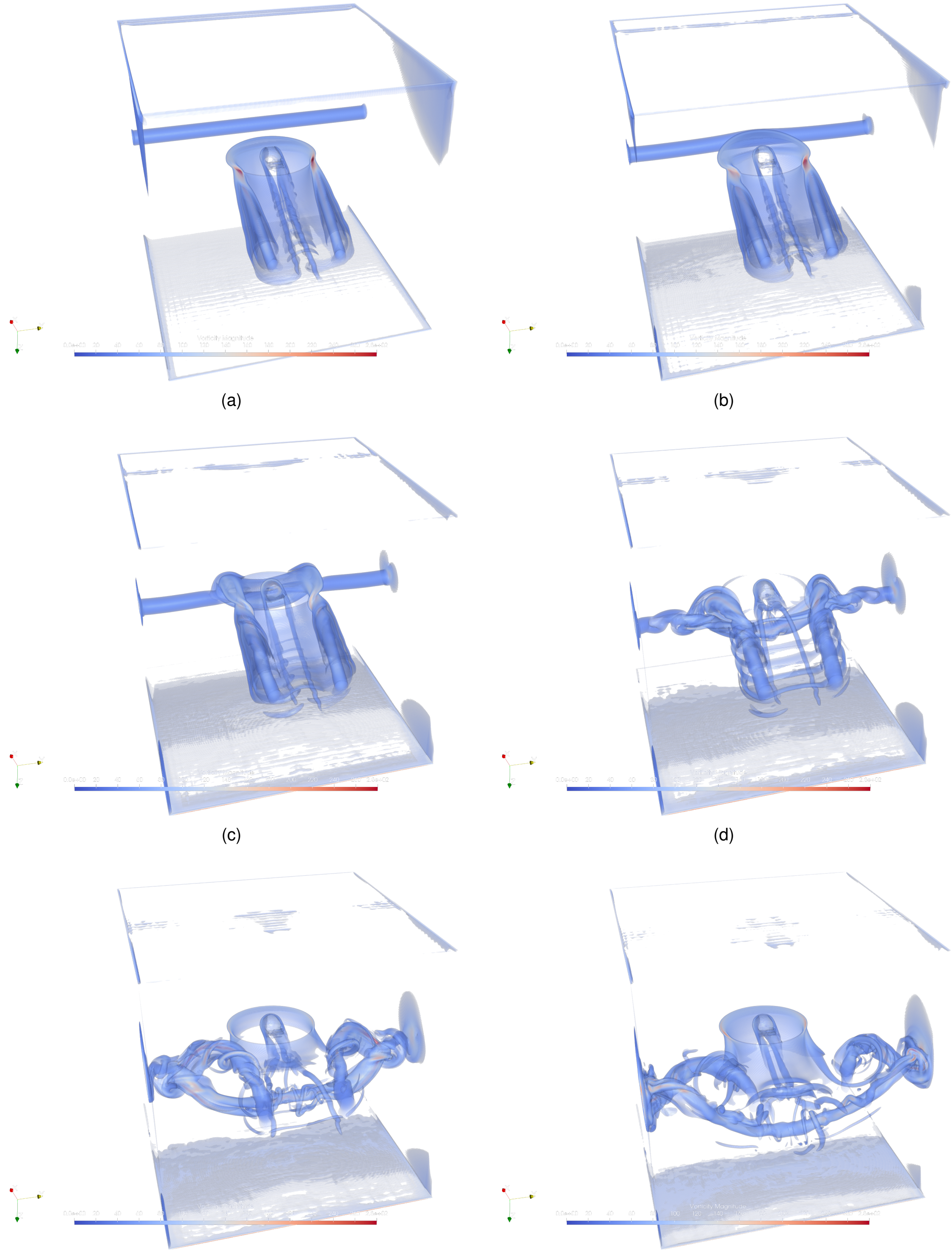

(a) (b) (c) (d) (e) (f)

**Figure 102** Visualization of the vortex encounter simulated with the linear-harmonic inflow model. Contour shows vorticity.

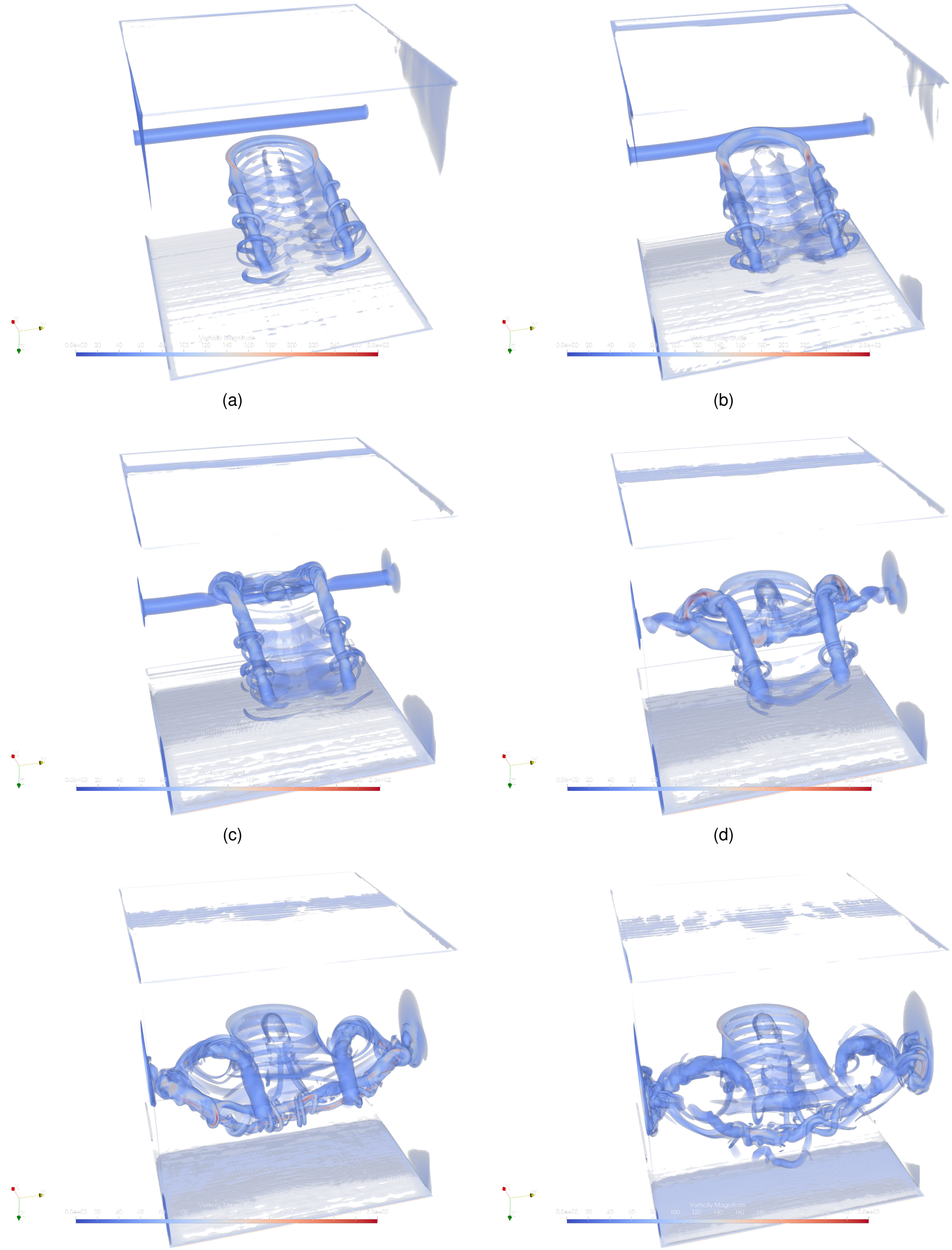

(a) (b)

(c) (d)

(e) (f)

**Figure 103** Visualization of the vortex encounter simulated with the Bessel-Fourier inflow model. Contour shows vorticity.

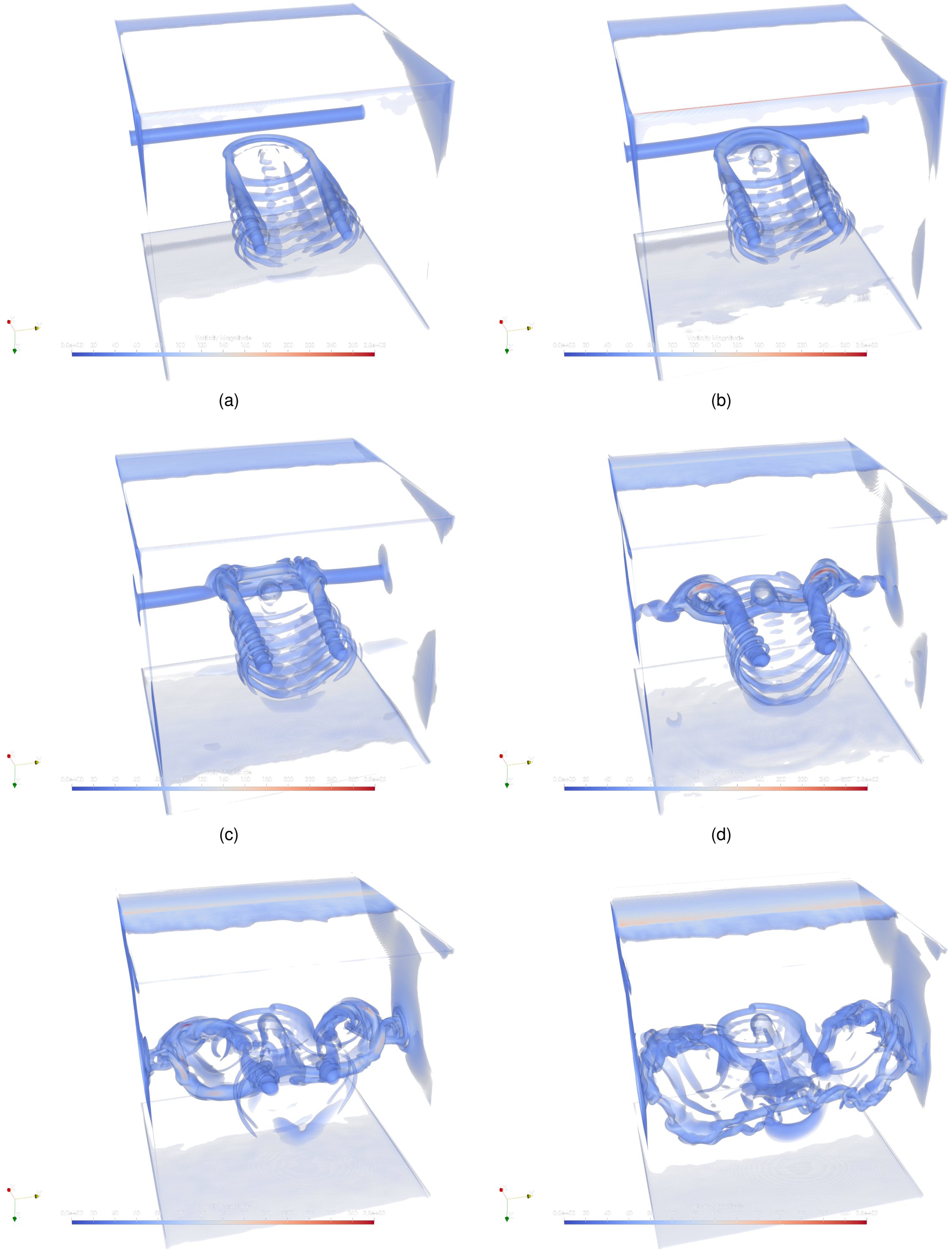

(a)

(b)

(c)

(d)

(e)

(f)

**Figure 104** Visualization of the vortex encounter simulated with the ACL inflow model using a spherical force kernel. Contour shows vorticity.